

Intelligent Health Management for Micro-Scale Wind Turbine Bearings

by

Ahmed N-s Abufroukh

A thesis submitted in partial fulfilment for the requirements for the degree of MSc (by Research) at the University of Central Lancashire

January, 2018

STUDENT DECLARATION FORM

Concurrent registration for two or more academic awards

I declare that while registered as a candidate for the research degree, I have not been a registered candidate or enrolled student for another award of the University or other academic or professional institution

Material submitted for another award

I declare that no material contained in the thesis has been used in any other submission for an academic award is solely my own work

Signature of Candidate _____ *Ahmed Abufroukh* _____

Type of Award _____ MSc (By Research) _____

School _____ School of Engineering _____

Intelligent Health Management for Micro-scale Wind Turbine Bearings

Ahmed N-s Abufroukh

University of Central Lancashire, School of Engineering

Master of Science (By Research)

ABSTRACT: The noticeable expansion of the wind turbine industry in the UK has been encouraged by the government, which announced a range of incentives to meet the increased demand for wind turbine technologies, as a contribution to the effects against climate change. The UK is embracing the challenge of preventing 0.8 million tonnes of pollution through deploying approximately 806MW of small and medium turbines by 2023. Consequently, appropriate maintenance strategies to lengthen the life of turbine elements, including main shaft, bearings, gearbox and generator should be considered. Bearings tend to be one of the most common defective elements. Defects may occur for many reasons including contamination, lubrication problems and excessive operational conditions; thus, failure can take several forms and could arise in any part of the bearing elements. These factors are not included in the basic rating life (L_{10}) – calculation proposed by ISO281. Thus determining the life of the bearing is challenging.

A thorough literature review was conducted to investigate the research field including, common failures that occur in micro-scale wind turbine elements such as: bearings, generator, brake and main shaft. This was followed by mutual condition monitoring techniques that are currently used to detect failures. Lastly, intelligent methods that can be incorporated to enhance the performance of the machinery were highlighted.

Illustrations of hardware and software developments were covered in the next chapter, including all the equipment used to construct the test bench throughout this research and all the sensors and controllers that were interfaced to develop the IHMS.

The system then underwent preliminary verification, and finally several tests including bearing system failure and bearing life, were conducted to be studied graphically. Conclusions were drawn from this work, and future directions considered.

This thesis presents a prototype of an Intelligent Health Management System (IHMS) for micro-scale wind turbine bearings. This development addresses various issues in determining bearing life, detecting failure in the machinery. It proposes the use of an intelligent analysis approach that integrates information from key sensors to monitor bearing life. The IHMS was evaluated using a test apparatus developed by the author.

Table of Contents

STUDENT DECLARATION FORM	ii
ABSTRACT	iii
Table of Contents	iv
List of Figures	vii
List of Tables	xii
List of Equations	xiii
List of Acronyms	xiv
Nomenclature	xviii
Acknowledgments	xx
Dedications	xxi
Chapter 1. Introduction	1
1.1. Background	2
1.1.1. Scope	3
1.2. Research aim and objectives	4
1.3. Thesis Structure	5
Chapter 2. Literature review	6
2.1. Introduction	6
2.2. Domestic Wind Turbine Evolution	7
2.3. Defects	9
2.3.1. Bearings	10
2.3.2. Lubrication	19
2.3.3. Generator	21
2.3.4. Brake	22
2.3.5. Main shaft	23
2.4. Condition monitoring techniques	25
2.4.1. Temperature analysis (Thermography)	27
2.4.2. Vibration analysis (VA)	28
2.4.3. Oil Debris Analysis (ODA)	34
2.4.4. Acoustic Emission (AE)	36
2.4.5. Current Signature Analysis (CSA)	39
2.5. Intelligent Condition Monitoring Methods	42
2.5.1. Fuzzy Logic methods	42
2.5.2. Artificial Neural Networks (ANNs)	45

2.5.3.	Genetic Algorithms (GA).....	47
2.5.4.	Expert systems.....	47
2.5.5.	Model-Based Parametric Method Algorithms	48
2.5.6.	Advanced Digital Signal and Image Processing	49
2.6.	Summary.....	51
Chapter 3. Intelligent Health Management System Development for micro-scale wind turbine bearings.....		53
3.1.	Introduction.....	53
3.2.	Description of the test bench.....	54
3.3.	Bearing Loading Mechanisms.....	57
3.3.1.	Radial Loading Mechanism	59
3.3.2.	Brake Loading Mechanisms.....	61
3.4.	Development of Test Bench Input / Output Control System	62
3.4.1.	Sensors	64
3.4.2.	System Controllers.....	74
3.5.	Test Bench Control Software	78
3.6.	Bearing Life Monitoring System	81
3.7.	Bearing Diagnostic System.....	87
3.7.1.	Actuator System for Bearing Failure Detection.....	90
3.8.	Summary.....	93
Chapter 4. Results and Discussion.....		95
4.1.	Introduction.....	95
4.2.	Experimental Test Specifications	96
4.2.1.	Testing procedures.....	97
4.3.	Preliminary Tests.....	102
4.4.	Final Tests.....	105
4.4.1.	First Test: Bearing System Failure; Shaft Failure.....	106
4.4.2.	Second Test: Bearing System Failure; Shaft Failure.....	111
4.4.3.	Third Test: Bearing System Failure; Coupling Failure	121
4.4.4.	Fourth Test: Bearing Life Test	132
4.5.	Advanced Digital Signal and Image Processing	140
4.6.	Summary.....	144
Chapter 5. Conclusion, Recommendations and Future Works		146
5.1.	Conclusion and Recommendations.....	147
5.2.	Experimental Conclusion	149
5.3.	Future work.....	150

Appendix A – Bearing Housings	xxiii
Appendix B – NTC PCB Board	xxv
Appendix C – Thermistor Resistance Vs Temperature	xxvi
Appendix D – Torque Meter Riser	xxvii
Appendix E – Bearing life Calculation codes	xxviii
Appendix F – Bearing diagnostic system code (Vibration analysis)	xxxi
Appendix G – Relay PCB Board	xxxiv
Appendix H – First Test: Bearing System Failure; Shaft Failure	xxxv
Appendix I – Second Test: Bearing System Failure; Shaft Failure	xxxvi
Appendix J – Fourth Test: Bearing Life Test	xliv
Appendix K – Image Subtraction Code	xlviii
Appendix L – ARMA code in LabVIEW	xliv
Appendix M – Publications	xxiii
References	xxiii

List of Figures

Figure 1. 1: SKF Insight (SKF, 2013).....	3
Figure 2. 1: Wind turbine and Solar Panel (Sarah Bray, 2011)	7
Figure 2. 2: An illustration of the differences between all the micro-turbines types - (i): HAWT, (ii) VAWT, (iii) building mounted and (iv) Pole mounted (Rob B., 2017).....	9
Figure 2. 3: Frequent failure mode in a typical wind turbine (Berthold., 2005)	10
Figure 2. 4: Roller and ball bearing	11
Figure 2. 5: Bearing defects (Radu C., 2010)	12
Figure 2. 6: Excessive loads defect (Barden P. B., 2011).....	14
Figure 2. 7: Overheated bearing (Barden P. B., 2011).....	14
Figure 2. 8: Corrosion symptoms (Barden P. B., 2011).....	15
Figure 2. 9: Fretting corrosion (SKF , 1994)	15
Figure 2. 10: Deep-seated rust (SKF, 1994).	15
Figure 2. 11: Fatigue damage in the outer ring raceway (Kuhnell B.T., 2004)	16
Figure 2. 12: Contamination Failures (Barden P. B., 2011 and Noria C., 2010).....	16
Figure 2. 13: Example of shaft misalignment (Barden P. B., 2011)	17
Figure 2. 14: Proper alignment and misalignment (Lubsys., 2003).....	17
Figure 2. 15: Loose and tight fit failure (Barden P. B., 2011)	18
Figure 2. 16: Lubrication failure symptoms (Barden P. B., 2011).....	19
Figure 2. 17: Causes of failure in rolling bearings (Katz S. and Mike S., 2017).....	19
Figure 2. 18: Bearing Greasing (Wes C. and Rick James, 2013).....	20
Figure 2. 19: Generator installed into Nacelle (Chong P. K., 2013).....	21
Figure 2. 20: Generator (Chong P.K., 2013).....	21
Figure 2. 21: Failures which occur in the different parts of the generator (Nivedh B.S., 2014).....	21
Figure 2. 22: Brake installed into nacelle (Mahon N. M., 2013)	22
Figure 2. 23: Suco Technologies brake (Nic. S., 2013)	22
Figure 2. 24: Main elements of a typical hysteresis brake (Magtrol, 2012)	23
Figure 2. 25: Fracture types (After Teja G. V., 2014)	24
Figure 2. 26: Warning signs (Takousting et al., 2014).....	25
Figure 2. 27: Thermography analysis on cylindrical bearing (Fuentes A. et al., 2012).....	27
Figure 2. 28: Typical frequency response of an accelerometer – the highlighted region illustrates the linear frequency response of an accelerometer (National Instrument, 2007)	29
Figure 2. 29: Wear caused by vibration (Thakar D., 2014)	30
Figure 2. 30: Bearing element (Thakar D., 2014).....	31
Figure 2. 31: Sin waveform example (After Gaatjes, W., 2012)	32
Figure 2. 32: Resampling example (National Instrument, 2007).....	34
Figure 2. 33: (Leavers V.F., 2005)'s classification (Leavers V.F., 2005)	35
Figure 2. 34: AE process chain (Vallen, 2006).....	38
Figure 2. 35: AE measurement chain (Vallen, 2006).....	38
Figure 2. 36: Healthy and Faulty (Sukhjeet S. et al, 2014).....	40
Figure 2. 37: Time domain of faulty bearing - B2 (Sukhjeet S. et al, 2014).....	41
Figure 2. 38: Time domain of healthy bearing - B1 (Sukhjeet S. et al, 2014)	41
Figure 2. 39: Frequency domain of healthy bearing - B1 and faulty bearing - B2 (Sukhjeet S. et al, 2014).....	42
Figure 2. 40: Intelligent CBM architecture (Kothamasu, R. and Huang, S. H., 2007)	44
Figure 2. 41: Backpropagation network (William G. F et al., 2001)	46
Figure 2. 42: Kohonen feature map (J. P. Petersen., 2010a).....	46
Figure 2. 43: Structure of a Genetic Algorithm (GA) (J. P. Petersen., 2010a)	47
Figure 2. 44: Typical expert system (Mitchell M., 1998)	48

Figure 2. 45: A typical image subtraction example	50
Figure 3. 1: Simmal Aluminium Extrusion (Simmal, 2009).....	54
Figure 3. 2: Previous Test Bench.....	54
Figure 3. 3: The developed test bench	55
Figure 3. 4: TEC motor and Optidrive E ² inverter (TEC Electric Motors Ltd., 2010 and Evans P., 2009)	55
Figure 3. 5: HRC coupling (Fenaflex, 2014)	56
Figure 3. 6: NJ 205ECP and 6205-2RSH	56
Figure 3. 7: Radial loading arrangement.....	57
Figure 3. 8: Contact angle of ball bearing (Kaydon, 2014)	57
Figure 3. 9: Roller / cylindrical bearing housing	58
Figure 3. 10: Fit classification (V. Mulani, 2015)	59
Figure 3. 11: Bearings installation	59
Figure 3. 12: Hydraulic bench press (Ali B., 1999).....	60
Figure 3. 13: Tested bearing housing including piston hole	61
Figure 3. 14: Hydraulic press with the new dimensions	61
Figure 3. 15: The resulting moment load (Kaydon, 2014).....	61
Figure 3. 16: Torque / Current Curve (Magtrol, 2015b)	62
Figure 3. 17: IHMS System overview	63
Figure 3. 18: Pressure sensor installed using T-junction	64
Figure 3. 19: Load measurement flowchart	65
Figure 3. 20: NTC temperature sensor.....	66
Figure 3. 21: Temperature sensor connection.....	67
Figure 3. 22: Temperature measurement	68
Figure 3. 23: Thermistor resistance Ω VS Temperature C [°] (Arroyo I, 2016).....	69
Figure 3. 24: Installation of the NTC sensor.....	69
Figure 3. 25: Torque Meter / Transducer (TM309) (Magtrol, 2013).....	70
Figure 3. 26: Torque transducer configuration	70
Figure 3. 27: Magtrol's inline torque meter: main elements (Magtrol, 2013)	71
Figure 3. 28: Inside view of TM309 (Magtrol, 2013).....	71
Figure 3. 29: Torsional Coupling (Magtrol, 2015a).....	72
Figure 3. 30: Proximity probe (Figliola and Beasley, 2011).....	73
Figure 3. 31: Piezoelectric accelerometer (Stud mounting).....	73
Figure 3. 32: Vibration sensor mounting threaded holes	74
Figure 3. 33: DSP7000 front and rear panel (Magtrol, 2015c)	75
Figure 3. 34: SBB configuration (Magtrol, 2014)	75
Figure 3. 35: NI myRIO connectors.....	76
Figure 3. 36: NI cDAQ 9191 & 9234	77
Figure 3. 37: NI USB 6003	78
Figure 3. 38: Acquired data using TM309 and M-Test	80
Figure 3. 39: Estimation of the minimum kinematic viscosity at operating speed (ISO281, 2007)	84
Figure 3. 40: Life modification factor a_{ISO} for ball bearings (ISO281, 2007)	85
Figure 3. 41: Bearing life monitoring system flowchart	86
Figure 3. 42: Bearing diagnostic system flowchart.....	87
Figure 3. 43: Typical RMS level on Healthy bearing	88
Figure 3. 44: Typical RMS level on Unhealthy bearing – inner race defects	88
Figure 3. 45: Vibration spectrum in Frequency domain using the inner race defected bearing	90
Figure 3. 46: Typical SPDT Configuration (after Oberhammer et al., 2006).....	91
Figure 3. 47: Block diagram of the developed Active Condition Monitoring system (ACMs).....	91
Figure 3. 48: Relay PCB connection.....	91
Figure 3. 49: NTC PCB board - ARES model	xxv

Figure 3. 50: NTC PCB board - ISIS model	xxv
Figure 3. 51: NTC Printed Circuit Board (PCB)	xxv
Figure 3. 52: Initial bearing life calculator (front panel) – offline code	xxviii
Figure 3. 53: Initial bearing life calculator (block diagram) – offline code.....	xxviii
Figure 3. 54: Final bearing life code development - front panel.....	xxix
Figure 3. 55: Final bearing life development code - block diagram	xxx
Figure 3. 56: Vibration analysis code – front panel of LabVIEW	xxxi
Figure 3. 57: Torque measurement code - Front panel of LabVIEW	xxxi
Figure 3. 58: Vibration analysis code – Block Diagram illustration.....	xxxii
Figure 3. 59: Torque measurement code - block diagram	xxxiii
Figure 3. 60: Relay PCB Schematic – ISIS model	xxxiv
Figure 3. 61: Relay PCB Schematic - ARES model	xxxiv
Figure 4. 1: System overview	96
Figure 4. 2: Kinematic viscosity (v_1) against the pitch diameter with respect to running speed (ISO281, 2007)	98
Figure 4. 3: Life modification factor a_{ISO} for ball bearings (ISO281, 2007).....	99
Figure 4. 4: RMS value – Unloaded bearing	103
Figure 4. 5: Crest Factor values – Unloaded bearing.....	103
Figure 4. 6: Max-Min value – Unloaded bearing.....	103
Figure 4. 7: Peak value – Unloaded bearing	104
Figure 4. 8: RMS value – 10kN loaded bearing	104
Figure 4. 9: CF value - 10kN loaded bearing.....	104
Figure 4. 10: Max-Min value - 10kN loaded bearing	105
Figure 4. 11: Test bearing with two external circlips.....	107
Figure 4. 12: An illustration of the final observed results from the bearing system failure test – first sample	107
Figure 4. 13: RMS value of the first bearing system failure test	108
Figure 4. 14: Crest Factor (CF) value of the first bearing system failure test.....	108
Figure 4. 15: Vibration parameters of the first bearing system failure test – (a): Max-Min, (b): Peak	109
Figure 4. 16: First Sample results – Temperature measurement in C°	110
Figure 4. 17: An illustration of fatigue propagation in the main rotary shaft of the second bearing system failure test – (i) shows where the fatigue started/initiated, (ii) illustrates the fatigue zone where the cracks grow slowly, (iii) shows where instantaneous zone where the crack growth rate increases vastly.....	111
Figure 4. 18: Illustration of the RMS value during the last stage in the second test.....	112
Figure 4. 19: Exploded view of circled segment in Figure (4.18)	113
Figure 4. 20: CF value during the last stage of the second test.....	113
Figure 4. 21: Exploded view of the circled area in Figure (4.20)	114
Figure 4. 22: An illustration of two vibrational parameters during the second test of bearing system failure – (a): Kurtosis value, (b) Max-Min value.....	115
Figure 4. 23: Peak value during the last stage – sudden higher peak resulted from the catastrophic failure in the main rotary shaft.....	116
Figure 4. 24: Shaft rotational frequency using frequency domain technique	117
Figure 4. 25: Shaft rotational frequencies and its harmonic using Time-Frequency domain	117
Figure 4. 26: Second test in the bearing system failure results - (a): The applied radial load (kN), (b): The acquired bearing temperature (C°).....	118
Figure 4. 27: A pictorial representation of the main rotary shaft after applying load radially – (a): Slave bearings housing, (b): Rigid couplings, (c): Hydraulic press piston, (d): Thermal insulation material, (e): Tested bearing	119
Figure 4. 28: Frictional torque during the second test in the last stage.....	119

Figure 4. 29: AR Coefficients during the second test – (a) healthy system, (b) faulty system (shaft fracture).....	120
Figure 4. 30: Illustration of the fractured couplings – (i) is an exploded fractography view of the red-circled area. It can be seen that the crack is propagated/initiated at the weakest point in the coupling surface resulting in a fatigued element.	122
Figure 4. 31: Third test results - radial load (kN)	122
Figure 4. 32: illustration of the RMS value of the third sample in the bearing system failure test.....	124
Figure 4. 33: Illustration of the CF value during the third test in the bearing system failure test.....	125
Figure 4. 34: Kurtosis (Ku) value	126
Figure 4. 35: Max-Min during the bearing system failure test – Third test	126
Figure 4. 36: Peak value.....	127
Figure 4. 37: Friction bearing torque (Nm).....	128
Figure 4. 38: Evolution of the developing defects in the “test” bearing elements using the frequency domain technique – (a) after 9 hours, (b) after 27 hours and (c) after 61 hours.	129
Figure 4. 39: Time-frequency domain results	130
Figure 4. 40: AR Coefficients before and after the failure occur in the coupling – (a) healthy system, (b) faulty system (coupling fracture)	131
Figure 4. 41: RMS value during the Bearing life test	132
Figure 4. 42: CF level during the bearing life test	133
Figure 4. 43: The Max-Min value during the bearing life test.....	134
Figure 4. 44: Peak pattern during the bearing life test	134
Figure 4. 45: Highlights the evolution of the bearing elements defects using frequency-domain philosophy – (a): after 30 operational hours, (b): after 78 hours, (c): after 122 hours and (d): after 162 hours.....	136
Figure 4. 46: Representation of the time-frequency domain results during the bearing life test (fourth sample) – (a): after 30 hours, (b): after 78 hours, (c): after 122 hours and (d): after 162 hours. These figures support the results from the frequency domain.....	137
Figure 4. 47: Frictional Torque during the bearing life test.....	138
Figure 4. 48: Ball surface presents few failure modes, namely pitting. It is an indication to bearing fatigue as the bearing exceeded the theoretical life and was operating under harsh environment – being loaded radially.....	138
Figure 4. 49: Cracks appeared on the ball surface, indicating that the bearing was operating under harsh environment.....	139
Figure 4. 50: Pitting of chunk on the outer race.....	139
Figure 4. 51: Inner race surface with different failure modes – (a): crack, (b): pitting. This figure highlights few failure modes which elucidate that the bearing was experiencing developing defects which help in diminishing its life.....	139
Figure 4. 52: Inner race defects. This figure shows crack initiation / propagation and fatigue striation leading to final failure in the bearing element.	139
Figure 4. 53: Image subtraction block diagram	140
Figure 4. 54: Small sample of what occurs when two images are uploaded into the developed code.	141
Figure 4. 55: Images from surveillance video – (Image A) captured at the outset. Image (B) captured after the first 50 seconds, Image (C) after 1 minute, Image (D) 1m 30sec, Image (E) 2 minutes, Image (F) 2 min 30 sec, Image (G) 2 min 40 sec, Image (H) 2 min 50 sec, Image (I) 3 minutes, Image (J) 3 min 30 sec, Image (K) 4 minutes, Image (L) 6 minutes, Image (M) 9 minutes and Image (K) at 9 min 17 sec.	142
Figure 4. 56: First bearing system failure test results – (a) The applied radial load in kN, (b) the Frictional Torque in Nm	xxxv
Figure 4. 57: RMS value throughout the second bearing system failure test.....	xxxvi

Figure 4. 58: Results during the Second bearing failure test – (a) the applied radial load in kN and (b) Operational Temperature in C°	xxxvii
Figure 4. 59: The Max-Min value during the second test	xxxix
Figure 4. 60: Peak value during the second test.....	xl
Figure 4. 61: Kurtosis value during the second bearing system failure test.....	xli
Figure 4. 62: CF value during the second test.....	xli
Figure 4. 63: Frictional torque during the second test	xlii
Figure 4. 64: Logged data from the fourth sample – (a): applied radial load measurement and (b) operational temperature (C°)	xliv
Figure 4. 65: Friction bearing torque (Nm).....	xlv
Figure 4. 66: Vibration parameters – (a): RMS level, (b): Crest Factor values	xlvi
Figure 4. 67: Max-min value during the bearing life test	xlvii
Figure 4. 68: Image Subtraction code in LabVIEW - block diagram pictorial.....	xlviii
Figure 4. 69: Block diagram of the ARMA development.....	xlix
Figure 4. 70: Front Panel of the ARMA development in LabVIEW	xlix
Figure 5. 1: Fuzzy Logic Architecture	151
Figure 5. 2: Flowchart of the proposed visionary-actuation system	152

List of Tables

Table 2. 1: Micro-scale wind turbines types (Aeolos, 2017; Windside, 2017; Aleko, 2017 and Marlec, 2013)	9
Table 2. 2: Types of corrosion (SKF, 1994)	15
Table 2. 3: Type of fits (NTN, 2013).....	18
Table 2. 4: Types of Machine Condition Monitoring (MCM) (National Instrument, 2007)	26
Table 2. 5: Bearing frequencies (Thakar D., 2014).....	31
Table 2. 6: Classification scheme of metallic wear debris by (Peng Z. and Kirk T.B., 1999).....	36
Table 2. 7: AE signals' types.....	37
Table 2. 8: ball bearing's specification – SKF(Sukhjeet S. et al, 2014)	40
Table 2. 9: Fuzzy model types (Hideyuki T., 1997)	43
Table 2. 10: Kothamasu, R. and Huang, S. H. (2007)'s Intelligent CBM architecture modules.....	44
Table 3. 1: Bearing dimensions (SKF, 2017a; 2017b).....	56
Table 3. 2: Bearing specifications (SKF, 2017a; 2017b).....	58
Table 3. 3: Hydraulic bench press and hand pump specifications (Ali B., 1999).....	60
Table 3. 4: Pressure transducer specifications (CPC, 2000)	64
Table 3. 5: DSP7000 specification (Magtrol, 2015c)	74
Table 3. 6: NI 9234 specifications (National Instruments, 2014a)	77
Table 3. 7: NI USB 6003 Specifications (National Instrument, 2014b)	78
Table 3. 8: Equation explanation	83
Table 3. 9: Life modification factor for reliability.....	83
Table 3. 10: Cleanliness / contamination factor e_c (ISO281, 2007).....	85
Table 3. 11: Relay specifications (Peng C. et al, 2009a)	91
Table 3. 12: Control terminal connection (Evans P., 2009).....	92
Table 3. 13: Thermistor Resistance (Ohms) Vs Temperature (Celsius)	xxvi
Table 4. 1: Theoretical bearing life calculation for single deep-groove bearing (6205-2RSH).....	101
Table 4. 2: Bearing elements' frequencies	102
Table 4. 3: Initial parameters of a healthy bearing, used as references to trigger the abort action	105
Table 4. 4: Conducted tests type throughout this research.....	105
Table 4. 5: Comparison of mild steel and silver steel	121
Table 4. 6: Bearing elements' frequencies and their harmonic frequencies	128

List of Equations

Eq. 2. 1: Basic rating life	13
Eq. 2. 2: Modified rating life	13
Eq. 2. 3: Shaft rotational frequency	31
Eq. 2. 4: Cage rotational frequency.....	31
Eq. 2. 5: Outer raceway frequency.....	31
Eq. 2. 6: Inner raceway frequency	31
Eq. 2. 7: Ball rotational frequency	31
Eq. 2. 8: Root-Mean-Square	32
Eq. 2. 9: Crest Factor	32
Eq. 2. 10: Kurtosis	33
Eq. 2. 11: Outer race fault frequency	40
Eq. 2. 12: Current Signature Spectrum	41
Eq. 2. 13: Fuzzy sets	43
Eq. 2. 14: AR model	49
Eq. 2. 15: ARMA model.....	49
Eq. 3. 1: Pascal's law	66
Eq. 3. 2: Voltage divider	67
Eq. 3. 3: Steinhart - hart.....	67
Eq. 3. 4: Basic rating life using radial load	82
Eq. 3. 5: Basic rating life using axial load	82
Eq. 3. 6: Basic rating life in operating hours	82
Eq. 3. 7: ISO modification rating life in million revolutions	83
Eq. 3. 8: ISO modification rating life in operating hours.....	83
Eq. 3. 9: Bearing Pitch Diameter	84
Eq. 3. 10: Kinematic viscosity ratio.....	84
Eq. 3. 11: Root-Mean-Square	88
Eq. 3. 12: Crest Factor	88
Eq. 3. 13: Kurtosis	88
Eq. 3. 14: Shaft rotational frequency	89
Eq. 3. 15: Cage rotational frequency.....	89
Eq. 3. 16: Outer race frequency	89
Eq. 3. 17: Inner race frequency	89
Eq. 3. 18: Ball rotational frequency	89
Eq. 4. 1: Shaft rotational frequency	97
Eq. 4. 2: Cage rotational frequency.....	97
Eq. 4. 3: Outer race rotational frequency	97
Eq. 4. 4: Inner race rotational frequency.....	97
Eq. 4. 5: Ball rotational frequency	97

List of Acronyms

%	Percent
.NET	Network
μ	Micro
μm	Micrometre
2D	2 Dimensions
3D	3 Dimension
A/D	Analogue to Digital
ABMA	American Bearing Manufacturers Association
AC	Alternative Current
ACMs	Active Condition Monitoring system
ADC	Analogue to Digital Converter
AE	Acoustic Emission
AE _{APK}	Acoustic Emission Peak Amplitude
AEWMS	Acoustic Emission Wireless Monitoring System
AFBMA	Anti-Friction Bearing Manufacturers Association
ANNs	Artificial Neural Networks
ANSI	American National Standards Institute
ARMA	Auto-Regressive-Moving-Average
ART	Artificial Resonance Theory
BNC	Bayonet Neill – Concelman
C°	Celsius / Centigrade
cDAQ	Compact Data Acquisition
CM	Condition Monitoring
CMS	Condition Monitoring System
CNC	Computer Numerical Control
COM	Common
CPU	Central Processing Unit
CSA	Current Signature Analysis
cSt	Centistokes
D	Drain
DAQ	Data Acquisition
DC	Direct Current
DIG	Dial Indicator Gauge
DIN	Deutsches Institut für Normung (German Institute for Standardization)
DSP	Digital Signal Processing

EMF	Electromagnetic Field
F°	Fahrenheit
FEM	Finite Element Model
FFT	Fast Fourier Transform
FPGA	Field Programmable Gate Array
G	Graphical
G	Gate
GA	Genetic Algorithms
GND	Ground
GPa	Gega pascal
g/cc	Gram per Cubic Centimetre
HAWT	Horizontal Axis Wind Turbine
HMS	Health Management System
HRC	Hot Rolled Carbon
Hz	Hertz
I/O	Input / Output
I/P	Input
ICBM	Intelligent Condition-Based Monitoring
IHMS	Intelligent Health Management System
IMS	Intelligent Management System
ISO	International Standards Organisations
JIS	Japanese Industrial Standards
K°	Kelvin
kHz	Kilohertz
km	Kilometre
kN	Kilo Newton
kS	Kilo Sample
kW	Kilowatt
kΩ	Kilo Ohms
LabVIEW	Laboratory Virtual Instrument Engineering
LAN	Local Area Network
LBE	Lead-Bismuth Environment
LED	Light Emitter Diode
m	Metre
mA	Millie Ampere
Max	Maximum

MCM	Machine Condition Monitoring
MHz	Megahertz
MIC	Miniature Inline Couplings
Min	Minimum
MPa	Mega pascal
ms	Milliseconds
MSc	Master of Science
MW	Megawatt
MXP	MyRIO Expansion Ports
N	Newton
N/C	Normally Closed
N/O	Normally Opened
NASA	National Aeronautics and Space Administration
NI	National Instruments
Nm	Newton metre
NPT	National Pipe Thread
NTC	Negative Temperature Coefficient
O/P	Output
ODA	Oil Debris Analysis
OMM	Online Condition Monitoring
OMP	Online Machine Protection
Pa	Pascal
PC	Personal Computer
PCB	Printed Circuit Board
PdM	Predictive Maintenance
PID	Proportional Integral Differential
PRM	Proactive Reliability Maintenance
PSI	Pound per Square Inch
r	Radius
ROI	Region Of Interest
RPM / rpm	Revolution Per Minute
RTD	Resistance Temperature Detectors
S	Source
SBB	Signal Breakout Box
SEM.EDX	Scanning-Electron-Microscope Energy Dispersive X-ray
SKF	Svenska–Kullager–Fabriken

SPDT	Single Pole Double Throw
Std.	Standard
SWS	Small Wind Systems
TDA	Time Domain Analysis
TEC	Total Engineering Commitment
TM	Torque Meter
TSK	Takagi–Sugeno–Kang
TSS	Time Signal Series
UCLAN	University of Central Lancashire
UK	United Kingdom
UKWED	United Kingdom Wind Energy Database
USA	United States of America
USB	Universal Serial Bus
V	Voltage
VA	Vibration Analysis
VAC	Voltage Alternating Current
VAWT	Vertical Axis Wind Turbine
VB	Visual Basics
VDC	Voltage Direct Current
VDD	Voltage Drain Drain
WAN	Wide Area Network
Wi-Fi	Wireless Fidelity
WS	Wind turbine type
Ω	Ohm

Nomenclature

A	Fuzzy sets	N/A
A	Area	m ²
A, B and C	Stein-hart hart coefficients	N/A
a ₁	Life adjustment factor	N/A
a _{ISO}	Life modification factor	N/A
a _k	AR coefficients	N/A
B	Ball diameter	Mm
b _k	MA coefficients	N/A
C	Cage diameter	mm
C _a	Basic dynamic axial load	kN
CF	Crest Factor	N/A
C _r	Basic dynamic radial load	kN
C _u	Fatigue load limit	kN
D	Ball Diameter	mm
D	Pitch Diameter	mm
D _{PW}	Pitch Diameter	mm
e	Ball or roller	N/A
e _i	Gaussian error series	N/A
e _{i-k}	Model error series	N/A
F	Force	N
g	Acceleration of gravity	9.81 m/s ²
i	Index	N/A
I	Inner raceway diameter	mm
Ku	Kurtosis	N/A
L ₁₀	Bearing Basic rating life	Million revolutions
L _{10h}	Bearing Basic rating life	Operating hours
L _{nm}	Modified rating life	Million revolutions
L _{nmh}	ISO modification rating life	Operating hours
M	Integer i.e. 1, 2, 3, etc.	N/A
N	Number of Samples	N/A
N	Rotational speed	rpm
N _{b.winner}	Number of balls * shaft speed	rpm
O	Outer raceway diameter	mm

p	ARMA model	N/A
P	Pressure	MPa
P_a	Equivalent axial load	kN
P_r	Equivalent radial load	kN
q	ARMA model	N/A
R	Reference resistance for NTC	$k\Omega$
RMS	Root Mean Square	mg
R_T	A measurement of resistance at Kelvin temperature	K°
V_T	Voltage output from the NTC	V
X	Sampled Time Signal	N/A
X_{Peak}	Maximum Positive Peak	N/A
Z	Number of balls	N/A
α	Bearing angle of contact	Degree (°)
$\mu A(x)$	Membership Function of Fuzzy sets	N/A
π	pi = 3.14159265	N/A
e_c	Cleanliness level / contamination factor	N/A
f_b	Ball rotational Frequency	Hz
f_{bng}	Outer raceway fault Frequency	Hz
f_c	Cage rotational frequency	Hz
f_I	Inner raceway Frequency	Hz
f_O	Outer raceway frequency	Hz
f_r	Shaft rotational frequency	Hz
f_s	The supply frequency	Hz
$f_{or f}$	Current Signature Spectrum	Hz
i	Sample index	N/A
k	Kinematic viscosity ratio	N/A
v	Actual kinematic viscosity	mm^2/s
v_1	Kinematic viscosity	mm^2/s
σ^2	Variance	N/A

Acknowledgments

First and foremost, I am truly grateful to Almighty God, for what I have achieved so far and for everything.

Also, I would like to take this opportunity to thank Dr. Ahmed Onsy for fulfilling the role of director of this research. You have provided me with the needed help, support, advice and guidance throughout the research. All this was invaluable and I sincerely appreciate the opportunity; finally, thank you for the experience that will help me to accomplish future tasks.

Prof. Ian Sherrington I sincerely thank you for all the academic advice that has been incorporated in my research. All your time spent in accomplishing the role of second supervisor is appreciated and fully acknowledged.

“To my supervisory team – Thank You”

I would like to convey my appreciation to all the technicians in Wharf Building for helping me to manufacture all the needed elements during the research. My appreciation includes: Jonnie Meadowcroft, Phil Spence, Boz Boyle and Duncan Tylor. Likewise, to the School of Engineering technician and administration, all your efforts were treasured. Apple Faisiri, Andrew Wildman, Christopher Finnigan, Thomas Hoskins and Iain Hams – Thank you.

Great appreciation goes to colleagues at the Jost Institute for Tribotechnology, Intelligent Condition Monitoring / Tribotronics Laboratory at the University of Central Lancashire who have assisted me in the completion of the research. Jephin Thekemuriyil Philip, Jesvin George, Sanchit B. Chandile, Omoseye Abayomi Adeyemi, Wilbert Sinzara and Yedukrishnan – Thanks for all the academic and technical assistance.

Mom and Dad, you may not read the whole research, but every word is here because of you – thanks for your unwavering support, the mainstay of all my achievement. Halla N-s Abfuroukh, your name deserves to be at the front of my research – thanks for the care, support and positivity you have provided during difficult moments throughout this research – I wish you a bright future.

Lastly, a special thanks goes to my friends who have stood by me, enduring all the uncertainties from the outset.

Dedications



“This achievement is dedicated to my beloved family: my parents, Mom and Dad and my brother and sisters”

Chapter 1. Introduction

Rolling element bearings tend to be used in different environmental conditions, including harsh operational environments resulting in a huge variation between the estimated and actual lifespan of bearings. This MSc research focuses on developing the basic element of a prototype intelligent bearing for an application such as a micro-scale wind turbine. The research will contribute to determining the life of the bearing for the purpose of scheduling maintenance operations. This chapter introduces the main goals of the research.

1.1. Background

The use of renewable / sustainable energy sources is being encouraged all over the world and wind power is classified as one of the fastest growing forms of electricity generation (Belessiotis V. and Delyannis E., 2000). Such sources contribute to a stronger economy and will not compromise human health or climate change, as they are environmentally friendly. One application of such a technology is the wind turbine, which captures the wind's energy and converts it into a form of electrical energy. It was formerly only used for such as pumping water, grinding grain and sailing ships (Belessiotis V. and Delyannis E., 2000).

The UK is one of the leading producers of wind-generated energy in Europe, with 8,501 MW of onshore capacity and 5,098 MW offshore. Around 952 projects are currently powered by wind turbines in the UK, making it an ideal market for domestic turbines in Europe. These projects are either fully or partially powered by the wind, and various shapes / sizes of turbines are in use (Yates T., 2015). With the advanced technology, a micro-scale of the wind turbine has been introduced. It has the same concept of typical wind turbine but with smaller scale that makes it exemplary for domestic sectors. It is presently used to power many UK homes, farms, small businesses or even entire communities, also encouraging debate about the future of wind as a source of electricity. Since 2005, over 25,000 small and medium-scale wind turbines had been installed in the UK, as a sensible and practical way to secure affordable electricity. The UK is aiming to deploy around 806MW of small and medium turbines in order to reduce carbon output by 0.8 million tonnes. In 2009, Small Wind Systems (SWS) reported that around 3,280 small turbines were deployed with a total capacity of 8.26MW (RenewableUK, 2015).

The typical micro-scale wind turbine has three main elements: main shaft, bearings and generator. One of the most critical components in the domestic turbine element is the main shaft bearings, irrespective of whether it is used for a large or small turbine. The choice of main shaft bearing type depends on the rating and design of the turbine. Normally, small turbines employ either spherical roller bearings or deep-groove ball bearings for the main shaft. The specifications provide reliable and cost-effective bearing options.

Bearings are one of the most frequently defective elements and can be considered as the chief cause of turbine failure (Helmy et al., 2014). Because they fail frequently, maintenance strategies are needed. With the use of advanced maintenance strategies the lifetime of micro-scale wind turbines can be extended and their performance improved. These maintenance

strategies utilise online condition monitoring systems with different techniques such as vibration analysis, Acoustic Emission (AE) monitoring or Online Debris Analysis (ODA) to provide useful information about the condition of the turbine. Most online condition monitoring systems focus on detecting imminent failures, preventing catastrophic failures or identifying failure mechanisms, to perform reliability analysis. A few of these systems utilise intelligent algorithms with monitoring techniques such as vibration analysis to provide failure prediction (Onsy , 2013) and this is the aim of the research developed here.

For instance, in 2013 SKF announced SKF “Insight”. This development aimed to monitor bearings condition and provide diagnostic information about bearing’s health. The system is based on variety of sensors including speed, load and temperature. Also, it shares the bearing’s information wirelessly and identify parameters that affect its performance and reliability.



Figure 1. 1: SKF Insight (SKF, 2013)

1.1.1. Scope

Bearing lifespan is a design parameter in bearing selection, as its value must be identified to reduce secondary damage that bearing failure may cause to other machinery; it is also required for scheduling maintenance operations (ISO281, 2007). However, even with the use of standards such as: ISO (ISO281, ISO76, ISO 14728-1), ANSI/AFBMA (AFBMA Std. 9), JIS (JIS A, B, C 1518) and DIN (DIN ISO281) to calculate the bearing life, this value is an estimate as bearing life calculation is based on statistical probability. Also, several factors that affect the bearing’s life are difficult to readily include in the calculation, which can result in a large variation between the calculated and actual life of the bearing (Leturiondo U. et al., 2016 and Nam J. S. et al., 2016). These factors include contamination, lubrication problems, and higher operational condition (loads, moments, shocks, vibration, temperature) that differ from design values; and inaccurate bearing installation that causes clearance or damage to bearing elements. (ISO281, 2007). Thus, it will be very useful for many applications if the actual lifespan of

bearings could be predicted, in order to address the variation between calculated and actual life.

1.2. Research aim and objectives

This study is built on previous research conducted to develop Intelligent Health Management Systems (IHMS) (Onsy A. et al., 2011; 2010), and focuses on bearings to address current issues in determining bearing life (ISO281, 2007 and Leturiondo et al., 2016). It aims to develop a prototype of an Intelligent Management System (IMS) for a micro-scale wind turbine bearing that is able to monitor the bearing life and predict its failure. The system developed by the author monitors the condition of a typical ball bearing and provides a prediction for its life, to support proactive maintenance of the turbine, and increases its prediction.

In order to achieve the research aim the following objectives were proposed:

- Conduct a literature survey of intelligent machines, active condition monitoring systems, different sensors and instrumentation.
- Develop a Health Monitoring System (HMS) for micro-scale wind turbine bearings.
- Preliminary testing of different types of bearing conditions including faulty and healthy bearings.
- Experimental validation of HMS using micro-scale wind turbine bearings.
- Using an intelligent algorithm to develop an Intelligent Management System (IMS) for micro-scale wind turbine bearings.
- Validation of the IMS capabilities.

The literature review covers intelligent machines, active condition monitoring systems and sensory and instrumentation systems. Test apparatus was designed in order to develop the Health Monitoring System (HMS) for micro-scale wind turbine bearings. Preliminary testing of different types of bearing (faulty and healthy) was carried out to examine their characteristics. Then, an experimental validation of the HMS was carried out on the test apparatus. Through using intelligent algorithms, an Intelligent Management System (IMS) for the application was developed and its capabilities validated.

The hypothesis of this research is that it will be possible to develop a prototype IMS which can monitor the life of micro-scale wind turbine bearings and detect different bearing failures. It is proposed that with the use of an intelligent analysis approach that integrates key sensor

information, the bearing life can be identified to an accuracy which is better than statistical analysis.

1.3. Thesis Structure

This thesis is split into two main sections: equipment development and experimental study:

Chapter 1 outlines this MSc research: background, scope, aim and objectives, hypothesis and thesis structure.

Chapter 2 is a literature survey to acquire a fundamental understanding of intelligent machines, active condition monitoring systems and sensory and instrumentation systems. Mutual defects in the micro-scale wind turbine elements were undertaken, involving bearings, generator, brake and main shaft. The extended use of condition-monitoring methods, including thermography, vibration, acoustic emission, oil debris analysis and current signature analysis, was highlighted. Lastly, typical intelligent methods that could be adapted to provide a reliable action based on the operational conditions were covered.

Chapter 3 presents the hardware for the HMS, including the selection of the components and the development of a test apparatus capable of handling several types of test. Also, discusses the software development and explains the basic of the diagnostic system for the micro-scale wind turbine bearing.

Chapter 4 analyses and discusses in detail the preliminary and final results. Firstly, healthy references for each parameters were conducted through the preliminary testing, followed by final testing. This involved two main testing phases including bearing system failure and bearing life tests. Also, the usage of an intelligent algorithm to predict failures was implemented. An illustration of some visionary data was demonstrated.

Chapter 5 provides a summary and an experimental conclusion of the whole thesis and suggests further work that could be done in this field to fill any gaps left by this research.

Chapter 2. Literature review

2.1. Introduction

This chapter reviews the literature relating to common defects that occur in the micro-scale wind turbine (2.3), condition monitoring techniques including thermography, vibration, online debris analysis, acoustic emission and current signature analysis (2.4), and some intelligent methods (2.5) to respond to these defects. The chapter is summarised in Section 2.6.

2.2. Domestic Wind Turbine Evolution

Wind energy is one of the fastest growing of the clean, renewable and sustainable energy sources. Wind produces no emissions and can be used to generate income for local communities. It is used in many countries because of its environmentally friendly characteristics. Historically, Egyptians were the first to use wind as a never-ending source of energy, to propel boats. It was adopted in many sectors to pump water and grind grain as well as for sailing (Belessiotis V. and Delyannis E., 2000). Increasing the use of renewable and sustainable energy can lead to healthier lives with advantages for economy and climate (Michael B. et al., 2015).



Figure 2. 1: Wind turbine and Solar Panel (Sarah Bray, 2011)

With this vision of meeting sustainable needs from renewable resources, many countries have devised ways to generate clean electricity. Wind turbines are popularly used to harness wind to generate electricity, and as one of the windiest areas of Europe, it is not surprising that there are almost 1,000 wind turbine projects in the UK. Many sizes of wind turbine are in use in the UK (Yates T., 2015) with, according to the UK Wind Energy Database (UKWED), a total of 5,210 onshore and 1,465 offshore wind turbines.

In terms of installation, considerations include cost, reliability, performance and the size of the turbine to suit power needs. Micro-scale has a typical capacity up to 1.5 kW, a size of around 2 to 18 metres, with 100% of the generated electricity used on-site to power homes (on-grid).

Micro-turbines are employed to power homes, farms, small businesses and even entire communities encouraging debate about the future of the wind industry. They use similar concepts of a typical wind turbine but in a smaller scale that makes it exemplary for domestic sectors. Since 2005 over 25,000 small- and medium-scale wind turbines have been installed locally in the UK, a practical way of securing affordable electricity. The energy produced by

the micro-scale wind turbines is used on-site (powering homes), stored in batteries for use later (off-grid), or sold and fed into the ground (grid).

The UK has some 15 manufacturers of small- and medium-scale wind turbines, producing models from (0-100kW); 50% of the turbines are exported. The UK has set a goal to be achieved by 2023, to deploy around 806MW of small and medium wind turbines, to prevent emissions of 0.8m tonnes of carbon. In 2009, the Small Wind System (SWS) UK market reported that 3,280 small turbine units had been deployed, with 8.62MW capacity.

In Europe, wind power is responsible for approximately one-third of the installed electricity generating capacity. In 2007, this figure was only 3.7%, with over half the installed capacity in Germany and Spain. In Denmark wind energy contributes more than 20% of electricity production.

Globally, the total number of micro-scale wind turbines continues to grow significantly. In 2010 the total installed capacity was 0.66kW, in 2011 0.77kW, in 2012 0.84kW, and in 2013 0.85kW. Over 50% of the micro-scale turbine manufacturers are from five countries: Canada, China, Germany, the UK and the USA. Clearly, China continues to be the leader in terms of installed units, with 500,000 in 2013, 570,000 in 2014 and 625,000 in 2015, with 305,000 kW cumulative installed capacity. The USA market grew from 198,000kW in 2013 to 221,000kW in 2015 (Peacock A. D. et al., 2008; RenewableUK., 2015; Maeda R., 2013 and Stefan G. and Jean P., 2014).

There are four main types of micro-scale wind turbine: Vertical Axis Wind Turbine (VAWT), Horizontal Axis Wind Turbine (HAWT), Pole mountings and Building mountings. VAWT are suitable for areas of turbulent wind conditions. HAWT is by far the most commonly installed turbine, with three or more rotor blades which automatically orientate themselves with the direction of the wind, changing direction during high wind speeds to avoid damage. Pole-mounted (free-standing) and building-mounted (roof-mounted) turbines are designed to be attached to buildings either on a pole or fitted to the roof. Table (2.1) below shows some brands of micro-generation turbines, their types and origin (Aeolos, 2017; Windside, 2017; Aleko, 2017 and Marlec, 2013).

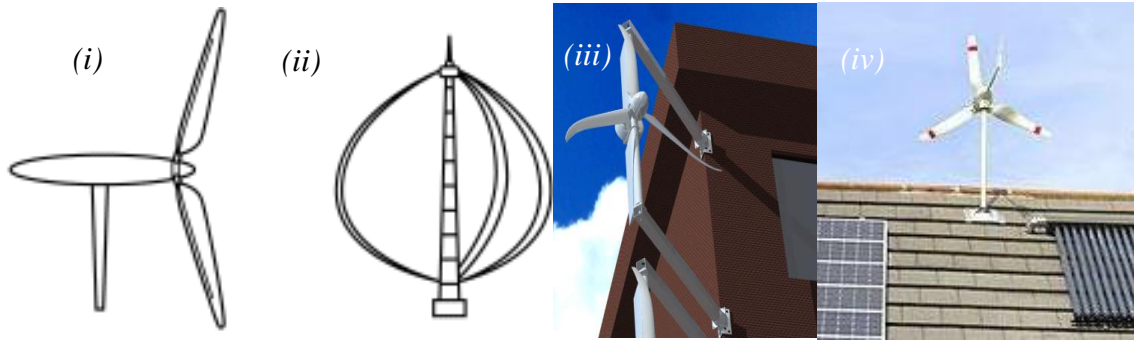


Figure 2. 2: An illustration of the differences between all the micro-turbines types - (i): HAWT, (ii) VAWT, (iii) building mounted and (iv) Pole mounted (Rob B., 2017)

Table 2. 1: Micro-scale wind turbines types (Aeolos, 2017; Windside, 2017; Aleko, 2017 and Marlec, 2013)

No.	Turbine name	Type	Origin
1	Aeolos-H 1k Wind turbine	HAWT	UK
2	WS-0.30	VAWT	Finland
3	Aleko R4	Building-mounted	USA
4	Marlec Rutland	Pole-mounted	UK

Micro-scale wind turbines have the same concept as full-size turbines in terms of generating electricity. Through wind energy the propeller (blades) will cause the rotor to spin; this is connected with the main shaft which spins the generator to produce electricity. To clarify, the turbine captures wind energy through converting kinetic energy into a form of electrical energy to produce power.

The construction of micro-scale wind turbine applications is based on a combination of electrical and mechanical elements. These elements may have defects resulting from constant overuse or inadequate maintenance. By diagnosing potential failures, the defects can be avoided and appropriate maintenance action taken (Abhishiktha T. et al., 2016).

2.3. Defects

The elements of the micro-scale wind turbine most subject to defects and affecting performance, are: bearings, main shaft, generator and brake. Defects tend to result from constant over-use, so various condition monitoring and maintenance techniques need to be applied in order to make the most efficient use of machine parts. The reliability of the system, components' lifespan, and performance of the overall system are all affected if not properly maintained.

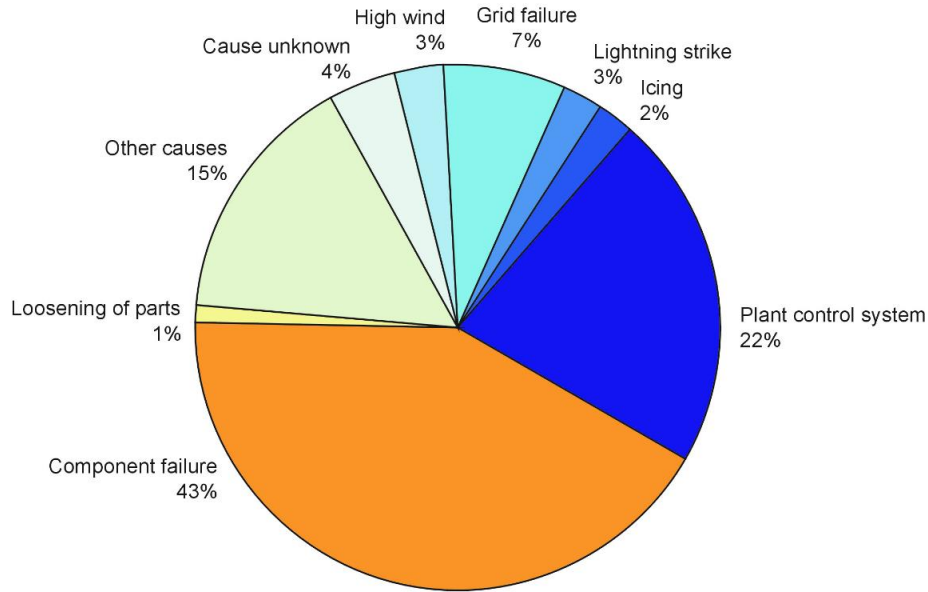


Figure 2. 3: Frequent failure mode in a typical wind turbine (Berthold., 2005)

A statistic revealed by (Berthold., 2005) illustrated that almost half of frequent failures occur in the wind turbines are based on component failures. This is including defects in: gearbox, bearing, main rotary shaft, generator, brake and other elements – some of these defects are explain as follows:

2.3.1. Bearings

Of all these elements, bearings are the most frequently affected and can be considered as a major cause of micro-scale wind turbine failure. There are several types of bearing that are designed and manufactured to suit different types of application. The differences between these types concern factors including load and ability to handle weight.

Bearings are commonly used in mechanical applications to help in reducing the amount of the friction produced through having two metal surfaces roll over each other. They consist of an inner raceway, outer raceway, roller (cylindrical) / balls or cages. The rolling elements in the bearing (balls / roller) are made of smooth metal that rolls against the inner and outer raceway surfaces, taking the load and allowing the element to spin. This load can be either radial (black arrow) or thrust / axial load (red arrow) as shown in Figure (2.4) below. Two common types of bearing are used: ball and roller (cylindrical).

Ball bearings, as known as deep-groove single-row or Conrad types of bearing, are common, with the ability to handle radial and thrust loads. They are typically used in applications where the applied load is light. The inner ring is fastened to the rotating element (shaft) and a circular

ball raceway is provided through the groove on the outer diameter. The outer raceway is mounted on the bearing housing. The applied load is transmitted from the outer raceway to the ball then to the inner raceway. The contact points between the ball and the outer raceway are very small, due to the spherical shape of the bearing; this also helps the ball to spin very smoothly. Therefore, if the applied load is excessive the rolling element will be deformed, ruining the bearing and affecting other elements within the application.

Roller bearings (cylindrical) have low-friction, high radial load capacity and high speed capability. They are used in many applications where enormous loads need to be carried, due to the distribution of the load. The contact between the outer raceway and inner raceway is a straight line not a point (as in the cases of ball bearings). Consequently, the load is distributed over a larger area due to the greater contact, which results in the roller being able to tolerate a heavier load than ball bearings (Olivia., 2011 and Gonzalez C., 2015).

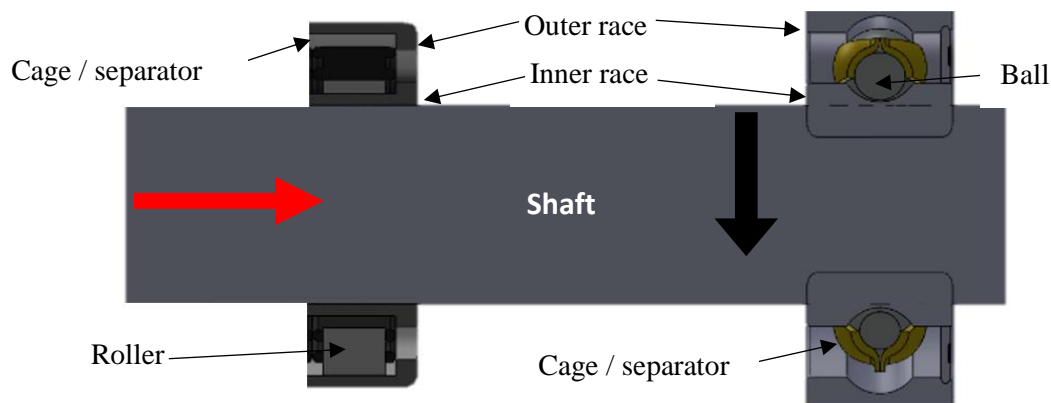


Figure 2. 4: Roller and ball bearing

Several researchers such as: Radu C., (2010), Tallian TE., (1992), Harris TA. and Kotzala MN., (2006) have suggested that excessive load, overheating, false brinelling, true brinelling, normal fatigue failure, reverse loading, contamination, lubricant failure, corrosion, misalignment, loose fits and tight fits are the main forms of bearing failure. These failure forms can result from inadequate maintenance, inappropriate selection for the desired application, or constant over-use. For instance, Radu C., (2010) shows that the rates and types of failure in bearings are: insufficient lubrication of the rolling elements 80%, inadequate bearing selection 10%, inappropriate mounting 5%, indirect failures 4%, and material defects and manufacturing error less than 1%. As well as, failures in bearings can also be caused as a result of faulty assembly, inadequate maintenance or from faulty manufacture. Bearing defects can take several forms

and may occur in any part of the bearing, including: outer raceway, inner raceway, balls / rollers or cage.

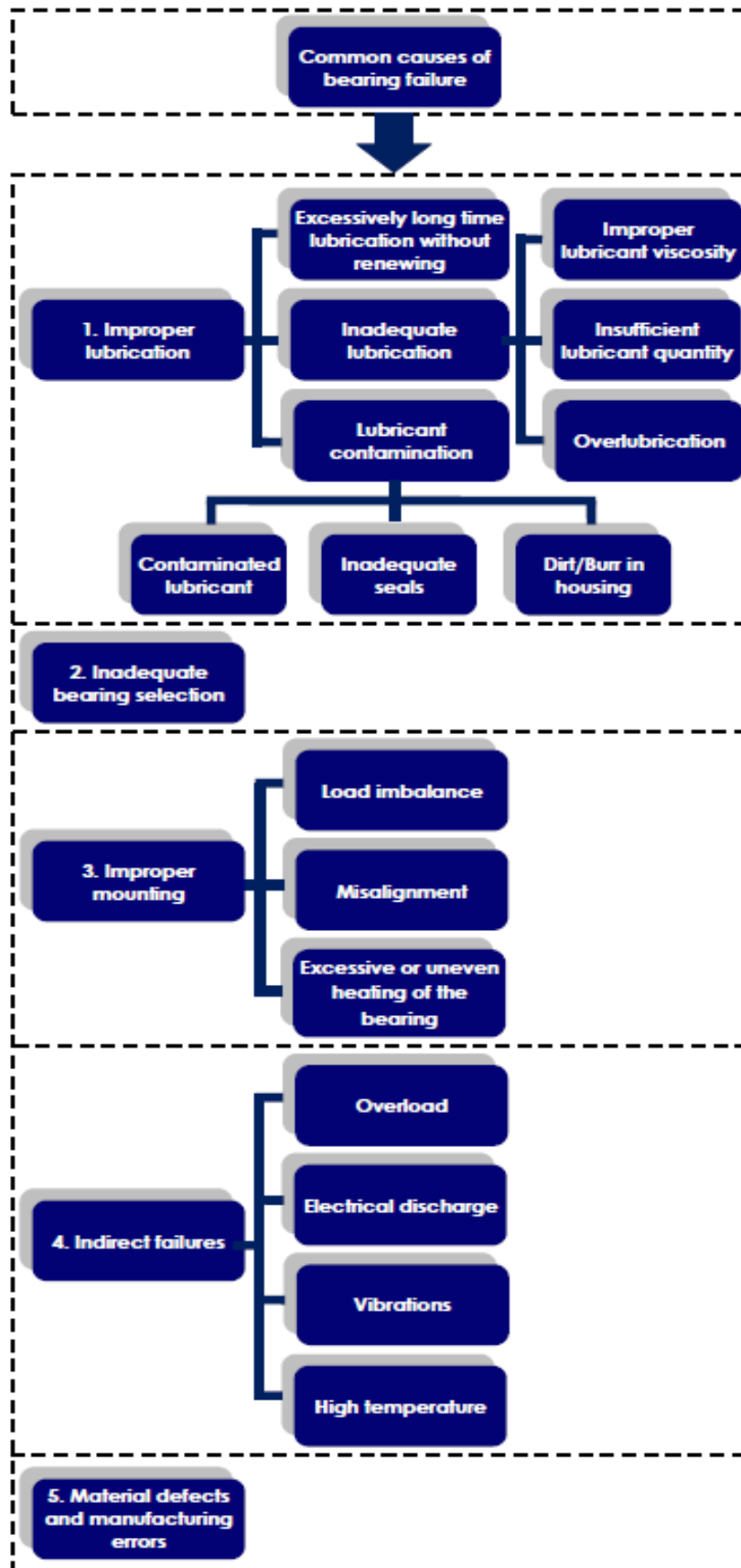


Figure 2. 5: Bearing defects (Radu C., 2010)

Tallian TE., (1992) classified the failure signatures in the bearing as defects or damage. If the failure occurs during manufacture or assembly, then it is a defect, but if it occurs during operation it is called damage. Tallian's list of failures consists of wear, spalling, galling and skidmarking, surface distress, denting, imbalance due to overheating, corrosion and electric erosion, cracks, lubrication failures and permanent failures.

Harris TA. and Kotzala MN., (2006) listed failures as follows: faulty lubrication, fretting that causes fracture of rings, excessive loading, cage fracture, pitting or indentation of the contact surfaces, wear, micro-pitting and fatigue.

In 2004, ISO15243 aimed to unify the failure classifications as: fatigue, wear, corrosion, electrical erosion, plastic deformation and fracture and cracking (ISO15243., 2004). Some of these failures typologies are discussed in the following sections.

Failure typology plays a vital role in determining a bearing's life. Therefore, in 1940s Lundberg G. and Palmgren A. were the first to illustrate an official formula in order to figure out the bearing life. Over time, this was updated in ISO281 for newer types of bearings. It was published in 2007 with the aim of presenting a methodology to calculate the rating of life using a constant load (ISO281., 2007). This standard is considered to estimate the life of a bearing with 90% reliability, using Eq. 2.1 below.

$$L_{10} = \left(\frac{C}{P}\right)^e \quad \text{Eq. 2. 1: Basic rating life}$$

Where C = dynamic rating load, P = applied load and e = 3 in the case of ball bearing and 10/3 in the case of roller.

For some applications, 90% reliability is insufficient. Thus, ISO281 proposed a modified equation as follows:

$$L_{nm} = a_1 a_{ISO} L_{10} \quad \text{Eq. 2. 2: Modified rating life}$$

These coefficient adjust the lifetime and therefore Eq. 2.2 is to be used under certain lubrication conditions with respect to the material and lubrication factors (a_{ISO}) and the failure probability (a_1).

- Excessive load

Excessive load has by far the greatest effect on bearing life, causing premature fatigue due to repeated loading on the races from severe spalling on the raceways. By repeating the loading of the rolling element on the races, tiny cracks will appear on the surfaces, growing and joining other cracks until a small part of the raceway material breaks off. This type of failure can be avoided either through reducing the load or using bearings with greater capacity (Timken, 2014).

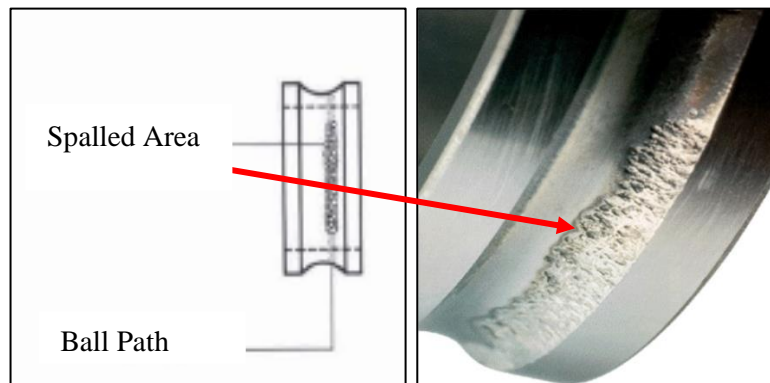


Figure 2. 6: Excessive loads defect (Barden P. B., 2011)

- Overheating

While the rolling element is rotating through the bearing bore, it normally generates variations in temperature, becoming overheated and leading to failure. One of the symptoms is discolouration, i.e. the rings, balls and cages will change from gold to blue (Mohammed Z. M. A., 2014).

Temperature in excess of 400°F (approximately 204.4°C) can anneal the ring and ball materials, causing a loss in hardness and reducing the bearing capacity, causing early failure as the balls and cages deform.

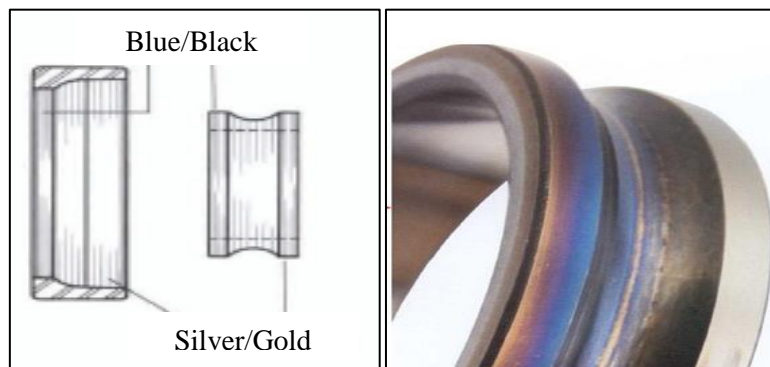


Figure 2. 7: Overheated bearing (Barden P. B., 2011)

- Corrosion

Corrosion mostly occurs in bearings exposed to corrosive fluids. It occurs after the surface of the bearing has been attacked by some chemical reaction, whether moisture, vapour or acid. The corrosion may reach the inside of the bearings (Kaydon., 2014.).

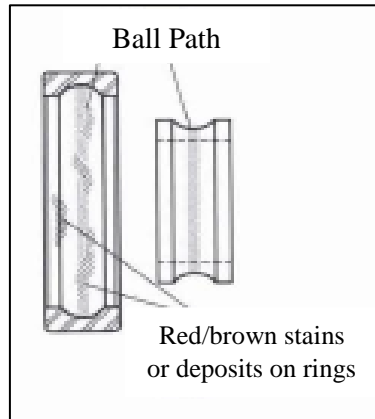


Figure 2. 8: Corrosion symptoms (Barden P. B., 2011)

SKF has suggested that there are two types of corrosion: deep-seated rust, and fretting corrosion. Deep-seated rust is a great risk to bearings as it can initiate flaking and cracks. Fretting corrosion is generated by rubbing or gnawing between two metal surfaces in bearings. Table (2.2) shows types of corrosion as suggested in SKF:

Table 2. 2: Types of corrosion (SKF, 1994)

	Deep-seated rust	Fretting corrosion (Chafing corrosion)
Appearance	Streaks of black /grey across the raceways	Rusted area on the outer ring or the inner ring
Cause	Presence of water, moisture or corrosion in the bearing over a long period of time	Errors of form in shaft or housing seat
Action	Improve sealing	Adjust seats

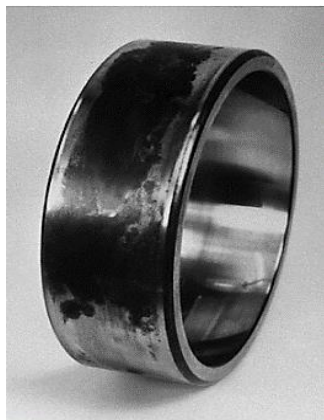


Figure 2. 9: Fretting corrosion (SKF , 1994)

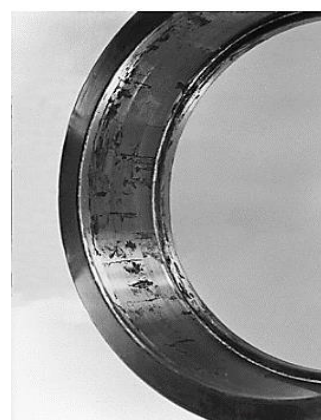


Figure 2. 10: Deep-seated rust (SKF, 1994).

Corrosions defects could be avoided either by following the advice of the manufacturer on how to protect the bearings, or by using stainless steel bearings (Barden P. B., 2011).

- Contamination

Bearings are designed and manufactured to have a long lifespan if operating in a clean environment, but exposure to contaminants will affect both lifespan and performance. One of the main reasons for early bearing failure is contamination of lubricant oil by solid particles. This will cause denting on the raceways and balls, resulting in wear and high vibration.

Contamination failures mostly occur when the bearing operates in a dirty environment, containing airborne dust, abrasive substance or any kind of dirt. After eventual fatigue in the surfaces of the bearings, damage such as bruising is likely to occur, shortening the lifespan of the bearing and reducing its efficiency (Noria C., 2010).

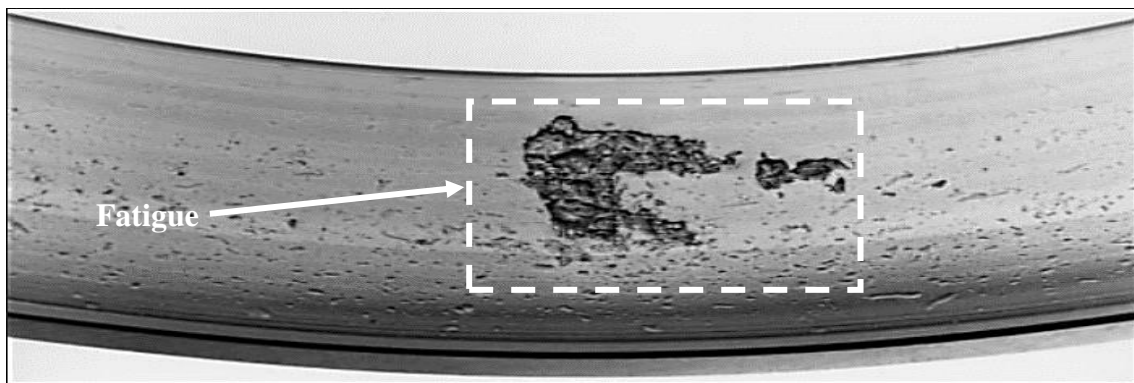


Figure 2. 11: Fatigue damage in the outer ring raceway (Kuhnell B.T., 2004)

A clean work environment / tools will usually protect the bearing from contamination. There are two ways to overcome this failure: either by fitting seals that prevent contaminants from entering the bearing form, or by fitting filters to ensure particles are removed from the machine before operation (SKF, 1994).



Figure 2. 12: Contamination Failures (Barden P. B., 2011 and Noria C., 2010)

- Misalignment

If there is misalignment an abnormally high temperature can be expected, in any part of the bearing elements, the housing or both (Barden P. B., 2011). Misalignment commonly occurs when the rolling element deflects under the operating load, as shown in Figure (2.13).

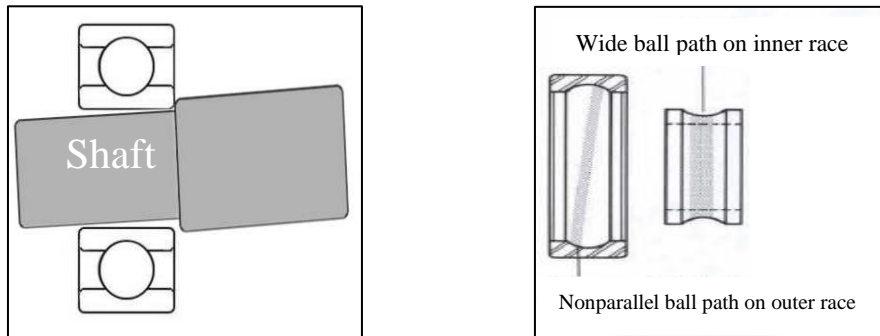


Figure 2. 13: Example of shaft misalignment (Barden P. B., 2011)

There are two types of misalignment: angular and parallel. Figure (2.14) shows the difference between misalignment and proper alignment (Lubsys., 2003).

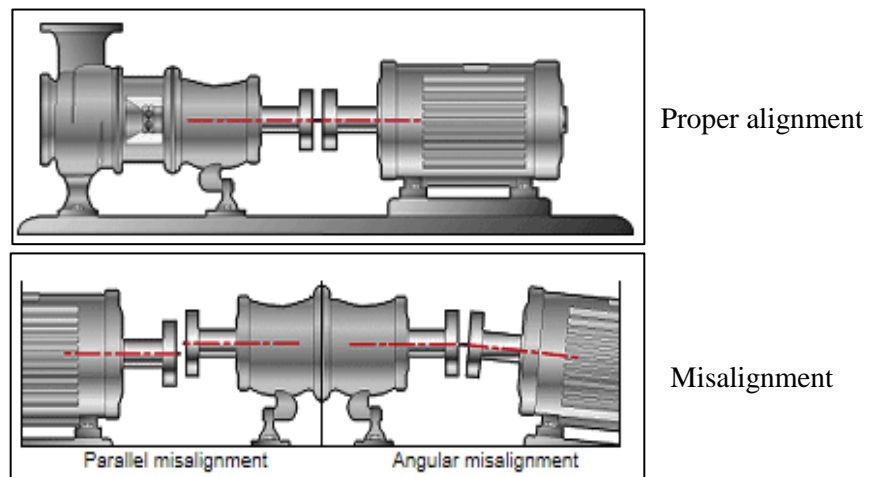


Figure 2. 14: Proper alignment and misalignment (Lubsys., 2003)

Proper alignment will ensure longer life for the bearing, minimal noises, and reduce the risk of overheating and lubricant leakage (Lubsys., 2003). To avoid this failure in bearings, Manney D., (2014) suggested that permissible misalignment depends on the bearing type and operating conditions, and summarised some solutions as follows:

- 1- Self-aligning ball bearings design – lower load capacity resulted after smaller contact angle between the balls and the raceways
- 2- Nylon cages rather than steel cages – this will accommodate misalignment better than steel

- Tight and loose fits

Bearings must be provided with the appropriate environment in order to support longer life. Regardless of type and size, shaft and housing must fit properly with the bearing to avoid premature failure. An inadequate fit could create contamination, again leading to early failure (NSK, 2010). Neither tight nor loose fit, is recommended for the bearings, so shaft and housing tolerance should be equal to the size of the bearing bore (Roberds K., 2017). Table (2.3) below shows the difference between tight and loose fits.

Table 2. 3: Type of fits (NTN, 2013)

	Type of fits	
	Loose fit	Tight fit
Description	Rolling element allowed to move axially	Rolling element not allowed to move axially
Cause	Bearing bore is larger than the shaft diameter	Shaft needs excessive pressure to fit on the bearing bore

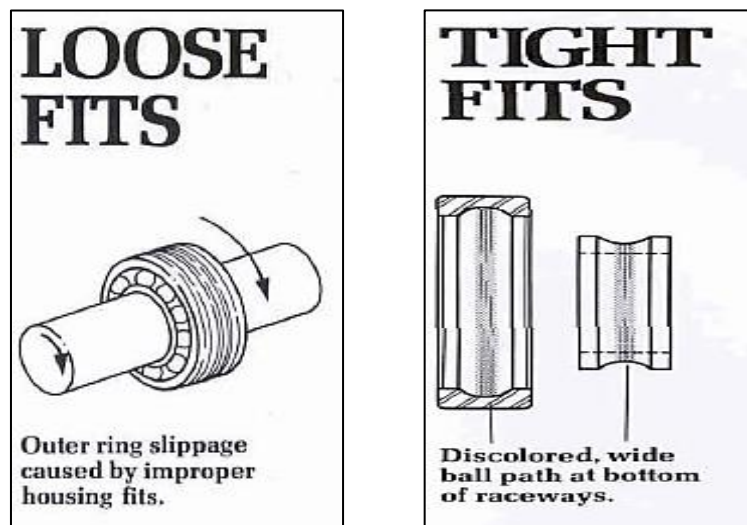


Figure 2. 15: Loose and tight fit failure (Barden P. B., 2011)

Loose fit leads to creep on the shaft, which causes vibration or excessive wear, or could lead to ring fracture in the worst case. If the shaft is too tight for the bearing bore, this will cause overheating and early failure. Based on Table (2.3), an appropriate fit must be considered to avoid early failure from either loose or tight fits.

To overcome this, shaft and housing tolerance should be fitted with an equal size of bearing bore. Akash P., (2014a) has suggested that adhesive produces a good fit but has disadvantages:

it may be attacked by lubricants or solvents. Also, it could get into the bearing and cause damage.

2.3.2. Lubrication

Inappropriate lubricants may also cause failure in bearings. The correct lubricant gives the rolling element a longer life with more accuracy while operating. Adequate performance of the rotating machinery will depend on how it is lubricated, because appropriate lubrication will minimise friction and prevent wear. Inappropriate lubricants will lead to excessive wear and overheating (Fischer K. et al., 2012).

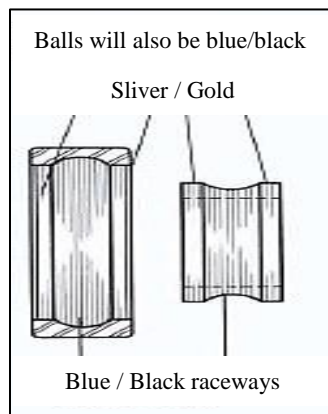


Figure 2. 16: Lubrication failure symptoms (Barden P. B., 2011)

Figure (2.16), shows the symptoms of lubricant failure, with discoloured balls and raceways. The colour of the raceways turns from black to blue because of overheating (Barden P. B., 2011).

Katz S. and Mike S., (2017) studied the causes of failure in rolling bearings, aiming to identify the most common causes in reducing bearing life. Figure (2.17) shows the result of this study: 45% of failures are the result of inappropriate lubrication, with old lubricant (20%), unsuitable lubricant (20%) or insufficient lubricant (15%).

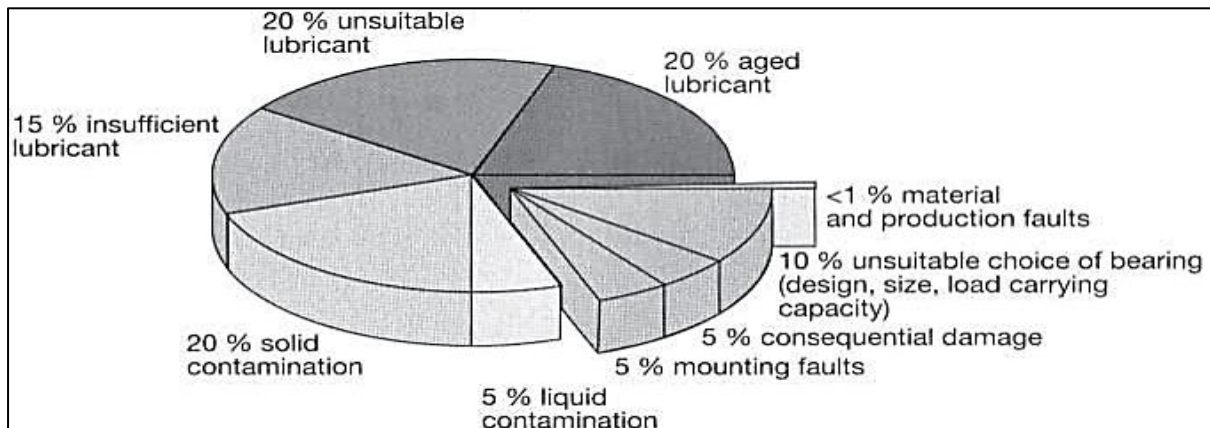


Figure 2. 17: Causes of failure in rolling bearings (Katz S. and Mike S., 2017)

There are three types of lubrication: oil, grease and solid film. Grease is normally applied to the head of the housing as shown in Figure (2.18), and is deposited between the balls and the raceways (from the circled area in Figure (2.18)). Oil is applied by the manufacturer, with the amount not specified, and is commonly used with miniature or instrument-type bearings (Wes C. and Rick James., 2013).

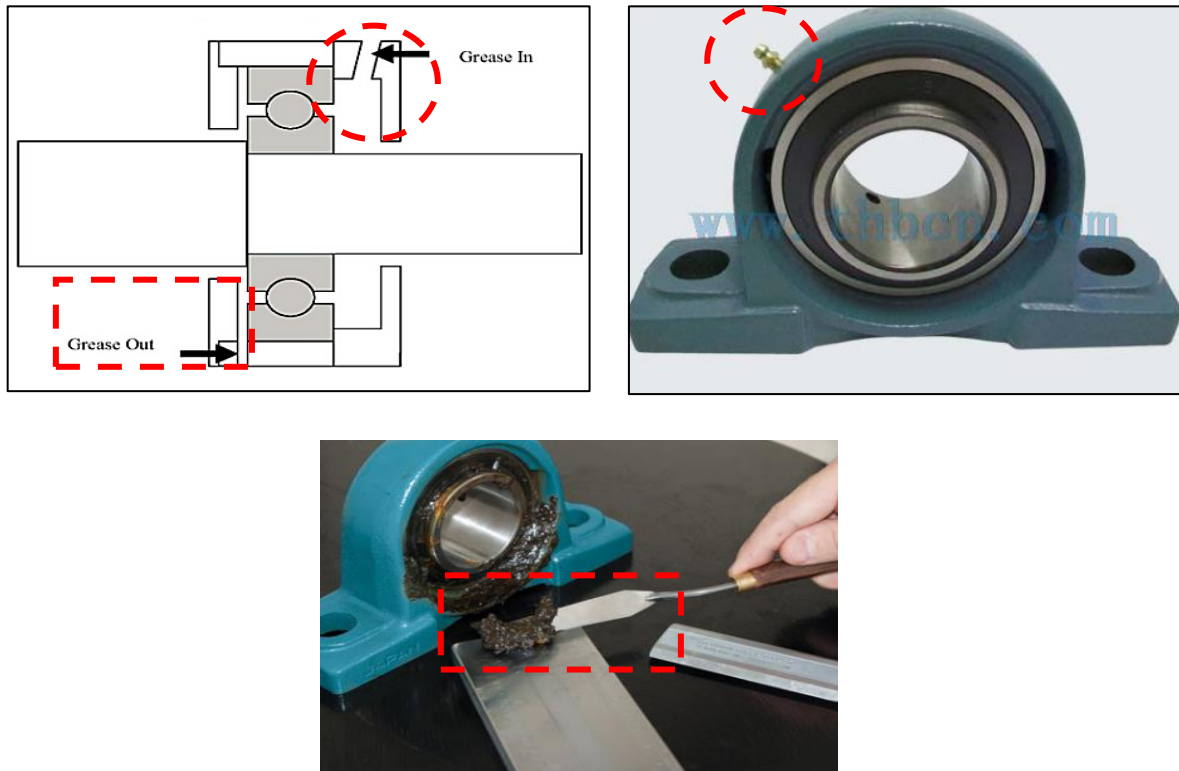


Figure 2. 18: Bearing Greasing (Wes C. and Rick James, 2013)

- Circled areas display where the grease enters the bearing
- Rectangular areas shows the exit for the grease

Oil is suitable for high-speed or high-temperature operations. Grease is commonly used to provide an appropriate lubricating environment for bearings because it is easy to handle and simplifies the sealing system (Wes C. and Rick James., 2013).

2.3.3. Generator

The generator is located inside the wind turbine nacelle and its purpose is to produce electricity by converting mechanical energy into a form of electrical energy. It commonly fails if the power source frequently fluctuates. One of the main categories of failure in generators is mechanical failure, for example when inappropriate lubricants result in early bearing fatigue (Nivedh B.S., 2014).

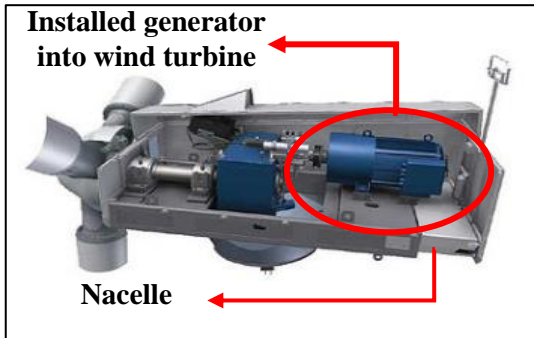


Figure 2. 19: Generator installed into Nacelle (Chong P. K., 2013)



Figure 2. 20: Generator (Chong P.K., 2013)

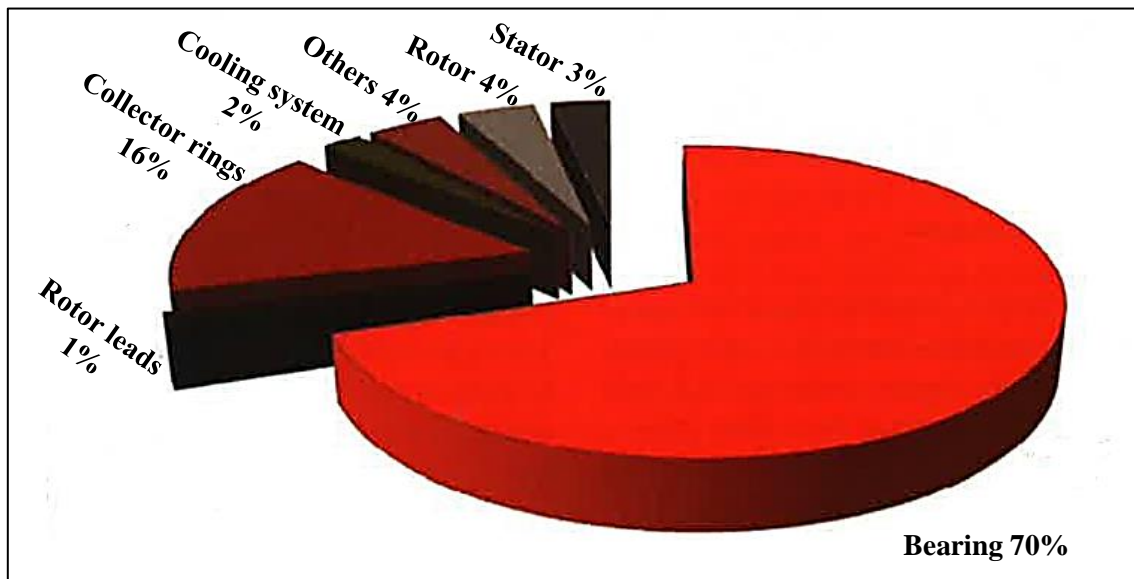


Figure 2. 21: Failures which occur in the different parts of the generator (Nivedh B.S., 2014)

Nivedh B.S., (2014) showed that 70% of failures in the generator are from bearings, as shown above in Figure (2.21). Sections (2.1.1. and 2.1.2.) covered failures that may occur in the bearings during operation.

2.3.4. Brake

In terms of safety regulations, a braking system is installed in the wind turbine nacelle to stop the rotor from rotating either mechanically, electrically or hydraulically in abnormal conditions. Failure in braking the turbine under abnormal conditions may lead to loss of the wind turbine structure. A safety brake system for small wind turbines was developed by Suco Technologies (Figure (2.23)) to protect them against damage from high wind speeds (Entezami M.E., 2013 and Nic. S., 2013).

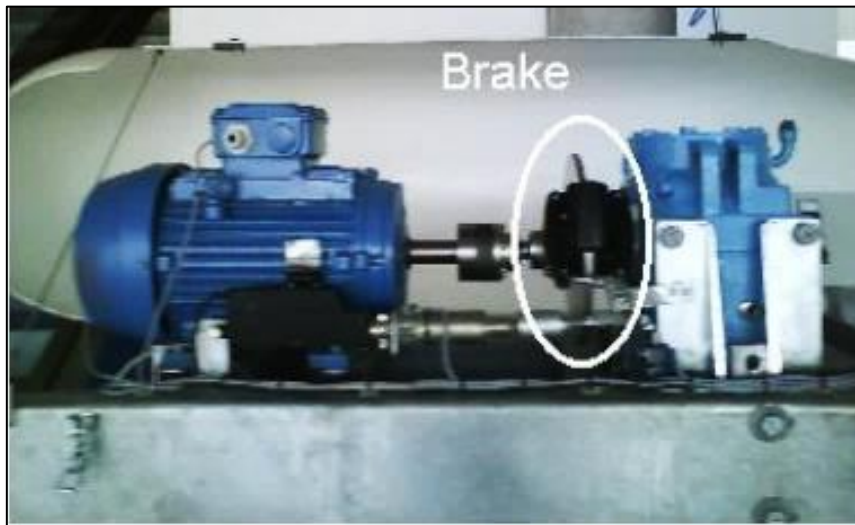


Figure 2. 22: Brake installed into nacelle (Mahon N. M., 2013)



Figure 2. 23: Suco Technologies brake (Nic. S., 2013)

Another type of brake is the hysteresis brake, which typically functions in torque measurement control in either open loop or closed loop systems. It uses an Electromagnetic Field (EMF) to apply load on the main shaft in order to stop the rotational speed. The main advantage of this kind of brake in micro-scale wind turbines is that it generates no wear, enhancing the efficiency of the whole operation. The main elements of the hysteresis brake are the rotor (drag cup) and the pole structure, as shown in Figure (2.24) below. The pole structure contains an inner pole, an outer case and a coil. Hence, an electrical current from a regulator will energise the coil

inside the pole structure, to generate a magnetic field. This will lead to a flux field in the air gap between the pole structure and the shaft. The rotor is magnetically restrained, providing a braking action. This braking action causes no wear since all the elements are connected without any physical contact (Magtrol, 2012).

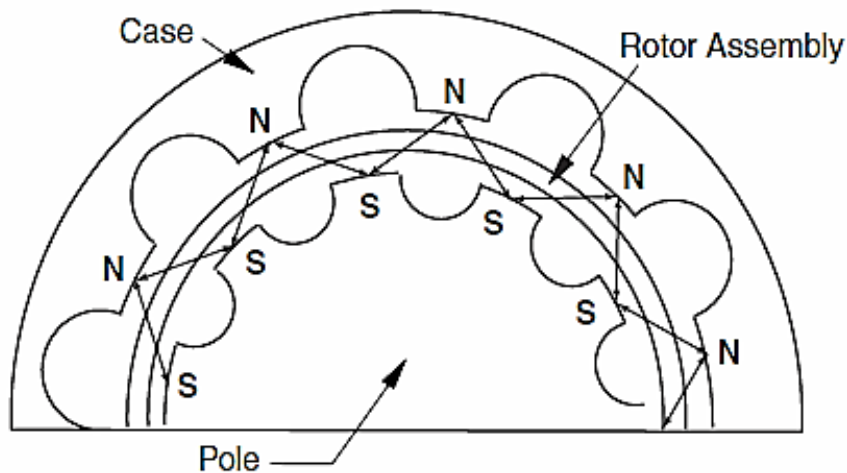
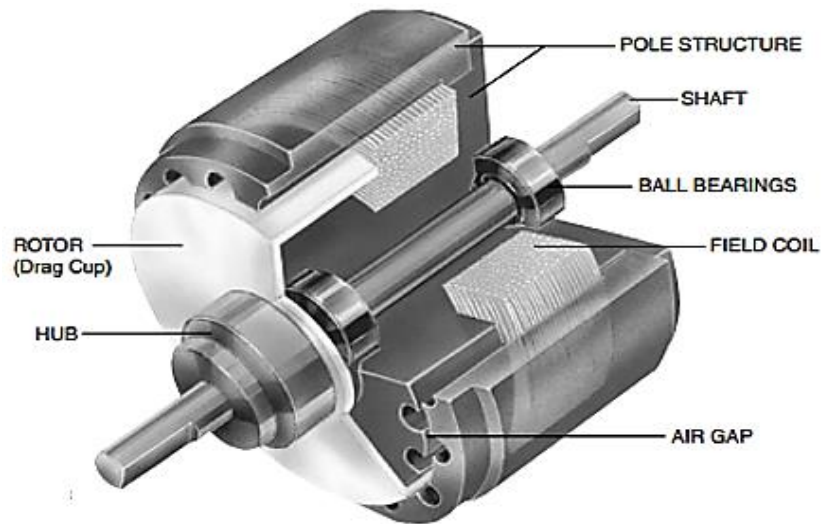


Figure 2. 24: Main elements of a typical hysteresis brake (Magtrol, 2012)

2.3.5. Main shaft

The main shaft is an especially important element in the micro-scale wind turbine as it is the connection between all the elements. During operation of the turbine, the shaft turns as a result of the spinning of the blades; this kinematic energy then goes to the generator through the bearing, to generate electricity. Thus, the sufficient shaft would be concern to avoid any failures.

Defects commonly occur in the main shaft due to constant over-use, with four main types of failure: corrosion, wear, overload and fatigue. Corrosion and wear rarely cause failure and they leave clear evidence. Fatigue is the most common failure in the main shaft, resulting from the load being applied constantly over many cycles; this cyclical stress leads to break or fracture. Shaft fracture is initiated at the surface of the shaft at points of imperfection, such as microscopic cracks accompanied by stress concentration at the edge of the crack. The shaft is fractured from either fatigue forces or overload forces. An overload can result in either a ductile or brittle fracture, i.e. fracture failure generally occurs when an overload is applied.

Ductile fracture is accompanied by significant plastic deformation, while brittle fracture is catastrophic and has little or no plastic deformation. Normally, ductile fracture occurs when a part distorts and can no longer hold the required load. The crack resists any additional extension unless there is an increase in the applied stress. In brittle fracture, cracks may spread very quickly with a little deformation. Also, these cracks are unstable, i.e. crack propagation will carry on without increasing the applied stress. Thus, ductile failures consist of one large piece of deformation, while brittle failures have the shape of a few pieces and small deformations (Gan T. H. et al., 2012 and Cyndi N.M., 2007).

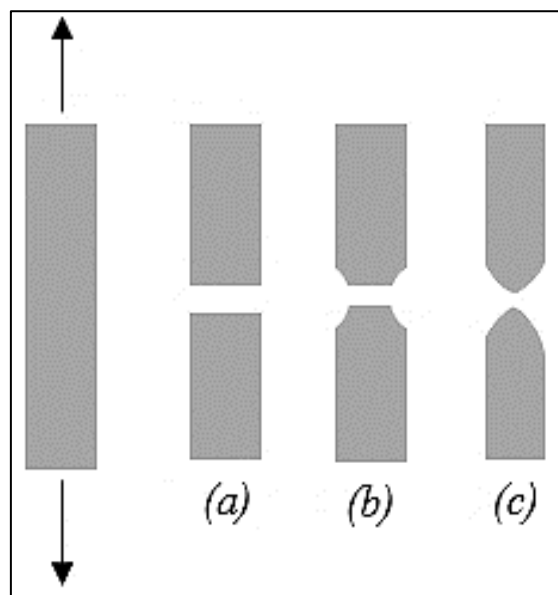


Figure 2. 25: Fracture types (After Teja G. V., 2014)

- (a) = Brittle fracture
- (b) = Ductile fracture
- (c) = Completely ductile fracture

2.4. Condition monitoring techniques

Condition Monitoring (CM) is defined as monitoring parameters of conditions in machinery such as vibration, temperature and emissions to identify any significant change which is indicative of a developing fault. The benefits of CM are: it provides information about the health of the machine, extends the operational life, improves machine productivity, minimises downtime, reduces product cost, improves quality and enhances safety (Takousting P. et al., 2014 and Jaber A. and Bicker R., 2014).

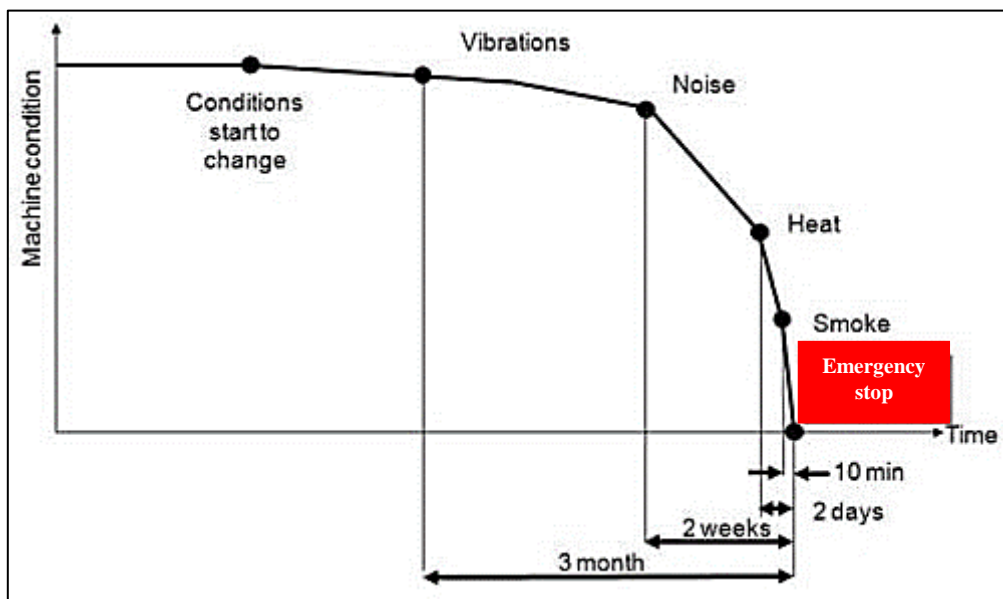


Figure 2. 26: Warning signs (Takousting et al., 2014)

Figure (2.26) shows that, through the parameters of the Condition Monitoring System (CMS), the required maintenance is provided before the failure occurs. For example, the failure starts as abnormal vibration and ends with detected smoke where the machine has to stop urgently.

The two main methods of CM are trend monitoring and condition checking. Trend monitoring is based on gathering data from the machine while it is operating, i.e. readings taken at regular time intervals, to specify differences in conditions between the machine and its components. Checking monitoring collects data from the machine only once while it is operating, i.e. readings are taken at one time while the machine is running, in order to check its condition. Other types of Machine Condition Monitoring (MCM) are Online Machine Monitoring (OMM) and Online Machine Protection (OMP), described in Table (2.4) below:

Table 2. 4: Types of Machine Condition Monitoring (MCM) (National Instrument, 2007)

Types of MCM	Role
Online Machine Monitoring (OMM)	<ul style="list-style-type: none"> - Data is gathered by an embedded system - Scheduling maintenance based on the data
Online Machine Protection (OMP)	Gathered data in the embedded system would be used to control the power of the machine, i.e. either on or off

Table (2.4) indicates the difference between OMM and OMP. The former schedules maintenance based on the data acquired in the embedded device, while the latter controls the power of the machine from the information acquired by the embedded device. All these methods aim to provide adequate maintenance of the machine in terms of avoiding catastrophic failures, improving the efficiency of the machine and enhancing its reliability (National Instrument, 2007).

Several maintenance strategies are applied to make subsequent use of the machine parts. For instance, Predictive Maintenance (PdM) is a technique designed to help determine the condition of in-service equipment by predicting when maintenance should be applied. NASA reported that PdM works to eliminate unexpected breakdowns and schedule maintenance downtime. On the other hand, Proactive Reliability Maintenance (PRM) maintains the reliability of machines or equipment, i.e. it explores machine failure and similar problems. It consists of preventive and predictive maintenance, focusing on determining the root of the machine failure and dealing with it before it occurs. It is a cost-effective maintenance strategy as it prevents machine failure by fix problems before it occurs. PdM involves monitoring vibration, heat, alignment, etc., while proactive maintenance monitors and corrects the root causes of failure (Neale M.J. and Woodley B., 2007 and Jaber A. and Bicker R., 2014).

Finally, Section 2.1. covers defects that commonly occur in different elements of the micro-scale wind turbine. While Section 2.2. covers CM techniques that can be used to help the to predict failure in micro-scale wind turbine bearings, including thermography, vibration, Online Debris Analysis (ODA), Acoustic Emission (AE) and Current Signature Analysis (CSA).

2.4.1. Temperature analysis (Thermography)

This analysis is used to diagnose abnormal temperature in machinery, which itself may indicate serious failure. For example, friction occurs in badly lubricated bearings and generates abnormal temperatures as shown in Figures (2.27) below.

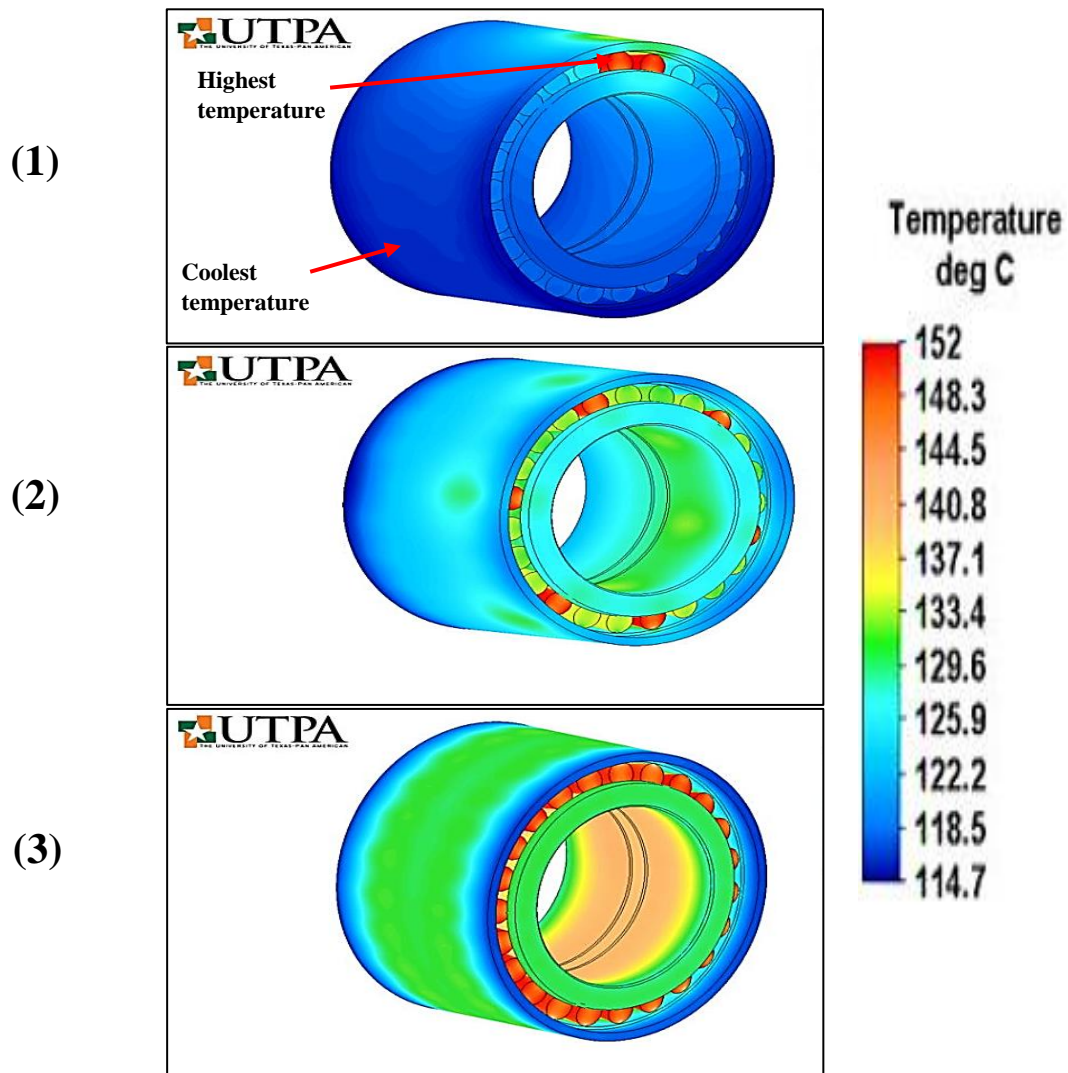


Figure 2. 27: Thermography analysis on cylindrical bearing (Fuentes A. et al., 2012)

From Figure (2.27):

- (1) At the beginning of the bearing operation, some of the cylinders start to overheat, whilst the rest of the elements maintain a normal temperature
- (2) Overheating spreads in different cylinders, while the bearing bore starts to heat
- (3) After the bearing has been in use for a long period of time, all the cylinders reach the highest temperature because of high friction; the edges of the outer race retain the coolest temperature

2.4.2. Vibration analysis (VA)

Vibration is defined as the “motion of a machine or its part back and forth from its position of rest”. It is one of the main techniques of Condition Monitoring System (CMS), and one of the earliest warning signs of failure, as shown in Figure (2.26). Vibration signals carry important information about the machine’s health, i.e. internal / external exciting forces, indicating imminent failure or serious damage to the machine parts. Through analysing this signal, avoidance of the failure may be possible, with reduction of downtime, minimisation of the maintenance budget, and other support for maintenance. However, difficulties in using vibration monitoring include the challenge of extracting useful information from the signal, the sensitivity of the signal in reacting with noise, and information required about the characteristics of the monitored system (Paresh G., 2004).

Vibration signals are used in order to make conditional maintenance on machines, so the measurement chain is: transducers, preamplifier, filter(s), detector / averager and output.

A. Measurement of vibration signals (Transducers)

Vibratory motion needs to be converted into a form of electrical signal to be measured. Three types of transducer are commonly used to obtain vibration signals: accelerometers, velocity transducers and displacement transducers. Each has its own characteristics that make it suitable for different applications (National Instrument, 2007), and selection of the appropriate one is based on several factors including measuring the frequency band and amplitude (Bruel and Kjaer., 1982).

i. Accelerometers

Accelerometer transducers are mostly commonly used for measuring vibration on stationary machinery. They provide a linear response involving frequency ranges (from a few hertz to tens of kHz).

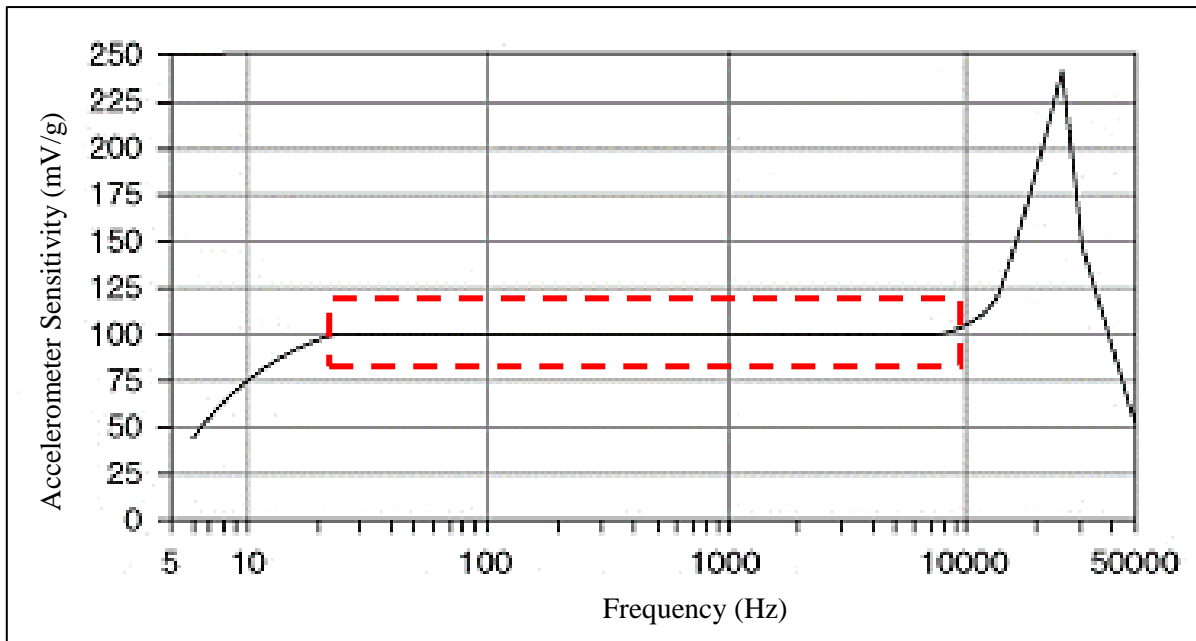


Figure 2. 28: Typical frequency response of an accelerometer – the highlighted region illustrates the linear frequency response of an accelerometer (National Instrument, 2007)

In Figure (2.28), the red rectangle represents the linear frequency response of an accelerometer. This type of transducer can be used to measure vibration in the main elements of a machine, including bearings and gearboxes. The piezoelectric accelerometer is universally used to measure vibration signals. It does not wear out because it has stationary parts, it does not need power as it is self-generating, and its output can be integrated with either velocity or displacement transducers (National Instrument, 2007).

Piezoelectric elements create a charge when strained, with different design configurations: compression, bending and shear. The transducer has to be well mounted, aligned with the frequency path. There are several mounting methods: stud mount, screw mount, epoxy, magnet and wax (adhesive). A non-secure mount can create a filtering effect. The stud mount accelerometer is the best for high-frequency measurement due to its robust design and reliability, with characteristics remaining stable over a long period of time (Bruel and Kjaer., 1998).

ii. Velocity Transducers

Velocity transducers measure the absolute motion of a system, in frequency response ranges from 15 Hz to 1.5 kHz, i.e. it is effective in medium-frequency ranges. They are often used to measure vibration in machinery casing. Eventually, by integrating the accelerometer velocity output will be obtained (Benko U. et al., 2004).

iii. Displacement transducers

This type of transducer is normally used measure displacement of the rotating shaft surfaces, by sensing shaft proximity. It is mounted on a stationary mechanical machine, to measure the distance between the probe tip and the rotating element surfaces. Electrically, it uses Direct Current (DC) and has signal response of 1.5 kHz. It is recommended for use in lower frequency measurements (National Instrument, 2007).

B. Bearing vibration signal

Bearing defects are a common cause of vibration. Worn bearings start to vibrate indicating a failure may occur. As shown in Figure (2.29) wear commonly appears on the surfaces of the raceways as a result of vibration. One of the main defects generating vibration in bearings is misalignment, due to friction from the operating load contacting the raceways. Several frequencies occur in the bearing elements and they are represented by the equations below (Thakar D., 2014).

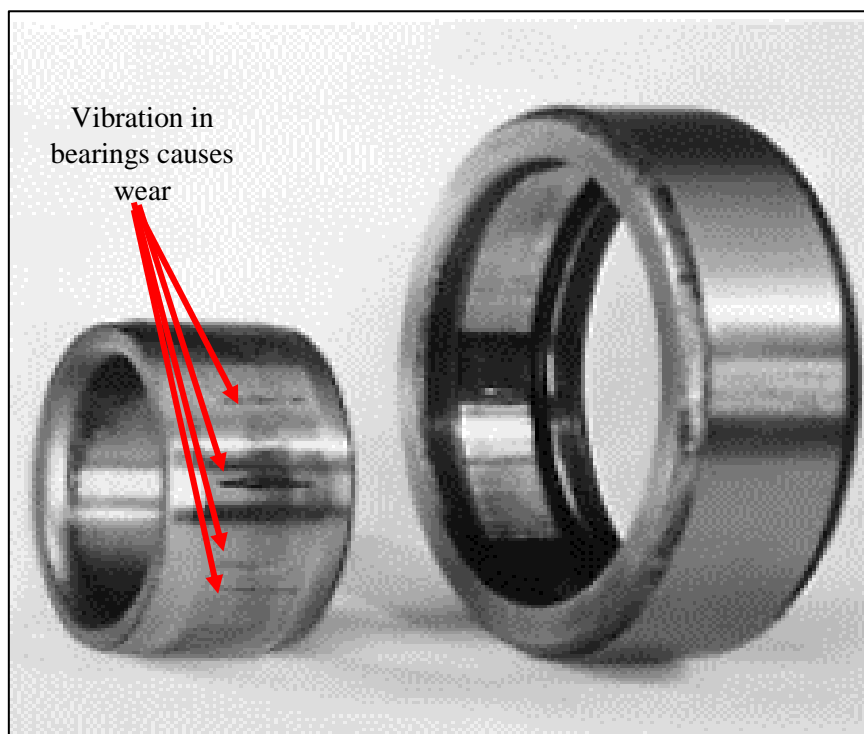


Figure 2. 29: Wear caused by vibration (Thakar D., 2014)

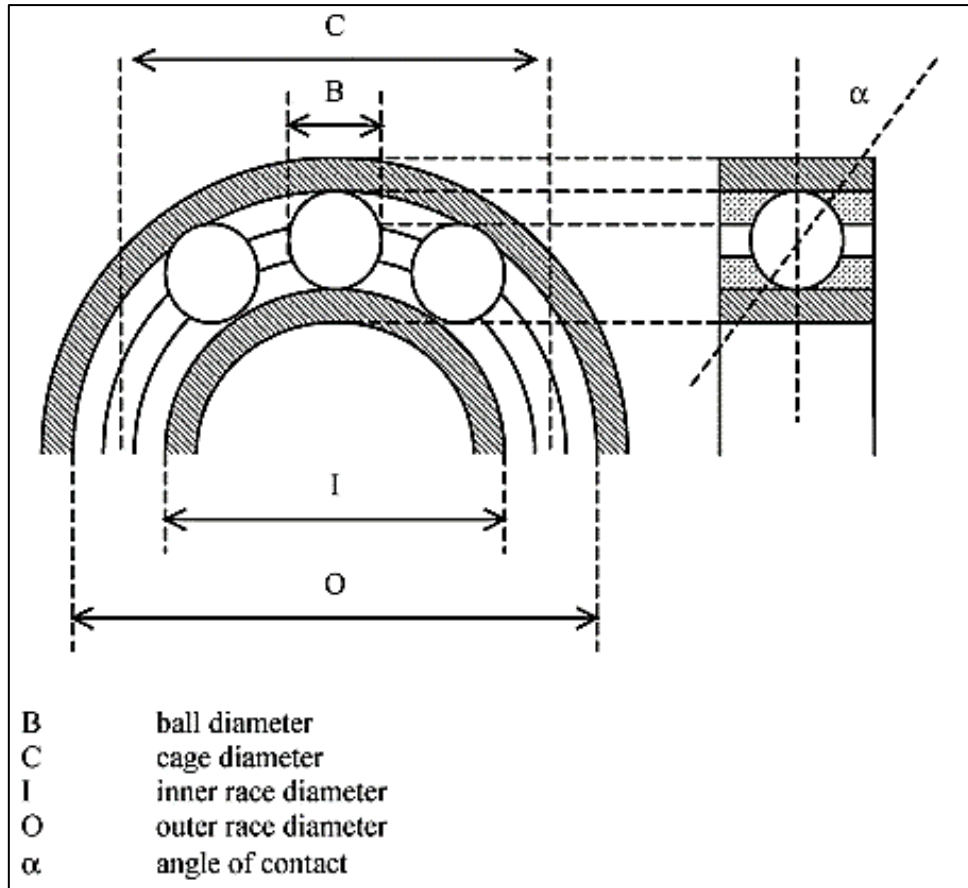


Figure 2. 30: Bearing element (Thakar D., 2014)

Table 2. 5: Bearing frequencies (Thakar D., 2014)

$f_r = \frac{\text{Shaft speed in r.p.m.}}{60}$	Eq. 2. 3: Shaft rotational frequency
$f_c = \frac{f_r}{2} \left(1 - \frac{B}{C} \cos \alpha \right)$	Eq. 2. 4: Cage rotational frequency
$f_o = \frac{f_r}{2} Z \left(1 - \frac{B}{C} \cos \alpha \right)$	Eq. 2. 5: Outer raceway frequency
$f_I = \frac{f_r}{2} Z \left(1 + \frac{B}{C} \cos \alpha \right)$	Eq. 2. 6: Inner raceway frequency
$f_B = f_r \frac{C}{2B} \left[1 - \left(\frac{B}{C} \cos \alpha \right)^2 \right]$	Eq. 2. 7: Ball rotational frequency

In Table (2.5), outer raceway frequency is minimised to $f_o = Z * f_c$. Where Z = number of balls.

C. Approaches to vibration analysis

Time domain, frequency domain analysis, time-frequency domain analysis and order domain analysis are some of the approaches to analysing vibration signals (Helmy M., et al., 2014).

i. Time domain analysis (TDA)

Time domain analysis is the behaviour of the signals over time. Onsy A. et al., (2011) used it to predict gear fatigue failures and diagnose fault by analysing the vibration signals. Samuel P.D. and Pines D. J., (2005) suggested that the simplest method to analyse vibration using the time domain method is to use Root-Mean-Squared (RMS), Crest Factor and Kurtosis. They have the capability to extract level of energy in the vibration signal as well as providing a measurement of the impulsive nature of the acquired signal.

1. Root-Mean-Squared (RMS)

$$\text{RMS} = \sqrt{\frac{1}{N} [\sum_{i=1}^N (X_i)^2]} \quad \text{Eq. 2. 8: Root-Mean-Square}$$

N = Number of samples

X = Sampled time signal

i = Sample index

Samuel P.D. and Pines D. J., (2005) described this equation as “the square root of the average of the sum of the squares of the signal samples”.

2. Crest Factor (CF)

Samuel P.D. and Pines D. J., (2005) defined CF as “the maximum positive peak value of the signal *x* divided by RMS”. The equation below explains the definition.

$$\text{Crest Factor} = \frac{X_{\text{peak}}}{\text{RMS}} \quad \text{Eq. 2. 9: Crest Factor}$$

X_{peak} = maximum positive peak

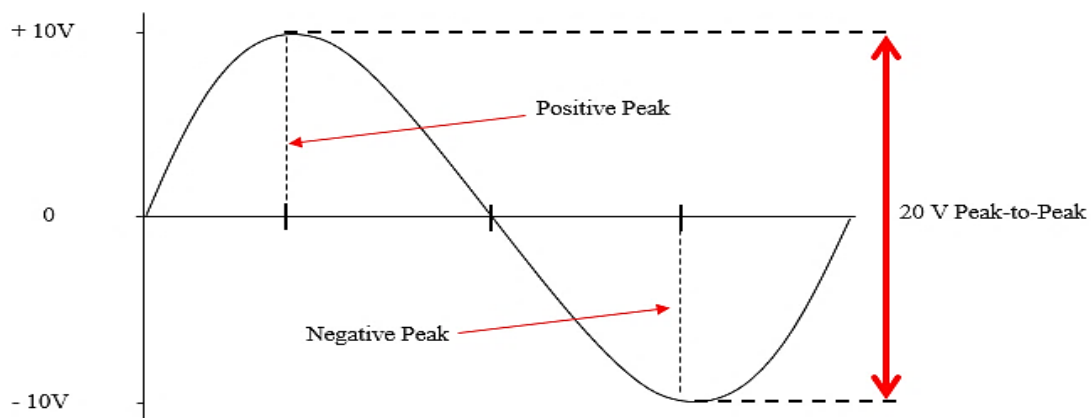


Figure 2. 31: Sin waveform example (After Gaatjes, W., 2012)

3. Kurtosis (Ku)

Another diagnostic technique is Kurtosis (Ku), which Samuel P.D. and Pines D. J., (2005) defined as “the fourth normalised moment of a given X i.e. the number of amplitude of peaks present in the signal”. This expression takes the form of the following equation:

$$\text{Kurtosis} = \frac{N \sum_{i=1}^N (x_i - \bar{x})^4}{[\sum_{i=1}^N (x_i - \bar{x})^2]^2} \quad \text{Eq. 2. 10: Kurtosis}$$

Where $x = \text{Given sampled time signal}$, $N = \text{Number of sample}$ and $i = \text{Sample index}$

ii. Frequency domain analysis

Frequency domain analysis is more commonly used in bearing diagnostics than time domain methods, due to its sensitivity and reliability. The easiest way to obtain narrowband spectra is to use Fast Fourier Transform (FFT), which is more efficient and accurate in diagnosing bearings faults, as the size of changes in spectrum are completely related to the nature of faults.

Based on the physical interactions between bearings elements, the resonant frequency is calculated, normally occurring above 5kHz. Mahdi K., (2006) suggested that bearings could be affected by geometry through shaft, speed, load distribution, type of load (radial and/or axial) or some other effect.

iii. Time-Frequency domain analysis

Time-frequency domain analysis is a new and powerful tool in the important field of diagnostics in stationary conditions. It provides joint distribution information for time and frequency domains, which obviously demonstrates the frequency of the signal changing as a function of time. Thus, it illustrates the signals in both time and frequency domains (Baydar N. and B.A., 2003).

iv. Order domain analysis

Order domain analysis is a technique to analyse sound and vibration signals from rotating or reciprocating machinery, such as turbines and pumps. These machines have various elements, each of which has a unique sound and vibration pattern. Sound and vibration can be identified and isolated to analyse the performance, reliability and quality of each element in the machine individually.

Order domain analysis uses two techniques: the Gabor transform and the resampling method. Gabor transform analyses the vibration signals in both time and frequency domains. The resampling method is used to organise the samples after applying FFT.

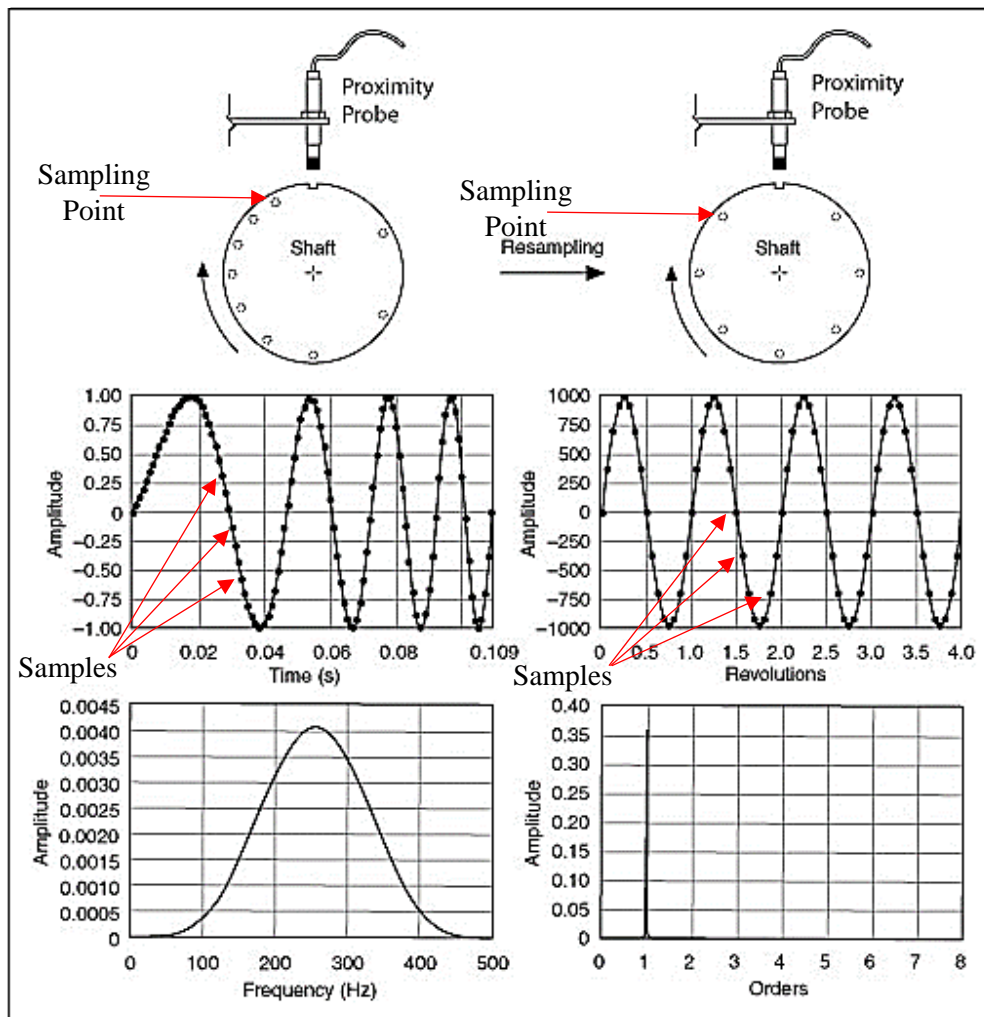


Figure 2. 32: Resampling example (National Instrument, 2007)

Figure (2.32) illustrates the effect of resampling on a vibration signal. Each point on each shaft represents a sampling point. After applying resampling method to the readings, it was noticed that all the samples appear with constant angle intervals. Before applying resampling, the readings were randomly plotted on the graph with different interval times, and after applying the resampling method the readings were plotted accurately with the same time intervals (National Instrument, 2007).

2.4.3. Oil Debris Analysis (ODA)

Oil Debris Analysis (ODA) is used to analyse the condition of the lubricant as well as monitoring the equipment's health while operating. It helps to identify the appropriate wear

process of the debris, and whether or not the equipment requires repairing or replacing. Therefore, it is used as an indication of the health of the machinery (Girdhar P. and Scheffer C., 2004).

Peng Z. and Kirk T.B. (1999) have suggested six types of metallic wear debris: rubbing, cutting, chunk, laminar, spherical and severe sliding. They also provided a classification scheme, part of which is shown in Table (2.6) below. Leavers V.F., (2005) illustrated another classification of the four primary types of wear debris, as shown in Figure (2.33):

- i. Mild sliding/rubbing wear: small particles with few surface features
- ii. Severe sliding wear: rough particles dark in colour because of high temperature
- iii. Fatigue: the particles are generated as a direct consequence of cyclic loading causing micro-pitting and sub-surface cracks
- iv. Cutting or abrasive wear: the harder surface acts as a cutting tool when two surfaces with dissimilar hardness come into contact.

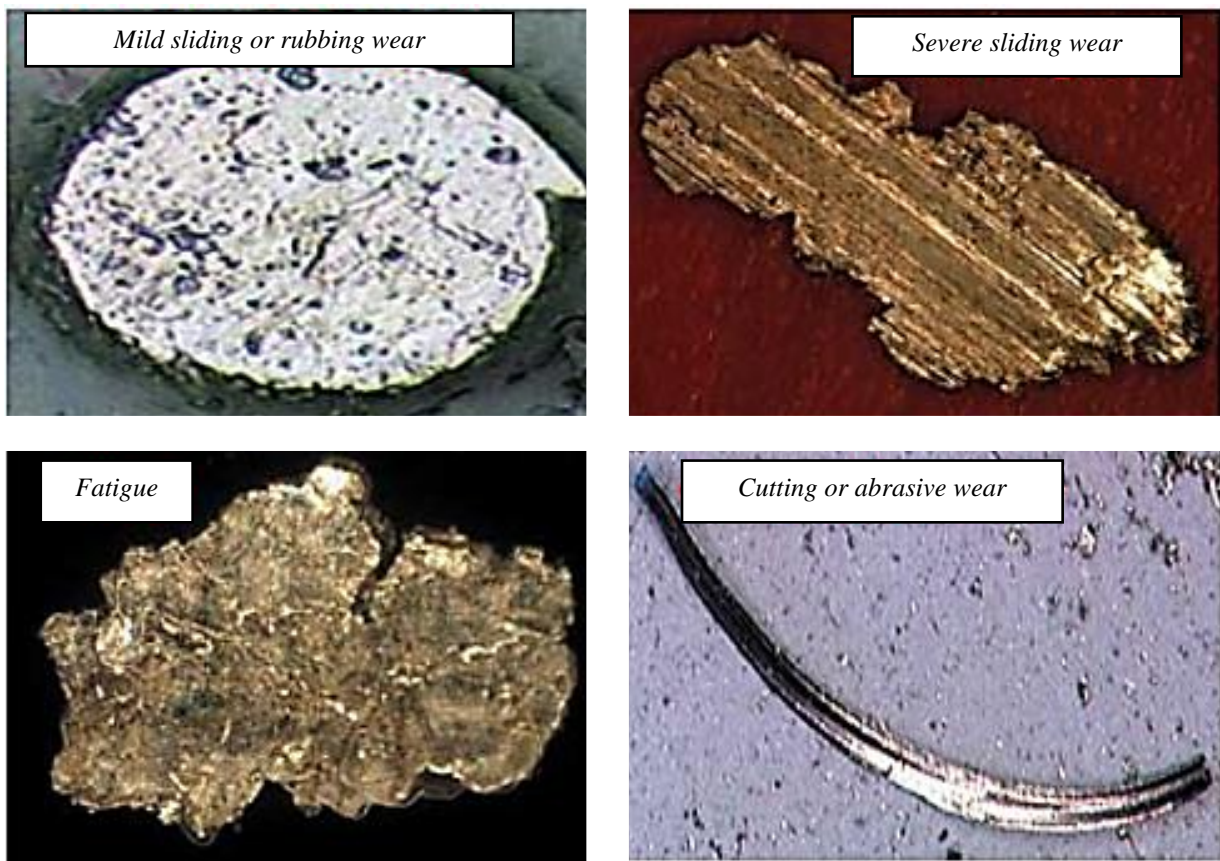


Figure 2. 33: (Leavers V.F., 2005)'s classification (Leavers V.F., 2005)

Table 2. 6: Classification scheme of metallic wear debris by (Peng Z. and Kirk T.B., 1999)

Types of particle	Morphology	Generation mechanism	Machine condition	Area (μm^2)	Length (μm)
Rubbing	Random outlines of shapes, smooth surfaces	The broken parts of the shear mixed layer	Normal wear particles	34	8
Cutting	Long, curved particles	Generated as a result of one surface penetrating another	Individual cutting wear particles is not significant but the presence of several of cutting wear particles indicates a severe cutting wear process being under way	227	38
Severe sliding	Scratched obtained in parallel grooved sets	Generated by severe sliding wear	Indicates an abnormal condition when these particles appear.	813	40

2.4.4. Acoustic Emission (AE)

Acoustic Emission (AE) is another CM technique used to indicate a machine's health. It can handle a wide range of applications, including non-destructive testing. Due to the flexibility of all solid materials, release of strain is achieved by allowing them to spring back as external forces are removed, i.e. the higher the force applied, the greater the elastic deformation. This will store elastic energy due to constant use. The rapid / frequent release of elastic energy will produce a wave (elastic wave) that increases through the surface and can be identified by an AE sensor (Vallen, 2006).

Tan C. K. et al., (2007) defined AE as "transient elastic waves generated due to a rapid release of strain energy caused by structural alteration in / on a solid material under mechanical or thermal stresses". The authors also identified the primary sources of AE:

- Crack initiation
- Crack propagation
- Plastic deformation
- Friction

In using the AE technique in CM, some important elements need to be considered (Vallen, 2006):

- 1- Selection of the appropriate AE sensor
- 2- The location and the type of sensor mounting
- 3- Sensitivity of the AE signal in the running conditions of
 - a. Torque
 - b. Speed
 - c. Temperature.

Vallen, (2006) classified two types of AE signal as shown below in Table (2.7).

Table 2. 7: AE signals' types

No.	Types	Description
1.	Transient signal	It has important features, such as signal start and end points and maximum peak
2.	Continuous signal	It has an amplitude with frequency variation and never ends

Features extracted from the transient signal include AE peak amplitude (AE_{APK}), Energy (RMS), Signal duration, Number of counts, Rise time and Arrival time (Vallen, 2006).

AE signals have a frequency range between 20 kHz and 1 MHz, and from 100 kHz to 300 kHz in metallic objects. Additionally, the technique requires less effort to extract the monitoring features comparing than does vibration analysis.

i. AE Chains

Figure (2.34) displays the AE process chain; by applying an external force the mechanical stress will be produced within the test object. After this, the behaviour of the materials and the point where the release of elastic energy has started (crack formation) will be influenced by the material's properties and the surrounding environment conditions. Propagation of an elastic wave through the material is detected, then converted into a form of electrical AE signal by using AE sensors. The sensed / detected signal bursts converted into feature data sets determine the location and calculate statistics. Finally, they are displayed graphically and/or numerically, respecting real time.

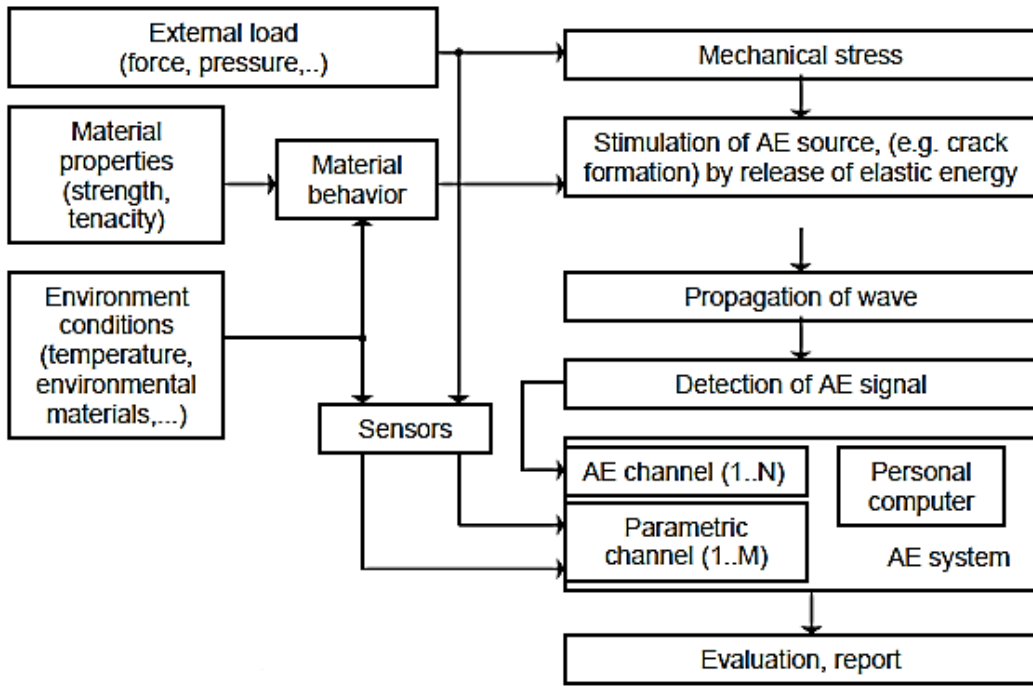


Figure 2.34: AE process chain (Vallen, 2006)

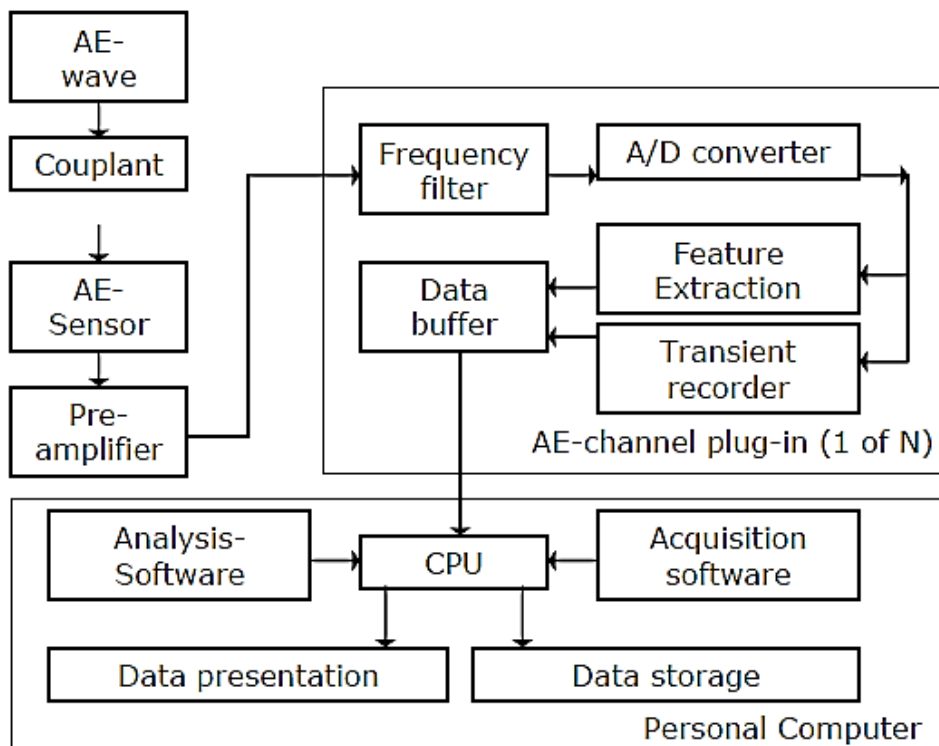


Figure 2.35: AE measurement chain (Vallen, 2006)

Piezoelectric sensors are the most appropriate for AE testing due to their greater sensitivity. The best frequency range is dependent on the expected AE sources, conditions of wave

propagation, wave attenuation and distances. The frequency range of AE signals is normally from 20kHz to 1MHz, but for metallic objects is between 100kHz and 300kHz. In Figure (2.35), the AE starts by picking up the wave at the sensor position through a coupling agent. The sensor then converts it into a signal that can to be amplified and transferred to the AE measurement system that processes, displays and stores the data (Vallen, 2006).

ii. Application of AE analysis in Health Monitoring Systems (HMS)

Onsy A., (2013) presented a novel Acoustic Emission Wireless Monitoring System (AEWMS) for rotating machinery which provided a decision-support feature using an intelligent approach to overcome any false alarms. It was evaluated on an automotive bearing application and could be modified to monitor the transmission systems in aircraft, industrial machinery and wind turbines. The study demonstrated the ability of AEWMS in detecting defects in bearings. The monitoring system was also experimentally validated on an automotive application, measuring a faulty wheel bearing that had been run for more than 50,000 km, using several validations. Then, the bearing was replaced with a new one and the same test procedure was applied for several runs. The new wheel bearing reached about 20,000 km of its service life after being operated in rough service. The author concluded that the new cost-effective AEWMS was able to detect different conditions of wheel bearings, and clearly identify its condition using only one AE sensor placed on the drive axle shaft.

2.4.5. Current Signature Analysis (CSA)

Compared to the other analyses (temperature, vibration, ODA and AE), CSA has proved its capability in monitoring inaccessible locations or remote places in devices like centrifugal pumps and motor drives in order to identify and/or analyse mechanical faults. It has emerged as highly sensitive, selective and cost-effective. It has been used successfully in detecting bearing faults (Sukhjeet S. et al., 2014). Jason R. S. et al, (2004) identified a method for detecting developing bearing faults via a stator current.

Sukhjeet S. et al, (2014) contributed to the same analysis through comparing the detection of bearing faults in mechanical systems using motor current signature and acoustic signatures. Their contribution was aimed at detecting bearing faults (outer raceway) through using motor signature analysis.

i. Application of CSA in HMS

An experiment was done to detect bearing faults (outer raceway) through using motor signature analysis and acoustics signatures. They used three ball bearings as shown in Figure (2.36) below.

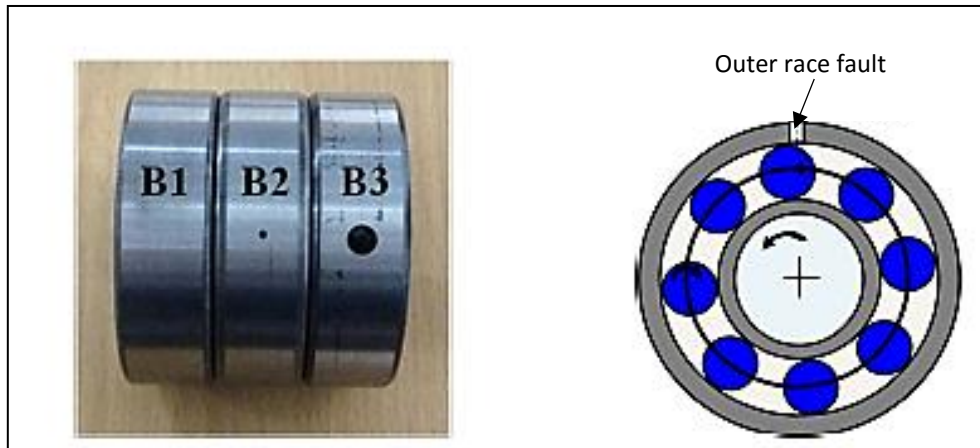


Figure 2. 36: Healthy and Faulty (Sukhjeet S. et al, 2014)

Table 2. 8: ball bearing's specification – SKF(Sukhjeet S. et al, 2014)

Number of balls (N_b)	8
Shaft speed (ω_{inner})	35 Hz = 2100rpm
Ball diameter (d)	7.938 mm
Pitch diameter (D)	33.5 mm
Contact angle of bearing (α)	0°

In Figure (2.36), B1 is the healthy bearing while B2 and B3 are the faulty bearings. B2 has 2 mm holes and B3 4 mm holes, both sets on the outer raceway. Using vibration and acoustic sensors, Sukhjeet S. et al., concluded that the amplitude range of the faulty bearing signals in the time domain, is greater than the range of healthy bearing signals. In the case of current signature, the increase in amplitudes was insignificant. The same signals were analysed in the frequency domain and it was found that the fault frequency for detecting a fault on the outer raceway using vibration and acoustic sensors was 105.9Hz, using the equation below.

$$f_{bng} = N_{b.\omega_{inner}} \left(\frac{1 - \frac{d}{D} \cdot \cos(\alpha)}{2} \right) \quad \text{Eq. 2. 11: Outer race fault frequency}$$

Where f_{bng} = outer raceway fault frequency considered for vibration

$$N_{b.\omega_{inner}} = \text{Number of balls} * \text{shaft speed}$$

d = ball diameter

D = pitch diameter

α = contact angle of bearing

Where the current signature is 141.7 Hz based on the following equation:

$$f_{or f} = |f_s \pm m * f_{bng}| \quad \text{Eq. 2. 12: Current Signature Spectrum}$$

Where $f_{or f}$ = current signature spectrum

f_s = The supply frequency

m = integer i.e. 1.2.3....etc.

f_{bng} = outer raceway fault frequency considered for vibration

Figures (2.37, 2.38 and 2.39) identified / analysed the results from this experiment as shown below:

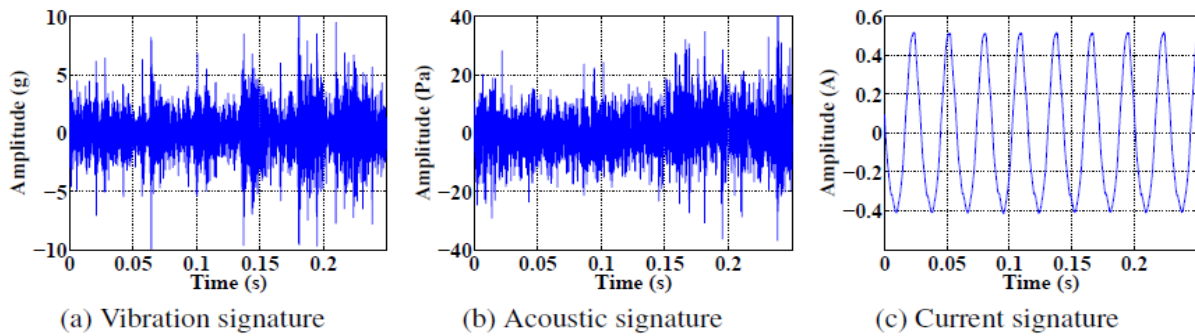


Figure 2. 37: Time domain of faulty bearing - B2 (Sukhjeet S. et al, 2014)

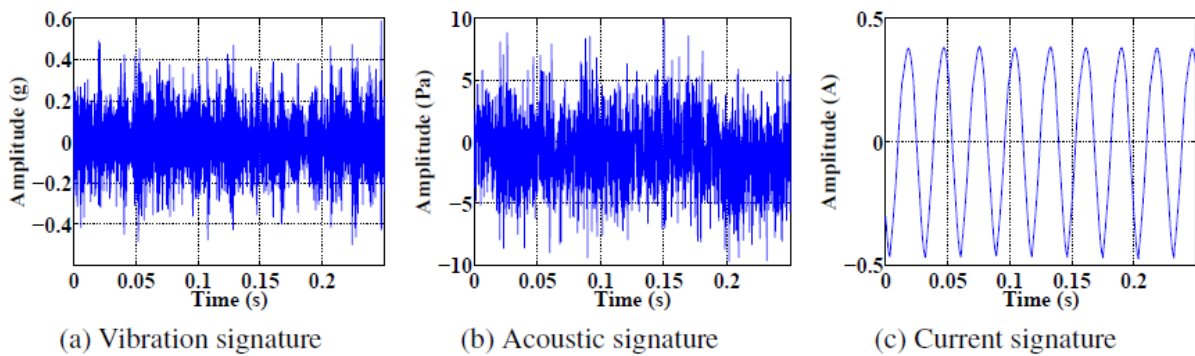


Figure 2. 38: Time domain of healthy bearing - B1 (Sukhjeet S. et al, 2014)

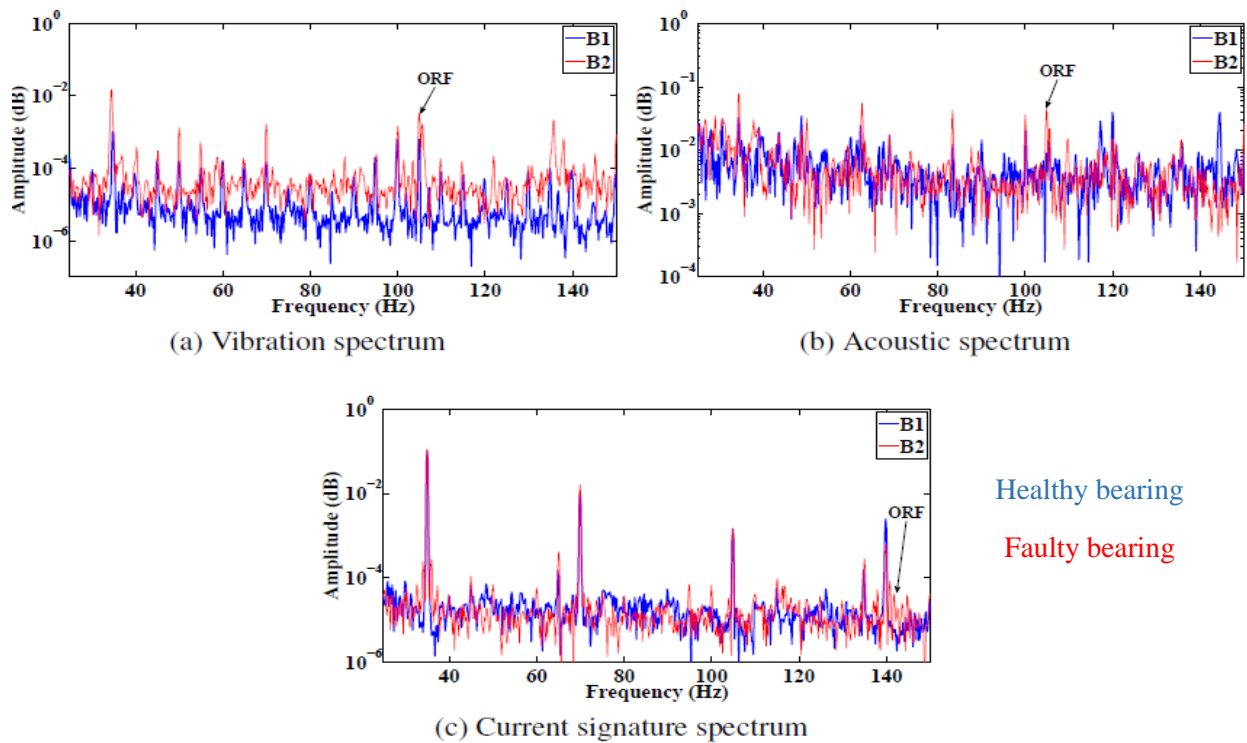


Figure 2. 39: Frequency domain of healthy bearing - B1 and faulty bearing - B2 (Sukhjeet S. et al, 2014)

2.5. Intelligent Condition Monitoring Methods

Several techniques are used to make industrial systems operate without human interaction, including ongoing research to develop or explore new intelligent methods to improve Health Monitoring Systems (HMS). Jain L.C. and De Silva C.W. (1998) have defined Artificial Intelligence as “the science of making machines do things that would require intelligence if done by humans”. Furthermore, such systems will be able to learn, adapt and make decisions based on the surrounding environment.

Therefore, the following sections consider the fundamental techniques of fuzzy logic, neural networks, genetic algorithms and expert systems and their use in intelligent control.

2.5.1. Fuzzy Logic methods

In any traditional Boolean logic, 1 indicates true and 0 indicates false. Fuzzy logic is based on degrees of truth, i.e. 0.7 could be partially true and 0.3 false (Hájek P., 1998). It was first developed by Lotfi in the 1960s to represent some types of knowledge that cannot be represented by Boolean algebra. Therefore, it is used to represent human knowledge in specific domains by making useful inferences.

The elements in a fuzzy set use grades of possibility, and membership function denoted by (μ). This will allow description of the behaviour of systems that are too complex to deal with mathematically. Jain L.C. and De Silva C.W., (1998) provided an identity for the fuzzy set (A) in the universe X, as shown below in (Eq. 2.13.).

$$A = \{(x, \mu_A(x)); x \in X, \mu_A(x) \in [0,1]\} \quad \text{Eq. 2. 13: Fuzzy sets}$$

Where $\mu_A(x)$ = membership function of A, i.e. grade of possibilities that x belongs to set A. The closer $\mu_A(x)$ is to 1, the more x is considered to belong to A, and vice versa.

Some of the main advantages of using fuzzy systems are their ability to represent complex input-output relationships as a set of simple I/O relations; and to modify fuzzy rules/membership functions when necessary, i.e. when logic and/or variables should be changed (Jain L.C. and De Silva C.W., 1998).

There are three main types of fuzzy model based on the expressions of the consequent part, summarised in Table (2.9).

Table 2. 9: Fuzzy model types (Hideyuki T., 1997)

Types of model	Mamdani	Takagi-Sugeno-Kang (TSK)	Simplified
Equation	$y = A$	$y = a_0 + \sum a_i x_i$	$y = c$
Comments	A is a fuzzy number	where a_i is a constant and x_i is a variable	c is a constant
Explanation	High-level control system, knowledge processing and expert systems	Indirect fuzzy control	Special case because the consequent parts are expressed by constant values

Mamdani has a fuzzy variable defined by a membership function in its consequent parts. In TSK, its consequent parts are expressed by a linear combination of weighted input variables (Jain L.C. and De Silva C.W., 1998).

i. Intelligent Condition-Based Monitoring (ICBM) / Fuzzy logic

Kothamasu, R. and Huang, S. H., (2007) developed an Intelligent Condition-Based Monitoring (ICBM) architecture. It had four modules: data acquisition (DAQ), feature extraction, model generation and model deployment (Figure (2.40) below). The features of each module are shown in Table (2.10) below.

Table 2. 10: Kothamasu, R. and Huang, S. H. (2007)'s Intelligent CBM architecture modules

Module name	DAQ	Feature Extraction	Model Generation	Model Deployment
Explanation	Acquiring data from the target system/its environment	Extraction of useful information from new data that may reflect the condition of the target	Building a predictive model from extracted data, by taking the extracted feature as an input and providing outputs based on whether prognostic or diagnostic	Integrating the created model into the monitoring system/establishing the proper channels for communication

Based on Table (2.10), diagnostic model generation could detect bearing failure. On the other hand, prognosis could estimate the future Root-Mean-Squared (RMS) or Kurtosis values.

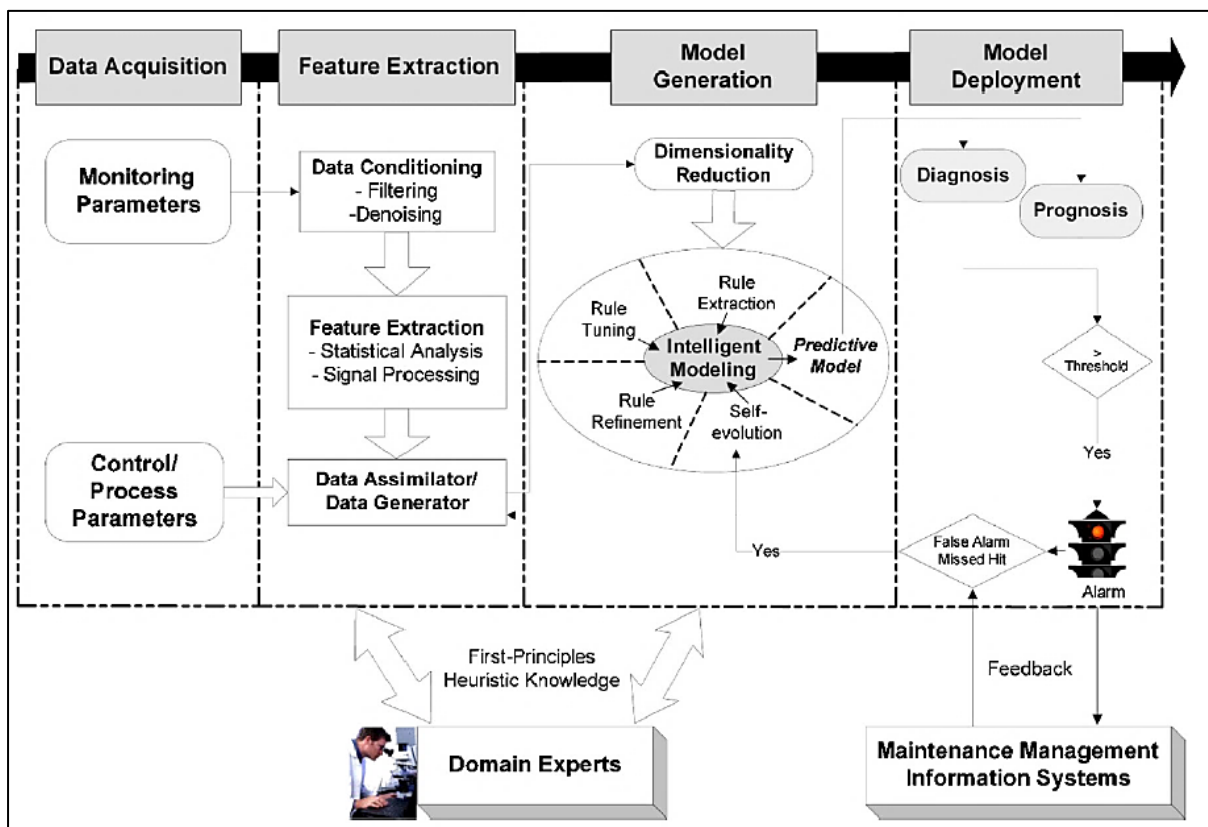


Figure 2. 40: Intelligent CBM architecture (Kothamasu, R. and Huang, S. H., 2007)

Onsy et al., (2010) developed an online ICMS using adaptive fuzzy logic algorithms and utilising features of vibration analysis, acoustic emission monitoring, online debris analysis

techniques, and torque-speed wireless measurement to predict both surface and bending fatigue failures of power transmission gears. The system was able to send prediction information to multiple users via Local Area Network (LAN) and Wide Area Network (WAN).

In conclusion, fuzzy techniques attempt to approximate human knowledge and the associated reasoning process.

2.5.2. Artificial Neural Networks (ANNs)

Jain, L. C. and de Silva, C. W., (1998) identified ANNs as hugely connected networks that can be trained in terms of representing complex non-linear functions where a high level of accuracy should be considered, i.e. analogous to human brain neurons. The ANN method has great potential in modelling non-linear systems and problems. Its procedures can be achieved through continuous interaction with the surrounding environment, giving automatic feedback about its response. This enables the system to learn, where interaction with the environment is part of learning. This enables the machine to perform with a level of autonomy and cognition.

There are two types of network architecture, Feed-Forward and Recurrent (William G. F et al., 2001). Feed-Forward occurs when there is no feedback between the layers; the previous input is commonly not remembered as only the current input is operated on. On the other hand, when there is feedback between the layers, the network will remember previous inputs, so it can be taught to perform and build an associative memory. In addition, multilayer perception is an example of Feed-Forward networks, and artificial resonance theory (ART) models an example of recurrent network architecture.

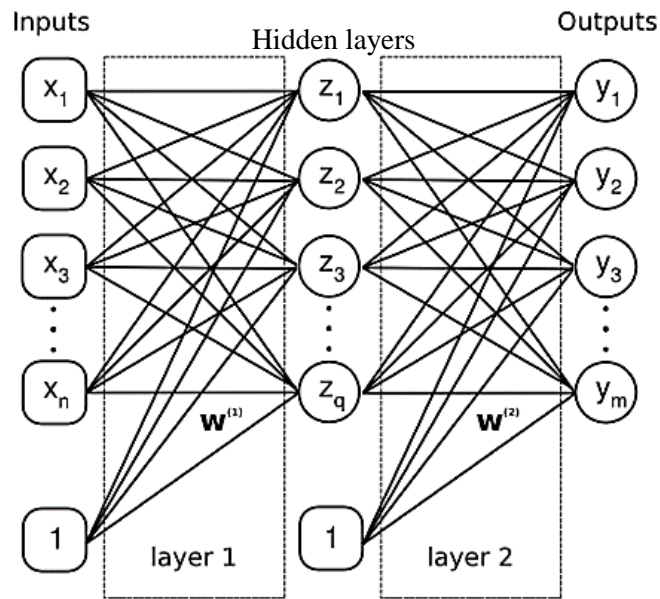


Figure 2. 41: Backpropagation network (William G. F et al., 2001)

Figure (2.41) shows a backpropagation architecture network, which consists of multiple layers of interconnected nodes (input, output and hidden layers). It can be trained using healthy data and different types of fault, and therefore used to determine the condition of future data. It has the ability to generalise, if it was well designed and trained, so training a backpropagation network must be supervised (J. P. Petersen., 2010a).

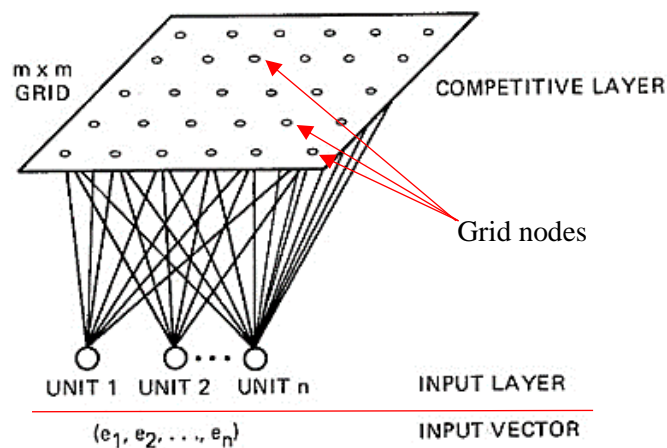


Figure 2. 42: Kohonen feature map (J. P. Petersen., 2010a)

A Kohonen network consists of two layers of nodes (input and output layers). The output layer is a 2-D grid consisting of nodes that are connected to every node in the input layer, as shown above in Figure (2.42). Thus, ANNs are a simplified representation of the neuron structure of the human brain.

2.5.3. Genetic Algorithms (GA)

Genetic Algorithms (GA) were designed to mimic some of the processes observed in natural evolution, and used to solve optimisation problems (Mitchell M., 1998). Thus, GA belong to the field of evolutionary computing, their approach being to evolve a solution that will retain the “most fit” components, analogous to biological evolution through natural selection, crossover and mutation (Jain, L. C. and de Silva, C. W., 1998); see Figure(2.43) below.

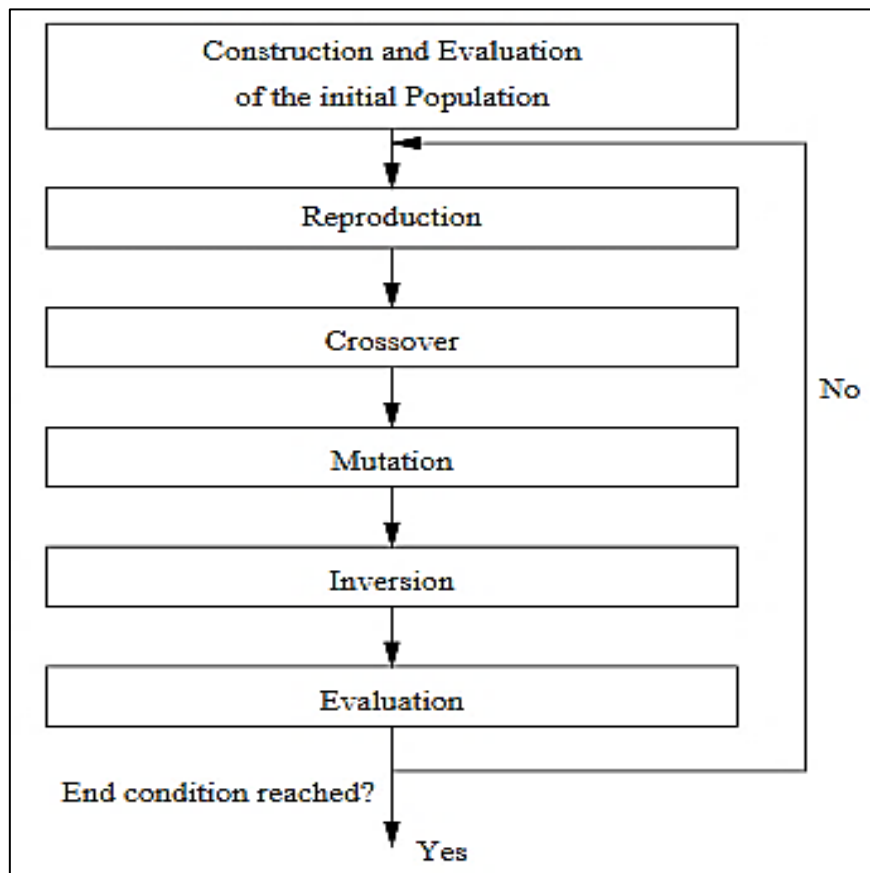


Figure 2. 43: Structure of a Genetic Algorithm (GA) (J. P. Petersen., 2010a)

2.5.4. Expert systems

Expert systems are concerned with using computers to simulate human intelligence. Jain, L. C. and de Silva, C. W., (1998) defined an expert system as “a software system with high symbolic and descriptive information content, which can simulate the performance of a human expert in a specific field or domain”. They normally acquire knowledge from human experts, and can deal with complex knowledge.

Domain data (from the knowledge engineer), knowledge base, inference engine and the user are the main components of an expert system:

- Expert knowledge engineer: organises the expertise gathered from a particular domain into the form required by a particular expert system.
- Knowledge base: is developed and arranged in the form required by the expert system
- Inference engine: the driver program, i.e. it draws conclusions based on the input

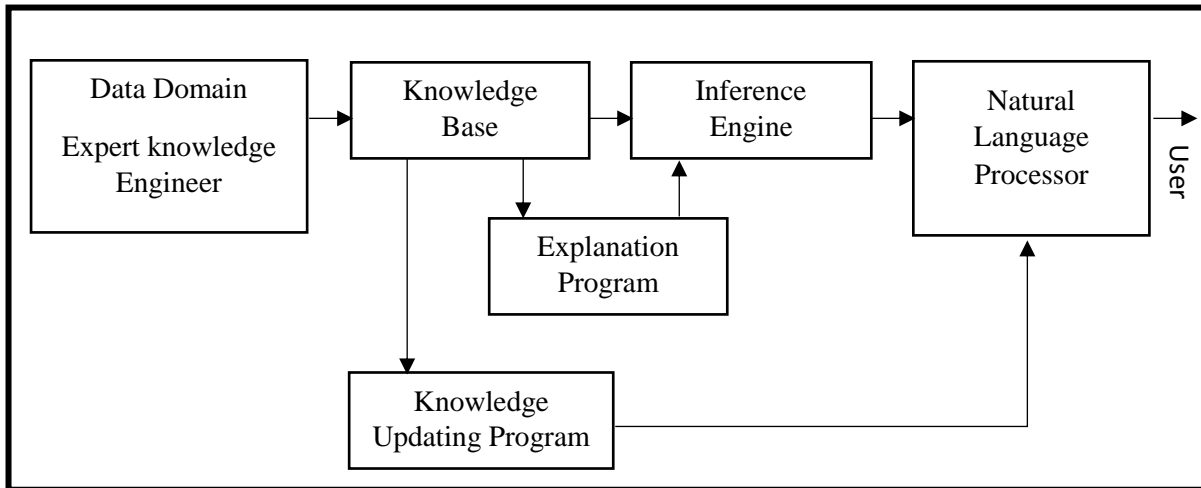


Figure 2. 44: Typical expert system (Mitchell M., 1998)

Expert systems are used to provide knowledge about system conditions. For example, Garcia M.C. et al., (2006) used an expert system in an intelligent wind turbine gearbox to provide information about maintenance and overall operation. Similarly, IHMS require the use of artificial methods such as ANNs and fuzzy logic.

2.5.5. Model-Based Parametric Method Algorithms

Parametric methods are based on mathematical modelling that fit a measured time series waveform data to a parametric time series model. Through using these models several valuable features in terms of detecting machinery failure can be extracted. Therefore, data can be collected from a healthy element to be sufficiently modelled, then the model can be used to detect any abnormal occasion from the operational to indicate changes in the parameters due to damage.

Mathematical modelling has proved to be capable of detecting vibration data directly and has advantages over the neural network-based model, as the signal does not need to be trained / pre-processed (Samuel P.D. and Pines D.J., 2005).

Currently, two main models are in use: the autoregressive (AR) and auto-regressive moving average (ARMA) methods. The AR modelling technique can be used either in the frequency domain as a spectral matching problem or in the time domain as a linear prediction problem.

The AR model for a time series x can be denoted by a linear regression of x , plus an error series, that is assumed to be noise having a Gaussian distribution. Hence, the following equation is the mathematical representation of the AR model (Samuel P.D. and Pines D.J., 2005):

$$x_i = - \sum_{k=1}^p a_k x_{i-k} + e_i \quad \text{Eq. 2. 14: AR model}$$

Where p = the model order and provide the number of past inputs required to model the signal, a_k = AR coefficients, i = sample index and e_i = Gaussian error series.

On the other hand, ARMA is a generalisation model of the AR and the mathematical representation is as follows:

$$x_i = - \sum_{k=1}^p a_k x_{i-k} + \sum_{k=0}^q b_k e_{i-k} \quad \text{Eq. 2. 15: ARMA model}$$

Where p and q = ARMA model order, a_k = AR coefficients, b_k = MA coefficient, i = index and e_{i-k} = model error series.

Several researchers have acknowledged the use of these models in providing machinery diagnostics (Onsy A. et al., 2014 and Samuel P.D. and Pines D.J., 2005). It was used to compute the dissimilarity measure between a vibration signal collected under a known operating condition and one collected under unknown operating conditions; satisfactory results were reported (Gersch et al., 1983). On the other hand, Rofe S., (1997) investigated ARMA modelling as a technique for fault detection that would compensate for changes in the transmission operating load. His study shows the success of using this model and it that it could effectively detect faults while compensating for load variations.

2.5.6. Advanced Digital Signal and Image Processing

Image processing is an extensively used and rapidly growing technology due to its ability to extract useful information. This technology can distinguish the target in an image and measure various objects. Therefore, it can be utilised to explore a better visualisation of the machinery's operation (Rafael G. and Richard W., 2008; Klein R. et al., 2014).

The method converts the picture into a digital form to get an enhanced image of otherwise invisible objects through three primary steps (Kunal, 2011):

- Importing / conducting images through either digital photography or an optical scanner
- Analysing and manipulating these images to extract patterns that are invisible to the naked eye
- Outputting the generated results in the form of alerted images or reports

Therefore, one of the image processing methods could be considered in the IHMS development the image subtraction technique, to determine the performance of the test elements. It also could enhanced the monitoring process through subtracting the digital value of the whole image from another image, helping to detect any minor changes in the operation. Thus, it can be used to illustrate whether a serious change has occurred, or any abnormal movements experienced. Figure (2.45) shows a typical example of the image subtraction technique

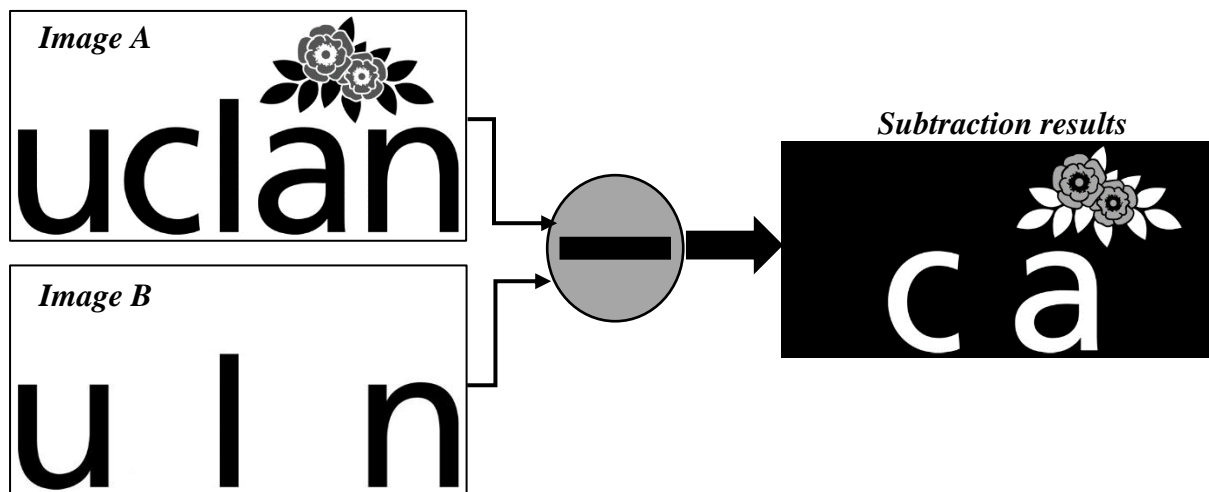


Figure 2. 45: A typical image subtraction example

2.6. Summary

Various sizes of wind turbine are already used worldwide, although there is still room for development of different sizes. This review has shown that through some parameters of the life of cycle of wind turbine attributes can be predicted: vibration, speed, load and temperature. These can be used to give an indication of either faulty or healthy conditions of any of the turbine's main elements. Furthermore, through using an intelligent methods, the life of cycle of the main rotary bearings can be predicted to improve performance and efficiency, with methods to optimise the wind turbine's performance and reliability.

The lifetime of a bearing is a design parameter in bearing selection, and identifying its value is important in avoiding any damage that bearings may cause to machinery, and in scheduling maintenance operation. However, even with the use of known standards, calculating the lifetime of the a bearing is still challenging, as this value is no more than an estimate as its calculation is based on statistical probability; several factors that affect a bearing's life are not included in the calculation, resulting in wide variation between calculated and actual length of life.

Recently SKF released SKF InsightTM, an innovation in the field of sensing bearings that enables monitoring the condition of bearings, especially in critical machinery and/or technically challenging applications. It offers potential to optimise the use of bearings in mechanical devices by making monitoring conditions more widely available, specifically in hazardous applications. Also, it offers an easy form of bearing diagnostics through monitoring the parameters that affect performance. Better control over the life cycle of machinery is also offered. This kind of technology will lower total costs and increase reliability, through reducing downtime and increasing capacity and efficiency. SKF Insight includes several sensors and smart networks, and is self-powering and simple. Its sensors can handle critical parameters such as velocity, load and temperature. It can communicate wirelessly within environments where traditional Wi-Fi cannot operate. It is self-powering through generating its own power to operate. From its "Mesh Network" a bearing can send information relevant to performance to be analysed.

The present study focusses on developing an Intelligent Health Management System (IHMS), and focuses on addressing current issues in determining the lifetime of bearings and detect its failure. It aims to develop an Intelligent Bearing as part of the Tribotronics and Intelligent

Condition Monitoring research plan of the Intelligent Machines and Maintenance group. The current development will contribute in the field of intelligent machine and through monitoring the life of an important element such as bearings. Hence, it will be very useful for many applications to measure the lifetime of bearings and address the variation between calculated and practically observed lifetimes.

Chapter 3 describes the development of the Health Monitoring System (HMS) and Intelligent Health Management System (IHMS) for the micro-scale wind turbine bearings. This includes details of the hardware and software development throughout this research.

Chapter 3. Intelligent Health Management System Development for micro-scale wind turbine bearings

3.1. Introduction

This chapter describes the development of a micro-scale wind turbine intelligent health management system. There are seven sections. Section 3.2 describes the pre-existing components of a basic test bench. Section 3.3 describes new bearing loading mechanisms for radial and torque loading. Section 3.4 explains the control system developed by the author including sensors and signal processors. Section 3.5 describes the software control system. Section 3.6 illustrates covers some publications that illustrate monitoring methods for the bearing's life and the ISO281 equations that were mainly used to fulfil the research aim. Finally, section 3.7 describes the diagnostic system development including the sensor, data acquisition (DAQ) cards and the actuation system. The whole chapter is summarised in section 3.8.

3.2. Description of the test bench

A pre-existing test bench was built on a set of aluminium extrusions assembled to create a robust frame on which to mount the bench components (Simmel, 2009).

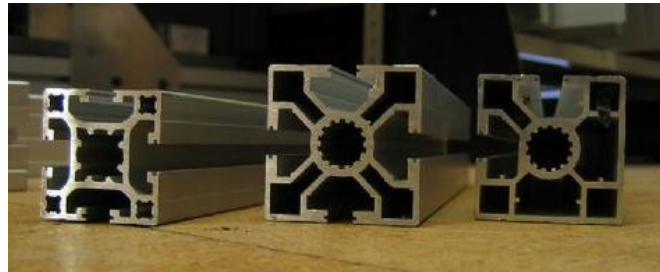


Figure 3. 1: Simmal Aluminium Extrusion (Simmel, 2009)

Previously, this test bench was used to observe the signature frequencies of failing ball bearing elements. It contained a motor, coupling, ball bearing, main shaft and a brake mechanism comprising brake pads and a bicycle disc, as shown in Figure (3.2).

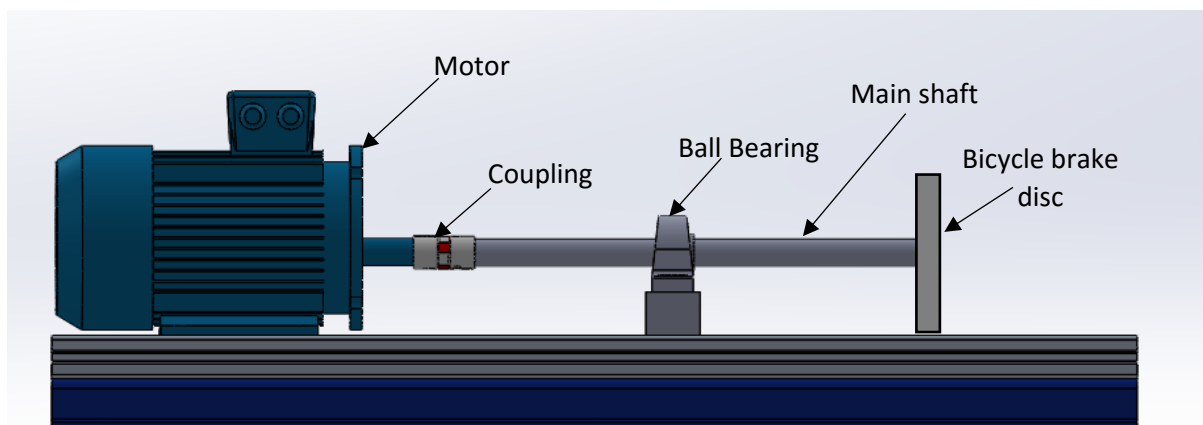


Figure 3. 2: Previous Test Bench

This test bench has been updated to develop an arrangement to test an intelligent management system for a micro-scale wind turbine bearing, specifically to investigate bearing life. To achieve this, some new components have been added. These components include a main shaft, an inline torque meter (to measure the operating torque), miniature inline couplings (MIC – to couple the inline torque meter with the other components), cylindrical bearings, deep-groove ball bearing, hydraulic bench press (to apply load radially on the test bearing), motor and inverter (to generate the rotational speed). Additionally, to meet health and safety requirements, some clear plastic sheets have been designed to screen rotating components. Figure (3.3) below shows the modified test bench.

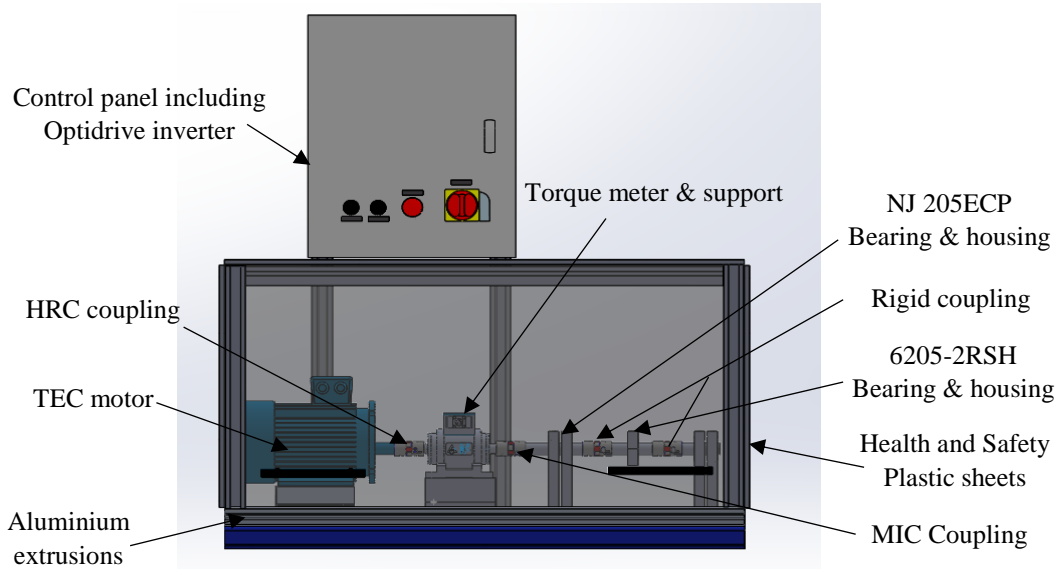


Figure 3. 3: The developed test bench

The motor used in this research is a 1.1kW, three phase motor with a maximum rotational speed of 2800 rpm and supplied by Total Engineering Commitment (TEC) (TEC Electric Motors Ltd., 2010). The motor is driven by an Optidrive E² inverter which works by driving the motor after converting the Direct Current (DC) to Alternating Current (AC). That is, it takes a single phase and converts it to three phase (Evans P., 2009).



Figure 3. 4: TEC motor and Optidrive E² inverter (TEC Electric Motors Ltd., 2010 and Evans P., 2009)

A Hot Rolled Carbon (HRC) coupling is used to link the main shaft with the motor shaft as they have different diameters. This coupling also accommodates incidental misalignment. It consists of two hubs with a rubber seal between them to reduce the vibration while rotating. It has been designed to support a torque of 31 Nm. It is coupled with a steel lay shaft to transfer the rotational speed from the motor to the bearing (Fenaflex, 2014).



Figure 3. 5: HRC coupling (Fenaflex, 2014)

NJ 205 ECP and 6205-2RSH bearings were selected for use in this research. NJ 205 ECP is a single row roller / cylindrical bearing and fulfilling the role of being the “slave” in carrying the applied load and 6205-2RSH is a single row deep-groove ball bearing (test bearings). They both have an inner: outer diameter ratio of 25:52 mm. They are manufactured by Svenska Kullager Fabriken (SKF). They are selected because they fit the pre-existing main shaft and the operating life can be tested within the laboratory environment. Other dimensions are provided by the manufacturer and are shown in Table (3.1).



Figure 3. 6: NJ 205ECP and 6205-2RSH

Table 3. 1: Bearing dimensions (SKF, 2017a; 2017b)

Bearing type	NJ 205 ECP	6205-2RSH
Manufacturer	SKF	SKF
Bearing diameter	52 mm	52 mm
Inner race diameter	25 mm	25 mm
Number of rollers	13	9
Pitch diameter	39 mm	39 mm
Roller / ball diameter	7.5 mm	7.938 mm
Contact angle	0°	30°

Upon consideration of the pre-determined bearings dimensions, suitable bearing housings have been designed and manufactured (Appendix A). The test bearing is loaded using a four ton

hydraulic bench press. This offers a measured radial load on the tested bearing – as shown in Figure (3.7) below.

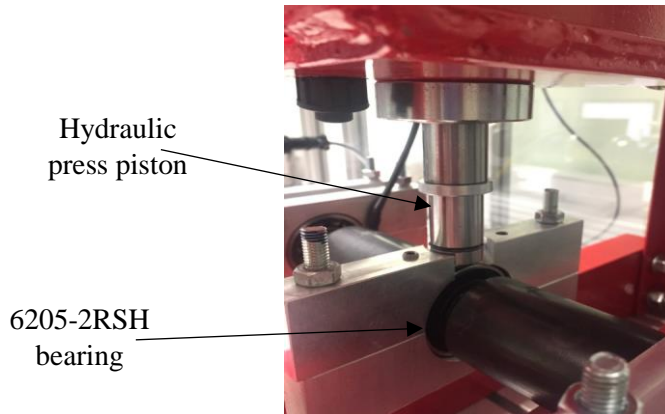


Figure 3. 7: Radial loading arrangement

Finally, a torque measurement is used to measure the operated torque in the bearing using a Torque Meter (TM309).

3.3. Bearing Loading Mechanisms

The roller bearing runs in cylindrical raceways and has low friction, high load capacity and high rotational speed capability. Deep-groove ball bearings runs in spherical raceways to maintain the separation between the moving parts of the bearing. They are widely used due to their versatility and they can support radial and axial loads. They comprise four parts including: outer raceway/ring, cage, ball/roller and inner race/ring.

The point of contact between the balls / rollers and the raceways is known as contact angle. The contact angle in the roller / cylindrical bearing is equal to zero since the point of contact is a line rather than an angle. This helps in distributing the load over a larger area and allows the bearing to carry a greater load comparing to ball bearing (Gonzalez C., 2015). In ball bearings, the contact angle is based on an estimation value or advised by the manufacturer as shown in Figure (3.8).

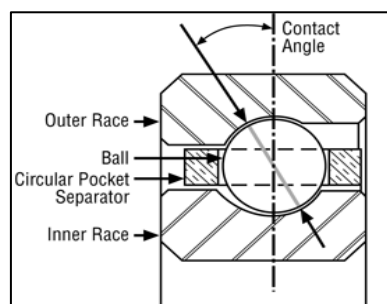


Figure 3. 8: Contact angle of ball bearing (Kaydon, 2014)

The cylindrical bearings “NJ 205 ECP” supports the radial mechanism on the tested bearing (6205-2RSH) since it can carry higher load based on its specification from the manufacturer – as shown in Table (3.2) below.

Table 3. 2: Bearing specifications (SKF, 2017a; 2017b)

	NJ 205 ECP – “Slave”	Deep-groove 6205-2RSH – “Test”
Dynamic load rating (kN)	32.5 (approx. 3 tons)	14.8 (approx. 1.5 tons)
Static load rating (kN)	27	7.8
Limiting speed (rpm)	16,000	8500

Suitable bearing housings for the chosen bearings were manufactured to meet the required bearing specifications. The material used was aluminium. The housing consists of two layers, upper and lower. The lower layer supports the bearing assembly to ensure its fitting.

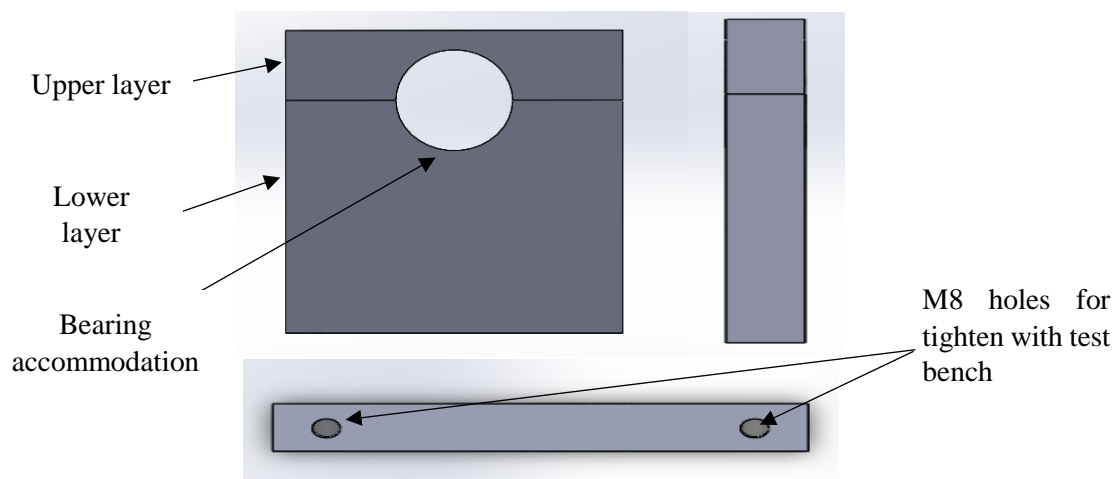


Figure 3. 9: Roller / cylindrical bearing housing

When two elements are to be assembled, the difference between their sizes before assembly is called the fit, which may be defined as the degree of tightness or looseness between the two parts. As covered in Chapter 2, tight and loose fit are some of the causes of bearing failure, and these should be avoided (Suhas S. J., 2010). There are three recommended fits / classifications in terms of mating two components, as follows:

- Clearance: when the difference in size between the hole and the shaft before assembly is positive
- Interference: when the difference in size between the hole and the shaft is negative
- Transition: when the tolerance zones of the holes and shaft overlap.

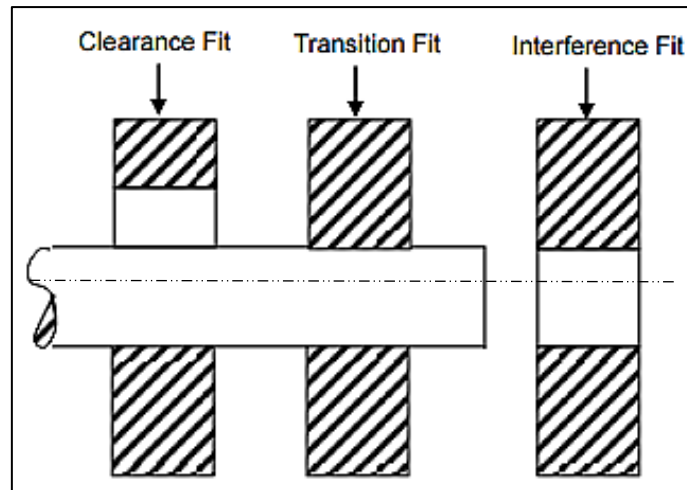


Figure 3. 10: Fit classification (V. Mulani, 2015)

The housings were manufactured with a proper tolerance as recommended by the manufacturer, SKF: a cylindrical / roller bearing and deep-groove ball bearing with a lightly loaded operation is classified as (j6), and the proper tolerance for NJ 205 ECP and 6205-2RSH fitting is $(52 + 9\mu\text{m})$ in accordance with ISO 286-2:2010 and SKF fit tolerance (SKF, 2008).

A proper transition fit was used to insert the bearings into the main shaft. A little Vaseline was used as a lubricant for sliding the bearing along the steel lay shaft with a little tapping force. While tapping the bearing, the tapping force must be always applied to the bearing with interference fit. Hence, all the bearings were aligned properly as shown in Figure (3.11).

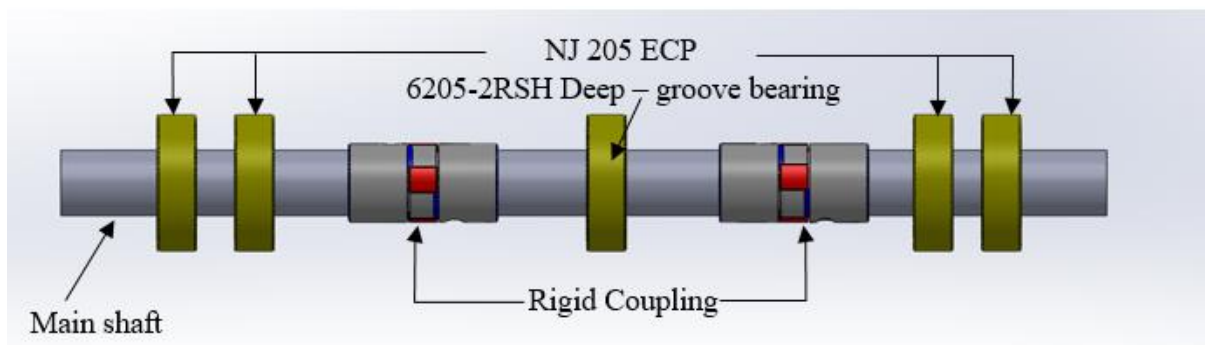


Figure 3. 11: Bearings installation

3.3.1. Radial Loading Mechanism

Load can be applied to a bearing in several direction with radial and axial components. These loads have a vital role influencing the operational life of the bearing. If the applied load is over the rating limit / capability, this will lead to failure in the bearing elements and could cause a catastrophic failure. For instance, from Table (3.2) if the applied radial load is over 32.5kN this will lead to deform / damage the NJ 205 ECP bearing. Excessive load is one of the main failure

modes in bearings, as discussed in Chapter (2). An appropriate load measurement should be followed to prevent possible failures. This research considers a radial loading mechanism to identify the variation in bearing life.

Several radial loading mechanisms were discussed, and in this case the bearing is loaded radially using a hydraulic bench press. The press was selected for its ability in most industrial purposes including forcing, clinching, modelling, blanking, punching, deep drawing and metal forming operations. It generates compressive force through using a hydraulic cylinder, and consists of a hydraulic pump, cylinder, piston and pipe, as shown in Figure (3.12).



Figure 3. 12: Hydraulic bench press (Ali B., 1999)

A four ton hydraulic bench press was used. It is made of steel with a powder-coated paint finish to help resist corrosion. It has a detachable hydraulic pump with a small gauge attached to it with a scale from 0 – 15000 PSI / 0 to 100MPa. Other specifications are listed in Table (3.3)).

Table 3. 3: Hydraulic bench press and hand pump specifications (Ali B., 1999)

Hydraulic bench press	
Capacity	4 tons
Overall height	630mm
Width	180mm
Length	200mm
Weight	31kg
Hydraulic hand pump	
Weight	5.2 kg
Width	350mm
Features	Gauged

Based on the test bench dimensions and Table (3.3), the structure of the hydraulic bench press was modified / minimised to suit the test bench. Also, the piston of the hydraulic cylinder was aligned to meet the centreline of the bearing (acting perpendicularly), offering a radial load on

the bearing. A pathway at the upper layer of the housing was made in order to guide press radially on the bearing, as shown in Figure (3.13). In addition, some holes were made in the base of the hydraulic press to ensure that it is fastened to the test bench.

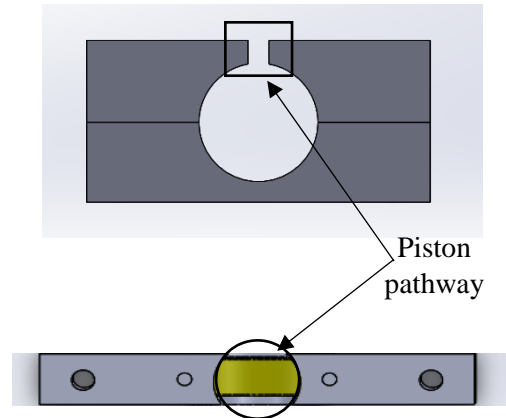


Figure 3. 13: Tested bearing housing including piston hole

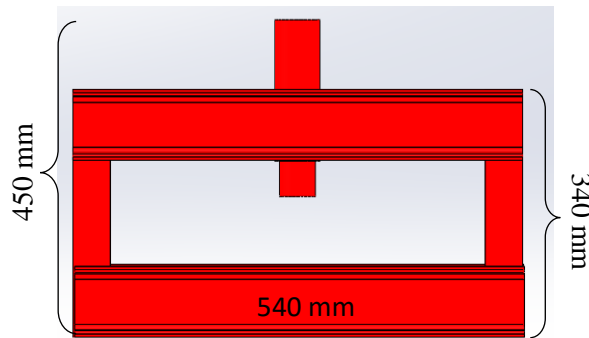


Figure 3. 14: Hydraulic press with the new dimensions

3.3.2. Brake Loading Mechanisms

Torque can simply be defined as a force that tends to cause a rotation (Damien H., 2003). It plays an important role in almost all mechanical applications. Previous studies illustrate that torque is needed and can be used in order to provide a braking action for rotating devices (Walker J., 2005b and Gritt P.S, 2011).

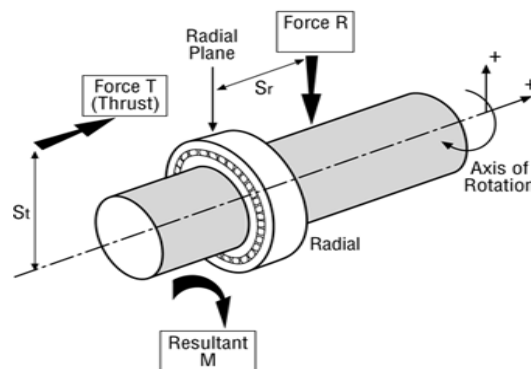


Figure 3. 15: The resulting moment load (Kaydon, 2014)

Torque affects the rotational speed of the shaft which will vary the operating speed for the tested bearing. Figure (3.15) shows that applying force to the shaft in a different direction generates moment and the torque is a moment of coupling.

Essentially, in this research the torque measurement is achieved using an inline torque transducer, as discussed in Section 3.4. Additionally, a hysteresis brake can be used to perform a closed loop torque loading system if required. The hysteresis brake is normally used to apply the braking action through applying load on the rotating shaft. Figure (3.16) represents a typical Torque vs. Current curve for a normal hysteresis brake. The torque for a given current changes as the control increases. This is due to the hysteresis in the rotor material.

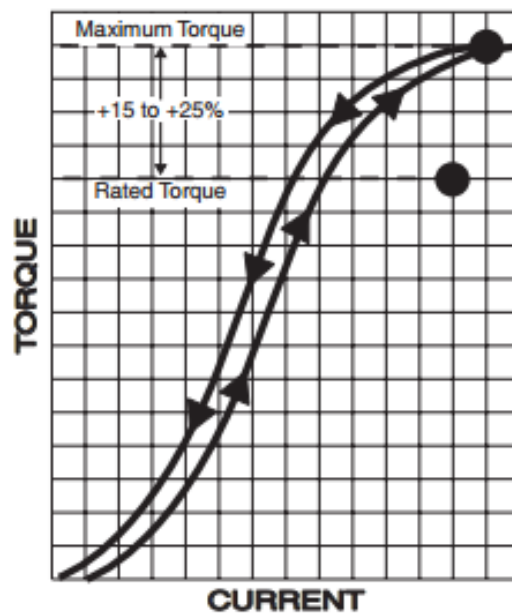


Figure 3. 16: Torque / Current Curve (Magtrol, 2015b)

3.4. Development of Test Bench Input / Output Control System

The test bench was developed to measure different parameters, including vibration, radial load, torque, speed and temperature measurements. To use proactive maintenance for any component, several parameters, including some design variables, are required. By monitoring these parameters during operation, a proactive maintenance strategy can be applied to micro-scale wind turbine bearings and their estimated life calculated.

This test bench was developed to evaluate a micro-scale wind turbine bearing, and to develop and evaluate the proposed IHMS system. However, the main focus of this research is to monitor a typical single row deep-groove and cylindrical bearings. Figure (3.17) demonstrates an overview about the proposed IHMS system.

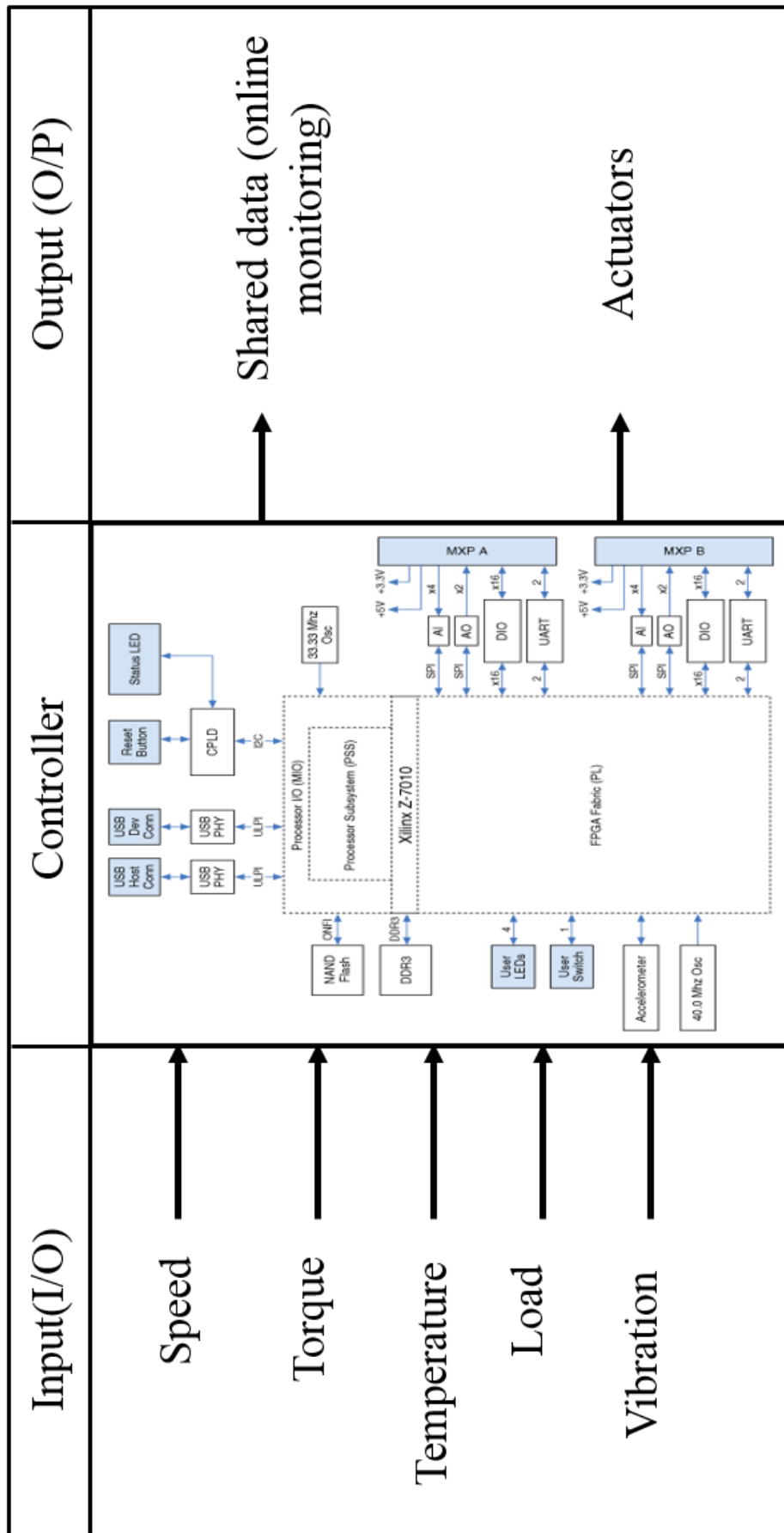


Figure 3. 17: IHMS System overview

3.4.1. Sensors

Monitoring the parameters that affect the bearing's operational life requires the use of multiple sensors. Load, temperature, torque, vibration and speed sensors are used to monitor the bearing's life and help in investigating possible failures.

i. Load measurements

A hydraulic radial loading system is used to load the bearing and a pressure sensor is installed into the hydraulic jack to monitor the amount of pressure in the loading mechanism. Further specifications for this transducer are given in Table (3.4).

Table 3. 4: Pressure transducer specifications (CPC, 2000)

Input	0 – 2500 PSI
Output	0.5 – 4.5 V
Thread type	1/8" NPT
Working temperature	-40 to + 120 C
Response time	≤ 1ms
Accuracy	± 0.5%

The pressure transducer has three wires: red (+5V), black (GND) and blue (analogue signal). The working principle of this transducer is voltage. If the acquired voltage is +4.5 V this is equivalent to 2500 PSI, based on the sensitivity equation (input / output). Pressure value can be converted from PSI to MPa (Megapascal): 1 PSI = 0.00689476 MPa (CPC, 2000).

The installation of the pressure sensor used a half-inch diameter stainless steel T-junction with reducers. Some reducers were involved to make a proper linkage, with sealing tape to prevent leakage of hydraulic oil. One of the reducers had been tapped to 1/8" NPT to match the threading style of the pressure transducer, as shown in Figure (3.18).

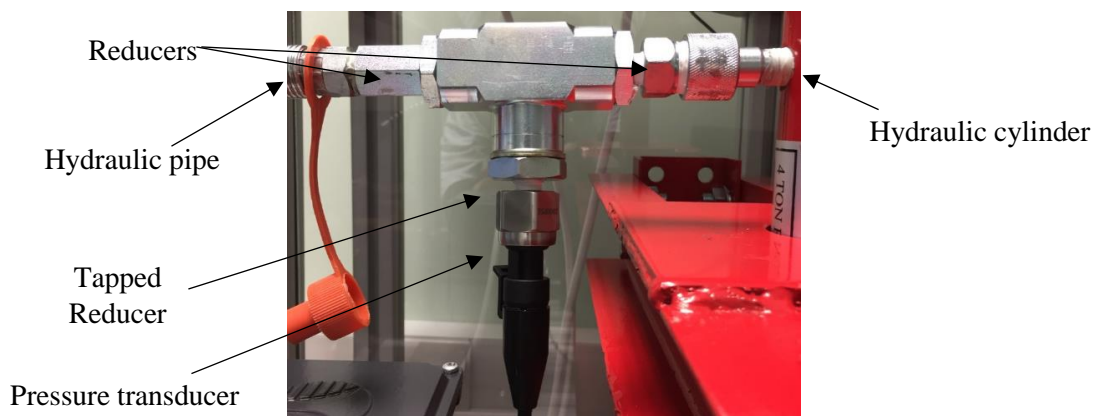


Figure 3. 18: Pressure sensor installed using T-junction

The following Figure (3.19) demonstrates the load measurement in the code developed by the author.

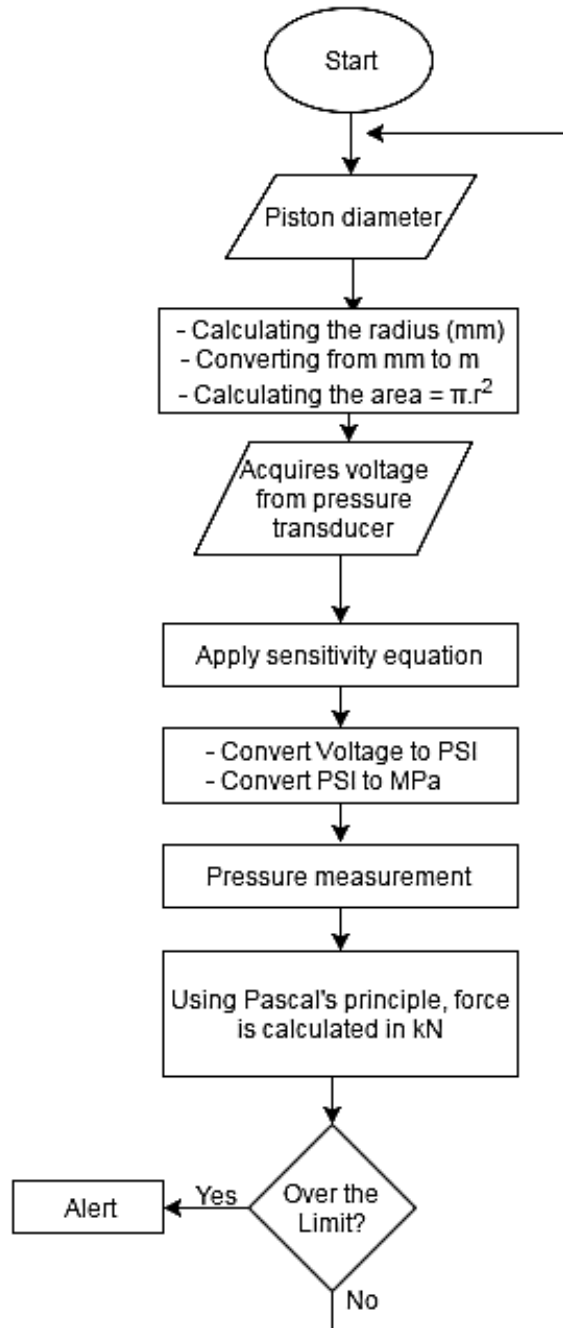


Figure 3. 19: Load measurement flowchart

From Figure (3.19), pressure transducer senses the variation in voltage. This variation is an indication of pressure value, and applying it in the sensitivity equation will generate a pressure in PSI. This value can be converted to MPa as 1PSI = 0.00689476 MPa. Thus, the pressure is calculated in MPa. The area of the hydraulic cylinder is calculated through inputting the inner diameter. Therefore, the applied force / load (P_r) was calculated using Pascal law i.e. $F = PA$.

The measuring capacity for the pressure transducer is 2500 PSI, or approximately 17MPa; the cylinder diameter is 38mm = 0.038 m, thus, $r = 0.038/2 = 0.019\text{m}$. So, the cylinder area = $(\pi * r^2) = (\pi * (0.019)^2) = 1.1341 * 10^{-3} \text{ m}^2$. Based on Pascal's principle:

$$\therefore P = \left(\frac{F}{A}\right) \quad \text{Eq. 3. 1: Pascal's law}$$

$$\therefore F = P.A = 17 \text{ MPa} * 1.1341 * 10^{-3} \text{ m}^2 = 19279.7 \text{ N}$$

$$\therefore \text{Converted from N to kg (dividing by 9.81)} = 1965.31 \text{ kg} \approx 2000\text{kg} = 2 \text{ Tons}$$

As a result, the maximum load that could be applied using 2500 PSI is 2 tons (1.96 kN). In addition, if the applied load / force is above the limit, an alarm warns the user.

ii. Temperature

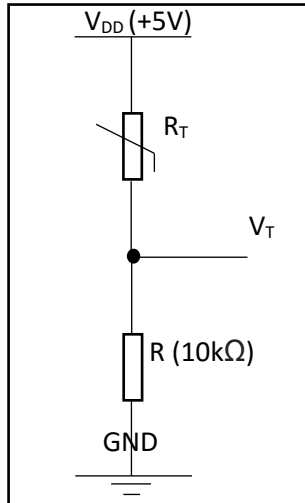
The temperature of bearings rises while rotating due to continuous “friction”, generating heat. Excessive heating may be an indication of some sort of failure, such as misalignment. This overheating may affect bearing performance resulting in catastrophic damage. Therefore, the operating temperature is one of the parameters which can be measured and monitored in order to identify failure.

A temperature sensor was selected to measure the operating temperature in the bearing. A Negative Temperature Coefficient (NTC) thermistor was used. The working principle in the NTC thermistor is based on the fact that its resistance drops as the temperature increases. It has a linear sensitivity of $(10\text{k}\Omega / 25\text{C}^\circ)$. The sensor measures electrical resistance and therefore helps in determining the temperature.



Figure 3. 20: NTC temperature sensor

The sensor used can read temperatures from -40 C° to 120 C° and needs +5 volts as power. A measurement of resistance at Kelvin temperature (R_T) was done using a voltage divider circuit and the following equations.



$$V_T = \frac{R}{R + R_T} \times V_{DD}$$

Eq. 3. 2: Voltage divider

$$R_T = R \left(\frac{V_{DD} - V_T}{V_T} \right)$$

Where V_T is the voltage output from the NTC sensor. Then, the acquired value out of R_T can be substituted in the Steinhart – Hart equation in order to obtain the temperature on Kelvin scale (Stanford research systems, 2012 and Instruments Arroyo I., 2016) with respect to A, B and C (Steinhart coefficients).

$$\frac{1}{T (K^\circ)} = A + B \times \ln(R) + C \times \ln(R^3)$$

Eq. 3. 3: Steinhart - hart

$$\therefore T (K^\circ) = \frac{1}{A + B \times \ln(R) + C \times \ln(R^3)}$$

The processed application was able to measure temperature using an NTC sensor and the Steinhart-Hart equation with a small Printed Circuit Board (PCB). The PCB included a resistor and a capacitor to help in acquiring the resistance, as shown below in Figure (3.21) and (Appendix B). This PCB was used to sense the variation in resistance as this helps to measure the temperature. Thus, 10kΩ resistor was used as a reference value since the used sensor measures 25C° when acquires 10kΩ.

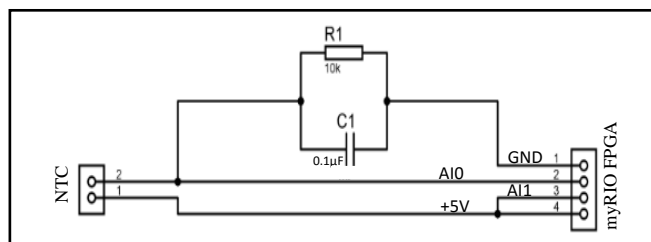


Figure 3. 21: Temperature sensor connection

Figure 3. 22: Temperature sensor connection

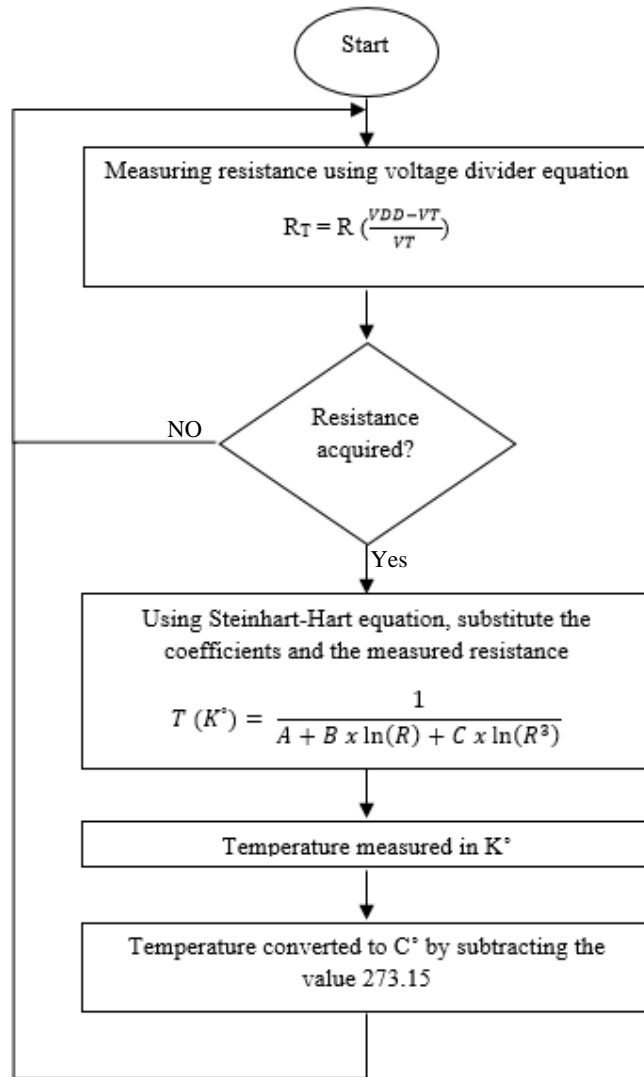


Figure 3. 23: Temperature measurement

The temperature was ascertained by measuring the differences in resistance using the voltage divider equation, as shown in Figure (3.22) and (Eq. 3.1). If there is no measurable resistance the program repeats the operation until it is achieved. After this, the measured resistance and Steinhart-Hart coefficients (A, B and C) are substituted in the Steinhart-Hart equation (Eq. 3.2) in order to measure the temperature in Kelvin (K°). Then, the temperature is converted to Celsius (C°) through subtracting the measured value by 273.15.

For instance, if the observed resistance is equal to 10k ohms (Ω):

$$\therefore T (K^\circ) = \frac{1}{0.00112924 + 0.000234108 \times \ln(10000) + 8.7755 \times 10^{-8} \times \ln(10000)^3}$$

$$\therefore T = 298.15 K^\circ$$

$$\therefore T = 298.15 - 273.15 = 25 C^\circ$$

Figure (3.23) below presents typical relation between the thermistor resistance (Ω) and temperature ($^{\circ}\text{C}$) using Steinhart-Hart coefficients. Additionally, (Appendix C) shows the values that were used to plot the graph below.

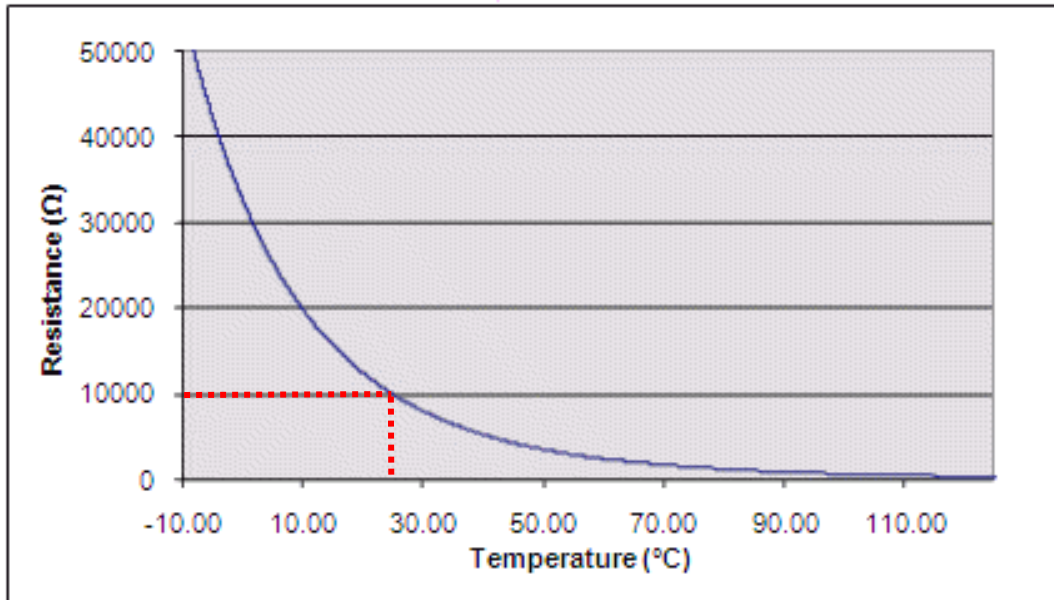


Figure 3. 24: Thermistor resistance Ω VS Temperature $^{\circ}\text{C}$ (Arroyo I, 2016)

The sensor was mounted with the hydraulic bench press piston where the contact point of the sensor is perpendicular to the bearing. When the load is applied to the bearing, the sensor's thermopile detector comes in direct contact with the bearing – as illustrated in Figure (3.24) below.

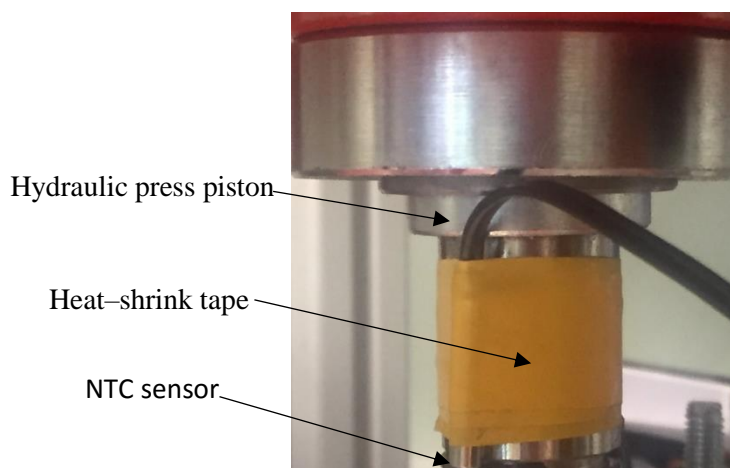


Figure 3. 25: Installation of the NTC sensor

iii. Torque

An inline torque transducer (TM309) was chosen for the test bench to measure the bearing torque, as shown in Figure (3.25).



Figure 3. 26: Torque Meter / Transducer (TM309) (Magtrol, 2013)

This transducer was selected for its specifications and compatibility with the application. It has an integrated conditioning electronic module providing 0 to ± 10 VDC torque output and 20 Nm as nominal rated torque with accuracy of $< 0.1\%$. The maximum rotational speed is approximately 10,000 rpm (Magtrol, 2013).

- Torque Measurement, Feedback and Control

In-Line Torque Transducers provide extremely accurate torque and speed measurement over a very broad range. There are several models and each has an integrated conditioning electronic circuit providing ± 10 VDC torque (depending on the direction of the torque) output as shown in Figure (3.26) below – using non-contact differential transformer torque measuring technology.

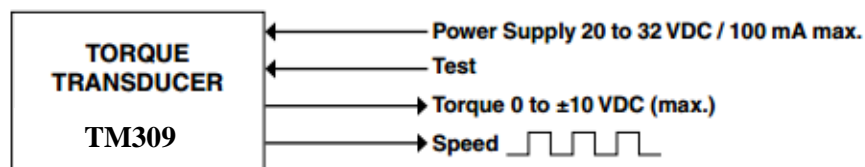


Figure 3. 27: Torque transducer configuration

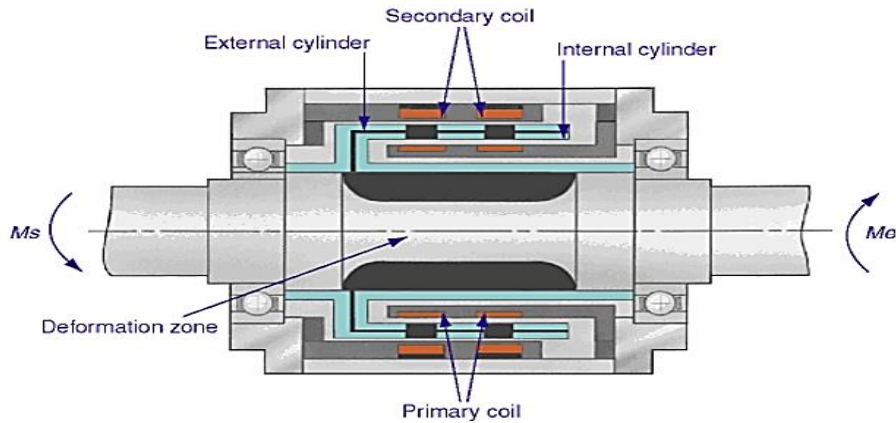


Figure 3. 28: Magtrol's inline torque meter: main elements (Magtrol, 2013)

The main elements in the Magtrol transducer are: two cylinders (internal and external), a shrunken shaft on each side of the deformation zone and two concentric coils (primary and secondary) attached to the housing, as shown in Figure (3.27) above. The two cylinders have coinciding rows of slots that rotate with the shaft inside each coil. Alternate Current (AC) with a frequency of 20 kHz flows through the primary coil. If the torque is not applied, the slots on the row do not overlap. Once the torque is applied, the slots begin to overlap in the deformation zone. Consequently, a torque-proportional voltage is on the secondary coil. Then the conditioning electronic circuit inside the transducer converts the voltage into a torque signal. In addition, a low-pass filter is added in order to adjust the torque frequency limitation.

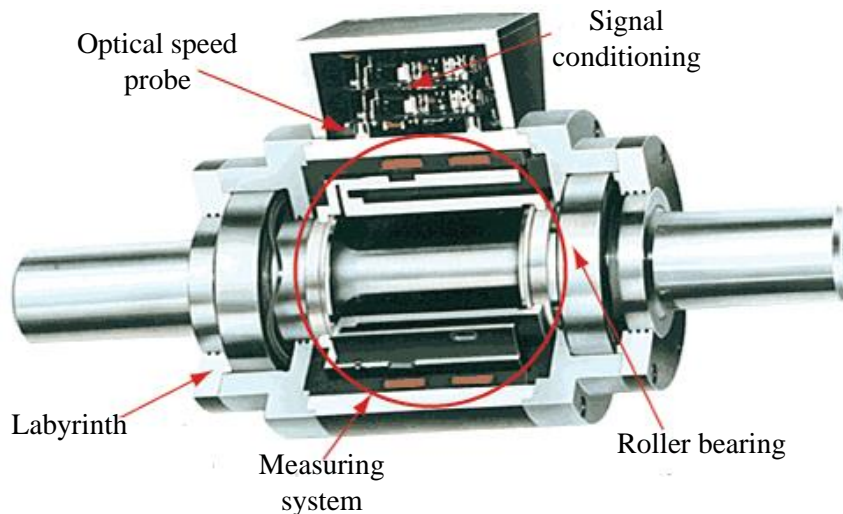


Figure 3. 29: Inside view of TM309 (Magtrol, 2013)

The TM309 transducer has an optical speed probe for speed measurement. It is integrated by means of inductive proximity. It is a non-contact electronic sensor used to sense the position of the toothed path into the outer cylinder and measure the speed. Also, it has a labyrinth for

keeping all particles out of the measuring system as well as a roller bearing for support (Magtrol, 2013).

In terms of installation, a support for the torque meter was designed and manufactured in order to align the rotational shaft in the whole test bench (Appendix D). The transducer was fastened to the 60 mm height support using M5 bolts and the riser tightened to the test bench to ensure stability.

Two miniature couplings were used to link the torque meter with other elements in the test bench. This coupling complemented the linkage of the inline torque transducer with the main shaft. It consisted of two disc packs, two clamping hubs and a spacer. They are torsionally stiff and flexible in order to compensate for axial, angular and radial misalignment when connecting the two shaft ends.



Figure 3. 30: Torsional Coupling (Magtrol, 2015a)

Based on the coupling specifications, a MIC-5-3620 manufactured by Magtrol was selected. It is suitable for use with the selected torque transducer and can handle a maximum torque of 50.7 Nm and operate at a maximum speed of 30,000 rpm (Magtrol, 2015a).

iv. Speed

Speed is measured in this research to calculate the frequency in each element of the bearing and the subsequent operating life. In addition to the speed measurement in Torque Meter (TM309), a proximity probe sensor was installed to measure the rotational speed. It measures the angular velocity of a rotating shaft. There are several types, including mechanical, electrical and optical. In this research the sensor used is an electrical inductive pick-up sensor which produces pulses that can be counted. A digital circuit is used to store the count, calculate and display the value in rpm units (Figliola and E. Beasley, 2011).



Figure 3. 31: Proximity probe (Figliola and Beasley, 2011)

The speed of the motor is controlled via an Optidrive E² inverter through adjusting the speed using a potentiometer. This speed adjustment occurs due to the voltage variation from the potentiometer (Evans P., 2009). The voltage output of the potentiometer was mapped (1 volt from the potentiometer is equal to 5 Hertz in the inverter and equal to 300 rpm in the motor). In this way, a sensitivity equation could be set to measure the demand speed.

v. Vibration sensor

To identify vibration signals to allow failures in the bearing to be diagnosed, a piezoelectric accelerometer is used; this detects vibrations to predict failures in the future helping to prevent catastrophic failures. Its elements create a charge when strained. It has a sensitivity of 100 mV/g and resolution of 0.002 g rms. The frequency range is 2.5 Hz to 10 kHz. This accelerometer is a uniaxial type, quartz shear and its weight is 35g; this is satisfactory to use with the bearing since it is less than 1/10 the mass of the system (PCB, 2015).

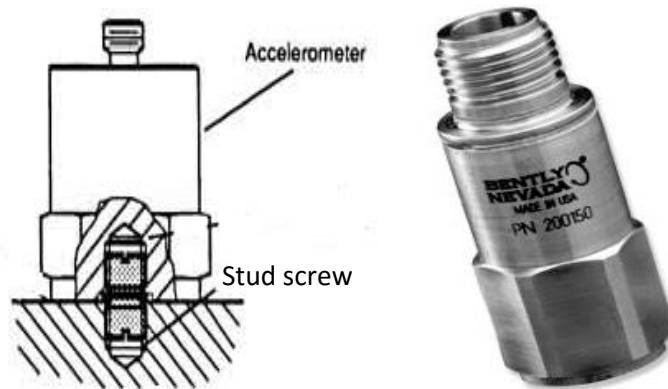


Figure 3. 32: Piezoelectric accelerometer (Stud mounting)

A stud is used to mount the sensor. The transducer is attached at the housing using a stud screw through a threading hole on the top and bottom of the housing. Consequently, two threaded holes were made on the manufactured housing, as shown in Figure (3.32) to allow the transducer to acquire the signals.

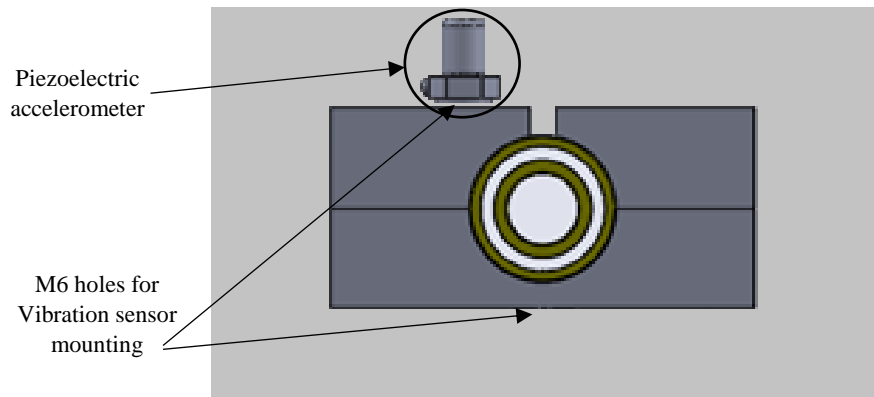


Figure 3. 33: Vibration sensor mounting threaded holes

3.4.2. System Controllers

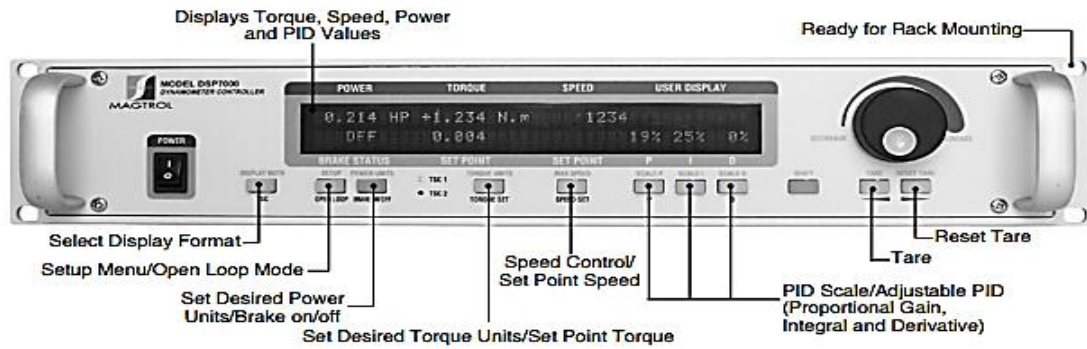
1- DSP7000

A Torque Meter (TM309) is interfaced with a Digital Signal Processing (DSP7000) in order to display the measured torque and speed. The DSP7000 is High Speed Programmable Dynamometer Controller, designed for use with in-line torque transducer. It can take 500 torque and speed samples per second and is ideally suited to the laboratory test environment. It has a PID adjustment capability for both speed and torque modes in order to provide the best system response. It contains two channels, enabling the user to test two instruments (Torque meters) with independent configurations. It can interface with the Data Acquisition (DAQ) system, as well as allowing the user to save acquired values within their configurations. It has a digital filter that removes undesired noise from the torque signal, and a built-in alarm system to notify the user when an electrical or temperature problem occurs. Figure (3.33) and Table (3.5) show some of the DSP7000 specifications.

Table 3. 5: DSP7000 specification (Magtrol, 2015c)

Maximum torque	99,999 units
Maximum speed	199,999 rpm
Voltage requirements	From 85 to 264 VAC (50/60 Hz)
Operating temperature	5 to 40 C°

FRONT PANEL



REAR PANELS

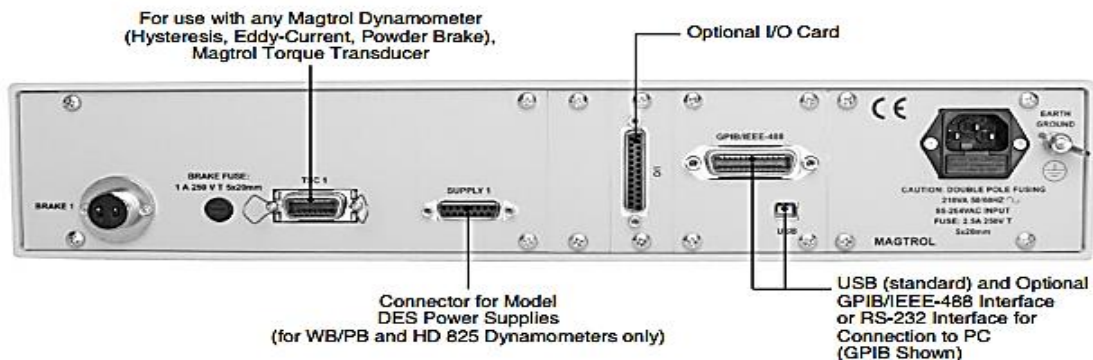


Figure 3. 34: DSP7000 front and rear panel (Magtrol, 2015c)

A Signal Breakout Box (SBB 14) was used to assist in monitoring data signals obtained from the DSP7000 controller. It was inserted in series between the controller and in-line torque transducer, as shown in Figure (3.34).

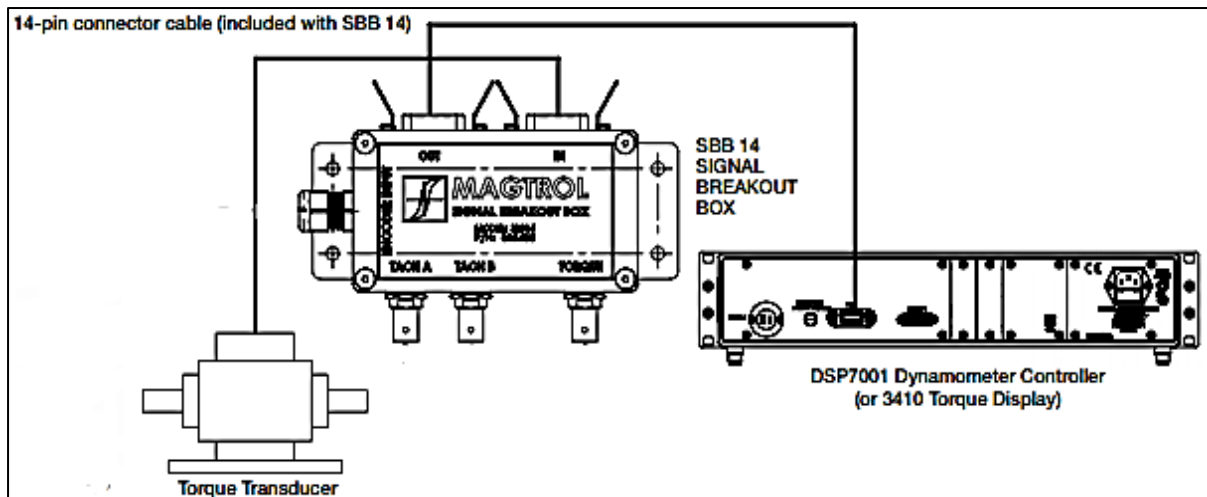


Figure 3. 35: SBB configuration (Magtrol, 2014)

2- NI myRIO module

A National Instrument (NI) myRIO-1900 controller is a portable reconfigurable input / output controller used to design control, robotics and mechatronics systems. It provides analogue input, analogue output, digital I/O, audio and power output in a compact embedded device. It

uses either a Universal Serial Bus (USB) connection or wireless to communicate with a host computer. It has a Xilinx Zynq-7010 processor operating at a speed of 667MHz. It consists of three myRIO Expansion Ports (MXP): A, B and C. Ports A and B have four analogue inputs and two analogue outputs, and 16 configurable digital pins (I/O). Connector C has eight configurable digital pins, two analogue outputs and two analogue inputs. Power channels are available on-board with 3.3V, 5V and 15V. MyRIO requests 6 to 16 VDC to be powered (approximately 14W).

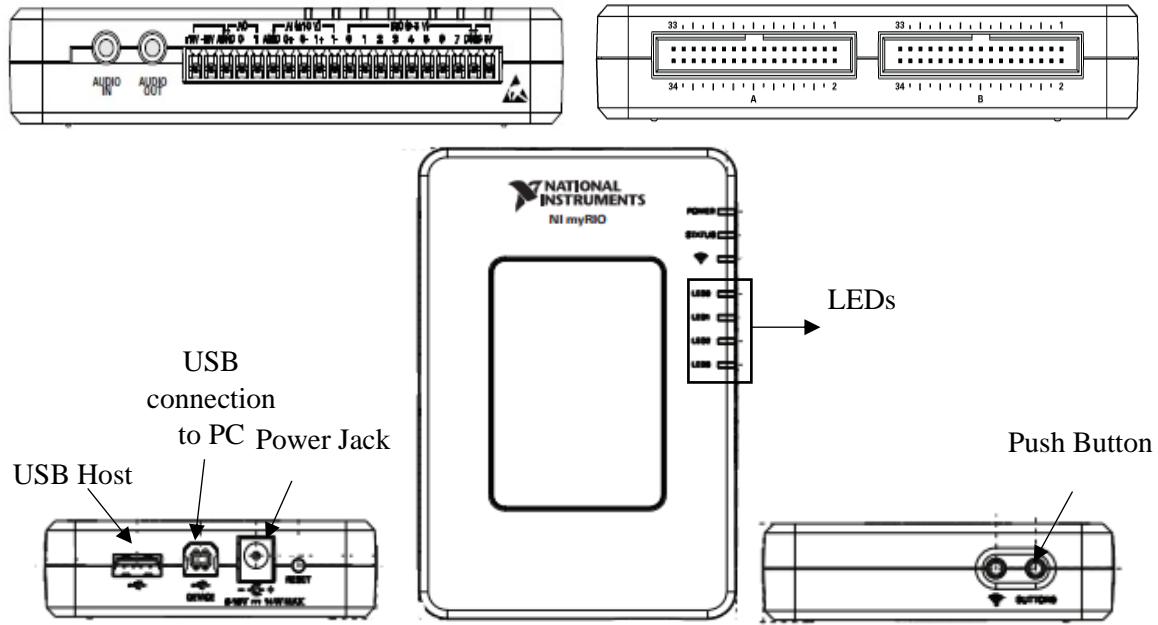


Figure 3. 36: NI myRIO connectors

Several components are built in on-board including four LEDs, push buttons and a three-axis accelerometer (National Instrument, 2011). All the sensors' information is displayed, monitored and logged to check any variation in the main parameters related to the bearing's condition and life, thus providing a facility for the online condition monitoring of micro-scale wind turbine bearings.

3- NI cDAQ (9191 & 9234)

An NI cDAQ (9191) is a 1 slot NI CompactDAQ 802.11 Wi-Fi chassis. It was used in this research to acquire vibration signals with the use of piezoelectric sensor. It has the ability to transit analogue input / output, digital Input / output, counter / timer and sensors measurements. The communication protocol with the host PC is via either Wi-Fi or Ethernet. It has the ability to transmit / receive the data with a high speed of sampling rate – 127 samples. This card has been used by others to monitor several parameters including thermocouples, RTDs, strain

gauges, load and pressure (National Instruments, 2014a). It is suitable for remote or distributed sensors and electrical measurement including use in a laboratory testing environment.



Figure 3. 37: NI cDAQ 9191 & 9234

The NI 9234 slot is a measurement system that measures four accelerometer / microphone channels at a rate of 51.2 kS/s with 24 resolution. Table (3.6) below shows some of the specifications.

Table 3. 6: NI 9234 specifications (National Instruments, 2014a)

General Specification	
Product family	Industrial I/O signal conditioning
Measurement type	Accelerometer
Communication protocol	USB, Ethernet or wireless
Analogue Input	
Differential channels	4
Input resolution	24 bits
Physical Specifications	
Operating temperature	-40 C° to 70 C°
I / O connectors	BNC connectors

Finally, all the observed data can be easily logged from this device in order to be used in analyses using NI LabVIEW, ANSI C/C++, Visual Basic, .NET and other programming applications (National Instruments, 2014a).

4- NI USB 6003

Another data acquisition card, NI USB 6003, was used to adjust the speed. It is a low cost controller. It uses a micro USB to power and communicate with the host PC, as shown in Figure (3.37). Table (3.7) shows more specifications.

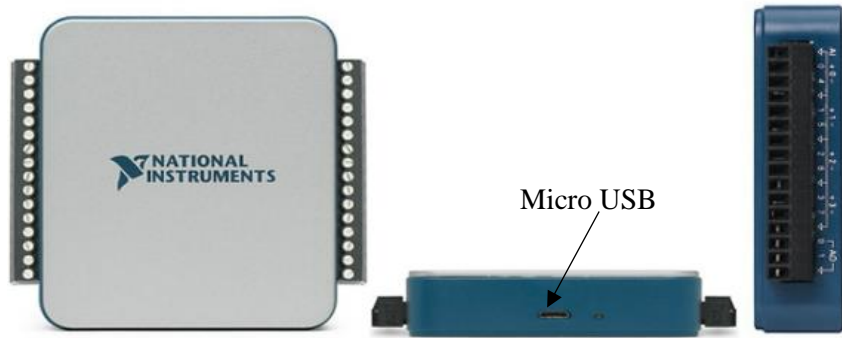


Figure 3. 38: NI USB 6003

Table 3. 7: NI USB 6003 Specifications (National Instrument, 2014b)

General Specifications	
Product family	Low-Cost Multifunction DAQ
Measurement type	Digital voltage
Communication protocol	USB
Analogue Input	
Number of channels	8
Differential channels	4
Input range & working voltage	$\pm 10V$
ADC resolution	16 bit
Maximum sample rate	100kS/s
Analogue Output	
Number of channels	2
Output range	$\pm 10V$
Digital Input / Output	
Number of ports	3 ports (0,1 and 2)
Number of channels	13 digital lines (8 channels in port 0, 4 channels in port 1 and 1 channels in port 2)
Physical Specifications	
Operating temperature	0 C° to 40 C°
Power supply	Bus Powered

The NI USB 6003 is a compact card whose sensors are connected using screw terminals connectivity. It can log / store data and it is compatible with a variety of fully supported programming languages including: ANSI C, C# .NET, VB .NET, LabVIEW, LabWindows™ / CVI, and Measurement Studio (National Instrument, 2014b).

3.5. Test Bench Control Software

Two main software applications were used in to collect data in this research: Magtrol (M-Test7) and Laboratory Virtual Instrument Engineering Workbench LabVIEW 2014. These software applications were involved in the preliminary testing and the final testing.

- **Magtrol-Test 7 (M-Test)**

Magtrol's torque 7 is used to automatically collect data from the inline torque transducer, including torque, speed and mechanical power. The observed data was logged and graphically displayed using Microsoft Excel.

This software application was used in the preliminary testing in order to generate initial data from the inline torque transducer. Several test modes are involved in M-Test7 including:

- i. Calibration display: data are taken from a specific parameter (torque, speed, power, etc.) to be displayed based on the sampling rate.
- ii. Curve: plotting a graph for a control parameter, identifying the high and low peaks as well as the dwell time; and the maximum brake current rate (%) to identify the braking rate.

Likewise, the PID coefficient is adjusted using the curve testing mode in terms of reducing / eliminating the errors in the system. Magtrol M-Test is an open platform source and is executable with LabVIEW (Magtrol, 2014a).

Figure (3.38) below demonstrates some results acquired by TM309 using M-Test. These results were logged into Microsoft Excel and graphs were plotted. Preliminary, a quick test was done to obtain torque and speed measurements using torque transducer. It covered 82 samples for almost 40 seconds with a sampling rate of one reading per 500ms. The test included running the test bench motor at 180 rpm while carrying un-loaded shaft.

As illustrated below, Figure (3.38 – a) shows that more torque was required in order to start acceleration of the bearing at the outset. Therefore, 0.297Nm was recorded as a high peak after it was 0.011Nm. Then, the torque fluctuated between 0.29 Nm and 0.2 Nm until the speed dropping observed (from 180 to 0 rpm). Then, torque went back to a lower peaks (0.041Nm) as there is no demanded speed.

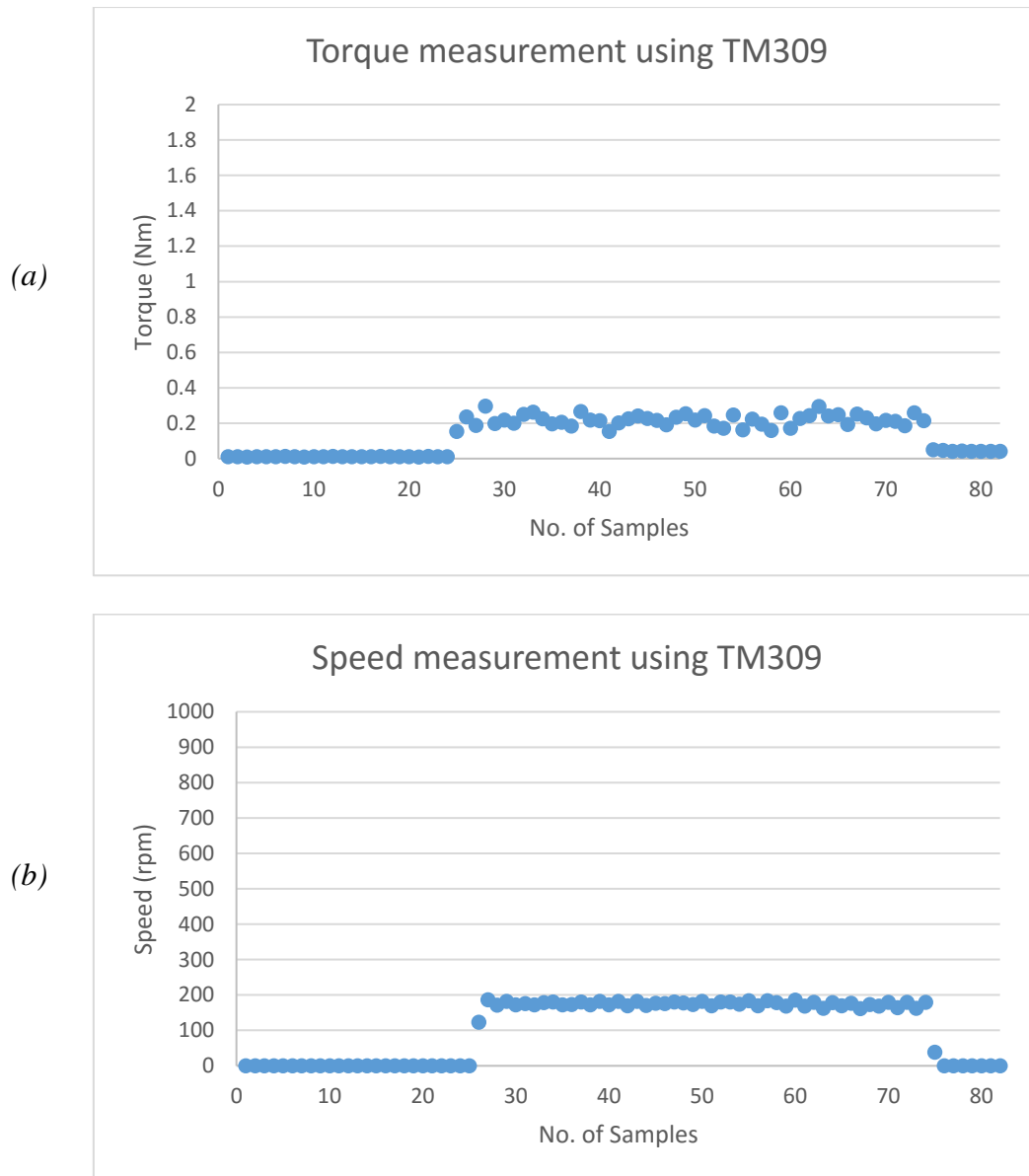


Figure 3. 39: Acquired data using TM309 and M-Test

Figure (3.38 – b) illustrates the acquired speed. The obtained speed was ranging between 0 to 180 rpm as shown in Figure (3.38 - b) above. The speed was adjusted randomly and the purpose behind this test was to test the logging ability from TM309 transducer using M-test7 and Microsoft Excel.

- **LabVIEW**

The Laboratory Virtual Instrument Engineering Workbench (LabVIEW) is a system-design platform and development environment for visual programming from National Instruments, widely used in industry allows applications that interact with real-world data or signals to be developed.

LabVIEW contains numerous components, and is suitable in terms of taking measurements or controlling applications. It uses a Graphical programming language (G) to allow users operate on data as soon as it is available rather than following the sequence line-by-line.

LabVIEW supports hardware items, including sensors, data acquisition DAQ, vision and actuation systems. Add-on packages and libraries are available for installation in the application, to provide more interaction allow such as control, simulation, sound and vibration analysis, machine vision and image processing and communication (El-Hajjar M. et al., 2012).

LabVIEW was chosen as the main programming platform for this research, to develop the software application. It was also used to monitor and diagnose the bearing health through logging and analysing data.

3.6. Bearing Life Monitoring System

Many publications have addressed the problem of calculating bearing life, largely successfully (Leturiondo et al., 2016 and Von Gesseneck et al., 2016). They help to diminish or avoid catastrophic failures that may occur to the machinery.

Leturiondo et al.,(2016) presented a method to calculate the fatigue life of rolling element bearings considering non-stationary conditions, with respect to the stress evolution in different components. This study considers cyclic loading and unloading processes rather than using a constant loading value, in addition to variations in the rotational speed. It uses a model-based approach to calculate contact loads between the different elements of the bearing, and the contact stresses through the finite element model (FEM). This information is used to perform fatigue analysis in studying over-loading in unhealthy bearings. Von Gesseneck et al., (2016), outline a condition based experimental method based on torque monitoring of radially loaded deep groove ball bearings in a lead-bismuth environment (LBE). They applied condition monitoring methods to measure bearing friction torque under inadequate lubrication, to study of roller bearing degradation under poor lubrication condition in a lead-bismuth environment (LBE).

Therefore, bearing lifespan is a design parameter in bearing selection, as its value must be identified to avoid any damage that bearings may cause to machinery, it is also required for scheduling maintenance operations (NMB, 2014). However, even with the use of standards such as (ISO (ISO281, ISO76, ISO 14728-1), ABMA (ABMA Std. 9), JIS (JIS A, B, C 1518), ANSI and DIN, calculating bearing life, is an estimate, as the calculation formula is based on

the statistical probability of failure. Several factors that affect bearing life are not included in the calculation, which can result in a large variation between the calculated and actual life of the bearing (Leturiondo, at el., 2016 and Nam, at el., 2016). These factors include: contamination, lubrication problems and secondary operational conditions (loads, moments, shocks, vibration, and temperature) that are different from design values. Additionally, inappropriate bearing installation can cause incorrect clearance or damage in bearing elements (NMB, 2014). Thus, it will be very useful for many applications if the actual lifespan of bearings is measured, in order to address the variation between calculated and actual lifetime.

ISO 281, (2007) presents a methodology to calculate the rating life based on a constant stationary load. It defines the bearing life as the number of revolutions until the first evidence of fatigue develops in any of the bearing elements (inner race, outer race, cage or rollers/balls). Two main load scenarios are illustrated in this standard considering the ratio of: basic dynamic radial load (C_r) / axial load (C_a); and dynamic equivalent radial load (P_r) / axial load (P_a). The standard presents an estimation of the “basic rating life”, calculated as shown below in Eq. (3.4) and Eq. (3.5).

$$L_{10} = \left(\frac{C_r}{P_r}\right)^e \quad \text{Eq. 3. 4: Basic rating life using radial load}$$

$$L_{10} = \left(\frac{C_a}{P_a}\right)^e \quad \text{Eq. 3. 5: Basic rating life using axial load}$$

$$L_{10h} = \left(\frac{10^6}{60 n}\right) * L_{10} \quad \text{Eq. 3. 6: Basic rating life in operating hours}$$

$e = 3$ for ball bearings and $\frac{10}{3}$ for roller or cylindrical bearings

L_{10} = basic rating life with 10% of failure probability in million revolutions

Eq. 3.4 and Eq. 3.5 demonstrate the basic rating life with respect to the basic dynamic and dynamic equivalent radial / axial load. These equations calculate the rating life in millions of revolutions. If the rotational speed is constant, it is preferable to use Eq. 3.6 to calculate the basic rating life in operating hours.

L_{10} proved its competency for calculating the basic rating life for many years with high quality material, manufacturing and with normal operating conditions. For many applications 90% reliability is insufficient, and, different level of reliability is required. Hence, a life modification factor (a_{ISO}) is introduced in addition to the modification factor for reliability (a_1). These factors

are multiplied with the basic rating life (L_{10}) to give the “modified bearing life” calculation under certain conditions of lubrication and contamination. The modified rating life is calculated as shown below in Eq. 3.7 and Eq. 3.8.

$$L_{nm} = a_1 a_{ISO} L_{10} \quad \text{Eq. 3. 7: ISO modification rating life in million revolutions}$$

$$L_{nmh} = \frac{10^6}{60 n} L_{nm} \quad \text{Eq. 3. 8: ISO modification rating life in operating hours}$$

Table 3. 8: Equation explanation

Variables	Description
L_{nm}	ISO rating life (millions of revolution)
L_{nmh}	ISO rating life (operating hours)
a_1	Life adjustment factor
a_{ISO}	Life modification factor
n	Rotational speed (rpm)
L_{10}	Basic rating life

Eq. 3.7 and 3.8 illustrates the modified rating life based on ISO281 with respect to the lubrication and contamination conditions. The life adjustment factor (a_1) is substituted in the equation based on the reliability level required as shown in Table (3.9) below.

Table 3. 9: Life modification factor for reliability

Reliability (%)	Failure probability (%)	Life adjustment factor (a_1)
90	10	1
95	5	0.64
96	4	0.55
97	3	0.47
98	2	0.37
99	1	0.25
99.2	0.8	0.22
99.4	0.6	0.19
99.6	0.4	0.16
99.8	0.2	0.12
99.9	0.1	0.093
99.92	0.08	0.087
99.94	0.06	0.080
99.95	0.05	0.070

The a_{ISO} considers the fatigue stress limit of the bearing steel to estimate the influence of lubrication and contamination on bearing life. This factor is calculated through measurements including: pitch diameter, oil viscosity ratio, fatigue load and level of cleanliness (contamination factor).

The pitch diameter of the ball or roller bearing (D_{PW}) is required to find out the rated oil viscosity. It is calculated using the following equation:

$$D_{PW} = \frac{(\text{inner race} + \text{outer race})}{2} \quad \text{Eq. 3. 9: Bearing Pitch Diameter}$$

The Figure (3.39) can be used to find the coinciding point of the reference kinematic viscosity (ν_1) that matches the pitch diameter under a specific speed and operating temperature.

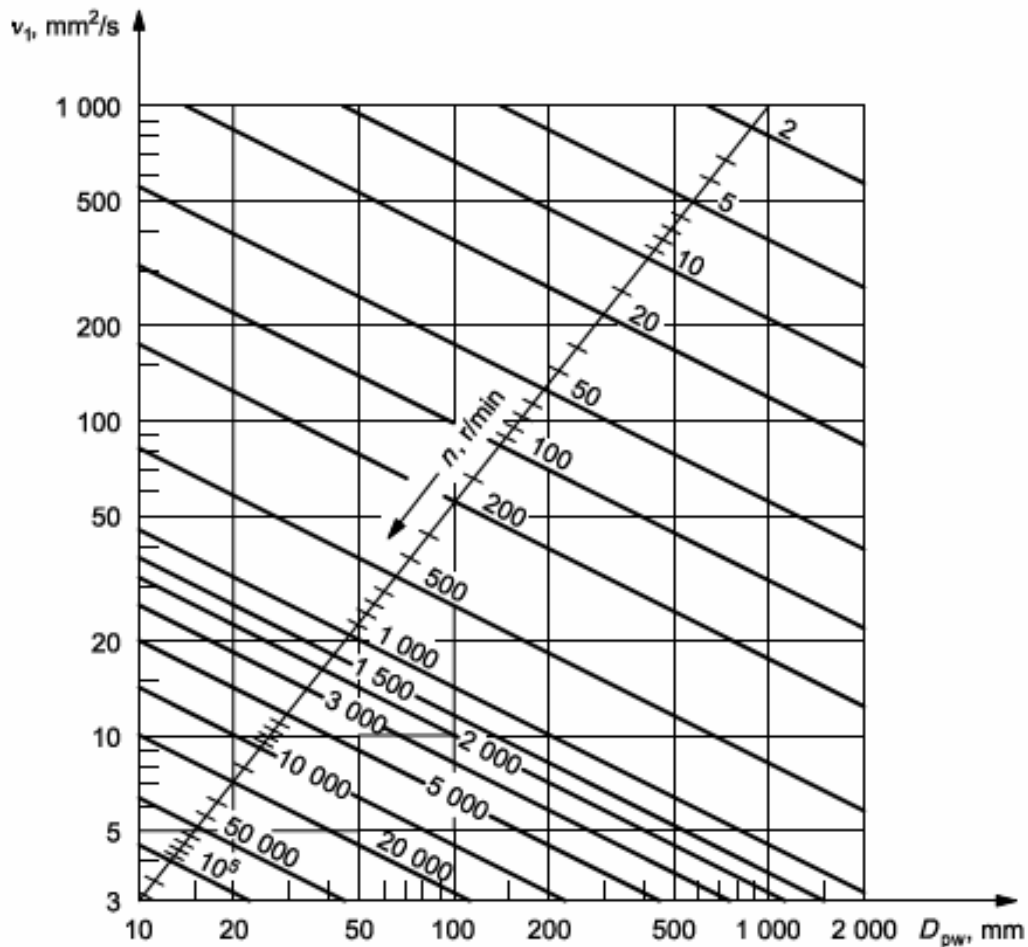


Figure 3. 40: Estimation of the minimum kinematic viscosity at operating speed (ISO281, 2007)

The kinematic viscosity ratio (k) is calculated by dividing the actual kinematic viscosity (ν) by the reference kinematic viscosity (ν_1).

$$k = \frac{\nu}{\nu_1} \quad \text{Eq. 3. 10: Kinematic viscosity ratio}$$

After that, the cleanliness level or the contamination factor (e_c) is considered to help in working out the (a_{ISO}) – based on Table (3.10) below.

Table 3. 10: Cleanliness / contamination factor e_c (ISO281, 2007)

Level of contamination	e_c	
	$D_{pw} < 100 \text{ mm}$	$D_{pw} \geq 100 \text{ mm}$
Extreme cleanliness Particle size of the order of lubricant film thickness; laboratory conditions	1	1
High cleanliness Oil filtered through extremely fine filter; conditions typical of bearing greased for life and sealed	0,8 to 0,6	0,9 to 0,8
Normal cleanliness Oil filtered through fine filter; conditions typical of bearings greased for life and shielded	0,6 to 0,5	0,8 to 0,6
Slight contamination Slight contamination in lubricant	0,5 to 0,3	0,6 to 0,4
Typical contamination Conditions typical of bearings without integral seals; course filtering; wear particles and ingress from surroundings	0,3 to 0,1	0,4 to 0,2
Severe contamination Bearing environment heavily contaminated and bearing arrangement with inadequate sealing	0,1 to 0	0,1 to 0
Very severe contamination	0	0

Then the fatigue load limit (C_u), the applied load (P) and the cleanliness factor (e_c) can be used to estimate the life modification factor (a_{ISO}) with the help of Figure (3.40).

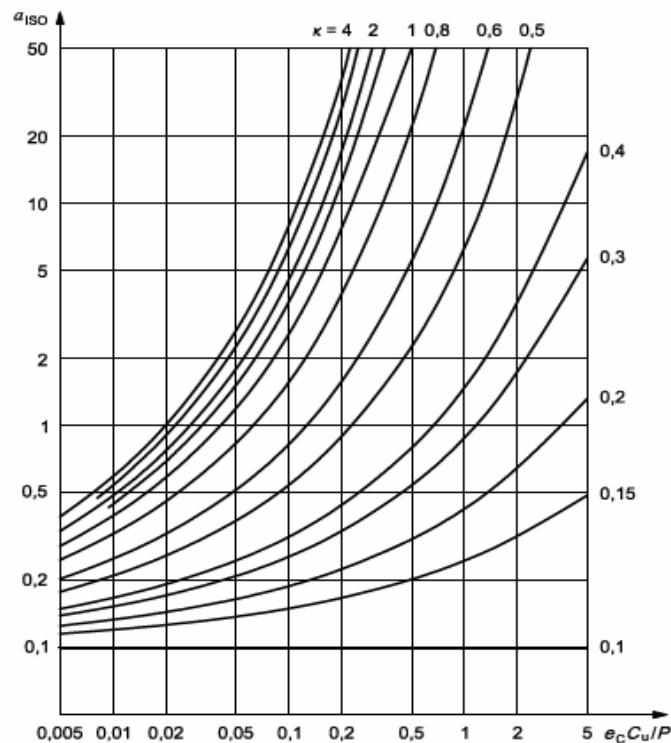


Figure 3. 41: Life modification factor a_{ISO} for ball bearings (ISO281, 2007)

Figure (3.40) shows the relation between $(e_c * \frac{C_u}{P})$ and the life modification factor respecting the kinematic viscosity ratio (k) for a typical ball bearing. Therefore, after estimating a_{ISO}

value, and with a certain value of reliability, Eq. 3.7 can be obtained. If the rotational speed is constant, it is preferable to calculate the rating life in operating hours using Eq. 3.8.

After ascertaining the temperature, speed and load the calculation of the bearing life starts as shown in Figure (3.41) below – code is attached in (Appendix E).

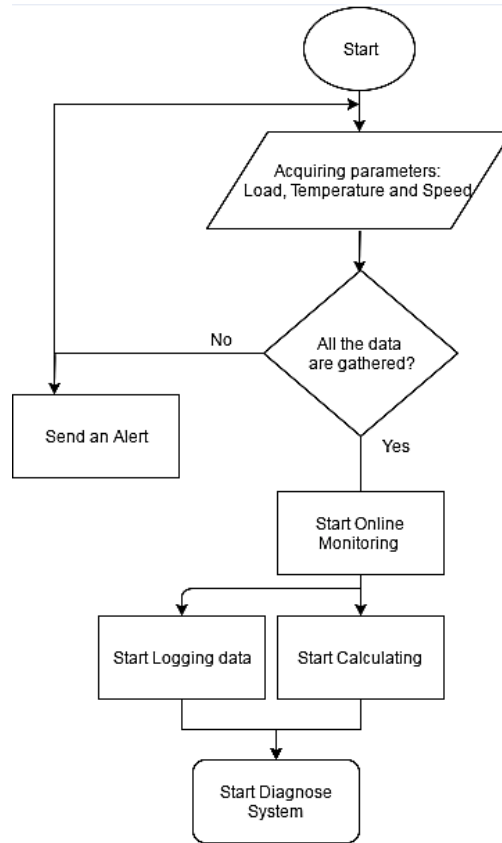


Figure 3. 42: Bearing life monitoring system flowchart

Worked example: by applying 800 kilograms (8kN) radially on a 6205-2RSH bearing at 2500 rpm the rating life is calculated as follows:

$$L_{10} = \left(\frac{C_r}{P_r}\right)^e = \left(\frac{14.8}{8}\right)^3 = 6.33 \text{ Million revolutions}$$

$$L_{10h} = \left(\frac{10^6}{60 n}\right) * L_{10} = \left(\frac{10^6}{60 * 2500}\right) * 6.33 \cong 42.2 \text{ hours}$$

Whilst, applying 1.4 tons (14kN) radially over NJ 205 ECP at 2500 rpm the rating life is calculated as follows:

$$L_{10} = \left(\frac{C_r}{P_r}\right)^e = \left(\frac{32.5}{14}\right)^{\frac{10}{3}} = 16.565 \text{ Million revolutions}$$

$$L_{10h} = \left(\frac{10^6}{60 n}\right) * L_{10} = \left(\frac{10^6}{60 * 2500}\right) * 16.565 \cong 110 \text{ hours}$$

The state of the bearings is diagnosed after completing the calculated number of hours, using vibration analysis technique as discussed in the following section.

This research considers using ISO281 equations to predict life for typical ball bearings, and by monitoring the parameters that affect the operating life. An application was developed for an Intelligent Health Management System (IHMS) for a micro-scale wind turbine bearing using a LabVIEW platform. It aims to enhance the monitoring technique for some of the parameters that play a vital role in affecting bearing life.

3.7. Bearing Diagnostic System

From all the condition monitoring techniques, vibration analysis was chosen to diagnose the bearing health. Vibration is an intermediate sign of mechanical failure. Normally, any abnormal mechanical elements starting to vibrate indicates that a failure is developing. Analysing these signals helps in diagnosing the bearing's health.

The diagnostic system consist of a piezoelectric accelerometer sensor (vibration sensor), USB DAQ 9191 & 9234 and the Optidrive E² inverter, with data signal transfer i.e. processing as illustrated in Figure (3.42) – code is attached in (Appendix F).

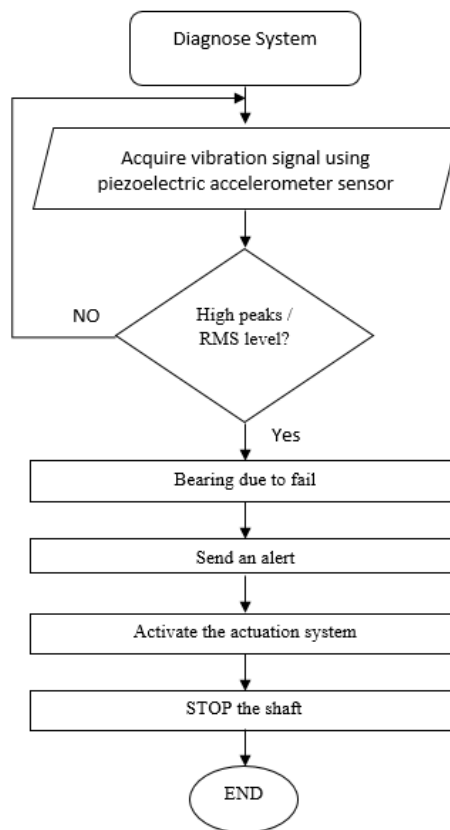


Figure 3. 43: Bearing diagnostic system flowchart

Figure (3.43 and 3.44) below shows a typical vibration signals from healthy and faulty bearings in the time domain. Defects that occurred in the bearing while running generate high peaks / RMS ratio as shown in Figure (3.44). Therefore, when a large number of defects occur, the RMS level is greater than expected.

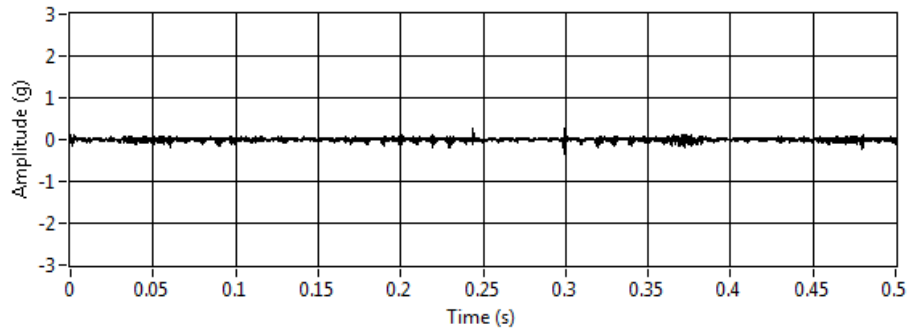


Figure 3. 44: Typical RMS level on Healthy bearing

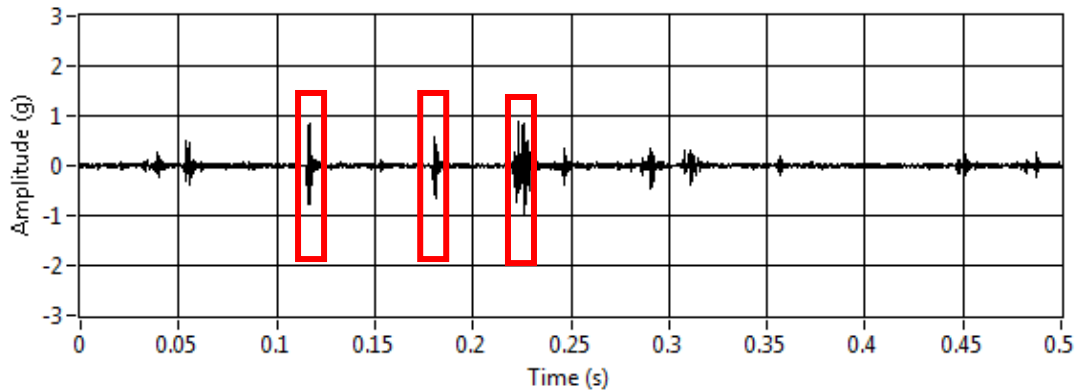


Figure 3. 45: Typical RMS level on Unhealthy bearing – inner race defects

Many approaches are used in diagnostic systems including: Time domain, Frequency domain and Time-Frequency domain. In Time domain approaches several factors can be monitored to provide in depth information about the bearing health such as: RMS, Kurtosis, Peaks and Crest Factor of the amplitude signal (Samuel P. and Pines D., 2005).

$$RMS = \sqrt{\frac{1}{N} [\sum_{i=1}^N (X_i)^2]} \quad \text{Eq. 3. 11: Root-Mean-Square}$$

$$Crest\ Factor = \frac{X_{peak}}{RMS} \quad \text{Eq. 3. 12: Crest Factor}$$

$$Kurtosis = \frac{N \sum_{i=1}^N (x_i - \bar{x})^4}{[\sum_{i=1}^N (x_i - \bar{x})^2]^2} \quad \text{Eq. 3. 13: Kurtosis}$$

Where N = Number of samples, X = Sampled time signal and X_{peak} = maximum positive peak.

Frequency domain data is also used to obtain narrowband spectra using the Fast Fourier Transform (FFT). The size of changes frequencies of signals in spectra is related to the nature of faults in the bearing as shown in Figure (3.44).

Time–Frequency domain provides the joint distribution information of time and frequency domain. It demonstrates frequency of the signal changing as a function of time, hence, illustrates the signals in both domains Time and Frequency (Samuel P. and Pines D., 2005).

Some frequencies characteristics can be calculated from the test bearing including: repetition rates for the inner race, outer race, rolling elements (ball) and cage using Eq. 3.14 to Eq. 3.18 (Benko U. et al., 2004).

$$f_r = \frac{\text{Shaft speed in rpm}}{60} \quad \text{Eq. 3. 14: Shaft rotational frequency}$$

$$f_c = \frac{f_r}{2} \left(1 - \frac{\text{Ball diameter}}{\text{Cage diameter}} * \cos(\text{angle of contact}) \right) \quad \text{Eq. 3. 15: Cage rotational frequency}$$

$$f_o = \frac{f_r}{2} * Z * \left(1 - \frac{\text{Ball diameter}}{\text{Cage diameter}} * \cos(\text{angle of contact}) \right) \quad \text{Eq. 3. 17: Outer raceway frequency}$$

$$f_i = \frac{f_r}{2} * Z * \left(1 + \frac{\text{Ball diameter}}{\text{Cage diameter}} * \cos(\text{angle of contact}) \right) \quad \text{Eq. 3. 16: Inner raceway frequency}$$

$$f_b = f_r * \frac{\text{Cage diameter}}{2 * \text{Ball diameter}} \left[1 - \left(\frac{\text{Ball diameter}}{\text{Cage diameter}} * \cos(\text{angle of contact}) \right)^2 \right] \quad \text{Eq. 3. 18: Ball rotational frequency}$$

Figure (3.45) below shows the vibration power spectrum using frequency domain technique. The graph was taken from an inner race defected bearing and it shows the first, second, third and fourth harmonic signal. The bearing has a roller diameter of 7.5mm, pitch diameter of 38.5 and contains of 13 rollers. The bearing was running at 121 rpm and the contact angle is zero. Therefore, using the inner rotational frequency equation the inner race frequency can be calculated as:

$$f_i = \frac{121}{60} * 13 * \left(1 + \frac{7.5}{38.5} * \cos(0) \right) = 15.6619 \text{ Hz}$$

Therefore, first harmonic = 15.6619Hz, second harmonic = 31.323Hz, third harmonic = 46.986Hz and fourth harmonic = 62.6476Hz

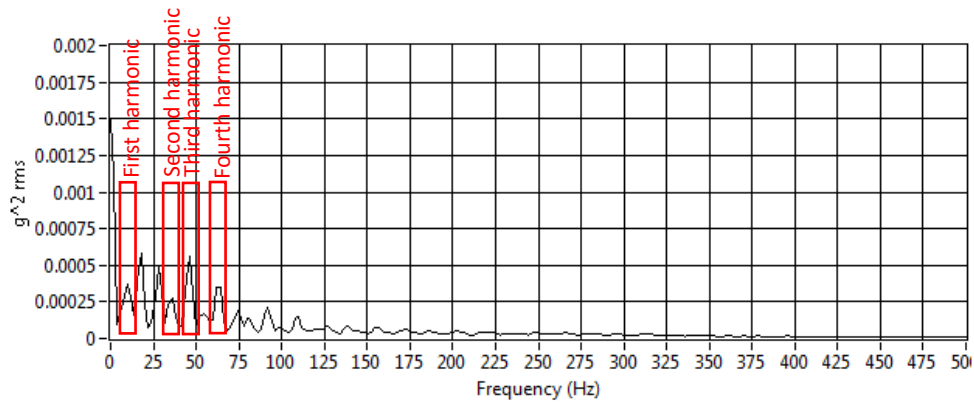


Figure 3. 46: Vibration spectrum in Frequency domain using the inner race defected bearing

3.7.1. Actuator System for Bearing Failure Detection

Monitoring different parameters in machinery performs a condition monitoring operation, whilst taking appropriate action during the monitoring operation is called active condition monitoring. Active condition monitoring helps in avoiding several types of failure, using the data acquired from sensors to activate an actuation system. An action can thus prevent failure. This active condition monitoring system may moderate the rotational speed of the shaft after it exceeds a threshold level.

Actuation in the bearing diagnosis system has been set to depend on the ratio high peak / RMS level in the vibration analysis technique. An increased amplitude in the vibration analysis will indicate a likely failure, as well as an increasing RMS level. The RMS value shows the measure of amplitude including a time history of the signal. This value is directly related to the energy content over an averaging period (Bruel and Kjaer, 1982). Thus, after exceeding the RMS level, a digital signal will be sent to the relay circuit board to activate the abort / response action.

Relays are involved in several applications to control the flow of current between a low-voltage circuits controlling a high-voltage circuit. A relay was used in this research to switch between the terminals in the inverter and allow control of the test bench, either manually using the potentiometer or automatically using a controller (NI USB 6003) and LabVIEW platform.

The relay used is a JZC-11F. It has a Single Pole Double Throw (SPDT) configuration to switch between throws, as shown in Figure (3.46) below. The specification is shown in Table (3.11) below (Peng C. et al, 2009a).

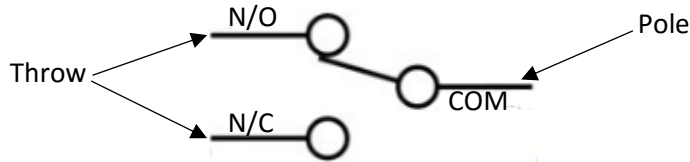


Figure 3. 47: Typical SPDT Configuration (after Oberhammer et al., 2006)

Table 3. 11: Relay specifications (Peng C. et al, 2009a)

Model No.	JZC-11F
Contact Material	Alloy
Maximum switching Voltage	250VAC or 30VDC
Maximum switching Current	5A
Minimum switching Load	10mA – 5VDC
Operating temperature	-40C° to +85 C°
Power consumption	200mV

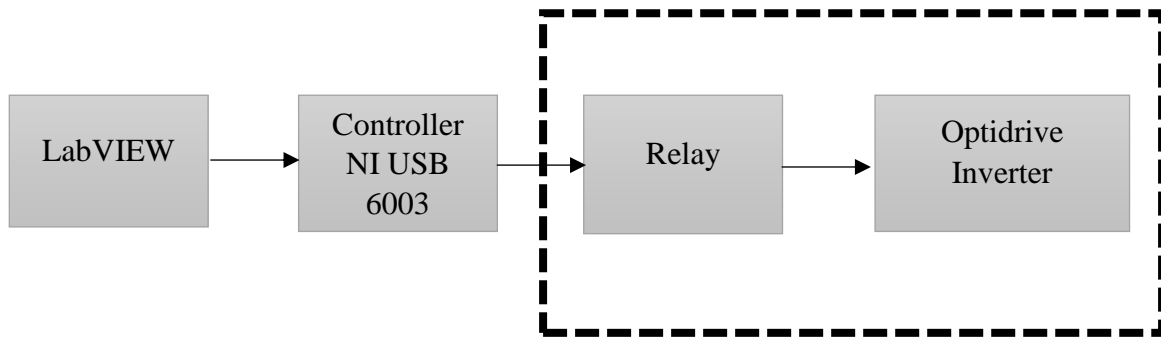


Figure 3. 48: Block diagram of the developed Active Condition Monitoring system (ACMs)

Figure (3.47) above illustrates the developed Active Condition Monitoring (ACM) system. If the RMS level is exceeded, a digital signal will be sent from the software platform (LabVIEW) using NI USB 6003 to the relay. This will switch between the terminals in the inverter to activate the abort action. Figure (3.48) below and (Appendix G) demonstrates the created PCB to facilitate the active condition monitoring system. This circuit board consists of relay, transistor (ZVP2110A), diode (1N4001) and terminal blocks.

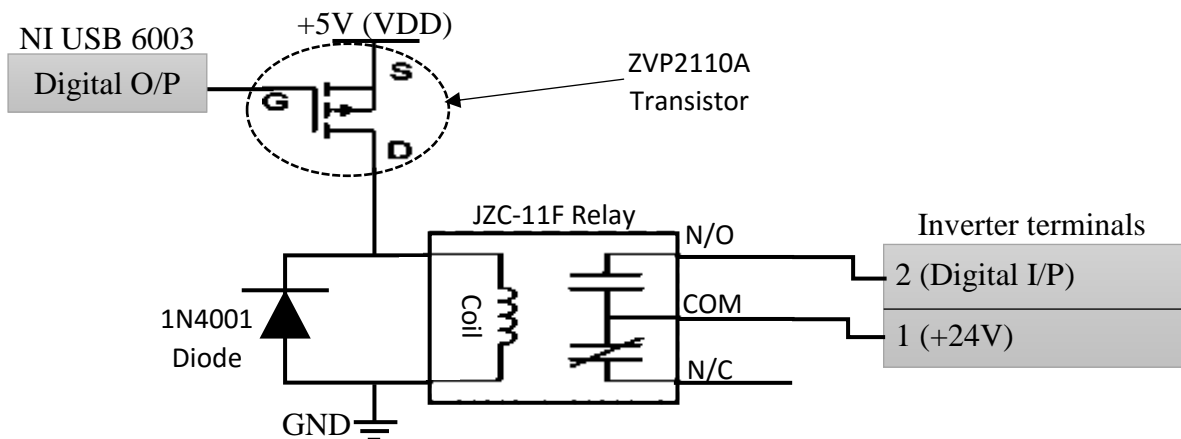
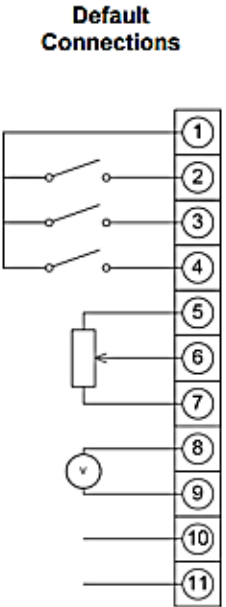


Figure 3. 49: Relay PCB connection

A ZVP2110 transistor was used in the circuit as a switch to turn the coil current on and off. It contains three pins: Gate (G), Source (S) and Drain (D). Gate (G) is connected to a digital output from NI USB 6003, Source (S) is connected to power supply (+5V) from the controller and Drain (D) is connected to the coil in the relay. With small voltage flowing from G to S, the transistor will be activated / turned on and it will allow a bigger voltage to be passed from S to D. Therefore, +5V will be passed to energise the relay coil. The purpose of using the transistor in this circuit is to allow use of +5V as a digital output, since the controller output is +3.3V. Therefore, with the use of ZVP2110A, a bigger voltage is passed to the relay which requires +5V. In addition, the 1N4001 diode was installed to protect the transistor from large voltage when ZVP2110 switches the coil.

The variation of the rotational speed is controlled by three-phase output Optidrive E² inverter. The analogue potentiometer signal is connected to terminal 6 to adjust the motor speed manually. Terminals 1 and 2 are connected to the relay board to activate the abort action automatically if needed. Table (3.12) below shows the control terminal connection of the inverter.

Table 3. 12: Control terminal connection (Evans P., 2009)



Control Terminal	Signal	Description
1	+24V User Output,	+24V, 100mA.
2	Digital Input 1	Positive logic "Logic 1" input voltage range: 8V ... 30V DC "Logic 0" input voltage range: 0V ... 2V DC
3	Digital Input 2	
4	Digital Input 3 / Analog Input 2	Digital: 8 to 30V Analog: 0 to 10V, 0 to 20mA or 4 to 20mA
5	+10V User Output	+10V, 10mA, 1kΩ minimum
6	Analog Input 1 / Digital Input 4	Analog: 0 to 10V, 0 to 20mA or 4 to 20mA Digital: 8 to 30V
7	0V	User ground connected terminal 9
8	Analog Output / Digital Output	Analog: 0 to 10V, 20mA maximum Digital: 0 to 24V
9	0V	User ground connected terminal 7
10	Relay Common	
11	Relay NO Contact	Contact 250Vac, 6A / 30Vdc, 5A

3.8. Summary

This chapter describes the components of a test bench for an Intelligent Health Management System (IHMS), for the main rotor bearing in a micro-scale wind turbines. Although, the IHMS is being developed for micro-scale wind turbine bearings, it could be used in any bearings systems. The focus of this development is to monitor different types of bearing. The IHMS will be able to monitor bearing life and predict bearing system failure through monitoring the main parameters that affect the bearing operations. Several sensors interfaced with controllers are installed to accomplish this.

Also, this chapter outlines an intelligent monitoring system to test a micro-scale wind turbine bearing. It reviews current studies including methods for the calculation of the fatigue life of rolling element bearings considering stationary conditions and a torque-based method for remote monitoring of radially-loaded deep groove ball bearings. The common objective of these studies was to monitor the bearing health / life and diminish the likelihood of failure.

According to ISO281, the lifespan of the bearing can be defined as the number of revolutions until the first evidence of fatigue appears in any of the bearing elements (inner race, outer race, cage or rollers/balls). Likewise, it presents a methodology to calculate the rating life based on a constant stationary load. The constant load could be radial or axial, although this research is examining the effect of the radial load on the ball bearing. The load is applied using a hydraulic bench press and measured with pressure transducer. The operating life of the bearing is calculated using the equations in the ISO standard.

The concept behind this research is to increase the reliability percentage by introducing an embedded system in addition to the mechanical elements (bearing elements) with the use of multiple sensors. These sensors iteratively monitor the life and update the user with any changes in the parameters that affect the lifespan / operation.

While the system is running, a diagnostic examination of the bearing's health is carried out, using a piezoelectric accelerometer (vibration sensor) and DAQ card (cDAQ9234).

If the bearing starts vibrating abnormally this is identified and may indicate an upcoming failure. Thus, action can be taken when the bearing is due to fail. An intelligent monitoring system can be used to prevent catastrophic bearing failures and damage to the other elements in the micro-scale wind turbine. In this instant, this is achieved through either increasing or decreasing the rotational speed or completely stopping the spinning operation of the main shaft.

The acquired speed from the speed sensor is compared with the requested speed from the inverter and a decision is made accordingly.

Chapter 4 introduces the testing methodology and the some example results by applying the process explained in Chapter 3. Also, it presents the results details of the outcome of using an advanced mathematical algorithm to provide failure prediction and the use of image processing algorithm to extract some features during the failure progression in the bearing system.

Chapter 4. Results and Discussion

4.1. Introduction

This chapter details the different stages of testing and validation of the IHMS through a series of preliminary and final tests. Section 4.2 describes the experimental test specifications; Section 4.3 presents the preliminary tests; Section 4.4 illustrates the final testing, which includes two types of tests; bearing system health monitoring that includes failures detection, and bearing life testing. In addition, the chapter present the results of using advanced algorithms to support failure prediction namely, ARMA and image processing algorithms, as illustrated in Section 4.5. The chapter is summarised in Section 4.6.

4.2. Experimental Test Specifications

This research undertook preliminary and final testing. Data from the preliminary testing were used as a reference to identify when to trigger the test equipment to abort the operation, to constitute an active condition monitoring system. Final testing considered bearing system failures' detection and bearing life testing. Focus was on typical bearing system failures that occur in the main shaft and coupling, and monitoring bearing life was recorded in this chapter.

Data collected throughout these tests includes variations in the vibrational parameters during the initiation / propagation of system failure and changes during the lifetime of the bearing. Additionally, torque, speed, load and temperature measurements during all the tests were detailed, as illustrated in Figure (4.1).

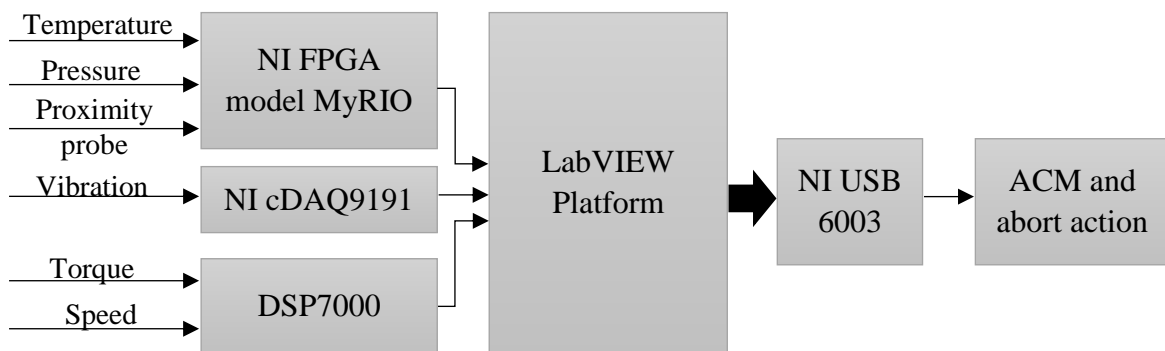


Figure 4. 1: System overview

Figure (4.1) shows the experimental system overview; four controllers are involved, each with a distinctive role in gathering the required data. All are interfaced on one software platform (LabVIEW).

Using NTC, NI myRIO the equipment was able to record temperature, pressure (to calculate the applied radial load), speed using the proximity probe sensor, and to calculate the bearing life based on ISO281 equations. An NI cDAQ 9191 was used to carry out vibration analysis using the piezoelectric accelerometer sensor. The code developed was able to record vibrations and evaluate time domain parameters (RMS, Peak, Crest Factor and Kurtosis) and frequency domain parameters. The calculation of the bearing elements' characteristic frequencies was achieved through the following equations (ISO20958, 2013):

$$f_r = \frac{\text{Shaft speed in rpm}}{60}$$

Eq. 4. 1: Shaft rotational frequency

$$f_c = \frac{f_r}{2} \left(1 - \frac{\text{Ball diameter}}{\text{Cage diameter}} * \cos(\text{angle of contact}) \right)$$

Eq. 4. 2: Cage rotational frequency

$$f_o = \frac{f_r}{2} * Z * \left(1 - \frac{\text{Ball diameter}}{\text{Cage diameter}} * \cos(\text{angle of contact}) \right)$$

Eq. 4. 3: Outer race rotational frequency

$$f_i = \frac{f_r}{2} * Z * \left(1 + \frac{\text{Ball diameter}}{\text{Cage diameter}} * \cos(\text{angle of contact}) \right)$$

Eq. 4. 4: Inner race rotational frequency

$$f_b = f_r * \frac{\text{Cage diameter}}{2 * \text{Ball diameter}} \left[1 - \left(\frac{\text{Ball diameter}}{\text{Cage diameter}} * \cos(\text{angle of contact}) \right)^2 \right]$$

Eq. 4. 5: Ball rotational frequency

From the equations above, it can be seen that the outer raceway frequency is minimised to $f_o = Z * f_c$ and $Z =$ number of balls.

A DSP7000 was used to establish two of the main parameters, the torque due to bearing friction and the main shaft speed, to give the speed of the running bearing. An NI USB 6003 was used to perform Active Condition Monitoring (ACM) through applying an abort action as required, based on a thresholding algorithm. For instance, if an abnormal pattern of the vibrational parameters was detected, then the abort operation would take place indicating an abnormal occasion is recognised. This was done by sending a digital signal to the relay board, causing a switch in the connection between the terminals in the inverter. These data were then logged in text format to be studied graphically.

4.2.1. Testing procedures

Several procedures were followed in order to provide the same testing conditions for each test. These testing procedures began by running:

- myRIO
- DSP7000
- DAQ9191
- DAQ6003

Then radial load was applied gradually until it reached the desired load in each test. After that, the motor speed was increased gradually until it reached the required speed (2000 rpm). Hence, identifying all the parameters began by:

- Logging data from myRIO with one sample every half second.
- Logging data from DSP7000 with the same rate as myRIO.

- Logging vibration parameters from the DAQ9191 with the same rate, including graphs using different approaches, the time domain and the frequency domain. Also, several values such as RMS, Crest Factor, Peaks and Kurtosis were logged. The raw vibration data in the time domain was logged every minute to allow re-playing the vibration signal to learn more about the failures.

Finally, at the end of each test, the bearing with the shaft was replaced with a similar bearing type and using a similar installation method.

In theory, if the single deep-groove bearing (6205-2RSH) runs at 2000 rpm with 10kN radial load, the bearing can run for a basic rating life of 24 hours with 90% reliability, as shown by the following equations:

$$L_{10} = \left(\frac{C_r}{P_r}\right)^e = \left(\frac{14.8}{10}\right)^3 \cong 3.2 \text{ Million revolutions}$$

$$L_{10h} = \left(\frac{10^6}{60 n}\right) * L_{10} = \left(\frac{10^6}{60 * 2000}\right) * 3.2 \cong 27 \text{ hours}$$

Therefore, using the ISO modification, the basic rating life with 90% reliability would be calculated as follows:

$$\text{Pitch diameter } (D_{PW}) = \frac{(\text{inner race} + \text{outer race})}{2} = \frac{25 + 52}{2} = 38.5 \text{ mm}$$

From this, using Figure (4.2) below to identify the kinematic viscosity (ν_1):

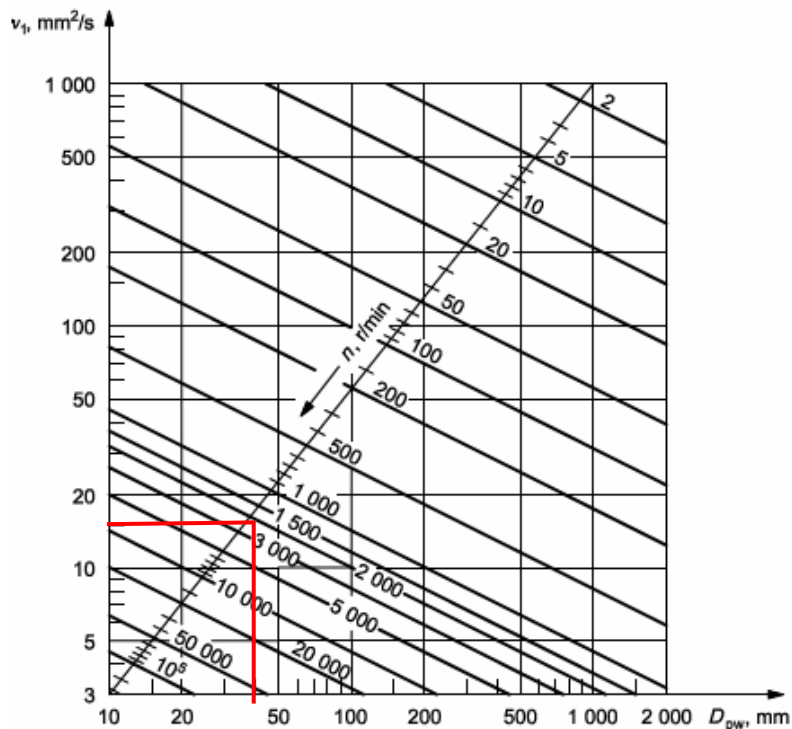


Figure 4. 2: Kinematic viscosity (ν_1) against the pitch diameter with respect to running speed (ISO281, 2007)

Therefore,

$$v_1 \cong 15 \frac{mm^2}{s}$$

From this, the viscosity ratio is calculated as follows:

$$k = \frac{v}{v_1} = \frac{30}{15} \cong 2$$

Where the base oil viscosity for 6205-2RSH is 30 cSt at 40°C and 6 cSt at 100°C based on DIN 51 562. The test bearing operates at a high cleanliness environment, thus:

$$e_c = \text{Extreme cleanliness} = 1$$

$$\therefore e_c * \frac{C_u}{P} = 1 * \frac{0.335}{10} = 0.0335$$

Hence,

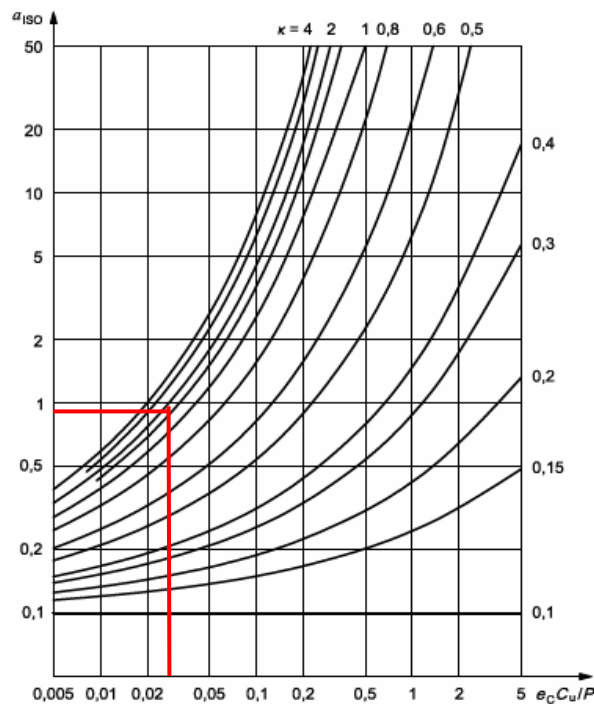


Figure 4. 3: Life modification factor a_{ISO} for ball bearings (ISO281, 2007)

Consequently,

$$a_{ISO} \cong 0.9$$

Finally, the bearing lifetime with 90% reliability is:

$$L_{10m} = a_1 a_{ISO} L_{10} = 1 * 0.9 * 3.2 \cong 2.9 \text{ million revolutions}$$

$$L_{10mh} = 2.9 * \frac{1000000}{60 * 2000} \cong 24.2 \text{ hours}$$

Table (4.1) shows the theoretical results for this research. It demonstrates the basic rating life with different levels of reliability at the same running speed (2000rpm) with different radial load rate.

Table 4. 1: Theoretical bearing life calculation for single deep-groove bearing (6205-2RSH)

No.	Speed (rpm)	Radial Load (kN)	Pressure (MPa) / PSI	Expected basic rating life (L ₁₀ – with 90% reliability)		Using ISO modifications (90%)		Using failure probability with 5%	
				Life in million revolutions	Life in operating hours	Life in million revolutions	Life in operating hours	Life in million revolutions	Life in operating hours
1	2000	6	5.3 / 769	15	125	13.5	112.6	9.6	80
2	2000	10	8.82 / 1279	3.2	27	2.9	24.2	2	17
3	2000	11	9.7 / 1406	2.4	20.3	2.19	18.3	1.56	12.9

4.3. Preliminary Tests

In order to validate the software development, several parameters, including speed, pressure, load, and vibration parameters (RMS, Kurtosis, Peak, Crest Factor and Max-Min) were recorded.

The purpose of these tests were to verify the capability of the developed IHMS software and to understand the initial parameters; it was also a reference for triggering the abort action. The testing comprised NI myRIO Xilinx-Z FPGA, USB DAQ9191, and DSP7000. It was conducted in two phases: un-loaded and loaded bearing. Both phases were run at 2000 rpm and the loaded phase embraced a 10kN radial load.

Therefore, using the equations illustrated earlier (Eq. 4.1 to Eq. 4.5), bearings elements' frequencies at 2000 rpm can be calculated as follows:

$$f_r = \frac{\text{Shaft speed in rpm}}{60} = \frac{2000}{60} = 33.33 \text{ Hz}$$

$$f_c = \frac{2000}{120} \left(1 - \frac{7.938}{38.5} * \cos(30) \right) = 13.69 \text{ Hz}$$

$$f_o = \frac{2000}{120} * 9 * \left(1 - \frac{7.938}{38.5} * \cos(30) \right) = 123.21 \text{ Hz}$$

$$f_i = \frac{2000}{120} * 9 * \left(1 + \frac{7.938}{38.5} * \cos(30) \right) = 176.783 \text{ Hz}$$

$$f_b = \frac{2000}{60} * \frac{38.5}{2 * 7.938} \left[1 - \left(\frac{7.938}{38.5} * \cos(30) \right)^2 \right] = 78.26 \text{ Hz}$$

Table 4. 2: Bearing elements' frequencies

	Shaft rotational frequency (f_r)	Cage rotational frequency (f_c)	Outer raceway rotational frequency (f_o)	Inner raceway rotational frequency (f_i)	Ball rotational frequency (f_b)
Slave (NJ205 - ECP)	33.33 Hz	13.42 Hz	174.46 Hz	258.87 Hz	82.31 Hz
Test (6205-2RSH)	33.33 Hz	13.69 Hz	123.22 Hz	176.783 Hz	78.26 Hz

Preliminary testing was done and all the initial values of the monitored are detailed in Table (4.3) and shown in the following Figures (4.4 – 4.10).

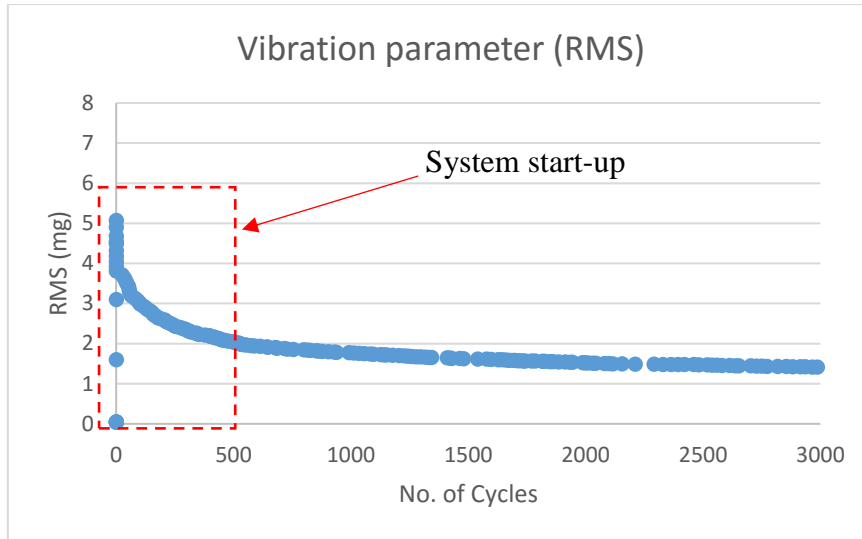


Figure 4. 4: RMS value – Unloaded bearing

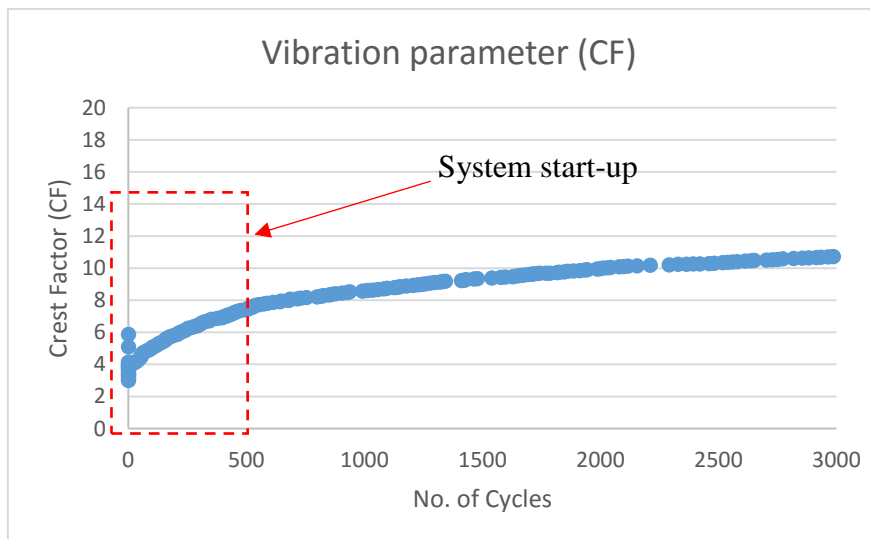


Figure 4. 5: Crest Factor values – Unloaded bearing

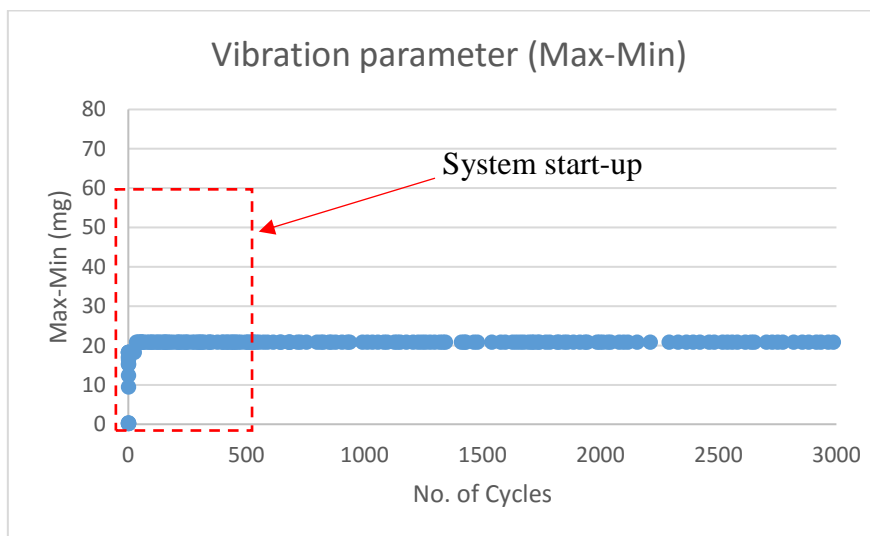


Figure 4. 6: Max-Min value – Unloaded bearing

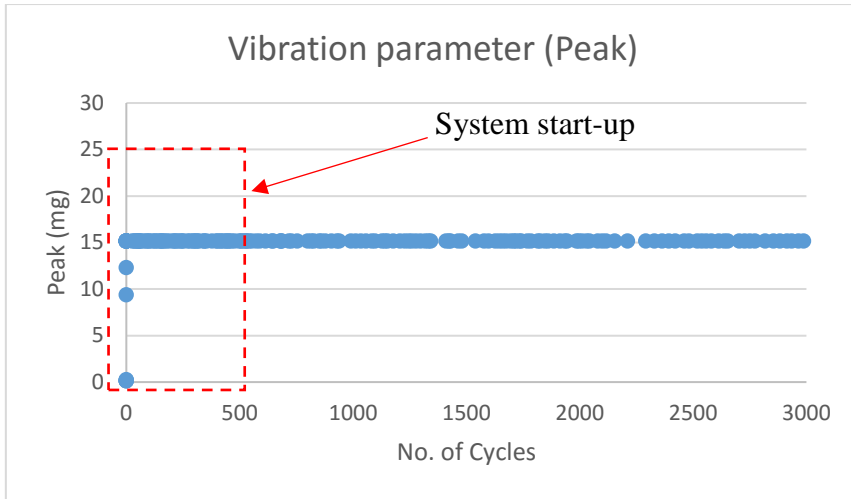


Figure 4. 7: Peak value – Unloaded bearing

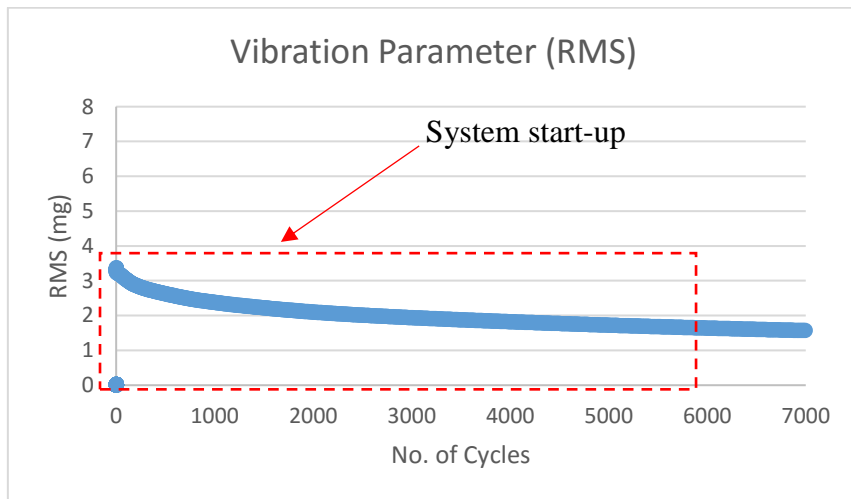


Figure 4. 8: RMS value – 10kN loaded bearing

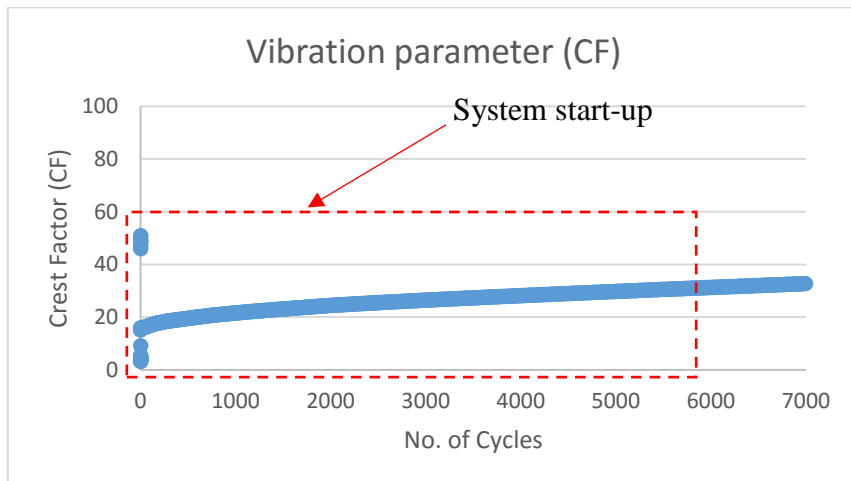


Figure 4. 9: CF value - 10kN loaded bearing

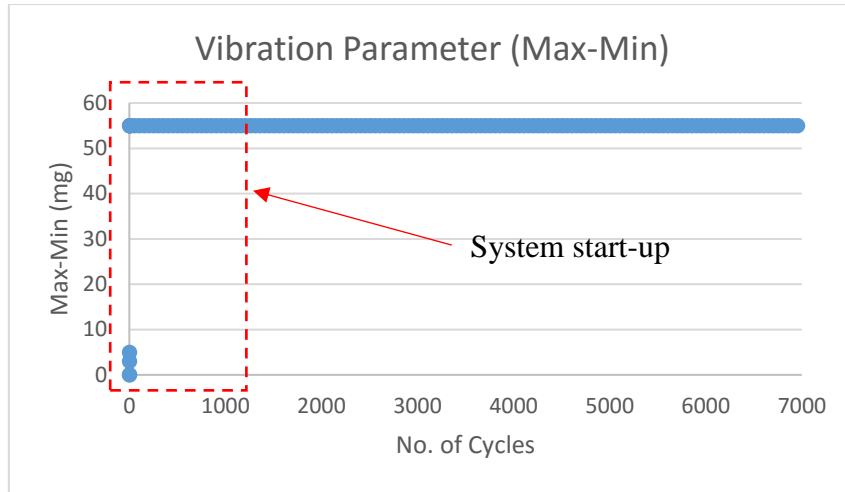


Figure 4. 10: Max-Min value - 10kN loaded bearing

Therefore, from all the above graphs, Table (4.3) can be conducted and used as a reference point of a healthy bearing.

Table 4. 3: Initial parameters of a healthy bearing, used as references to trigger the abort action

	Unloaded	Loaded (6kN)	Loaded (8-11kN)
RMS (mg)	1.3	< 0.7	< 1.5
Kurtosis	~3	~3	~3
Peak (mg)	15	< 25	< 30
Crest Factor	> 11	> 30	> 35
Max-Min (mg)	< 20	30 – 35	50 – 60

4.4. Final Tests

The following results demonstrate the ability of the developed system in terms of detecting bearing system failures and monitoring the bearing life. Four tests were conducted throughout this research. The first three tests shows the capability of the developed IHMS in detecting bearing system failures. The fourth test monitors the bearing's operational life.

Table 4. 4: Conducted tests type throughout this research

	Test Type	Test Duration ($\times 10^3$ cycles)
First Test	Bearing System Failure; shaft failure	60
Second Test	Bearing System Failure; shaft failure	555
Third Test	Bearing System Failure; coupling failure	7500
Fourth Test	Bearing Life Test	19000

Table (4.4) list the different types of tests conducted during the IHMS validation. The first test illustrates a typical failure mode in the main shaft, namely fatigue. This test comprised a main shaft with two circlips to accommodate the bearing. The second test embraced a similar failure mode but without using circlips as they diminish the material strength; instead, two shaft clamps were used to reduce stress concentration. The results of these tests were studied graphically as shown in Sections 4.4.1. and 4.4.2. The third test demonstrates fatigue failure in the coupling. During this test, the running couplings were stressed at the weakest point in the coupling, resulting in fatigue initiation / propagation and followed by a fracture, described in Section 4.4.3. Failures in the first three tests occurred due to the excessive radial load, resulting in fatigue initiation / propagation in different locations. Lastly, the fourth test demonstrated the ability of the developed software in monitoring the bearing life. This test illustrated the changes in the vibrational parameters during the bearing operation, all graphically represented in Section 4.4.4.

The results of the tests illustrated the sensor signals as a means to confirm the suitability of the equipment to detect failures. At the end of each sample, the main rotary shaft and the test bearing were replaced with the same installation methods to provide the next sample with the same conditions as the previous one. The salve bearings (NJ205 ECP) were lubricated using multi-purpose grease (LM2).

4.4.1. First Test: Bearing System Failure; Shaft Failure

This test was conducted for almost 60×10^3 cycles before a catastrophic failure occurred at the end of the test, as shown in Figure (4.12) below. Two 25mm external circlips were used to accommodate the bearing and to prevent it from moving axially. This was done through making a 1 mm groove along the shaft using the turning machine / Computer Numerical Control (CNC), as illustrated in Figure (4.11) below. Hence, the shaft material strength was intentionally minimised to capture bearing system failures in the main rotary shaft.

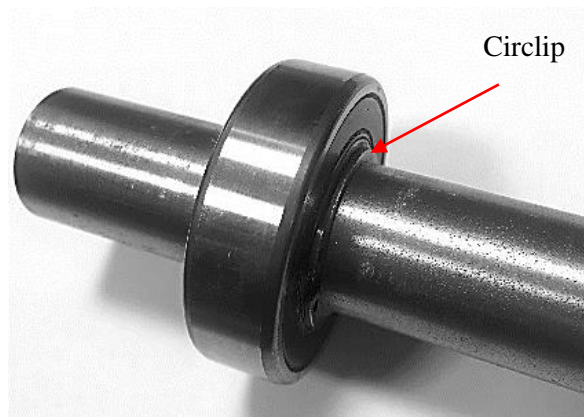


Figure 4. 11: Test bearing with two external circlips

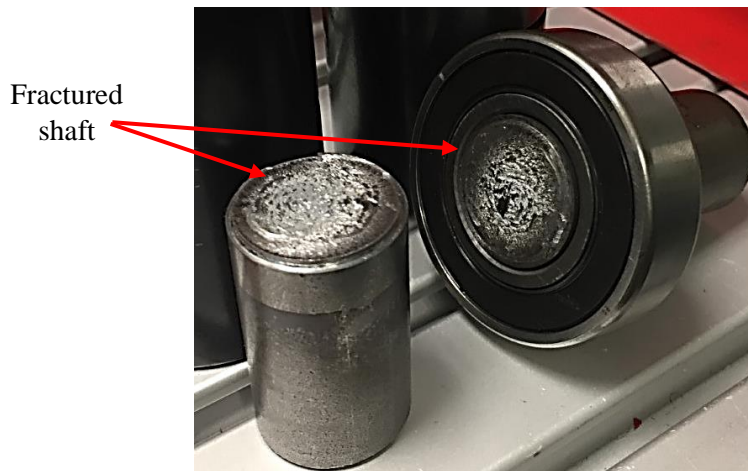


Figure 4. 12: An illustration of the final observed results from the bearing system failure test – first sample

During the first test, the bearing was loaded radially at 2000 rpm; the first 15,000 revolutions indicated that the applied load was 9kN, which was then increased to 10kN before the fracture failure occurred in the main rotary shaft. This was unintended and was due to an increase in the temperature inside the test cell due to the operation of the motor and the frictional heating from the Test bearing. The following graphs (Figures 4.13 – 4.16) illustrate the data plotted from the vibration analysis – other graphs are attached in (Appendix H):

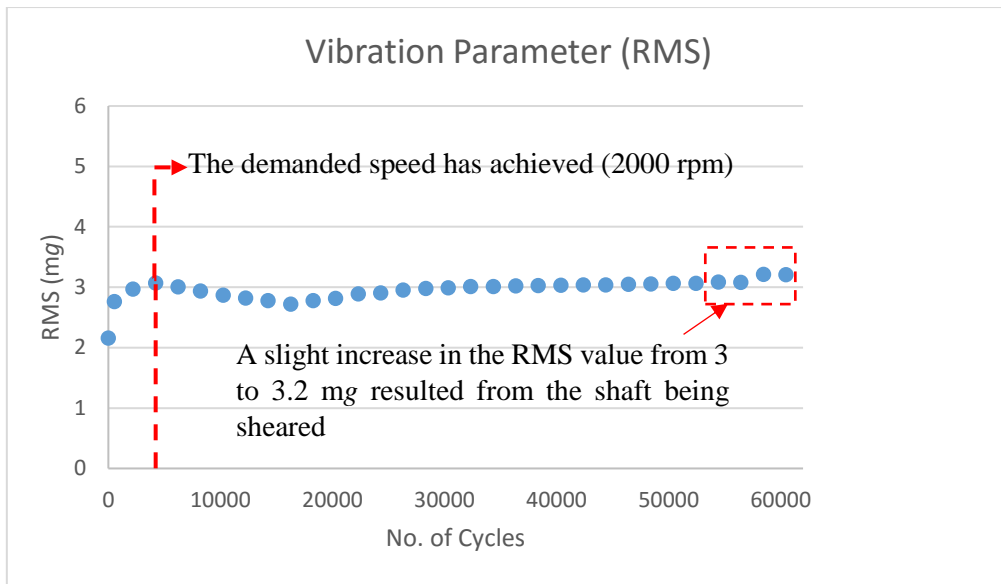


Figure 4. 13: RMS value of the first bearing system failure test

Based on Figure (4.13), the trend-line of the RMS value started over the reference value (<1.5mg), resulting in the system sending a notification indicating an abnormal occurrence. The notification has been intentionally overridden to continue the test and monitors the bearing system failure. However, the system remained running under supervision. Then, the RMS value followed a pattern of a straight line around 3mg and increased to 3.2mg when the shaft sheared owing to the increase of the energy level in the vibration signal.

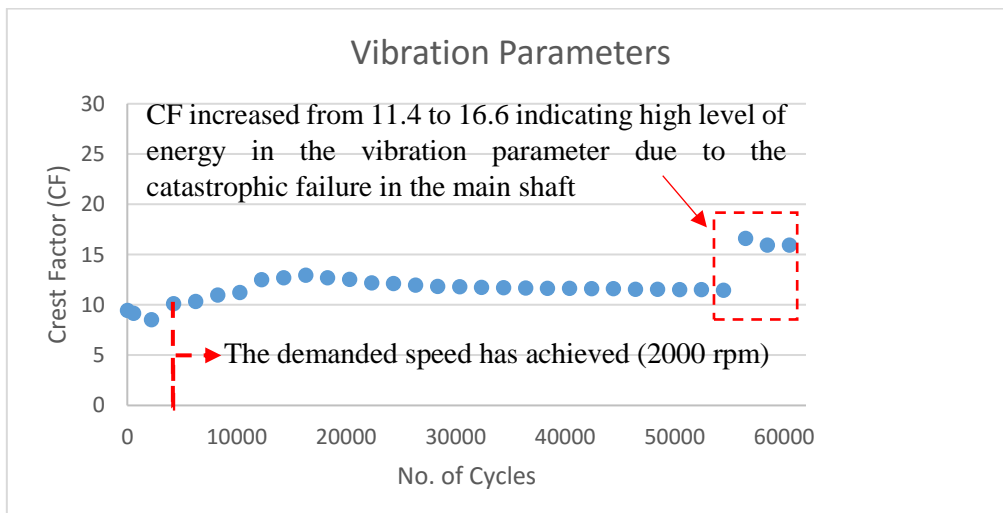


Figure 4. 14: Crest Factor (CF) value of the first bearing system failure test

The Crest Factor (CF) diagram shows that the value started at 10 beyond the reference value (>35), increasing to 11, then over 16 when the shaft fractured due to fatigue failure.

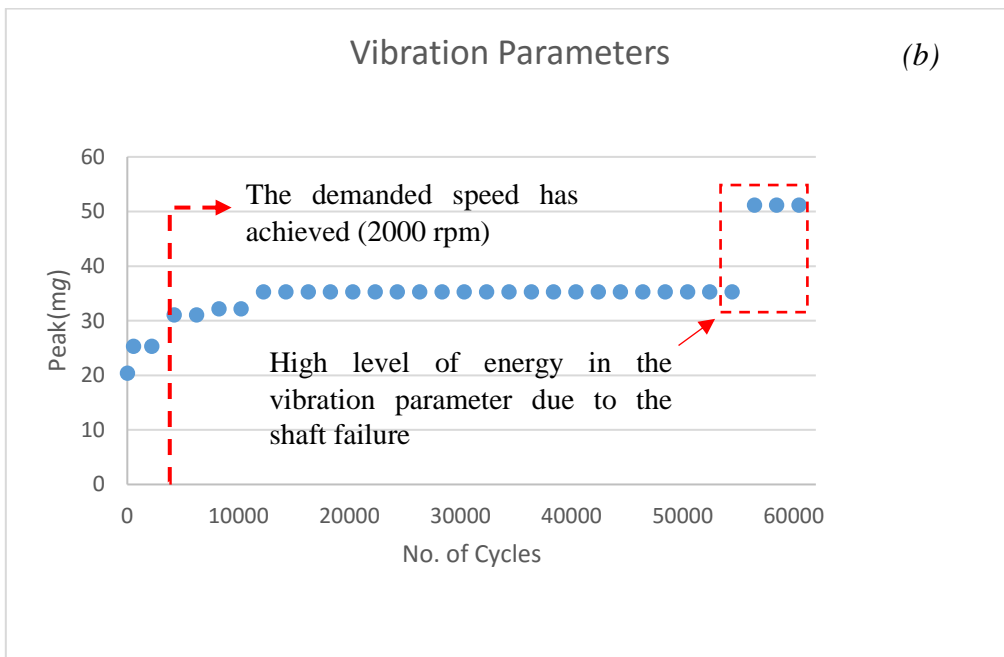
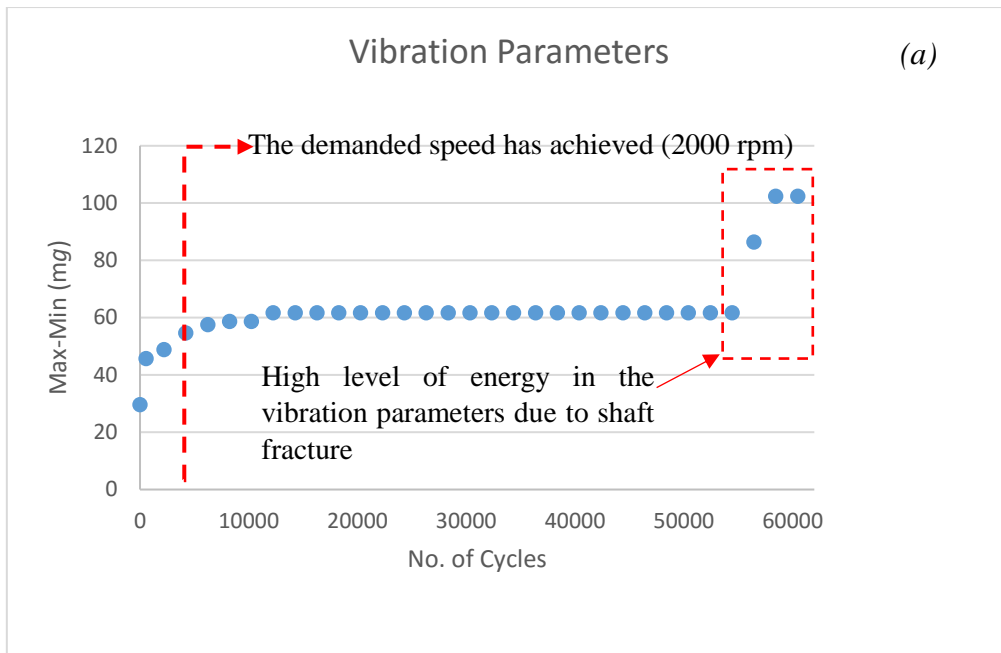


Figure 4. 15: Vibration parameters of the first bearing system failure test – (a): Max-Min, (b): Peak

Figure (4.15 – a) illustrates the Max-Min, which started with an increment towards 61.7mg, resulting in the system notifying the user that an abnormal occurrence was ongoing. A decision was made to ignore the notification, to investigate the failure mode further. The values remained constant at 61.7mg, increasing gradually after the fracture of the shaft to 102mg, while the peak value increased slightly until it remained at 35mg. When the fracture occurred, the peak value jumped from 35 to 51mg, as illustrated in Figure (4.15 – b).

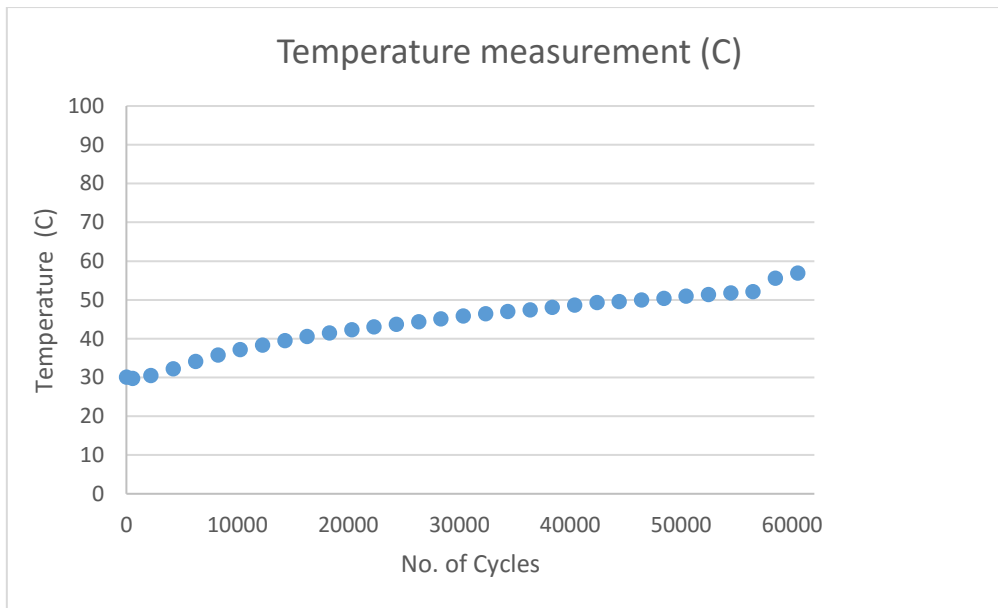


Figure 4. 16: First Sample results – Temperature measurement in C°

Figure (4.16) illustrates the bearing temperature in degrees Centigrade from the attached NTC sensor into the hydraulic piston. It was noticed that the temperature followed an almost straight-line pattern, starting at 29°C and ending at 57°C. The observed rise in temperature was due to the bearing being heavily loaded, using around 75% of its capacity (10kN out of 14.8kN). After the shaft fractured, it was recorded that the applied load dropped significantly, indicating that the distance between the hydraulic press piston and the bearing had changed sharply.

A closer look at the logged frictional torque of the bearing showed that it increased to around 1.7Nm, indicating the required frictional torque to start rotating the motor at the requested speed (2000rpm) under the applied radial load. It then followed a pattern of fluctuating around 1.2Nm until the fracture occurred. The torque dropped to 0.035Nm, indicating that the shaft had sheared and the bearing was no longer loaded, i.e. the shaft was not linked to the other elements in the test bench.

Conclusively, the shaft during this test embraced external factors which stressed the shaft resulting fatigue failure in the shaft. The capability of the developed system to detect failures during this test was verified. The decision to ignore all the notifications from the system was made to explore the failure modes further and to validate whether the system was predicting a fault indication, while the test remained under supervision. The next phase of testing includes the capability of the system in detecting failures in the main shaft without additional support (circlips).

4.4.2. Second Test: Bearing System Failure; Shaft Failure

Following the First Test, the mechanical design of the test bench has been updated to include new bearing housing, test bearing (similar type 6205-2RSH), new main shaft (with same material and shorter length) and use of two shaft clamps/ collars instead of circlips to resist any axial movements of the Test element. In addition, the necessary mechanical installation procedure was used to check the main shaft alignment.

Due to the mechanical system update, it is expected that the baseline signature of the vibration signal will be different from the First test, which has been taken into account by the system which used as the new baseline signature.

The second test was performed for around 555×10^3 cycles of operation before the fatigue propagated / initiated and sheared the main rotary shaft, as illustrated in Figure (4.17) below. The system notified the forthcoming failure and was run under supervision, then urgently aborted manually when the fracture occurred.



Figure 4. 17: An illustration of fatigue propagation in the main rotary shaft of the second bearing system failure test – (i) shows where the fatigue started/initiated, (ii) illustrates the fatigue zone where the cracks grow slowly, (iii) shows where instantaneous zone where the crack growth rate increases vastly

The following graphs Figures (4.18–4.23) demonstrate the logged data from the second bearing system failure test – further graphs illustrating the full stages are in (Appendix I).

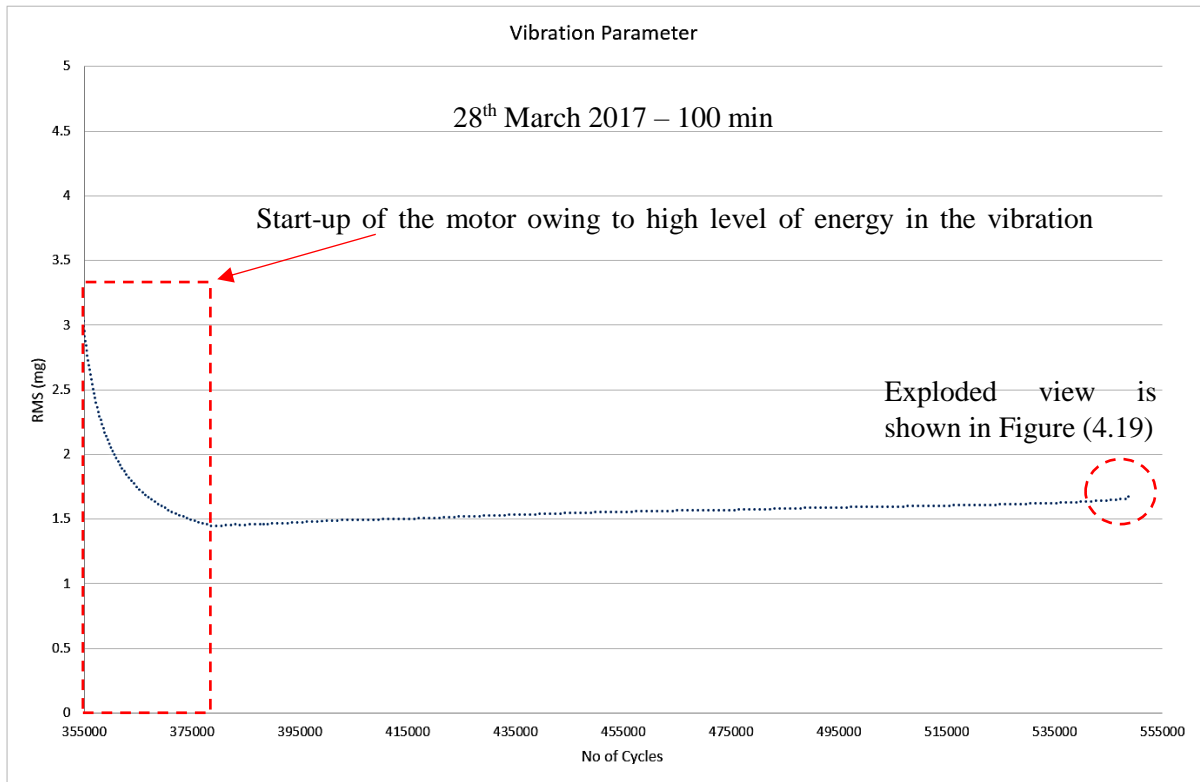


Figure 4. 18: Illustration of the RMS value during the last stage in the second test

Figure (4.18) displays the RMS value during the second test. A closer look at the logged results shows that the RMS value increased at the beginning of the run, then decreased significantly until it reached the desired value for the Test element, thus following a pattern. The bearing started running under a radial load after being constant; accordingly, high peaks are recorded/noticed at the outset. Figure (4.18) illustrates the final stage of the second test. It can be seen that the RMS approached the reference value, resulting in the system warning the user of imminent failure. The testing continued under supervision until the system was aborted manually after the shaft fractured. Figure (4.19) illustrates an exploded view of the sudden increase in the RMS value when the shaft fractured.

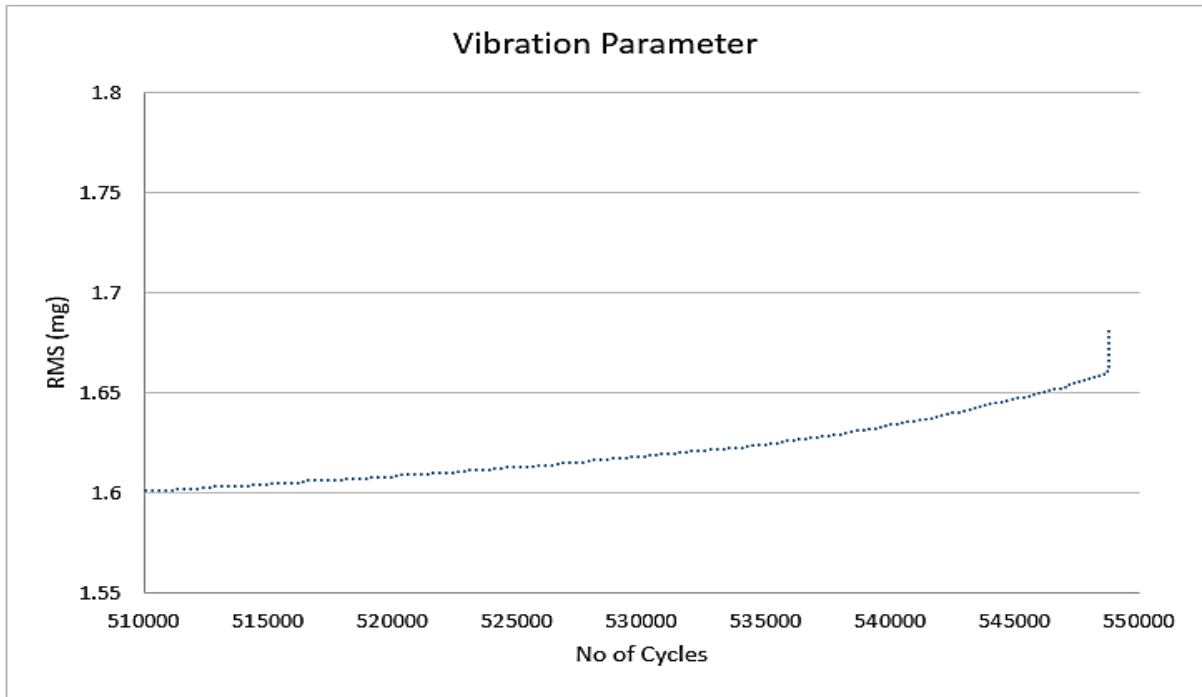


Figure 4. 19: Exploded view of circled segment in Figure (4.18)

Figure (4.19) elucidates what occurred when the shaft sheared. It can be seen that the RMS passed the reference value and increased from 1.5 to 1.68mg owing to the high energy level generated from the catastrophic situation. This can also be seen in other vibration parameters as follows.

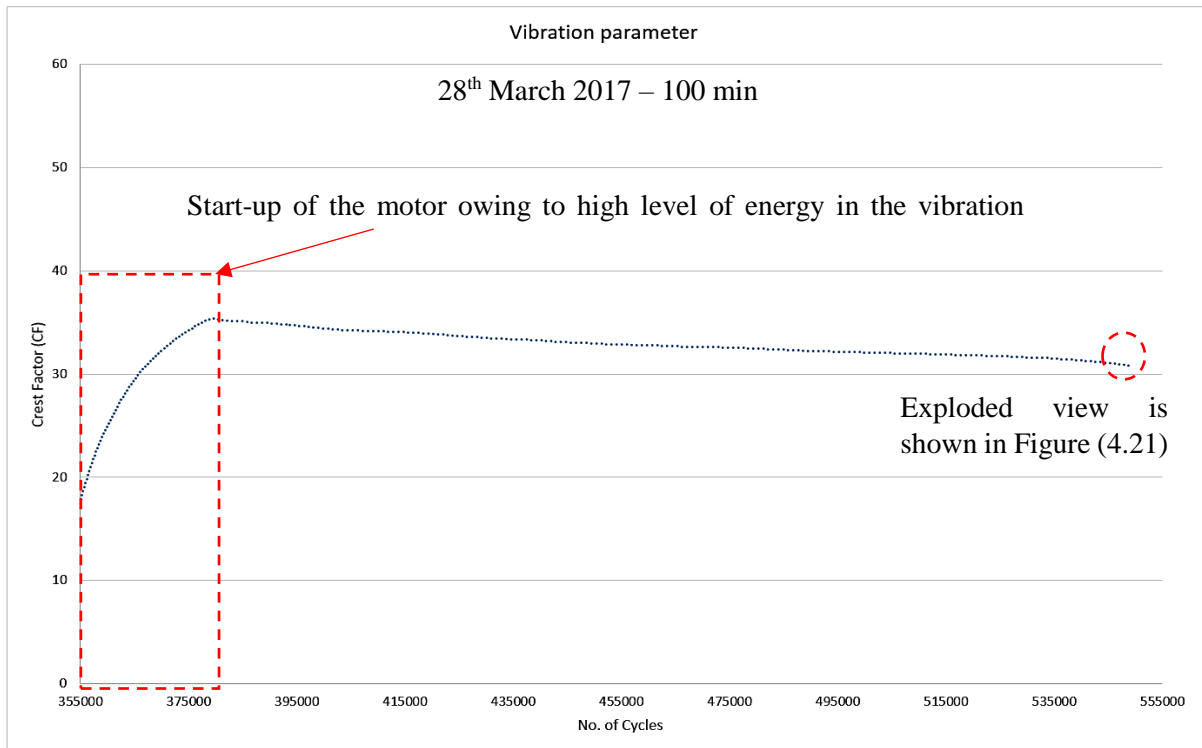


Figure 4. 20: CF value during the last stage of the second test

Figure (4.20) plots the Crest Factor (CF) value, which is defined as the positive peak over the RMS value. Due to the proportional relationship, the Crest Factor value has the opposite pattern to the RMS, decreasing as the RMS increases and vice versa. Figure (4.21) shows verification of the opposite response to the RMS. Referring to Table (4.3), the CF exceeded the initial value of the healthy operation owing to a failure about to occur; the system was deliberately left running to explore further the imminent failure. Figure (4.21) is an exploded view of the area circled in Figure (4.20).

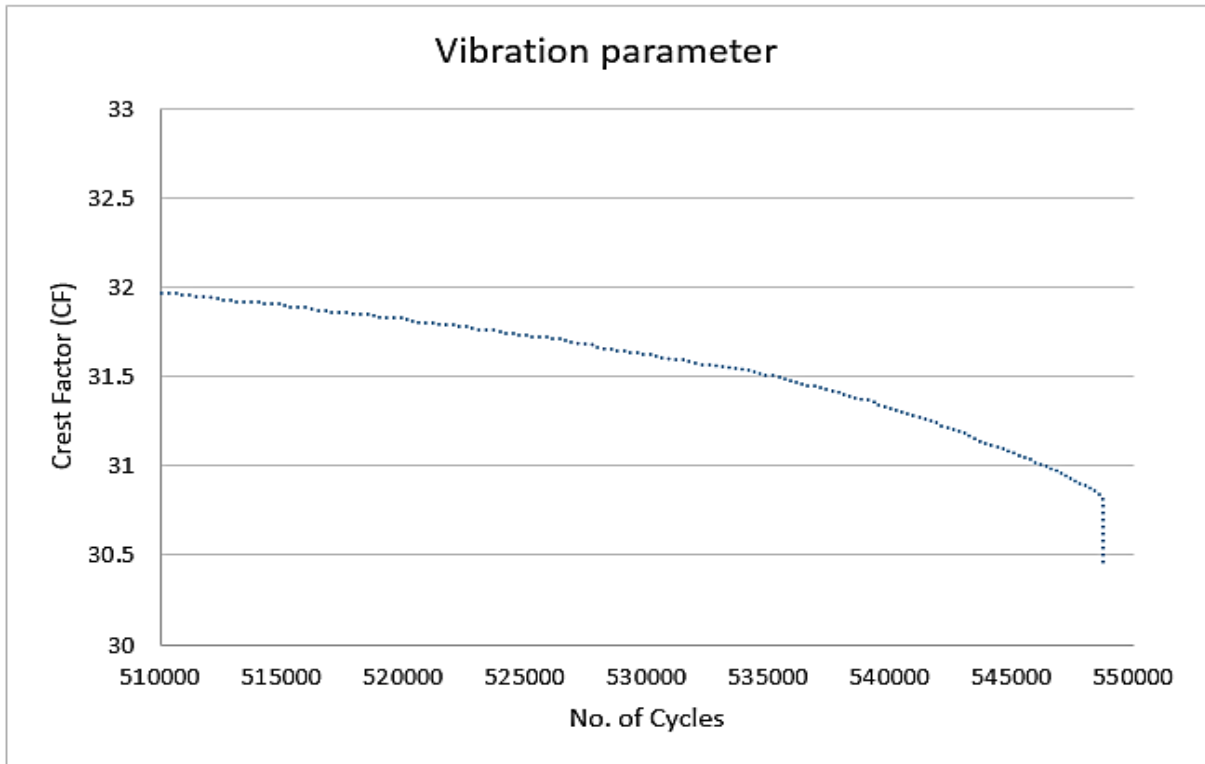


Figure 4. 21: Exploded view of the circled area in Figure (4.20)

Other vibrational parameters confirming the failure trend-line are shown as follows.

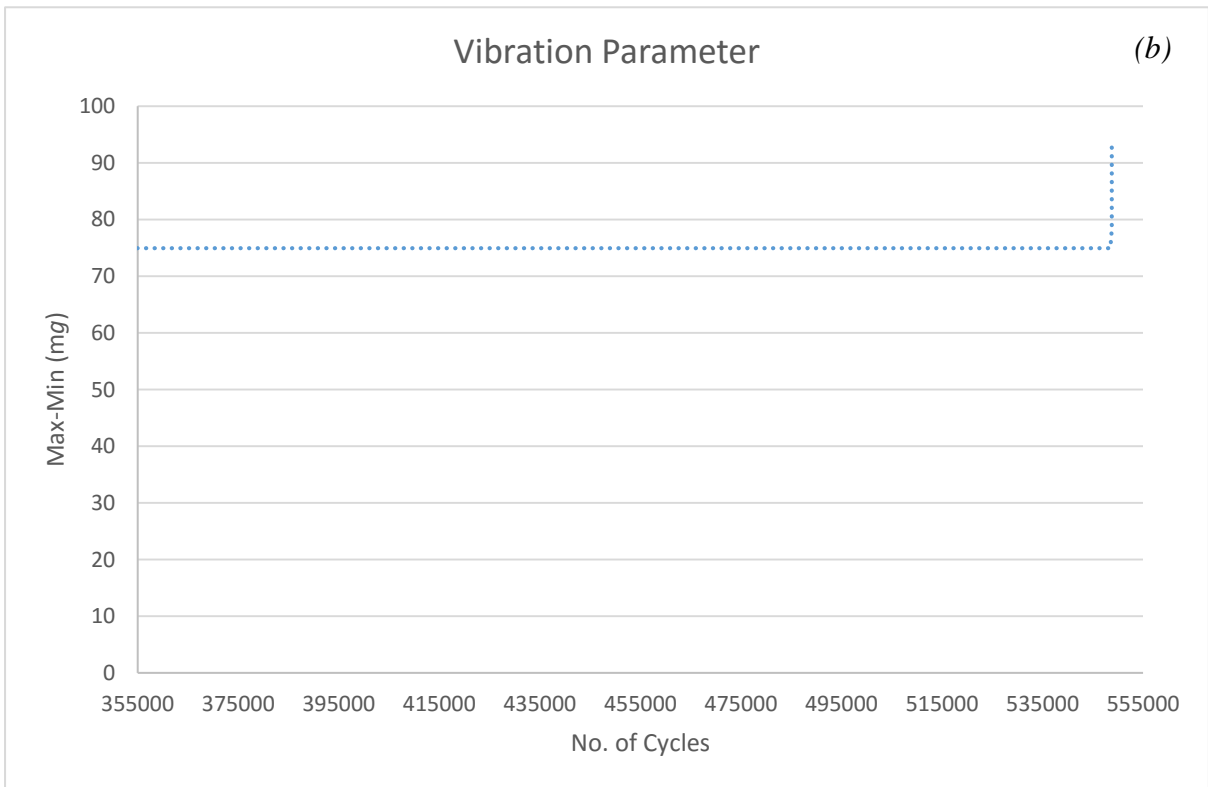
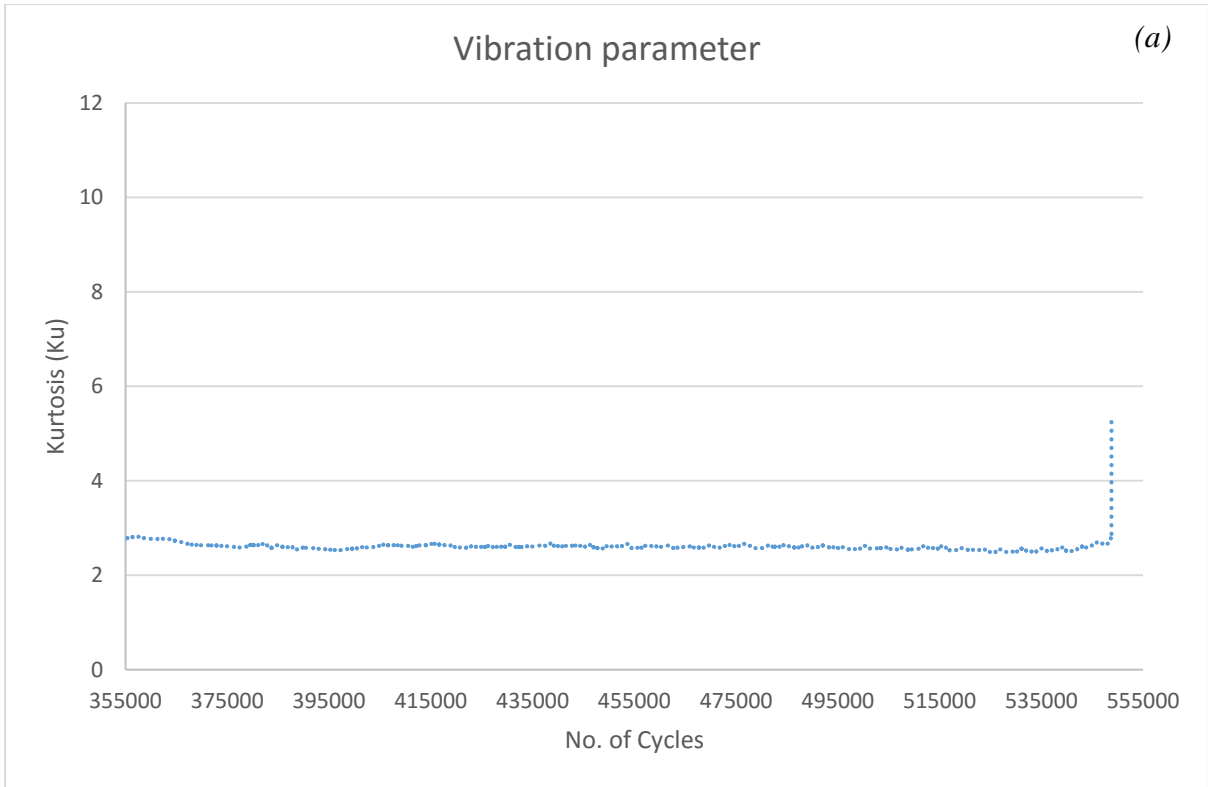


Figure 4. 22: An illustration of two vibrational parameters during the second test of bearing system failure – (a): Kurtosis value, (b) Max-Min value

Figure (4.22) shows the two vibrational parameters Max-Min and Kurtosis. From Figure (4.22–a), the Kurtosis value remained around 3 until the sudden occurrence took place, resulting in an increment in the value towards 5, representing a catastrophic failure. The graph in Figure (4.22–b) this illustrates the Max-Min value of the vibration signal. The value increased gradually until it passed the reference point; it increased sharply when the catastrophic failure occurred in the last stage.

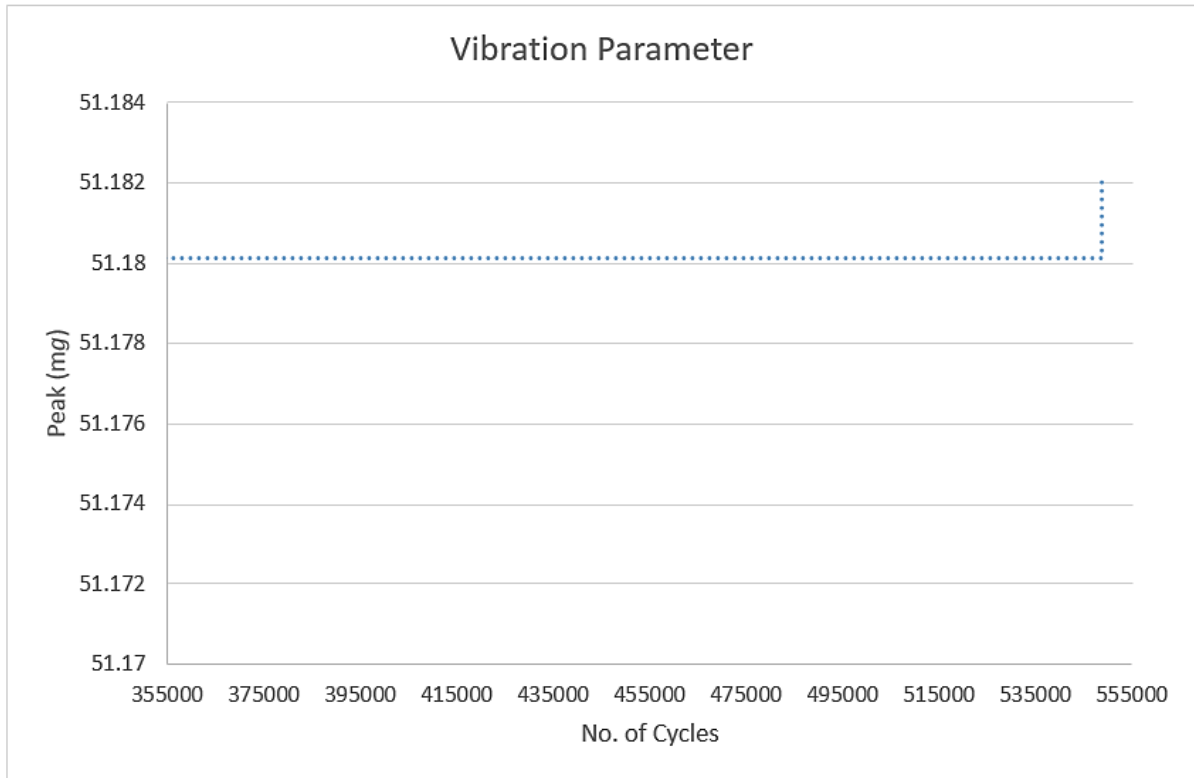


Figure 4. 23: Peak value during the last stage – sudden higher peak resulted from the catastrophic failure in the main rotary shaft

Figure (4.23) is a pictorial view of the changes in the Peak value during the last stage. The value started higher than the reference point given in Table (4.3). This predicts an abnormality, and the stage ended with a fracture failure in the main rotary shaft.

RMS, CF, Peak, Kurtosis and Max-Min were graphically represented using the time-domain technique. The following graphs illustrate two extra domains in the vibration analysis, the frequency- and time-frequency domain.

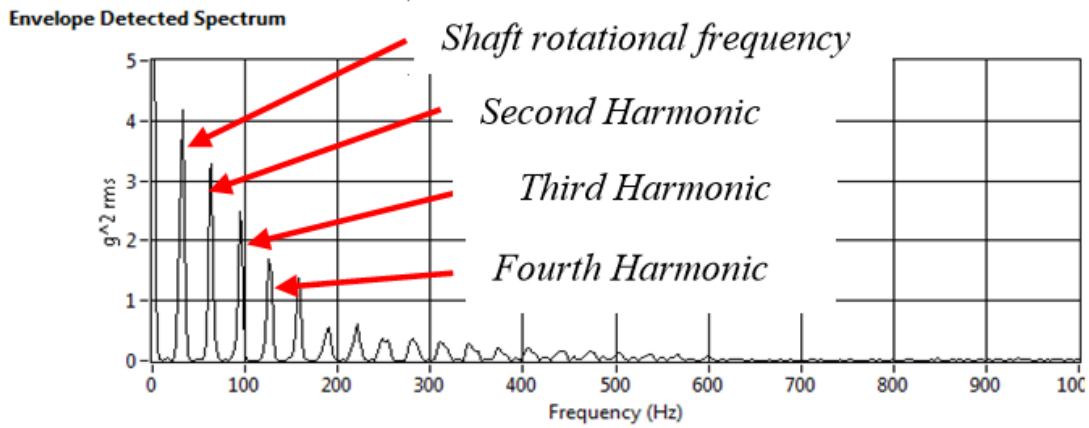


Figure 4. 24: Shaft rotational frequency using frequency domain technique

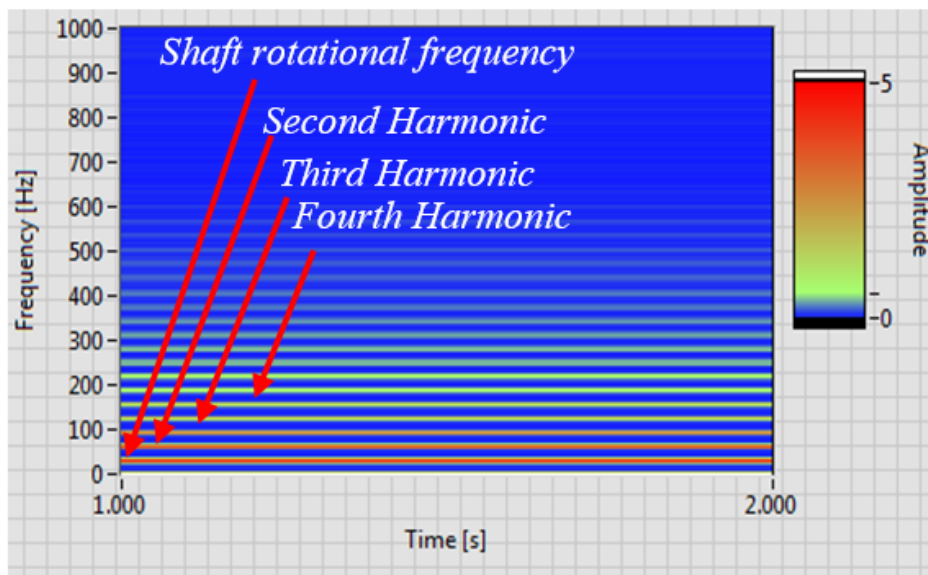


Figure 4. 25: Shaft rotational frequencies and its harmonic using Time-Frequency domain

Figures (4.24 and 4.25) show the shaft rotational frequency and its harmonic in the two different domains. Figure (4.24) represents the frequency domain, showing that the shaft rotational frequency has the highest amplitude resulting from the catastrophic failure in the main rotary shaft. Figure (4.25) confirms the trend-line that appeared in the frequency domain with respect to the time distribution.

Additional data such as temperature, torque and radial load were logged and are represented as follows.

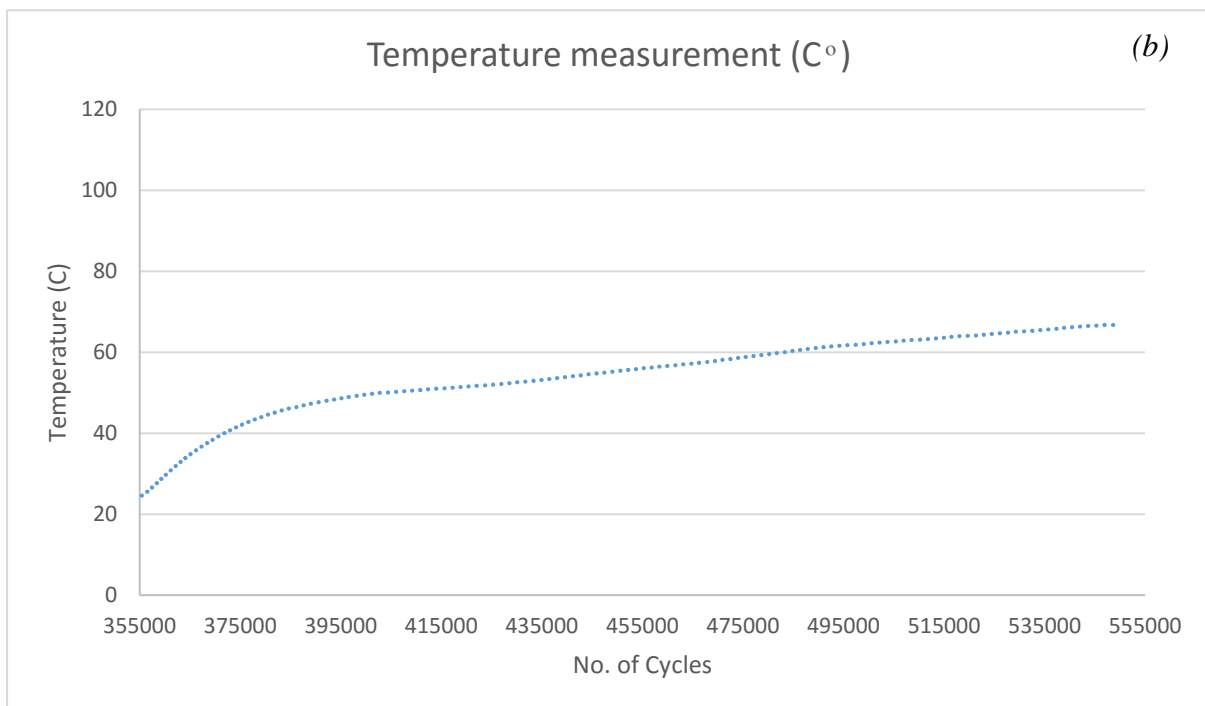
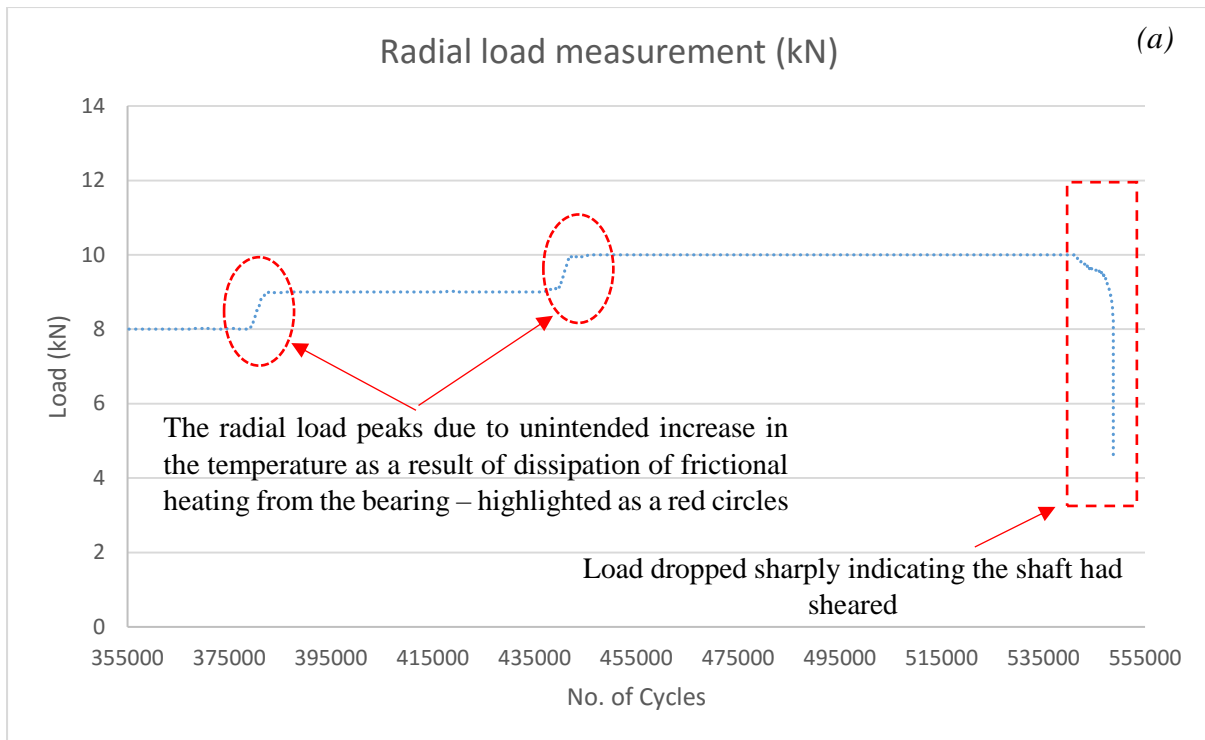


Figure 4. 26: Second test in the bearing system failure results - (a): The applied radial load (kN), (b): The acquired bearing temperature (C°).

Figure (4.26) represents the data from the pressure sensor and NTC, illustrating the applied radial load in kN scale and the bearing temperature in degrees C, from the last stage. The load changed from 8kN and 10kN and the temperature increased from 25 to 65C°. It was seen that applied load was not constant, as the requested load increased or decreased according to the situation. This was due to load being applied directly to the bearing, as the piston of the

hydraulic bench press conducted the heat from the bearing and heated the oil inside the hydraulic cylinder. This expanded the oil and air pressure inside the hydraulic press. Hence, the bearing housing was replaced with another housing that the hydraulic piston can accommodate with thermal insulation material that does not conduct the heat, as shown in Figure (4.27) below. Additionally, a cooling circulation using PC fans was proposed to keep the piston temperature down. An additional two temperature sensors were installed, one in the cabinet and the other attached to the piston to check whether the heat was being transmitted to the piston.

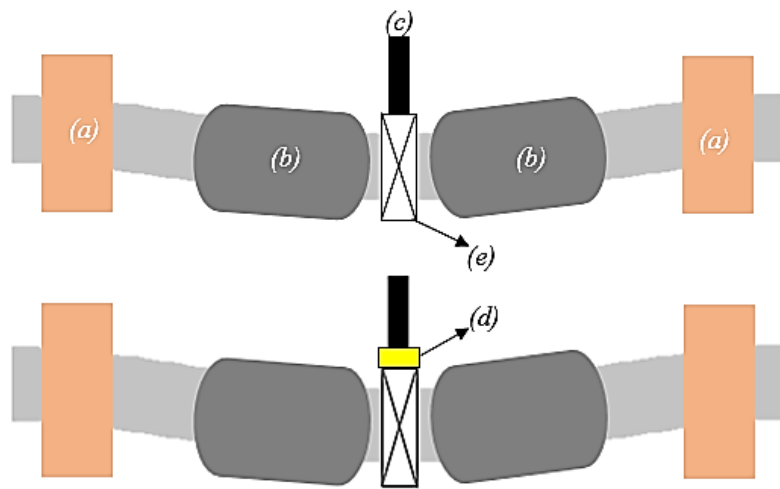


Figure 4. 27: A pictorial representation of the main rotary shaft after applying load radially – (a): Slave bearings housing, (b): Rigid couplings, (c): Hydraulic press piston, (d): Thermal insulation material, (e): Tested bearing

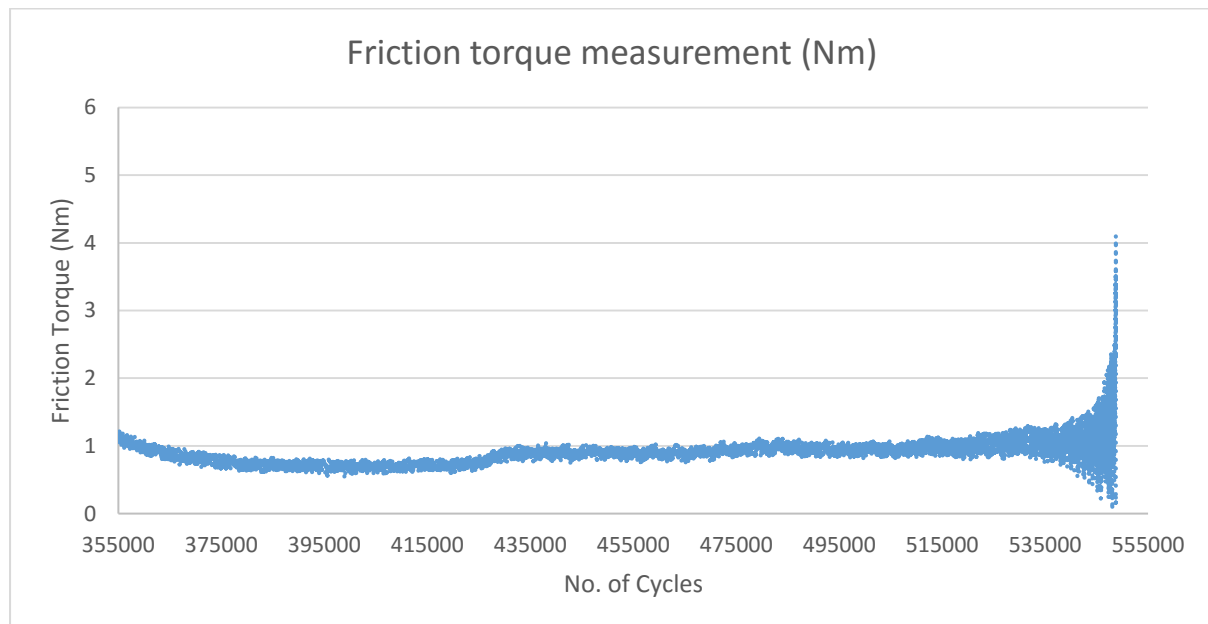


Figure 4. 28: Frictional torque during the second test in the last stage

The frictional torque followed a pattern around 0.9Nm in the early stage of testing. After that, it started fluctuating randomly, representing the initiation of cracks and followed by their

propagation in the main rotary shaft, resulting in a sharp increase in the pattern, reaching around 4Nm. Therefore, high frictional torque was seen at the end of the stage, resulting from shaft fracture Figure (4.28).

The logged vibration raw data was then used to examine the ARMA algorithm; the following figures illustrates the results.

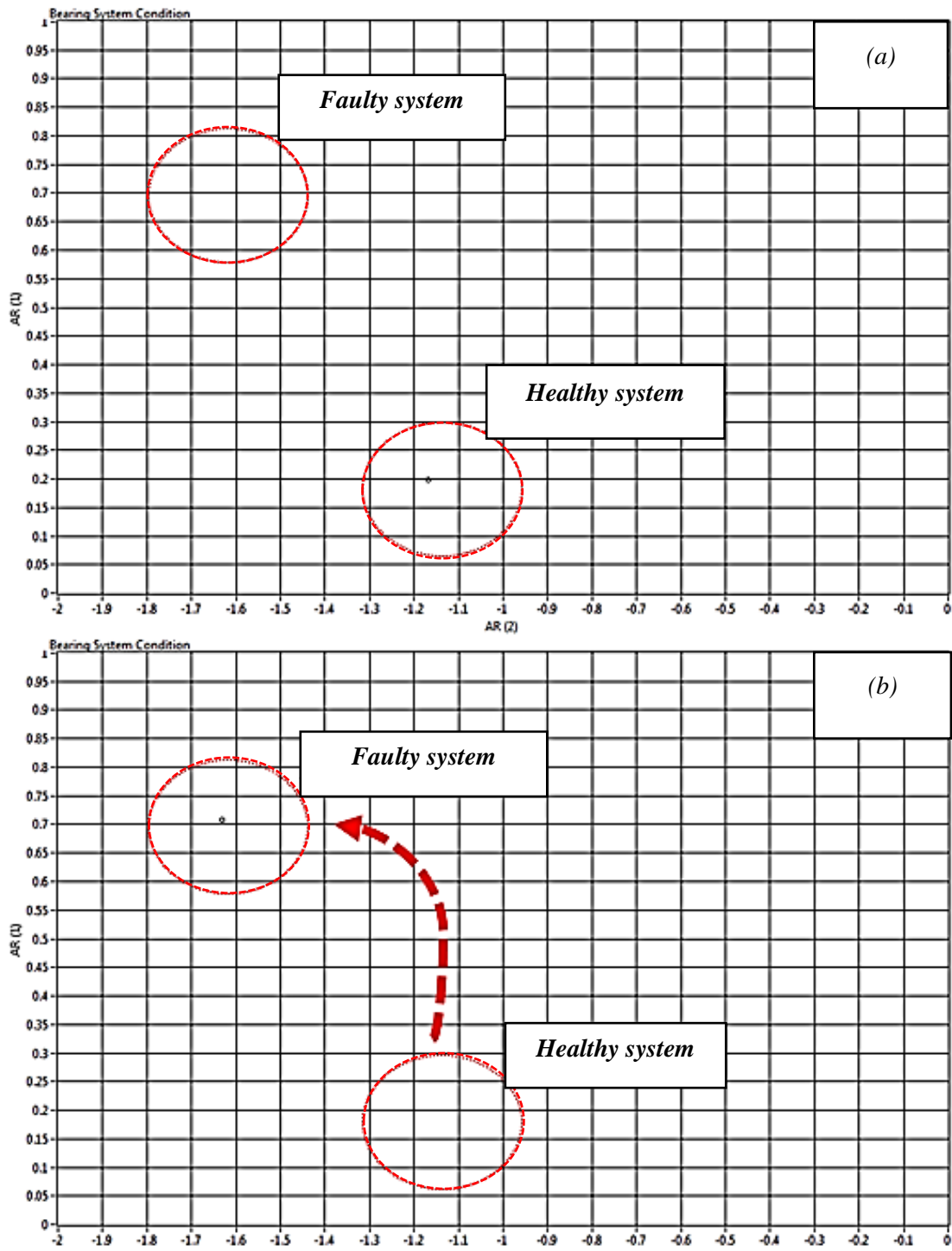


Figure 4. 29: AR Coefficients during the second test – (a) healthy system, (b) faulty system (shaft fracture)

Figure (4.29) shows an online pictorial of the AR models using the vibration data raw in the second bearing failure test. Figure (4.29 – a) illustrates healthy coefficients before the fracture had taken place. It shows the AR model coefficients at (0.2, -1.17), representing (a1, a2). Therefore, when the fracture of the shaft has occurred these coefficients rose to (0.71, -1.63) – as illustrated above in Figure (4.29 – b).

Conclusively, the developed system proved its capability of detecting the abnormality during the tests. This test illustrated the results from applying an excessive radial load on a mild-steel shaft to monitor the changes in the vibrational parameters. This test embraced an intelligent algorithm, namely ARMA. It was able to provide an online prediction of failures as illustrated previously. Therefore, it could be incorporated to perform an IHMS.

4.4.3. Third Test: Bearing System Failure; Coupling Failure

In this test, the mechanical design has been updated again so the shaft can sustain higher radial loading and for extended testing period. The development included, new main shaft with new material and shorter length, new test bearing (same type 6205-2RSH), and removal of shaft clamps. The main shaft (mild steel -carbon steel) material was replaced with a harder material, namely silver steel. The Silver steel is a higher-carbon steel supplied in the annealed condition with an average hardness of 270 Brinell. Other specifications are shown in Table (4.5). In addition, the main rotary shaft length was reduced from 100mm to 80mm, to minimise the distance between the slave bearings and reduce the possibility of fatigue in the main rotary shaft.

Table 4. 5: Comparison of mild steel and silver steel

	Mild steel (carbon steel)	Silver steel (BS1407)
Elongation (%)	15	20-35
Hardness (Brinell)	126	180-285
Modulus of Elasticity (GPa)	205	207
Density (g/cc)	7.87	7.83
Diameter (mm)	25	25.4

The silver steel shaft was machined using Computer Numerical Control (CNC) to bring the tolerance down from interference to transition fit, as this provides a better fitting for the bearing. The Slave bearing shafts were also replaced with the same material (silver steel) to provide smoother operation, as this gives a better fit and overcomes any axial movements

without using any additional support (e.g. circlips, spacers). In addition, the mechanical design update included, new test bearing (of the same type 6205-2RSH).

This failure test was carried out at the same speed and under the same excessive load with the aim of monitoring failures in the couplings. Therefore, it was rotated for around 7.5×10^6 cycles, representing 61 operational hours, before the rigid coupling sheared, as illustrated in Figure (4.30). At this point the system was aborted due to fatigue propagated in the weakest point in the rigid coupling, as depicted below.



Figure 4. 30: Illustration of the fractured couplings – (i) is an exploded fractography view of the red-circled area. It can be seen that the crack is propagated/initiated at the weakest point in the coupling surface resulting in a fatigued element.

The graph in Figure (4.31) plot the data logged throughout the third sample.

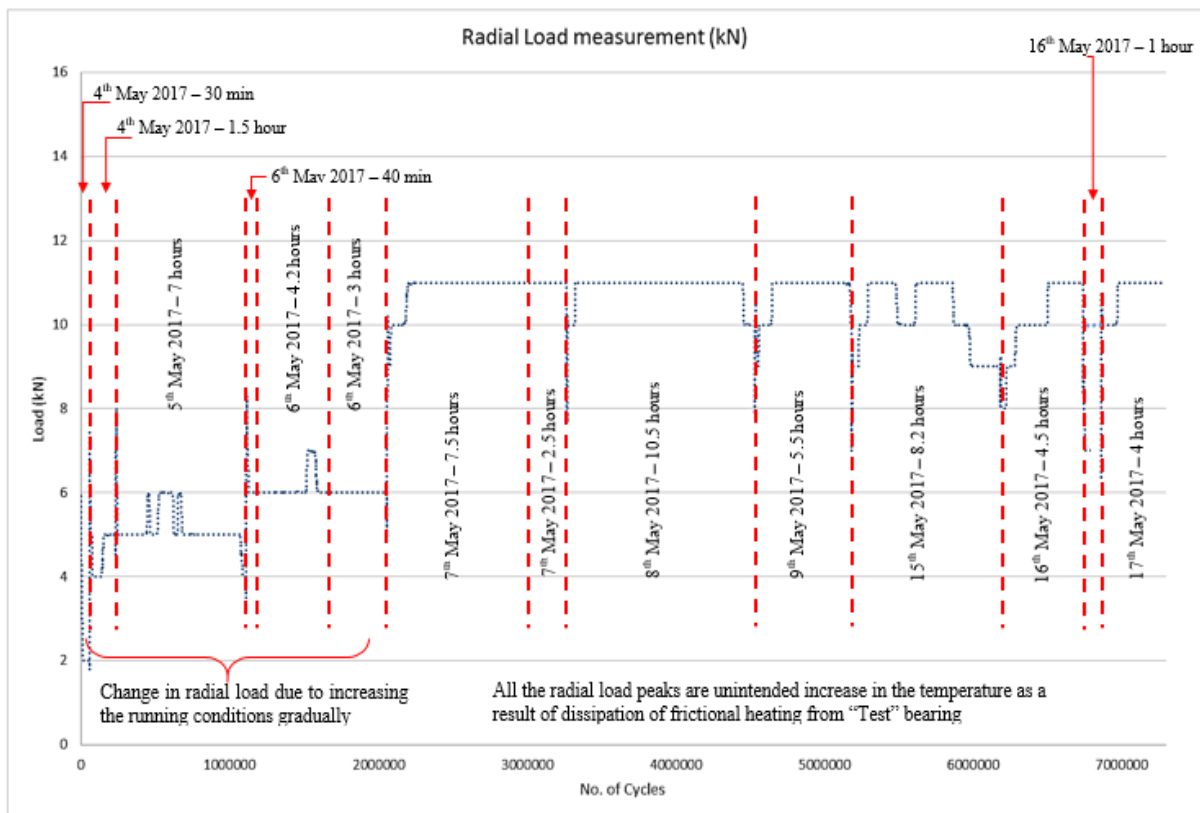


Figure 4. 31: Third test results - radial load (kN)

Figure (4.31) shows the applied radial load during the bearing system failure, the third test. Thus:

- At first, during the run-in period (4th – 6th May 2017) the test was operating at 4kN increasing gradually to 7kN. Then the radial load was increased to the required load (10kN). The temperature is represented by a specific trend-line from 22°C at the outset to around 47°C at the end of each stage, confirming a typical NTC response-time trend-line.
- From 7th – 17th May the applied radial load was 10kN. At the outset of each stage, the load was 10kN but over time it was found that the load increased to 11kN.

This was not intended and occurred because heat generate din the bearing and motor system caused expansion of the hydraulic fluid in the loading bench cylinder leading to an increased in the load of the test bearing. Therefore, the temperature was recorded through these stages as an increment from 22°C to 60°C, confirming a typical time response trend-line for the NTC sensor. On 8th May, the temperature increased slightly towards 71°C, due to high friction while fatigue was propagating in the weakest point in the coupling.

Due to the mechanical system update, it is expected that the baseline signature of the vibration signal will be different from the first two tests, which has been taken into account.

The Vibration parameters were applied in this test involving the time, frequency and time-frequency domains. The time domain parameters were RMS, Max-Min value, Peaks, Kurtosis (Ku) and CF, as shown in the following figures.

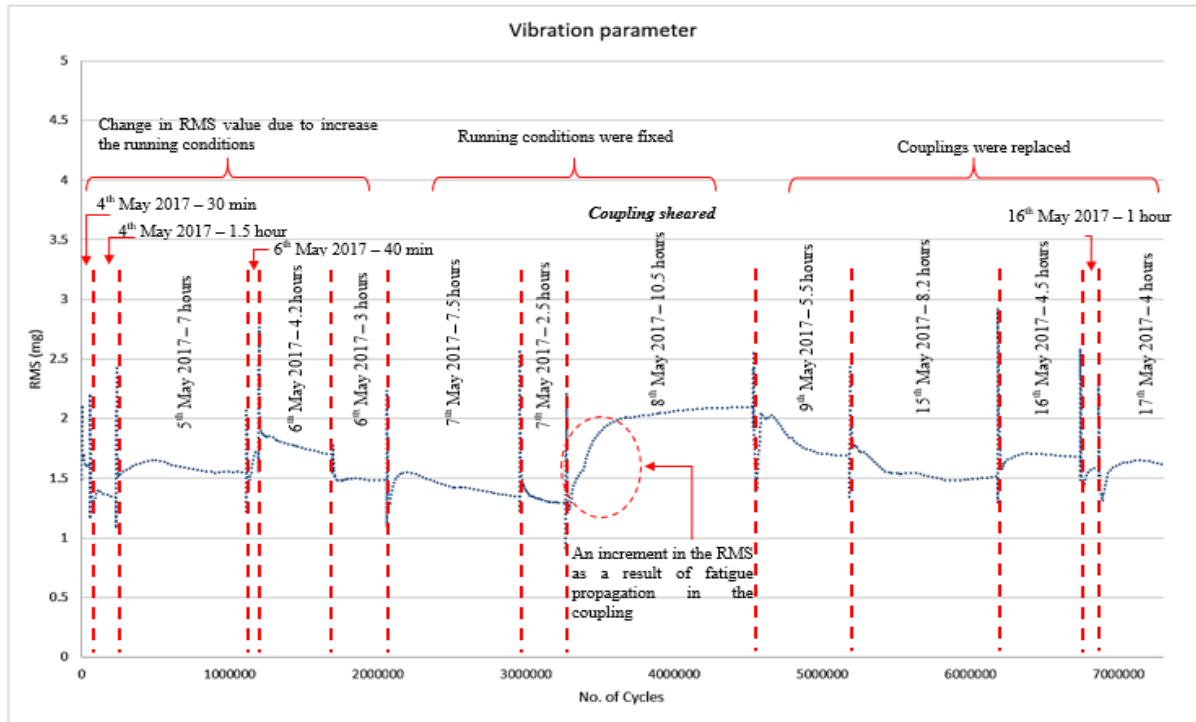


Figure 4.32: illustration of the RMS value of the third sample in the bearing system failure test

Figure (4.32) indicates one of the main parameters in the time-domain technique, namely RMS. During the running period, the RMS value increased at the beginning of each round indicating a high level of energy in the vibration signal, then decreased until it reached the required value, thus following a trend-line. Of all the stages, the maximum RMS of 2.2mg was achieved on 8th May after the bearing had undergone 37.5 hours, and was an indication of fatigue propagation in the couplings as they sheared at the end of the stage. The next stage experienced new couplings and the pattern went back to normal around 1.5mg. The system was alerted and prediction of failure was noted, after which the test was under supervision until it was manually aborted when the coupling sheared.

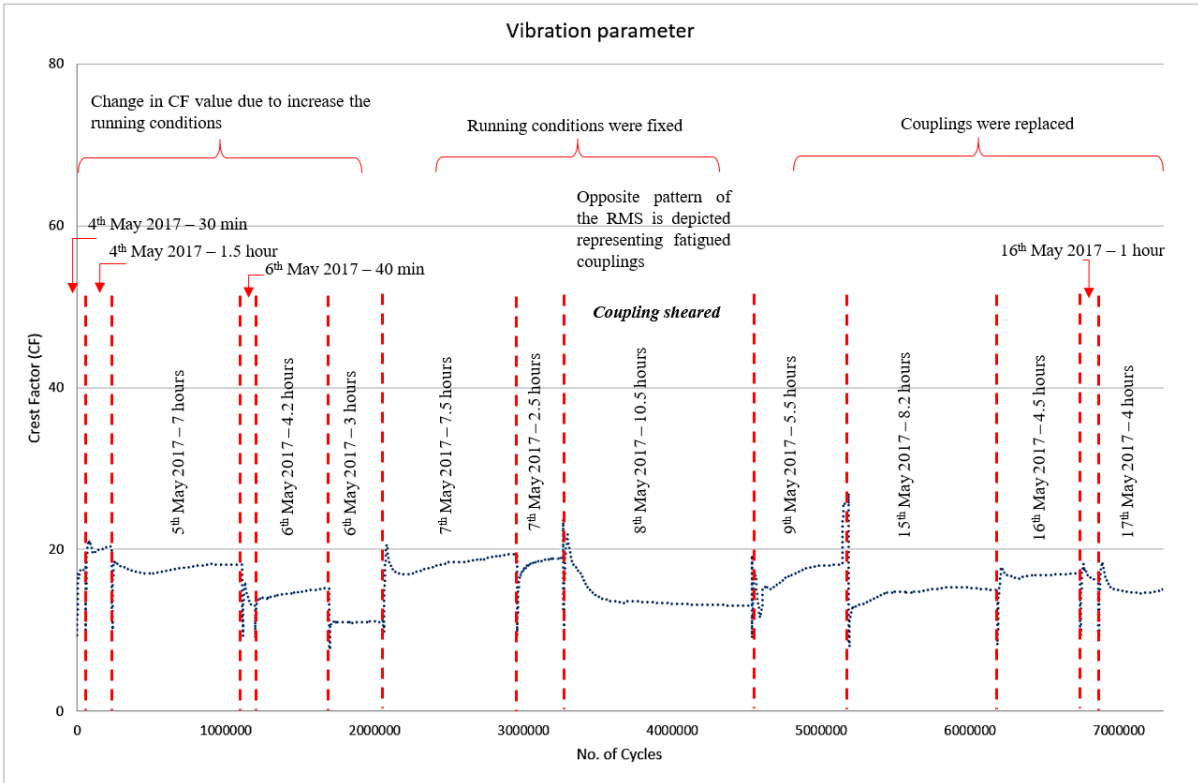


Figure 4. 33: Illustration of the CF value during the third test in the bearing system failure test

Prior to the proportional relation between the CF and RMS values, the pattern of the CF is shown in Figure (4.33). The highest peaks were logged at the outset of each round and followed by a pattern of decreasing or increasing values based on the RMS values. Thus, during the running period, the highest CF value was 20 in the first round at 10kN (7th May). It then started decreasing, to 18 and then 15. On 8th May the pattern decreased as the fatigue failure had occurred in the coupling, reaching 10. The coupling was replaced and the pattern of the CF returned to normal.

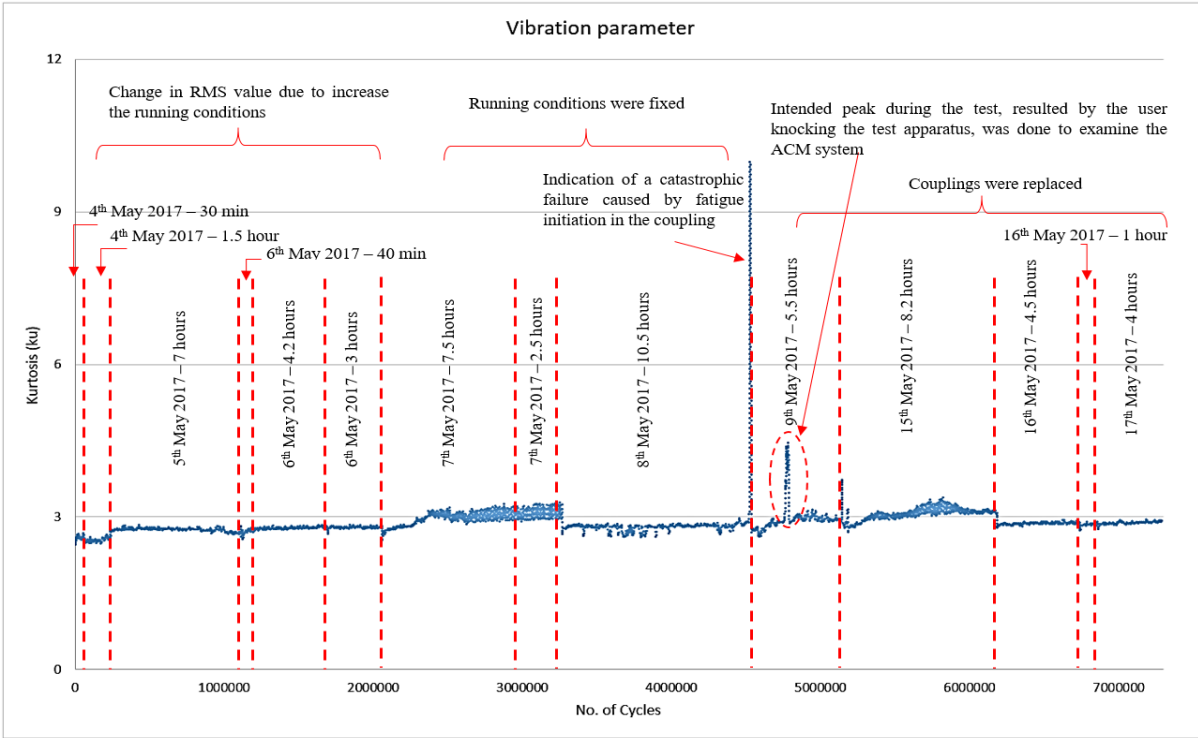


Figure 4. 34: Kurtosis (Ku) value

Figure (4.34) represents the Kurtosis value showing the measure of “Peakedness” of the time series signal (TSS). Typically, it fluctuated around 3 until the coupling sheared, when it rose to almost 10. During the test on 9th May, the user knocked the protection sheets of the test bench to examine the Active Condition Monitoring system, showing the high peak.

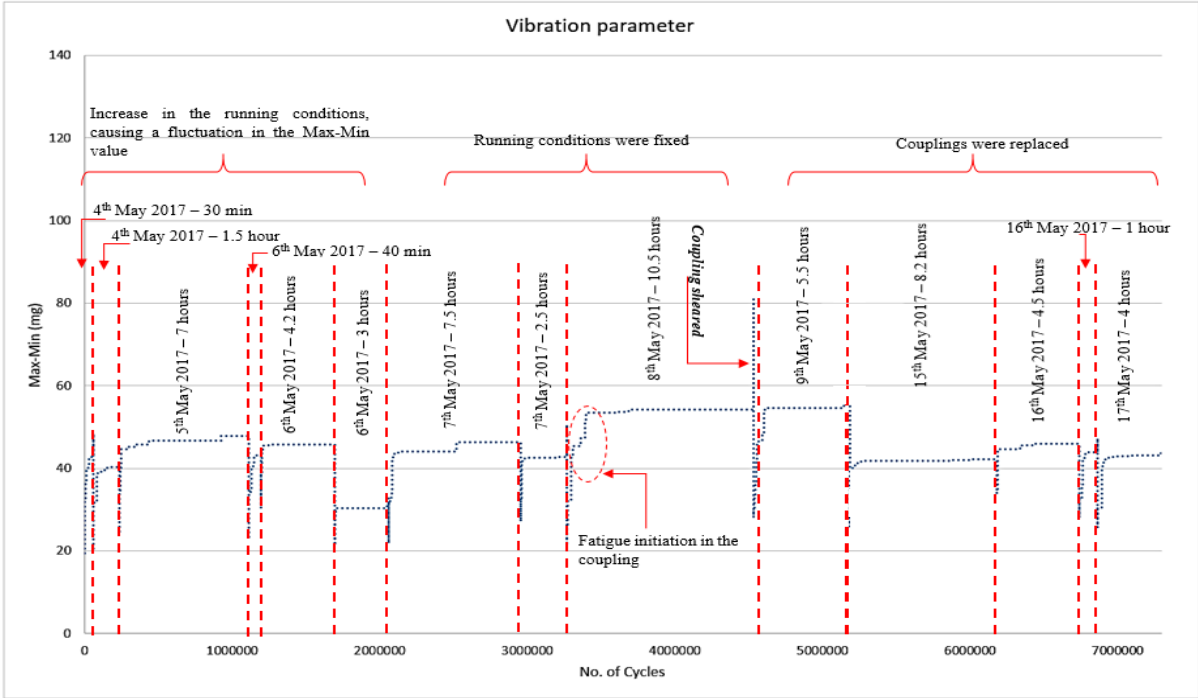


Figure 4. 35: Max-Min during the bearing system failure test – Third test

Figure (4.35) illustrates the Max-Min values of the third sample, showing the value increased gradually until it reached 88mg (4th to 8th May). This indicates that the running bearing system experienced failure as the Max-Min value passed the reference point (Table 4.3). This stage concluded with a fracture in the coupling, as cracks spread over its weakest point.

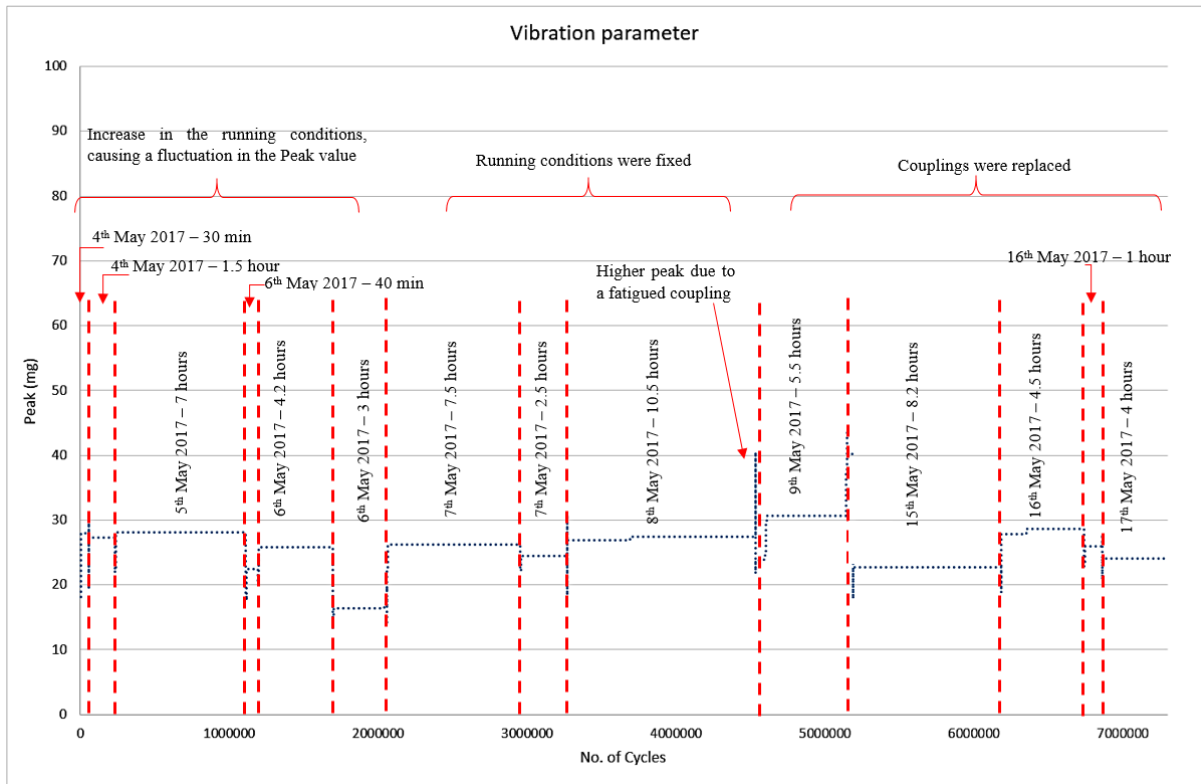


Figure 4.36: Peak value

Figure (4.36) plots the peak values of the vibration signal during this test. At the outset, the peak value increased significantly due to the high energy when the bearing system started to operate, reaching 28.6mg during the running period. On 8th May the peak value increased from 26.6 to 27.4mg, then passed the reference point and reached 41mg after the coupling sheared. In the next round, the couplings were replaced and the peak value decreased slightly, holding a pattern below the reference point in all the remaining stages.

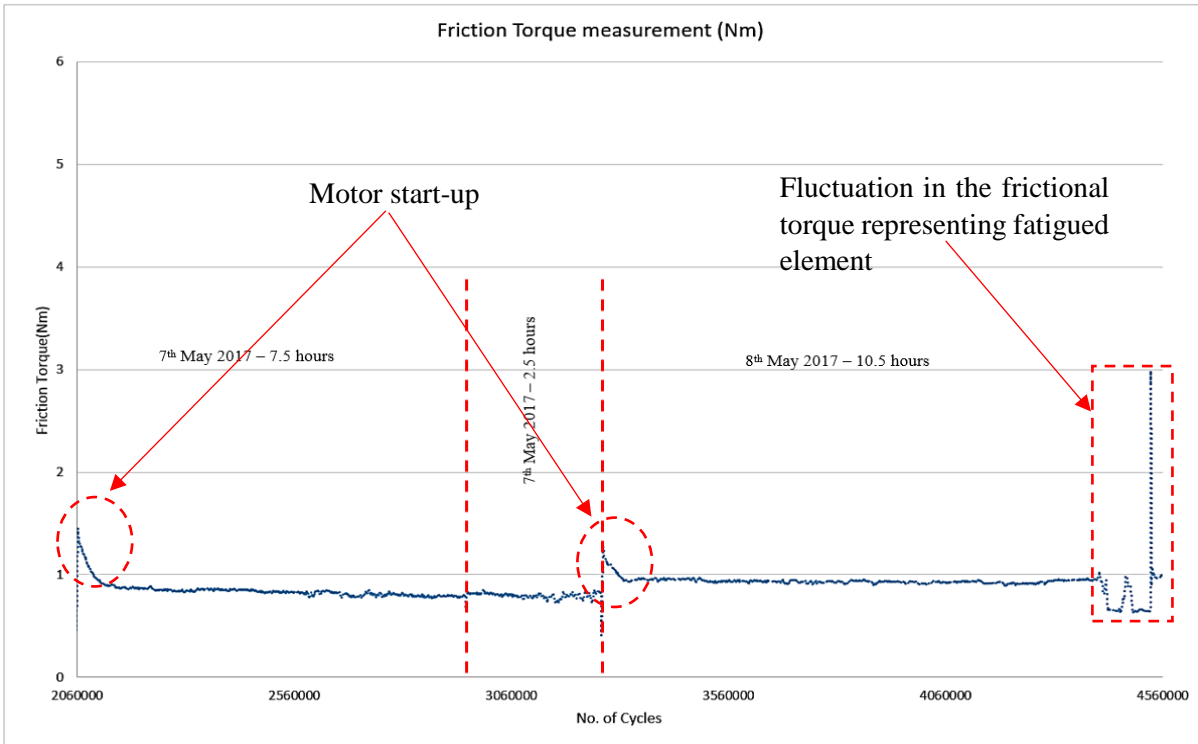


Figure 4. 37: Friction bearing torque (Nm)

The frictional torque during this test had a pattern between 0.7Nm and 0.9Nm when the testing conditions were fixed. This confirms that a fatigued element was involved in the testing as the running conditions were fixed. It then increased sharply to reach 3Nm when the coupling had sheared, as depicted in Figure (4.37).

All the above data illustrates different parameters using the time-domain approach, all of which were able to detect failure in the coupling during the bearing system failure test. Temperature, load and torque measurements were also made throughout this test. The following results confirm the failure detection system using two other domains, frequency and time-frequency, followed by implementing the AMRA algorithm to detect abnormality and predict failure.

Using the equations presented earlier, the bearing elements' frequencies were calculated as shown in Table (4.6) and illustrated in Figure (4.38).

Table 4. 6: Bearing elements' frequencies and their harmonic frequencies

	Shaft frequency	Outer race	Inner race	Ball	Cage
Bearing elements frequencies (Hz)	33.3	123.22	176.78	78.26	13.7
Second harmonic (Hz)	66.6	246.44	353.56	156.52	27.4
Third harmonic (Hz)	99.9	369.66	530.34	234.78	41.1

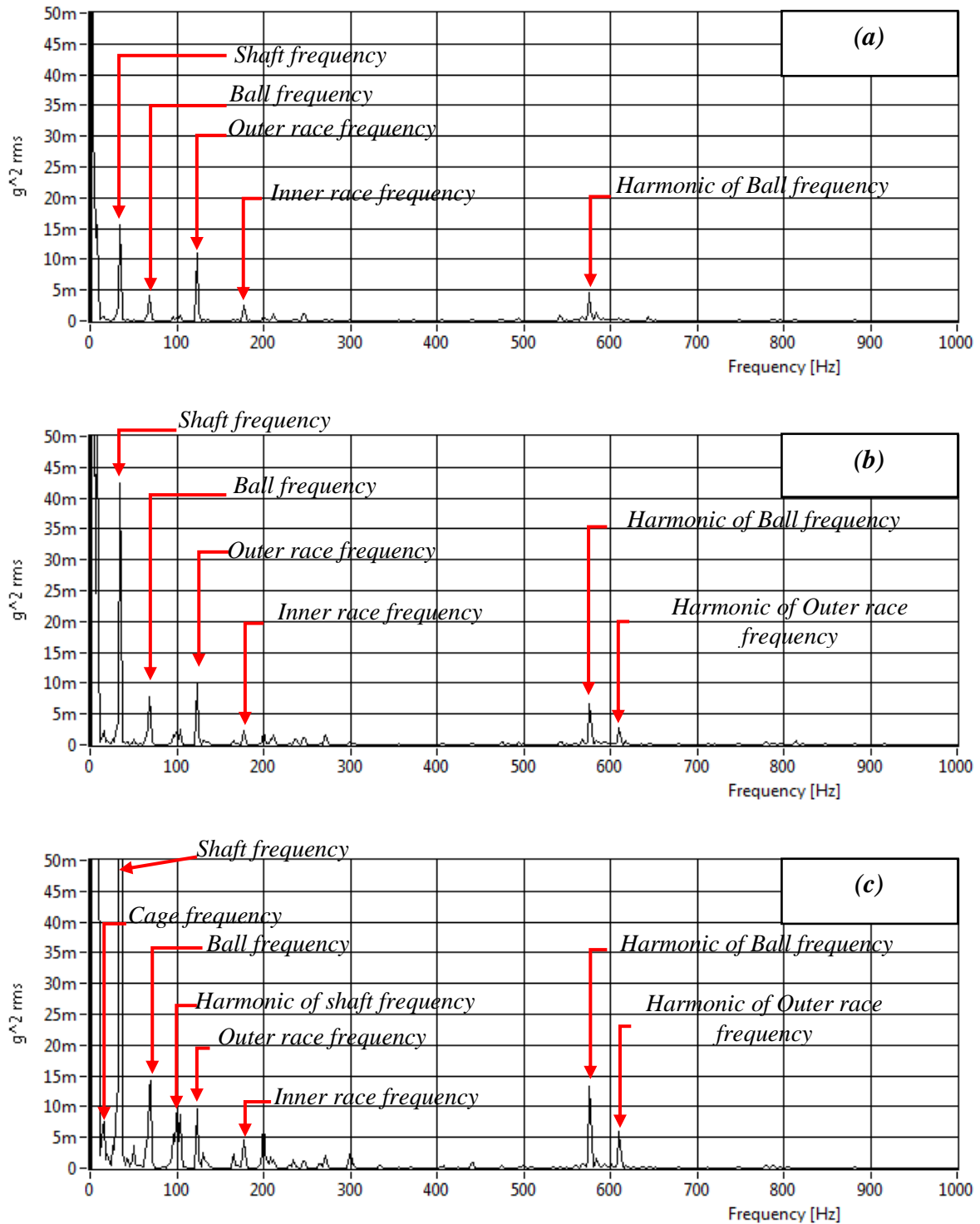


Figure 4. 38: Evolution of the developing defects in the “test” bearing elements using the frequency domain technique – (a) after 9 hours, (b) after 27 hours and (c) after 61 hours.

Figure (4.38 – a, b and c) indicates that the above frequencies shifted slightly when the load was applied. Rising peaks indicate that the “Test” bearing is fatiguing. Figure (4.38 – a) shows that after 9 operational hours, the frequency of each element in the bearing was rising. Consequently, these peaks were highlighted, based on (Table 4.6). After 27 hours, some of the

frequencies increased, representing high noise generated from the failure in the bearing, with some harmonics. Finally, after 61 hours an obvious change was seen in the bearing (Figure 4.38 – c). Figure (4.39) highlights and supports the results from the frequency domain using the time-frequency approach.

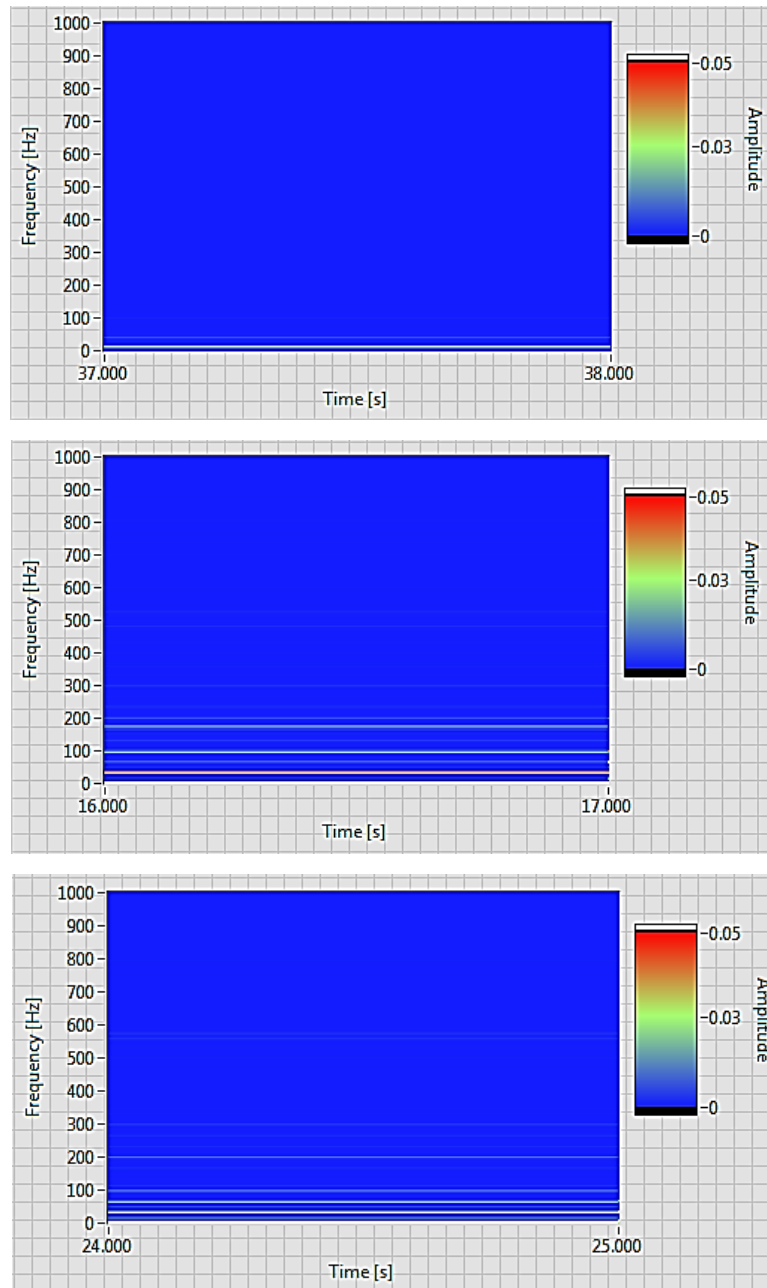


Figure 4. 39: Time-frequency domain results

The following results illustrate the changes in the ARMA coefficient, represented in Figure (4.40).

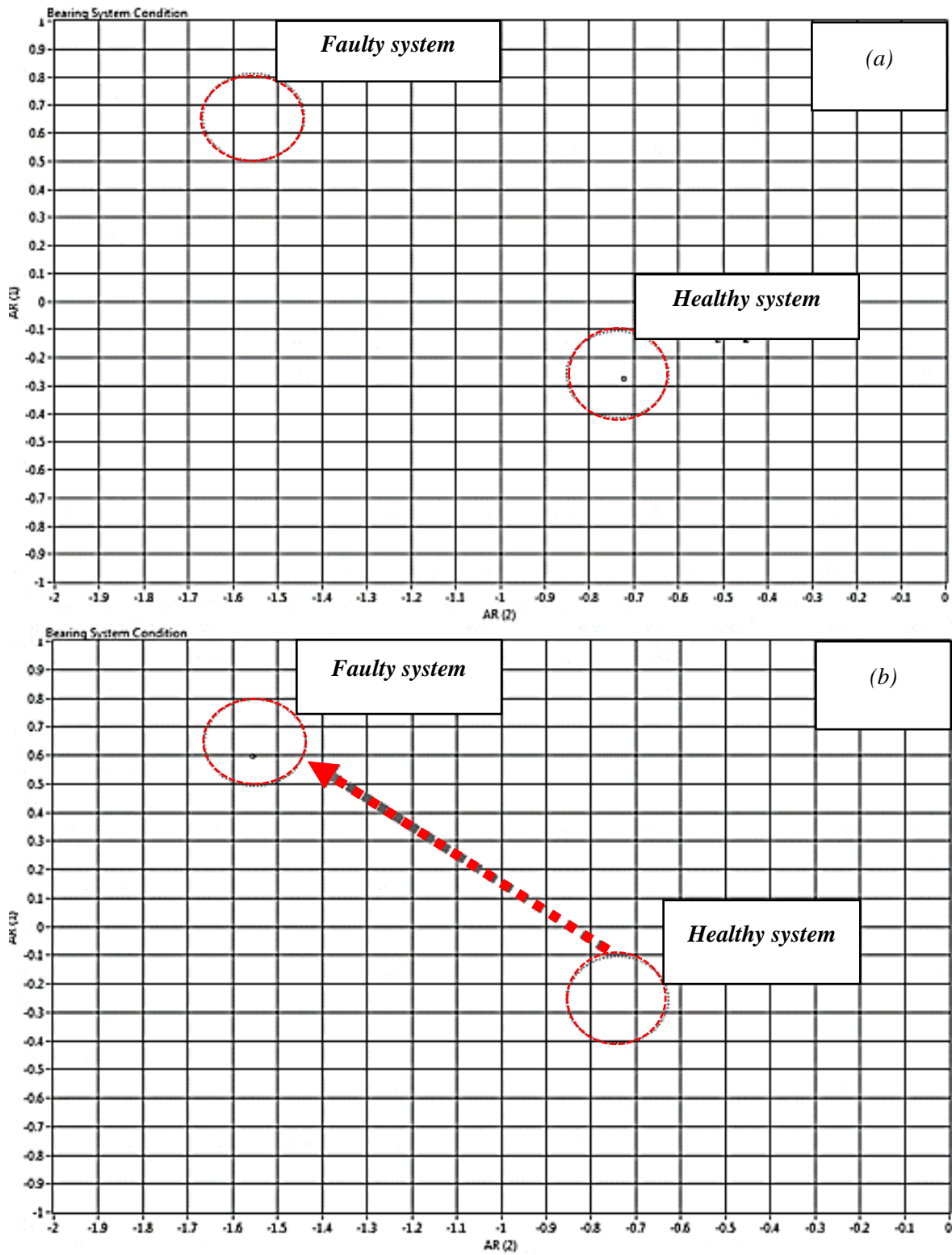


Figure 4. 40: AR Coefficients before and after the failure occur in the coupling – (a) healthy system, (b) faulty system (coupling fracture)

Figure (4.40) represents the online AR models using the vibration data raw in the third bearing failure test – coupling failure. Figure (4.40 – a) provides healthy coefficients before the fatigue has initiated / propagated. Therefore, in Figure (4.40 – b), it can be noticed that the coefficients moved from a healthy region to indicate an abnormal occurrence – from (-0.29, 0.73) to (-1.55, 0.6) representing failure had occurred.

4.4.4. Fourth Test: Bearing Life Test

This test illustrates monitoring the vibrational parameters during the bearing’s life. It therefore used 2000rpm and 6kN instead of 10kN to avoid heavy-duty operation on the test element, as this causes initiation / propagation of failure by fatigue, as illustrated in the bearing system failure tests. Therefore, using the 6205-2RSH bearing under the specified conditions, the theoretical bearing life would be approximately 125 operational hours with 90% reliability, using the ISO281 equation. The following figure plots the logged data – furthermore, (Appendix J) illustrates all the stages during the test.

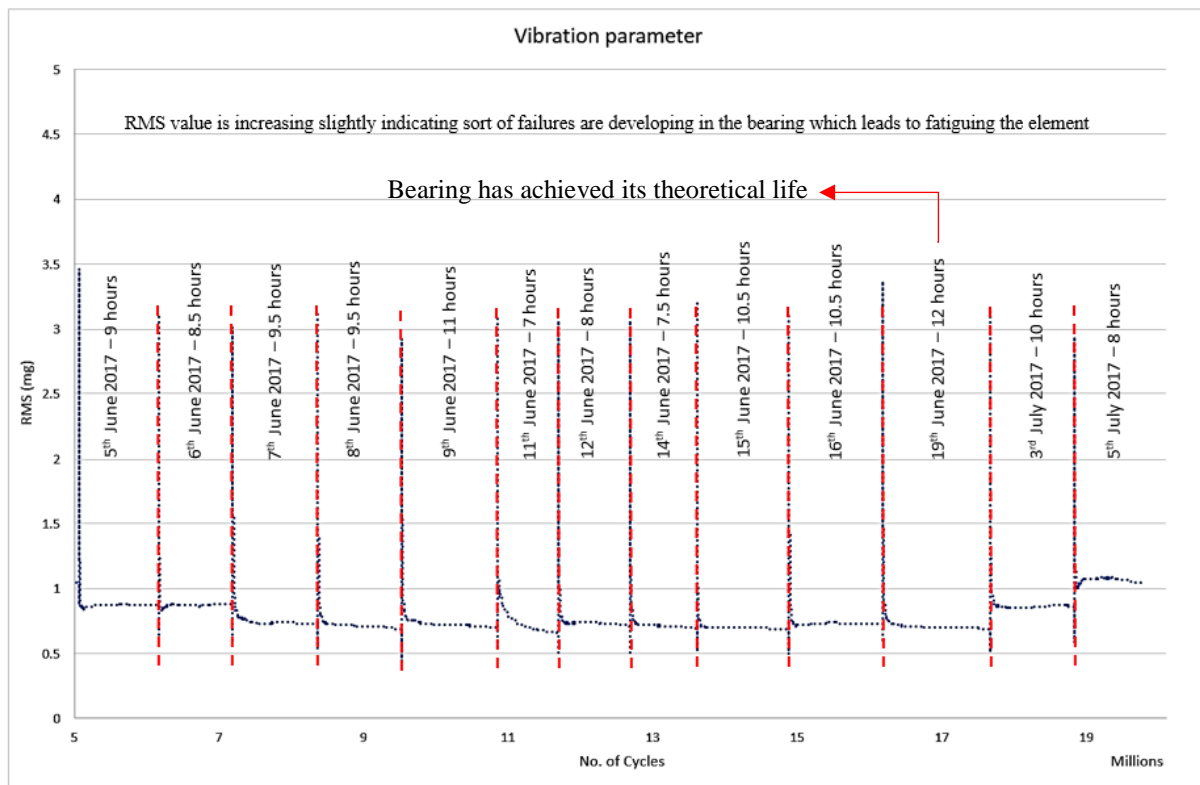


Figure 4. 41: RMS value during the Bearing life test

Figure (4.41) shows that the RMS level started at around 0.8mg during the test, after achieving 41 out of 125 hours. It decreased slightly, towards 0.7mg, on 7th, 8th, 9th and 11th June. After that, it returned to increase slightly during the stages from 12th June to 5th July (from 0.7 to

1.1mg) – after 19×10^6 cycles (162 operational hours). This confirms the development of some failures in the bearing elements. It also proves that the bearing was fatiguing causing the high level of energy in the vibrational parameters. Other parameters followed the same pattern, and can be shown as follows.

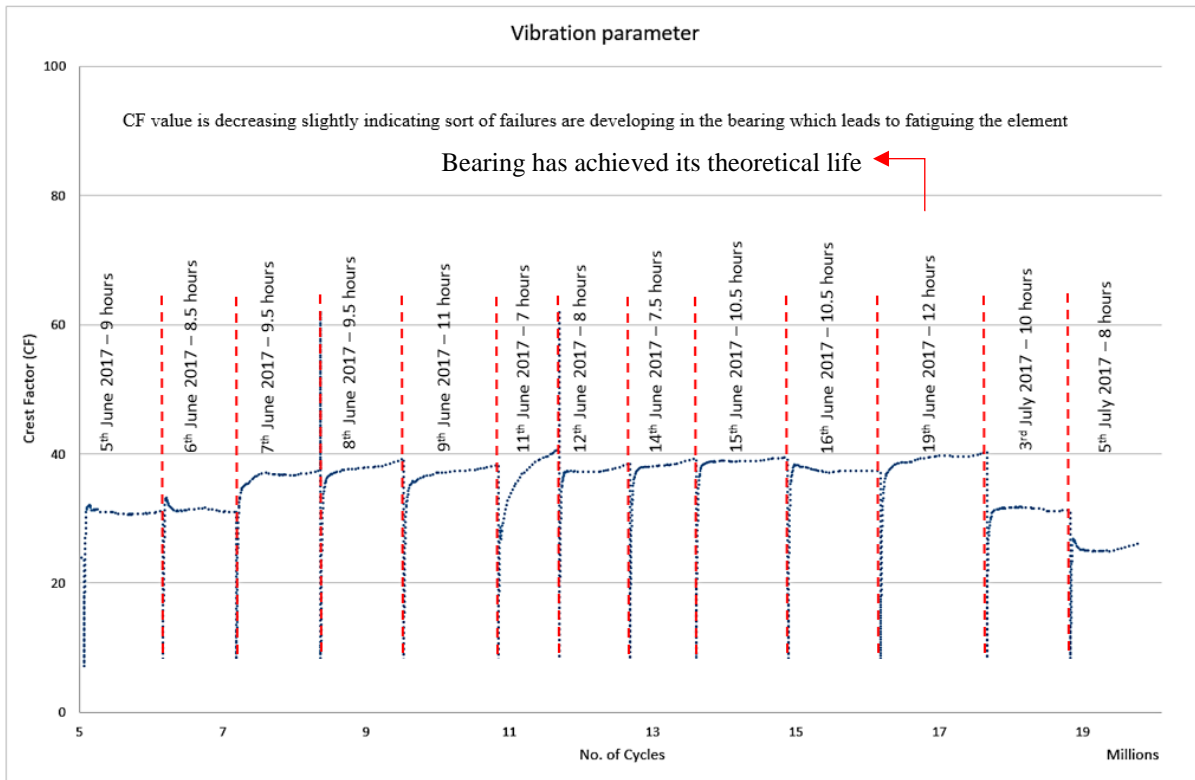


Figure 4. 42: CF level during the bearing life test

Figure (4.42) shows the effect of the CF during the bearing-life test. It increased towards 40, followed by a decrease in the value after achieving its theoretical life. This clarifies that the bearing elements were experiencing developing defects. Therefore, the pattern decreased slightly to pass the reference point during the last two stages.

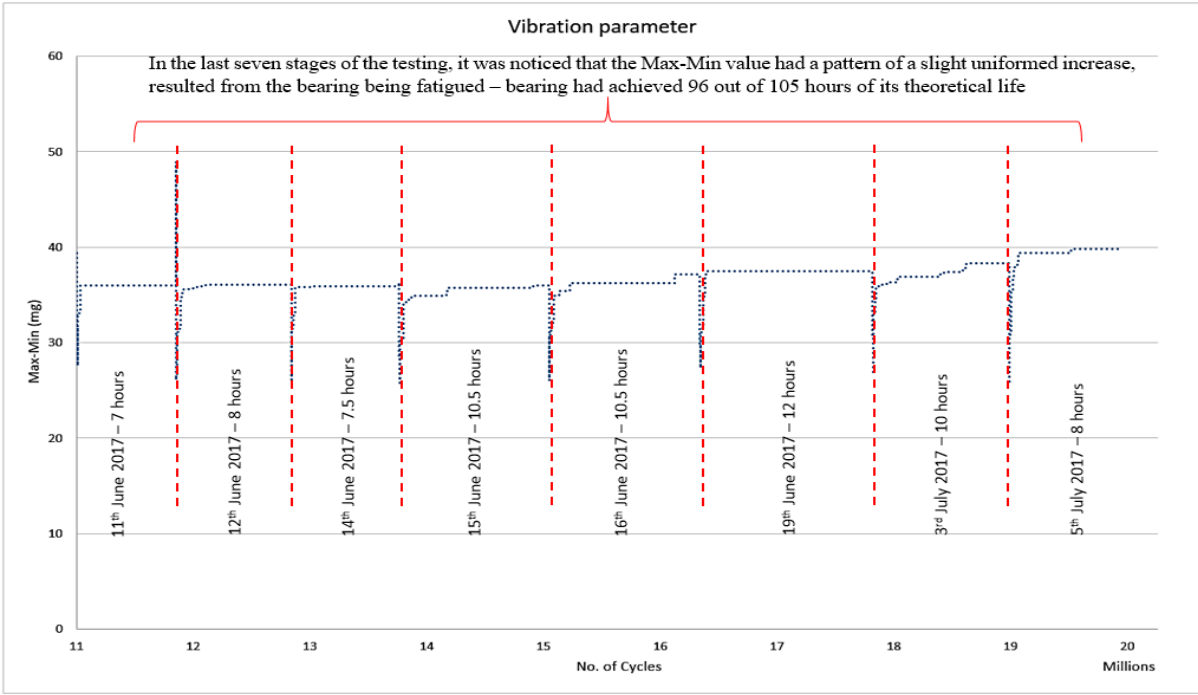


Figure 4. 43: The Max-Min value during the bearing life test

The Max-Min values also passed the reference point given in Table (4.3), after the bearing had achieved its theoretical life. It had a pattern of slight uniform increase which represents that the bearing is becoming fatigued. It started increasing gradually from 35mg on 11th of June to reach 40mg in 5th July – after achieving 162 hours.

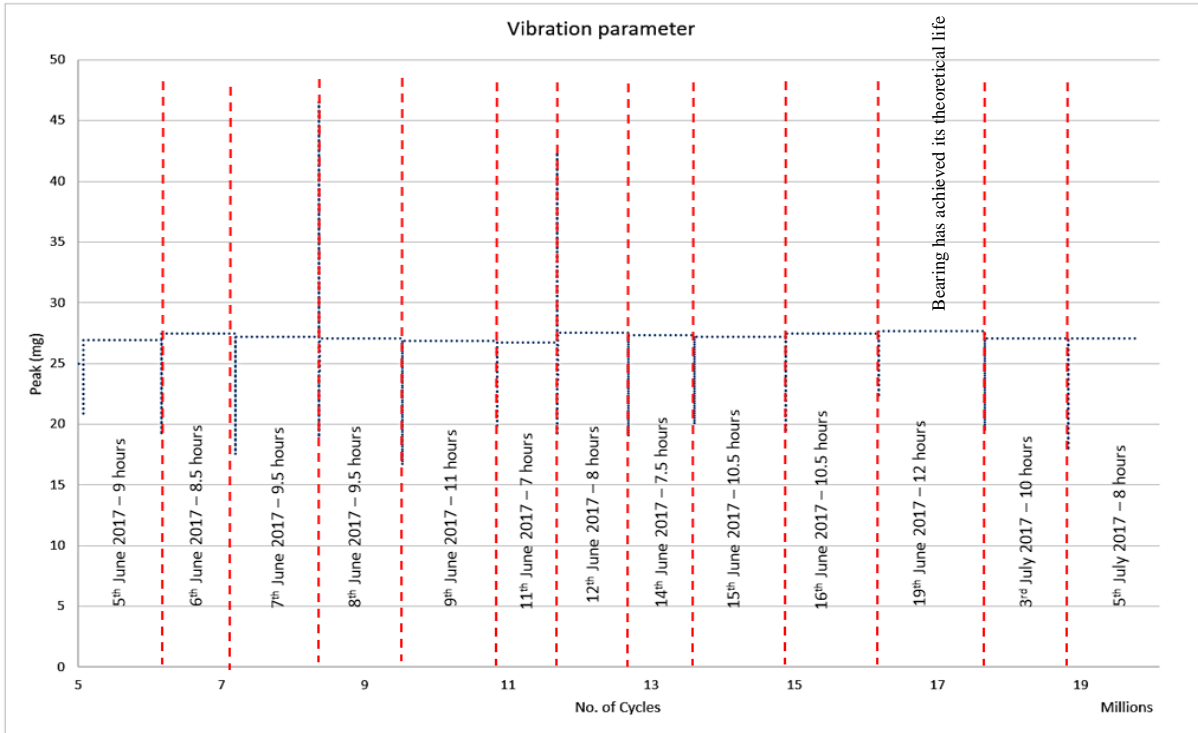


Figure 4. 44: Peak pattern during the bearing life test

During the last 13 stages, the bearing was achieving high peak values, representing a fluctuation around 27mg, passing the reference point. This confirmed that the bearing was experiencing developing defects in its element, which contributed to shortening the life of the component. The Kurtosis value during the bearing life testing remained around 3 showing the “Peakendness” value of the time series signal (TSS).

Lastly, the above data shows RMS, CF, Max-Min and Peak values and their changes during the bearing life test, representing the time-domain technique in the vibration analysis. The following graphs illustrate the evolution of the bearing elements’ defects using frequency domain and time-frequency domain techniques.

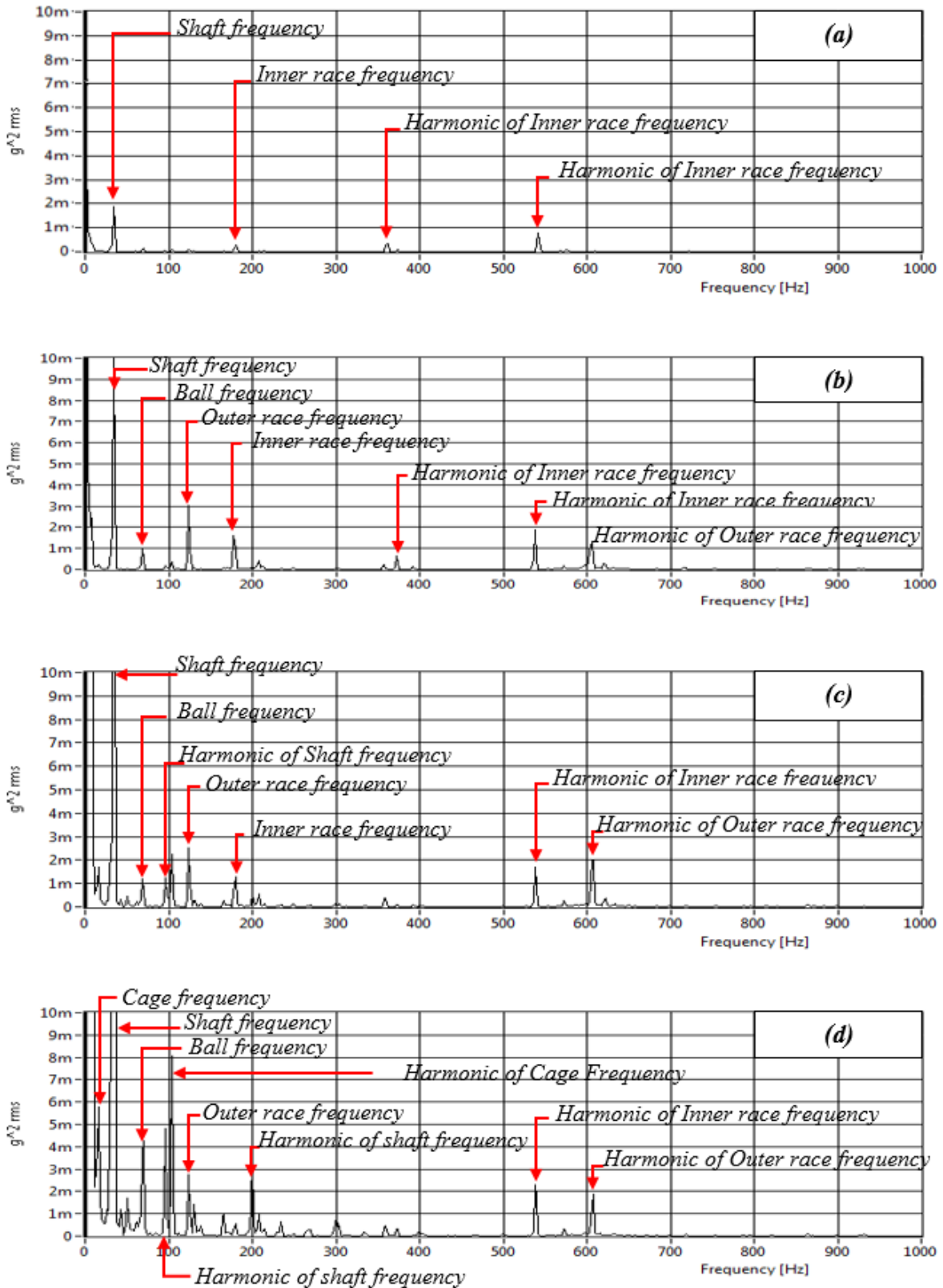


Figure 4. 45: Highlights the evolution of the bearing elements defects using frequency-domain philosophy – (a): after 30 operational hours, (b): after 78 hours, (c): after 122 hours and (d): after 162 hours.

Figure (4.45 – a, b, c and d) illustrates the development of several defects in the bearing elements. After 30 hours, peaks in the inner race frequency were noticed, as shown in Figure

(4.45 – a). After 78 hours a few extra peaks appeared including in the outer race and ball frequency (Figure 4.45 – b). Thereafter, graph (c) shows the peaks rising in amplitude after the bearing had achieved its theoretical life. Finally, after 162 hours, significant noise in the bearing elements was noticed, represented in Figure (4.45 – d). The following figures demonstrate the time-frequency results.

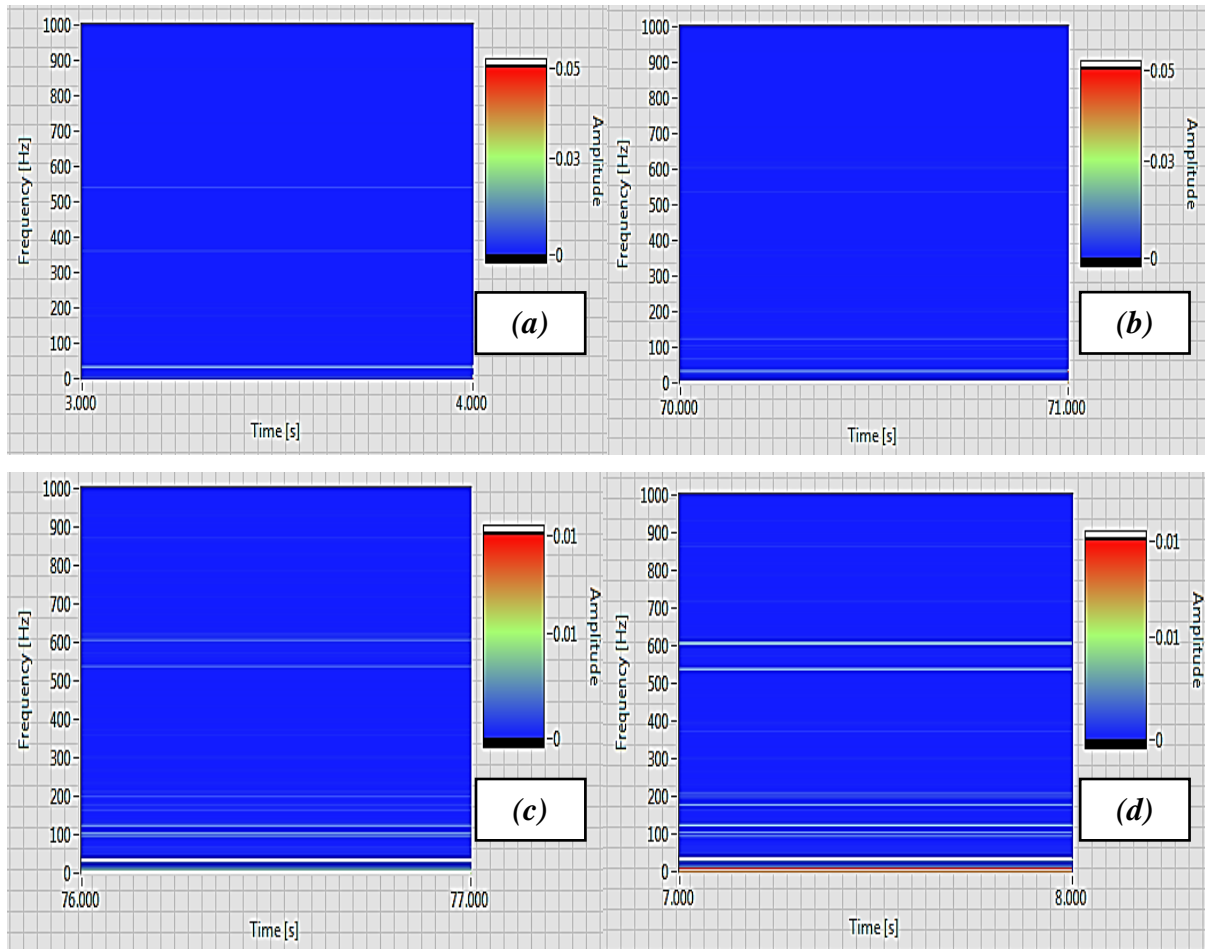


Figure 4. 46: Representation of the time-frequency domain results during the bearing life test (fourth sample) – (a): after 30 hours, (b): after 78 hours, (c): after 122 hours and (d): after 162 hours. These figures support the results from the frequency domain.

Additionally, torque measurements were carried out during this test, represented as follows:

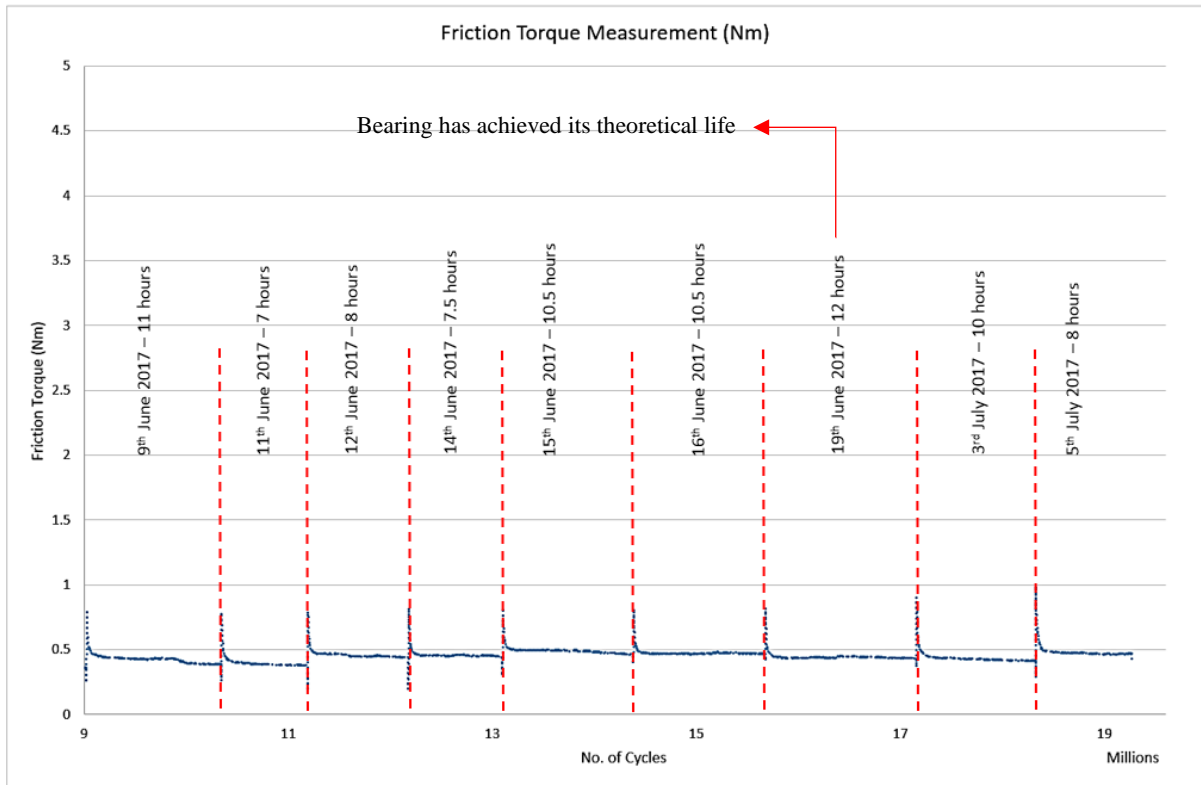


Figure 4. 47: Frictional Torque during the bearing life test

During the bearing life test, the bearing achieved 0.4Nm at the applied radial load. This pattern increased slightly towards 0.5Nm indicating that the bearing elements were fatiguing.

In order to confirm the above results, the bearing was dismantled into parts, including the inner race, outer race, balls and cage, and was inspected under two microscopes: Omniscan MicroXam 5000B 3d ADE Phase and Axiovert 40 MAT in the JOST Institute for Tribotechnology at the University of Central Lancashire. Figures (4.48–4.52) illustrate the surfaces of the bearing.

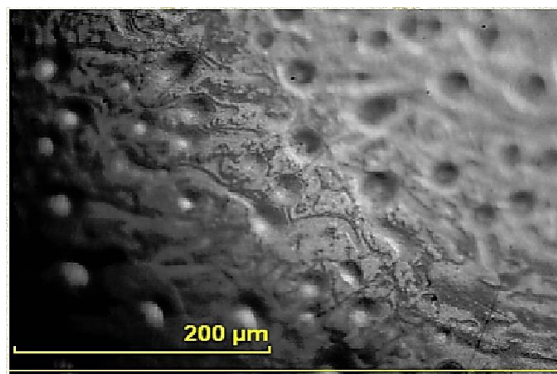


Figure 4. 48: Ball surface presents few failure modes, namely pitting. It is an indication to bearing fatigue as the bearing exceeded the theoretical life and was operating under harsh environment – being loaded radially.

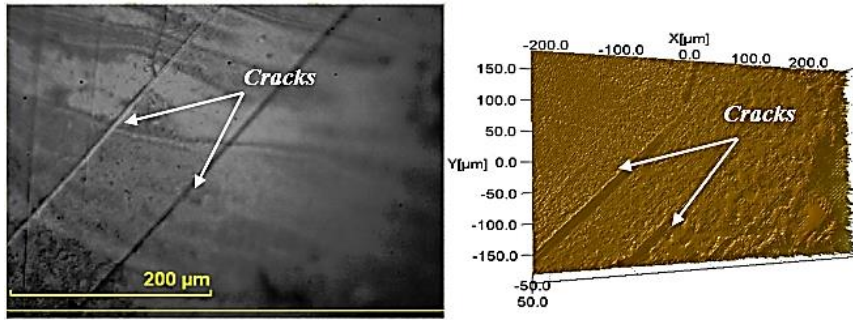


Figure 4. 49: Cracks appeared on the ball surface, indicating that the bearing was operating under harsh environment.

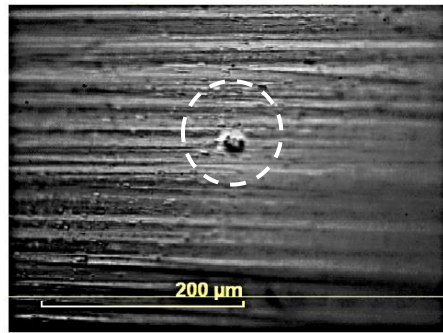


Figure 4. 50: Pitting of chunk on the outer race.

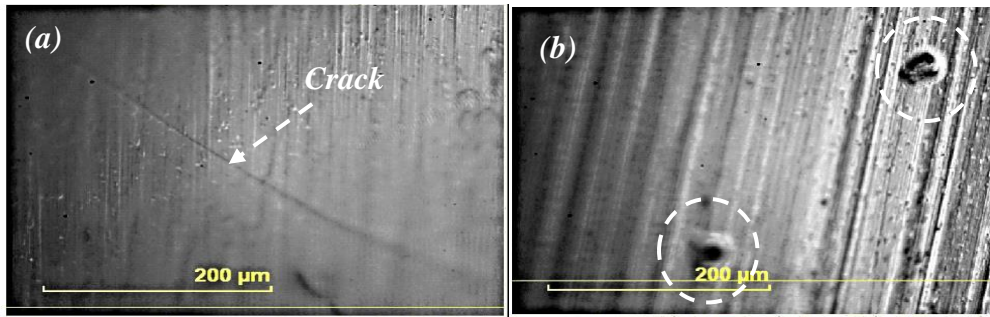


Figure 4. 51: Inner race surface with different failure modes – (a): crack, (b): pitting. This figure highlights few failure modes which elucidate that the bearing was experiencing developing defects which help in diminishing its life.

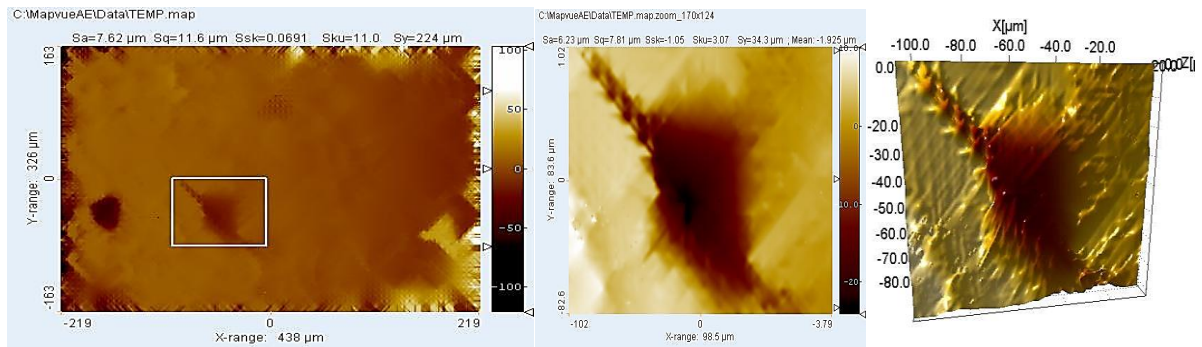


Figure 4. 52: Inner race defects. This figure shows crack initiation / propagation and fatigue striation leading to final failure in the bearing element.

4.5. Advanced Digital Signal and Image Processing

A code was developed in LabVIEW to perform an image subtraction analysis to extract valuable data from the video (see Appendix K). This to enhance the IHMS operation by using image processing technique. Figure (4.53) is a block diagram of the developed code.

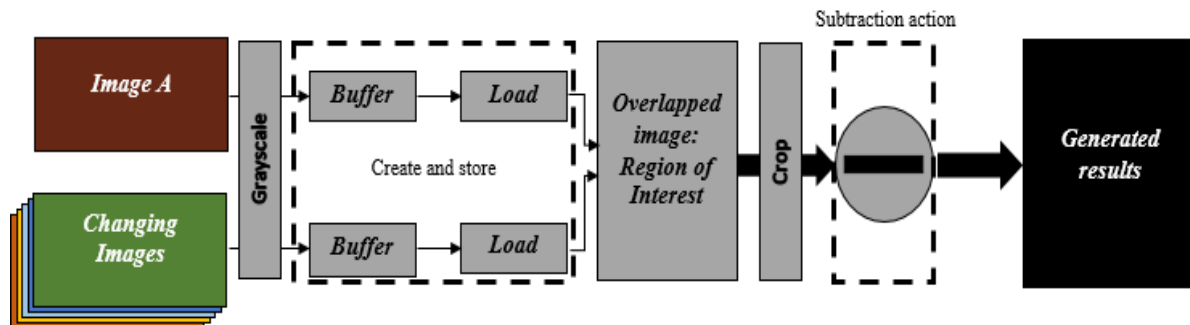


Figure 4. 53: Image subtraction block diagram

This algorithm has been validated in the second test (shaft failure test). A Canon EOS 750D camera was used to record the rotational movement of the test element, to extract information about the machine's performance. This camera produces detailed, high resolution images of 24.2 Megapixel, continuous shooting of five frames per second (fps) and maximum of 1080p fill HD video at 30fps (Conon, 2017).

The camera was fixed on a stand to record the performance during the experiment. The last 10 minutes of the life of the shaft in the second sample were used from which to subtract the image. This video held valuable data about the progression of fatigue in the shaft, providing useful information on failure analysis as by identifying developing features related to displacement due to failure. The video was split into a sequence of images using a VLC media player, to extract the required frames using the available preferences. From the tool tab, the scene video filter and the recording ratio may be adjusted.

First, two images are uploaded by the user. These are then converted from RGB to grayscale, as comparison in grayscale is easier than in RGB as it involves simple scalar algebraic operators, either plus or minus (+, -). Two buffers are created and each image is loaded / registered in each buffer. The region of interest (ROI) in each image had already been identified by the user; then, a crop action is considered to highlight the ROI. Subsequently, the two cropped images overlap and the subtraction action may be performed by visual inspection. Finally, the generated results are displayed as a black and white image, where black indicates

that no change has occurred and white demonstrates the level of changes. Figure (4.54) shows a sample of the analysis.

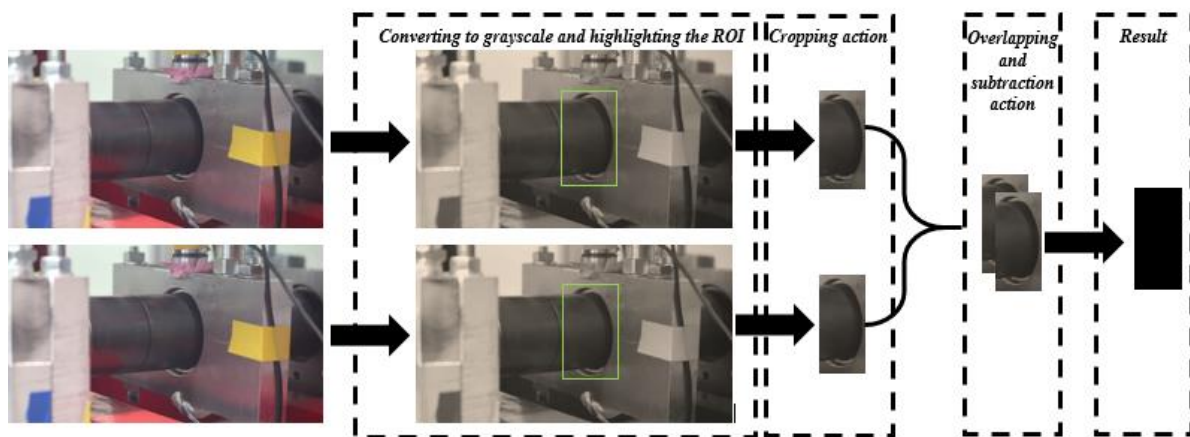


Figure 4. 54: Small sample of what occurs when two images are uploaded into the developed code.

Code was developed using LabVIEW and Figure (4.55) illustrates the images acquired from the recorded video and the subtraction results which extract the effect of fatigue progression and machine performance.

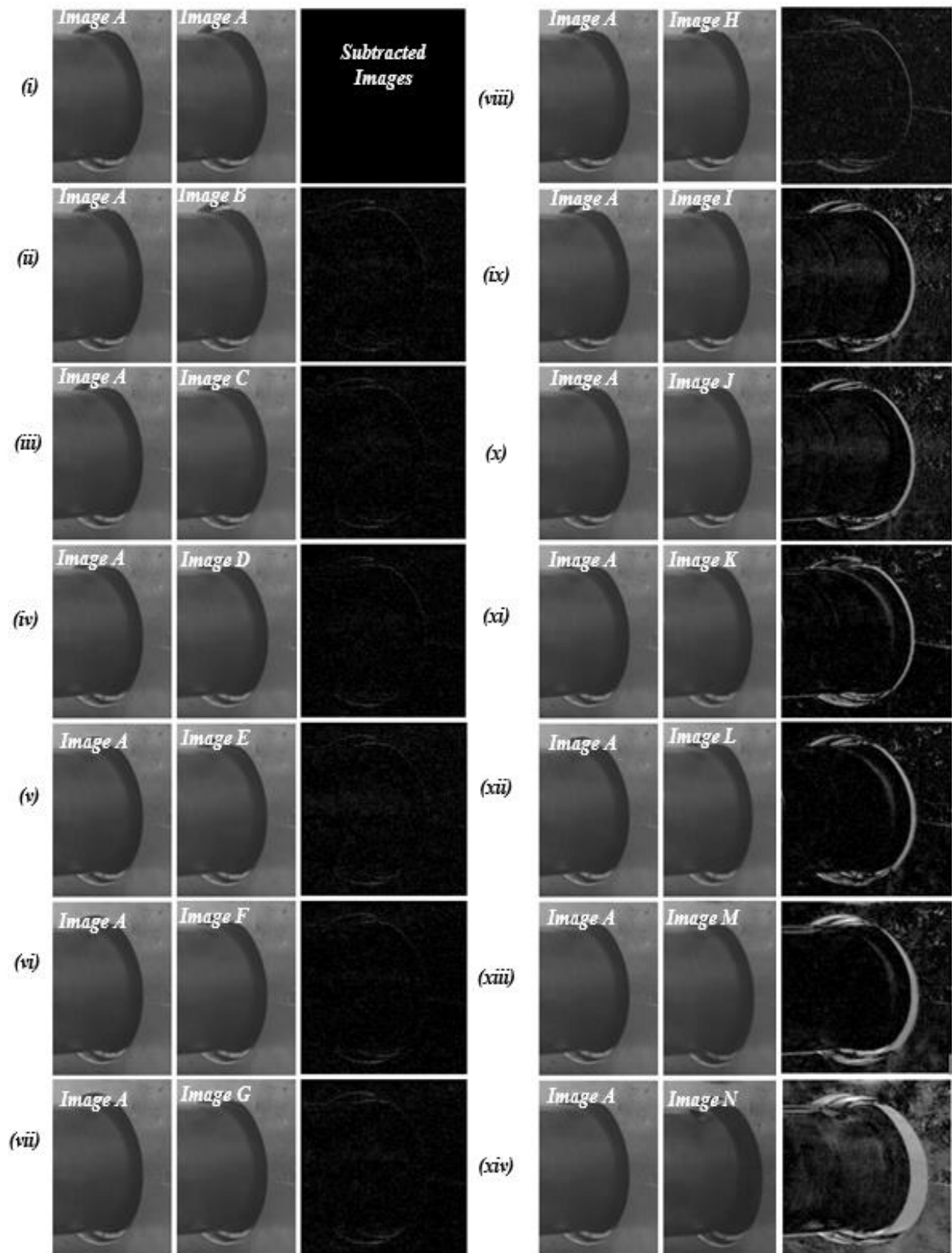


Figure 4. 55: Images from surveillance video – (Image A) captured at the outset. Image (B) captured after the first 50 seconds, Image (C) after 1 minute, Image (D) 1m 30sec, Image (E) 2 minutes, Image (F) 2 min 30 sec, Image (G) 2 min 40 sec, Image (H) 2 min 50 sec, Image (I) 3 minutes, Image (J) 3 min 30 sec, Image (K) 4 minutes, Image (L) 6 minutes, Image (M) 9 minutes and Image (N) at 9 min 17 sec.

Few images were taken during the experiment, Image (A) was taken at the beginning of the experiment and was used as a reference. All the acquired images were subtracted from Image (A) at different times. Image (N) illustrated the point at which the shaft was fully sheared. A closer look at the generated results during the subtraction operation, image (ii–xiv) shows that as failure develops, the motion of the parts due to the reduced stiffness arising from crack development. This is accompanied with the effect of vibration.

After enhancing the contrast and brightness, a better pictorial was observed which indicates slight difference in the position of some components. These features are not clearly visible in Figures (ii–viii). Hence, in Figures (4.55) (ix–viii) the difference becomes more obvious, indicating that the bearing housing is further displaced as a consequence of the developing fatigue crack.

These features indicate that such useful information can be applied to perform a failure analysis, as it illustrates the developing feature related to displacement due to failure. It could also be implemented with further image analysis to verify the depth of these results, although this has not been done here.

4.6. Summary

This chapter discusses the data collected from experiments using all the developments presented in the previous chapters. Two main testing phases were conducted: bearing system failure and bearing life tests.

An experimental test plan was structured to illustrate the system overview, including four main controllers each with a distinctive role. At the same time, multiple sensors were involved in the IHMS development and a system overview was presented. Further sections elucidated the experimental procedures followed for each sample to provide the same testing methods.

First, the software development was validated in two steps involving loaded and unloaded bearings. Initial data were acquired including speed measurements, pressure, load and various vibrational parameters (RMS, kurtosis, CF, peak and Max-Min). These data were used as references for triggering the abort action.

Next, four samples were involved in the final results as a means to investigate common failures in the bearing system and to fulfil the research aim. It was noticed that some parameters increased slightly during the bearing operation, while others decreased, based on their mathematical equations. For instance, RMS, torque, peak and kurtosis values increased slightly as the bearing due to be fatigued, and sharply increased when catastrophic failure occurred. On the other hand, the CF values had different pattern, decreasing slightly when the bearing due to end its life, and decreasing sharply when catastrophic failure occurred.

Additionally, each parameter was ascribed a threshold to form an active health monitoring system. If the limit of any of these thresholds is exceeded, action therefore will be taken. Such action consists of aborting the motor down to help in preventing damage to other elements within the application. For instance, based on the specification of the “Test” bearing, it could handle a maximum load of 14.8kN and maximum temperature is 120 C°, hence, if any of these limits is exceeded, the system will be closed down. Similarly, if the torque value fell and the motor speed remained at the same level, the system will be aborted indicating that the shaft has become disconnected.

Logged data was used to check the suitability of the ARMA algorithm and whether it could be adapted to monitor developing defects in the test element and to develop failure prediction system using a model-based parametric method algorithms. It suggested that it would be a

robust technique in detecting failures and taking preventative action. Results and algorithm validation are illustrated in this chapter.

Also, few features were conducted using a camera fixed on a stand using an image processing technique. Thus, some useful information regarding failure analysis were depicted as they can be used in failure analysis to identify developing features related to failure.

Finally, an inspection of the bearing elements under different types of microscope: Omniscan MicroXam 5000B 3D ADE Phase and Axiovert 40 MAT was presented. Thus, several magnified views of the bearing elements' surfaces were obtained to clarify the failure modes that occurred in the bearing, as illustrated earlier in this chapter.

Chapter 5 summarises the research conducted in this project and suggests future work that could enhance the system performance and fill in gaps left by the current project.

Chapter 5. Conclusion, Recommendations and Future Works

This chapter presents a summary of the work undertaken throughout this research. Each chapter is discussed and the experimental outcomes illustrated. Lastly, suggestions are made for further work to fill any gaps left by this research.

5.1. Conclusion and Recommendations

Bearings are a primary component in almost every mechanical application. They are used extensively to reduce the friction that may occur resulting from rotational or linear movements, enhancing speed, performance and efficiency. Several types are available, including ball and roller / cylindrical, and each type is used for a specific purpose and designed to suit a specific application.

In Micro-scale Wind Turbine applications, the bearings operate in a harsh environment which exposes them to contamination. This contamination makes determining the life of the bearing challenging, as it is not included in the theoretical equation provided by ISO (ISO281, ISO76, ISO 14728-1), ANSI/AFBMA (AFBMA Std. 9), JIS (JIS A, B, C 1518) and DIN (DIN ISO281). In the author's equipment, with the use of advanced technology, sensors were able to notify the user of the up-to-date performance of the bearing, which helped in determining when the maintenance action should be provided. This mirrors the SKF Insight bearing which was developed in 2013 with the aim of monitoring several parameters including speed, load and temperature and providing diagnostic information about the bearing's health. Therefore, the aim of the present research was to develop a prototype of an Intelligent Health Management system for Micro-scale Wind Turbine Bearings that is able to monitor the bearing life and detect common failure that occurs during the bearing's operation.

A. Palmgren., (1924) was the most significant contributor to the rolling-element bearing technology, and the first to suggest a sensible approach for calculating a bearing's life (Zaretsky, E.V., 1997). In 1924 he highlighted a method for calculating bearing life and suggested that it was not a deterministic value, rather distributive, i.e. if two bearings were run in a group under certain conditions, they would not fail at the same time. He therefore proposed the concept of basic rating life for rolling bearings that was used throughout this research, with 90% reliability.

Later, numerous standards emphasised Palmgren's contribution and illustrated a modified version of the basic rating life to calculate the maximum reliability from the theoretical rating. Several researchers addressed issues in determining the actual bearing life, to contribute to developing a sensible way of detecting when an element is due to fail.

Along with all the contributors for determining bearing life, this research used numerous sensors and an advanced mathematical algorithm. Despite all these technologies, it was

challenging to determine the exact life of the test element, because of all the sudden failures that occurred during testing, regardless of the test element or the surrounding equipment. Also, the bearing manufacturers' specifications were based on approximate values, recommendations in the manuals normally providing around 90 to 95% of the machine design applications for safe and reliable design. The remaining percentage requires specialised knowledge and analysis to avoid accumulative errors. Additionally, use of empirical data acquired under a wide range of different operating environments is recommended to generate a system that could become more reliable in calculating the exact life and enhance the existing standards.

The driven recommendation for IHM application in real life could be explained as follows:

- Developing a compact and low cost system that can provide reliable results
- Generalising the IHM system in different applications to test reliability
- In order to create a user-friendly system with wireless communication that enables shared data
- GUI interface with up-to-date performance feedback – accessible through handheld devices i.e. mobile phones, tablets

Therefore, literature review in Chapter 2 was conducted to illustrate the challenges in the research field and to acquire a fundamental understanding of intelligent machines, active condition monitoring systems and sensory and instrumentation systems. Common failures in the micro-scale wind turbine elements were discussed, involving bearings, generator, brake and main shaft defects. The extended use of condition-monitoring techniques, including thermography, vibration, acoustic emission, oil debris analysis and current signature analysis, was illustrated. Lastly, this chapter covered typical intelligent methods that could be adapted to provide a reliable action based on the operational conditions.

Chapter 3 highlighted test bench development for validating the proposed IHMS to test a micro-scale wind turbine bearing. It included presenting a bearing loading mechanism involving radial loading and brake loading to satisfy the hardware development throughout this research. Software development included all the sensors, controllers and actuators. A bearing-life monitoring system and diagnostic system were then described in detail. Finally, a sensory-actuation system for bearing failure detection was tested.

5.2. Experimental Conclusion

Monitoring the bearing life and detecting the developing defects in the bearing system under various conditions was presented in this research. Several parameters were tracked to observe the changes in them while the bearing was in operation. Four bearings samples were involved in the experimental testing with the aim of monitoring the changes in some vibrational parameters in the bearing while operating and detecting common failures. So, Chapter 4 presented the testing plan, preliminary and final testing results using the developed software platform.

The conclusions that can be drawn from this simple study are limited for many reasons. For example:

- The number of experiments being very small is a limiting factor along with no statistical analysis being possible
- The test only considered one machinery, other machines may behave differently
- Accumulatively, these issues diminish the ability to generalise data

Extended use of sensors and a condition-monitoring technique proved to be capable of elucidating the evolution of the bearing defects to illustrate the bearing's life while operating under various conditions. These sensors were able to provide variations in the operational parameters. For instance, piezoelectric sensors successfully showed the changes in the vibrational parameters, including RMS, Kurtosis, Crest Factor, Peak, and Max-Min, in addition to recording the trend-line of each vibrational parameter.

In the time domain, a slight increase in RMS represented the bearing as developing defects in its elements; similarly, with Peak values and Max-Min. On the other hand, the value of the Crest Factor followed a different trend-line, decreasing slightly as the bearing became fatigued – this is due to the proportional relation with the RMS level. The Kurtosis value represents a measure of flattening of the density probability function near the average value; for a healthy bearing it should represent a trend-line around 3, but it increased with the growth of defects in the bearing elements (Samuel, P. D. and Pines, D. J., 2005).

In the frequency domain, the use of the bearing element frequency equations proved capable of detecting the developing defects in the bearing elements. With the frequency domain, where the defect had occurred could be determined. Thus, using an envelope detection technique, characteristic defect frequencies of the bearing were extracted, overcoming the noise in the

FFT spectrum from a demodulation technique. The resulting graphs illustrate the development of defects in the bearing elements and the level of energy in the vibration signals.

Similarly, the Time – Frequency domain was used to provide joint distribution information to help detecting changes in the frequency as a function of time. Graphs were employed previously to identify the variation in both domains: time and frequency. This technique confirmed the results of using the frequency domain.

Other parameters, such as speed, radial load, operating temperature and frictional torque, were highlighted. These parameters were able to identify changes resulting from the bearing becoming fatigued.

A predictive health monitoring system using a model-based parametric method algorithm was used, namely ARMA. It confirmed the use of an advanced mathematical model-based algorithm in conjunction with a condition-monitoring technique to develop an IHMS that is capable of detecting mechanical system failures. This was validated, in two tests: main shaft failures and coupling.

Further developments were considered to capture images from the bearing operation, to extract some features by image processing technique. It was concluded that, with the use of the recorded surveillance video, a simple image processing algorithm such as image subtraction could be used to track failure progression, as illustrated in Chapter 4.

Finally, at the end of each test, the bearing was dismantled and magnified images illustrated the changes that the bearing elements had experienced during the test were recorded. Thus, clarification of the bearing surfaces was obtained. Several defects were identified under a microscope, including cracks, wear, rolling wear, sliding wear and pitting. These failure modes were illustrated in Chapter 4 and occurred due to operational conditions, indicating that the bearing's life was fatiguing.

Thus, further development of this research will use a method to distinguish further details about the bearing's life, to expand development of the current IHMS system and to make a new contribution to the field.

5.3. Future work

First, further development of the IHMS will focus on generating an empirical data to drive an equation that could contribute more in the field of monitoring the bearing life and address the

limitations of this research to expand it for a higher level (PhD). Also, incorporating another intelligent algorithm such as fuzzy logic into the developed IHMS to explore monitoring the bearing life, will better handle uncertainty and nonlinearity and the permit use of linguistic variables. It can also control machines and consumer products. Thus, designing a fuzzy control system includes:

- Fuzzification: identify the inputs, outputs and process tasks, classify the linguistic variables and define the fuzzy sets and memberships.
- Rules: use fuzzy sets and linguistic variables to create the fuzzy rules and to determine the output based on the inputs and generated rules.
- Defuzzification: combine all fuzzy actions into a single fuzzy action and transform the single fuzzy action into crisp, executable system output.

With the use of the data from the sensors in this research, a pictorial view of the implementation of fuzzy logic control is shown in Figure (5.1).

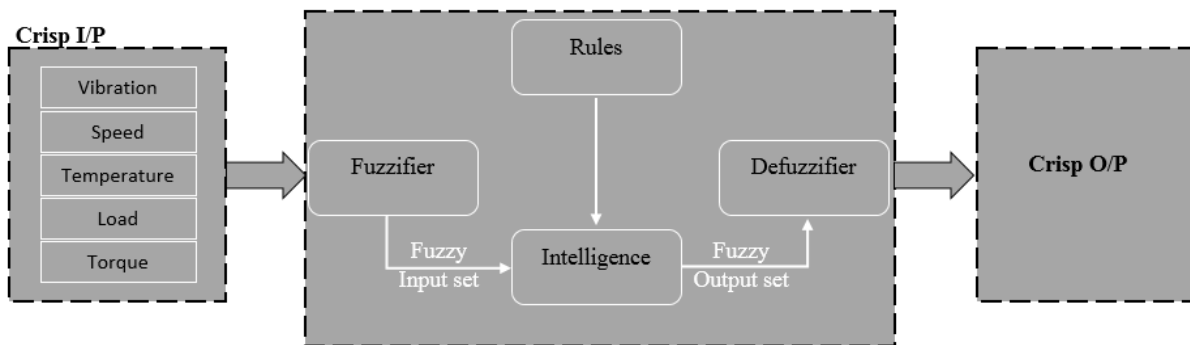


Figure 5. 1: Fuzzy Logic Architecture

Secondly, the camera was able to extract useful visual information that can be applied in an appropriate maintenance technique. This makes possible the development of a low-cost vision-actuation system to detect failures and observe changes in the test element features.

The camera would be used to capture some features within the operation; therefore, if significant variation between the features is found, action will be taken. A simple flowchart to illustrate the vision-actuation system is shown in Figure (5.2).

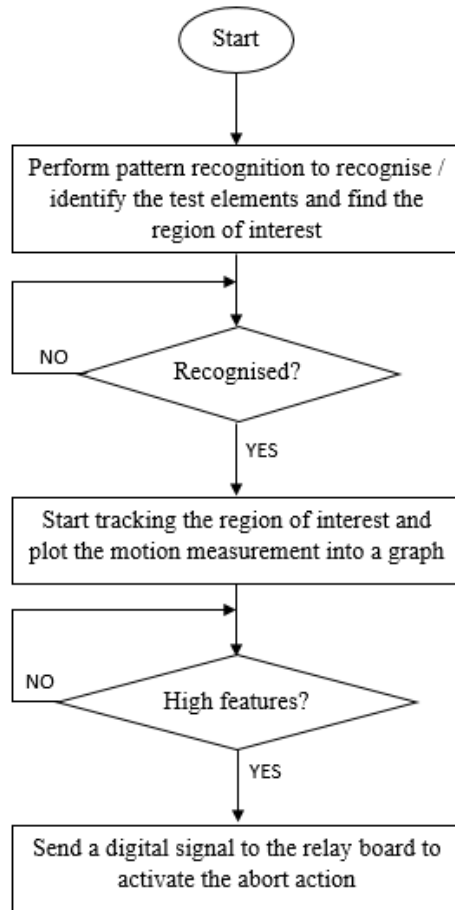


Figure 5. 2: Flowchart of the proposed visionary-actuation system

The ROI is identified either by selecting the desired area manually or by using a machine-learning technique. The process will not proceed until the ROI is recognised / identified, otherwise an alarm is activated. The ROI is then tracked during the operation / testing and a motion measurement graph plotted to illustrate the variation in motion for the test element. If high features are recorded, a digital signal will be sent from the controller to the relay board to activate the abort action. A threshold can be determined, so that if any abnormal activity is detected, action will be taken.

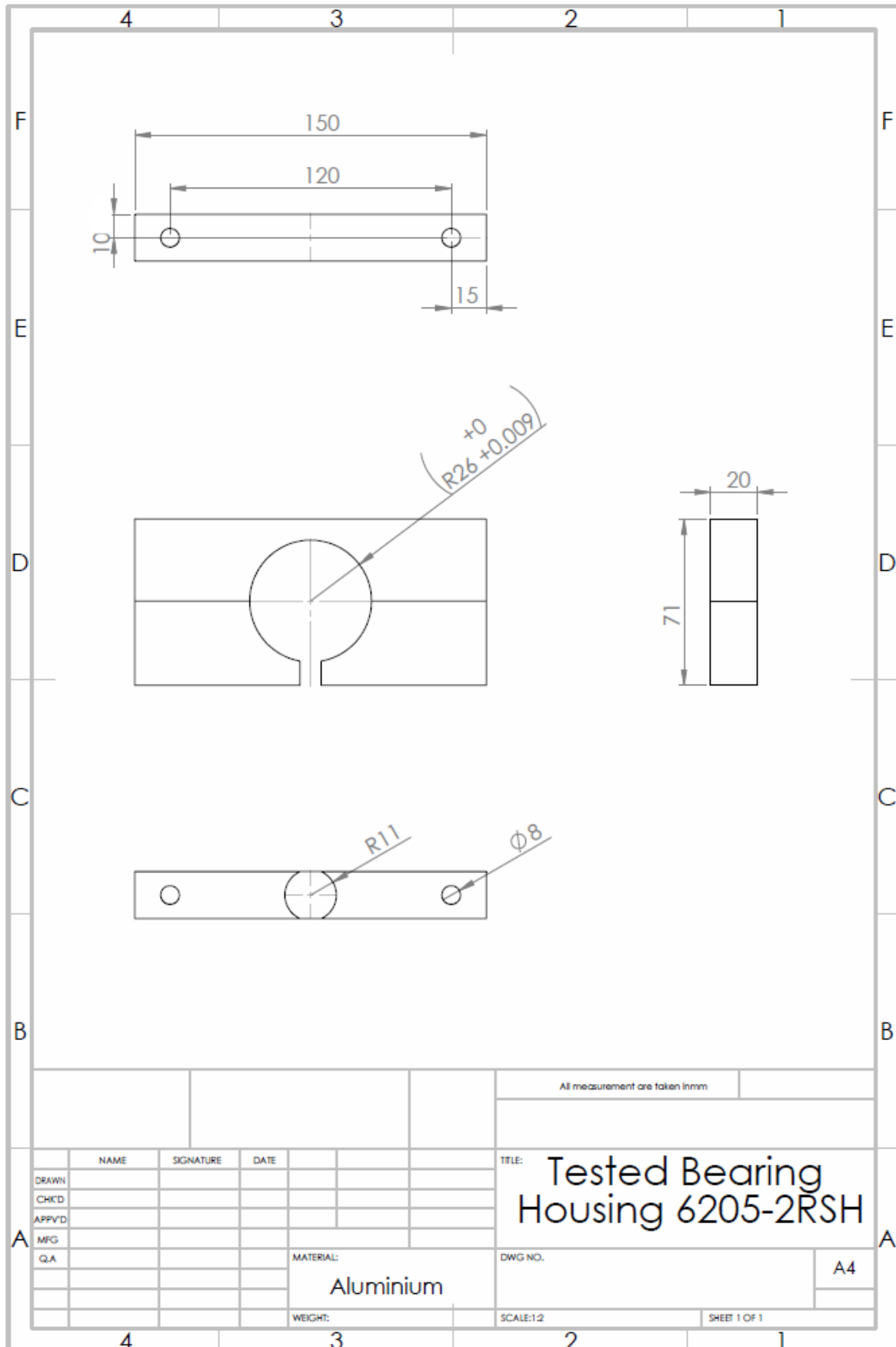
Thirdly, using a cost-effective vibration sensor such as Grove-Piezo Vibration could be used to perform vibration analysis. This sensor can detect vibrations, flexibility and impact by bending the tip of the sensor. Thus, a certain voltage is generated indicating that the tip has experienced vibrations. This sensor senses in a wide dynamic range from 0.001Hz to 1000MHz with supply voltage of 3.3 V to 5V.

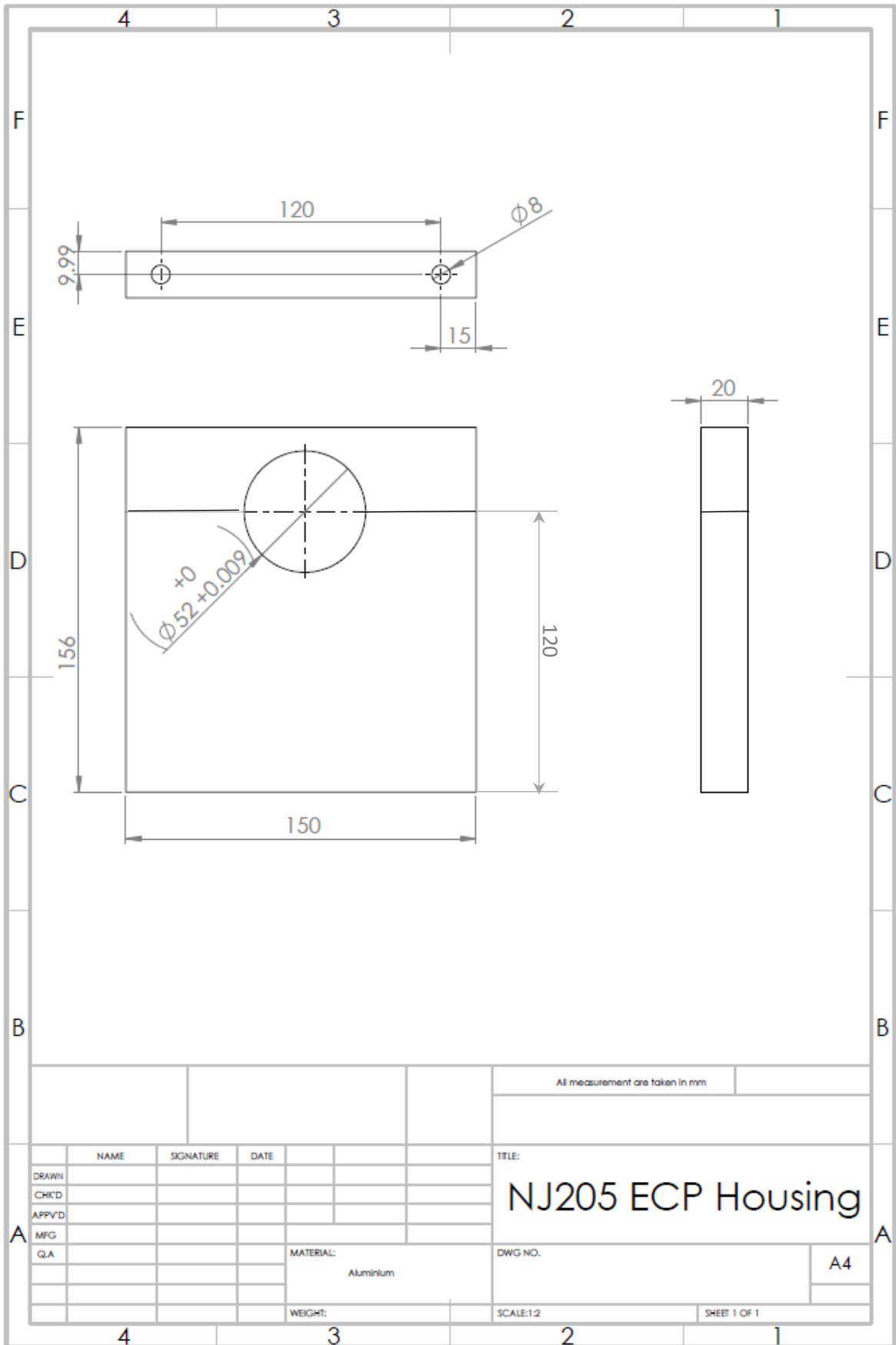
Several vibration analysis techniques can be conducted using the Grove-Piezo sensor, including time, frequency and time-frequency domains. In the time domain approach,

parameters can be determined through substituting their equation, resulting in monitoring the variation in these parameters.

Using the results from the mathematical equations for the test element, this could help in determining the vibration in the frequency domain. Thus, by using envelope detection, a better picture of the defective element could be obtained. A time-frequency domain could be used to identify any variation in the vibration in both time and frequency domains.

Appendix A – Bearing Housings





Appendix B – NTC PCB Board

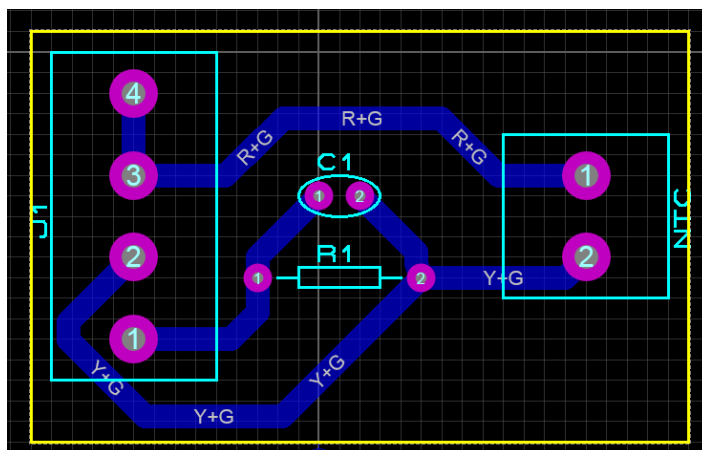


Figure 3. 50: NTC PCB board - ARES model

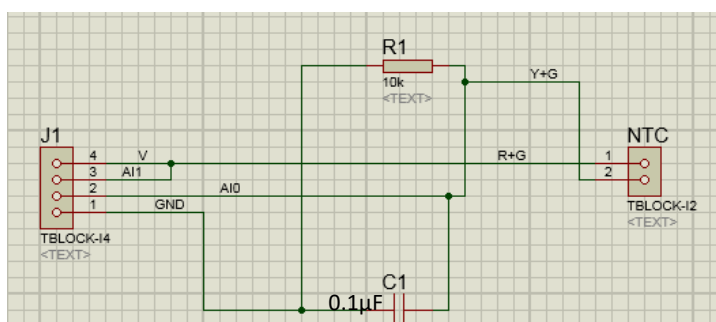


Figure 3. 51: NTC PCB board - ISIS model

A small PCB board was made to help in measuring the temperature using NTC sensor. This board contains terminal blocks, resistor and capacitor. The two terminals block is connected to the NTC sensor while the four terminals block is connected to myRIO. The four terminals block uses terminal 1 and 4 to power the circuit through connecting pin 4 to +5V and pin 1 to ground (GND) in the controller (myRIO). Terminal 2 and 3 they are responsible about acquiring the data therefore they are connected to analogue input pins.

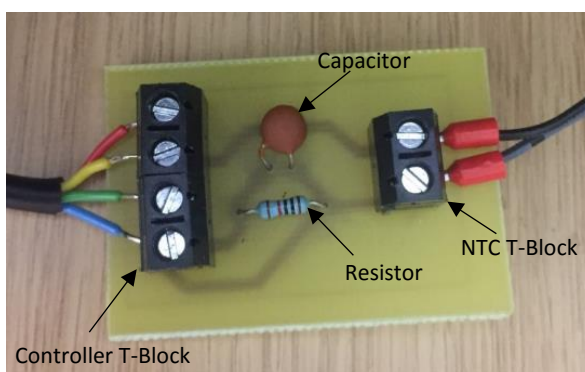


Figure 3. 52: NTC Printed Circuit Board (PCB)

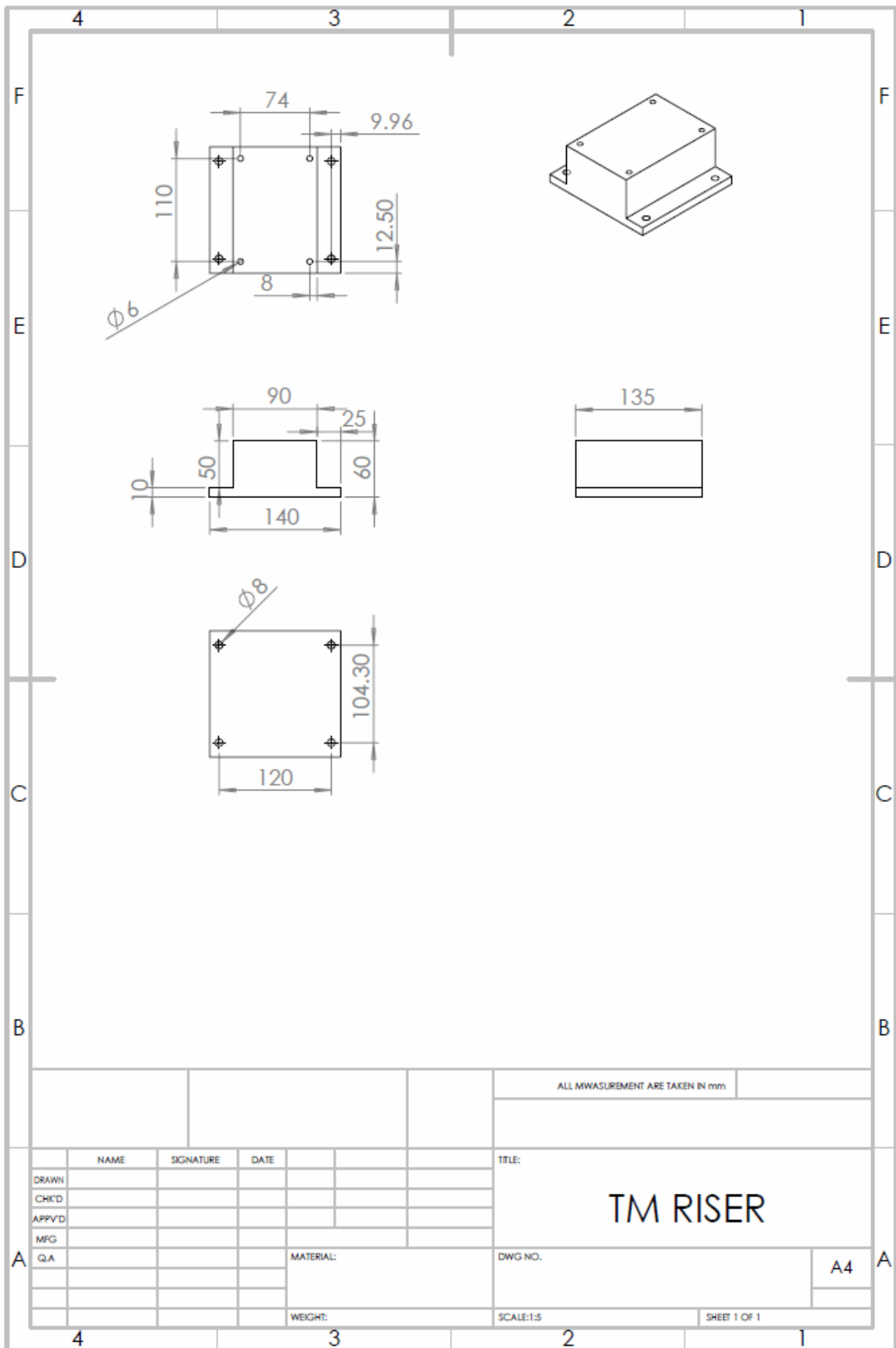
Appendix C – Thermistor Resistance Vs Temperature

Table 3. 13: Thermistor Resistance (Ohms) Vs Temperature (Celsius)

°C	R Val (Ω)	°C	R Val (Ω)	°C	R Val (Ω)	°C	R Val (Ω)	°C	R Val (Ω)
-80	7,296,874	-30	176,683	20	12,493.70	70	1,751.60	120	388.59
-79	6,677,205	-29	166,091	21	11,943.30	71	1,693.00	121	378.44
-78	6,114,311	-28	156,199	22	11,420.00	72	1,636.63	122	368.59
-77	5,602,677	-27	146,959	23	10,922.70	73	1,582.41	123	359.05
-76	5,137,343	-26	138,322	24	10,449.90	74	1,530.28	124	349.79
-75	4,713,762	-25	130,243	25	10,000.00	75	1,480.12	125	340.82
-74	4,327,977	-24	122,687	26	9,572.00	76	1,431.87	126	332.11
-73	3,966,352	-23	115,613	27	9,164.70	77	1,385.37	127	323.67
-72	3,655,631	-22	108,991	28	8,777.00	78	1,340.68	128	315.48
-71	3,362,963	-21	102,787	29	8,407.70	79	1,297.64	129	307.53
-70	3,095,611	-20	96,974	30	8,056.00	80	1,256.17	130	299.82
-69	2,851,363	-19	91,525	31	7,720.90	81	1,216.23	131	292.34
-68	2,627,981	-18	86,415	32	7,401.70	82	1,177.75	132	285.08
-67	2,423,519	-17	81,621	33	7,097.20	83	1,140.71	133	278.03
-66	2,236,398	-16	77,121	34	6,807.00	84	1,104.99	134	271.19
-65	2,064,919	-15	72,895	35	6,530.10	85	1,070.58	135	264.54
-64	1,907,728	-14	68,927	36	6,266.10	86	1,037.40	136	258.09
-63	1,763,539	-13	65,198	37	6,014.20	87	1,005.40	137	251.82
-62	1,631,173	-12	61,693	38	5,773.70	88	974.56	138	245.74
-61	1,509,639	-11	58,397	39	5,544.10	89	944.81	139	239.82
-60	1,397,935	-10	55,298	40	5,324.90	90	916.11	140	234.08
-59	1,295,239	-9	52,380	41	5,115.60	91	888.41	141	228.50
-58	1,200,732	-8	49,633	42	4,915.50	92	861.70	142	223.08
-57	1,113,744	-7	47,047	43	4,724.30	93	835.93	143	217.80
-56	1,033,619	-6	44,610	44	4,541.60	94	811.03	144	212.68
-55	959,789	-5	42,314.60	45	4,366.90	95	786.99	145	207.70
-54	891,689	-4	40,149.50	46	4,199.90	96	763.79	146	202.86
-53	828,865	-3	38,108.50	47	4,040.10	97	741.38	147	198.15
-52	770,880	-2	36,182.80	48	3,887.20	98	719.74	148	193.57
-51	717,310	-1	34,366.10	49	3,741.10	99	698.82	149	189.12
-50	667,828	0	32,650.80	50	3,601.00	100	678.63	150	184.79
-49	622,055	1	31,030.40	51	3,466.90	101	659.10		
-48	579,718	2	29,500.10	52	3,338.60	102	640.23		
-47	540,530	3	28,054.20	53	3,215.60	103	622.00		
-46	504,230	4	26,687.60	54	3,097.90	104	604.36		
-45	470,609	5	25,395.50	55	2,985.10	105	587.31		
-44	439,445	6	24,172.70	56	2,876.90	106	570.82		
-43	410,532	7	23,016.00	57	2,773.20	107	554.86		
-42	383,712	8	21,921.70	58	2,673.90	108	539.44		
-41	358,806	9	20,885.20	59	2,578.50	109	524.51		
-40	335,671	10	19,903.50	60	2,487.10	110	510.06		
-39	314,179	11	18,973.60	61	2,399.40	111	496.08		
-38	294,193	12	18,092.60	62	2,315.20	112	482.55		
-37	275,605	13	17,257.40	63	2,234.70	113	469.45		
-36	258,307	14	16,465.10	64	2,156.70	114	456.76		
-35	242,195	15	15,714.00	65	2,082.30	115	444.48		
-34	227,196	16	15,001.20	66	2,010.80	116	432.58		
-33	213,219	17	14,324.60	67	1,942.10	117	421.06		
-32	200,184	18	13,682.60	68	1,876.00	118	409.90		
-31	188,026	19	13,052.80	69	1,812.60	119	399.08		

Table (3.13) was used to validate the obtained measurements by the temperature sensor (NTC) using Steinhart-Hart equation and its coefficients (A, B and C). Where $A = 1.12924 * 10^{-3}$, $B = 2.34108 * 10^{-4}$ and $C = 0.87755 * 10^{-7}$. It was used as well to plot the graph in Figure (3.23). As illustrated above in Table (3.13), resistance of 10kΩ is an indication to 25°C.

Appendix D – Torque Meter Riser



Appendix E – Bearing life Calculation codes

Initially an offline code was developed to perform a calculation of the bearing life based on ISO281 equations and SKF modifications.

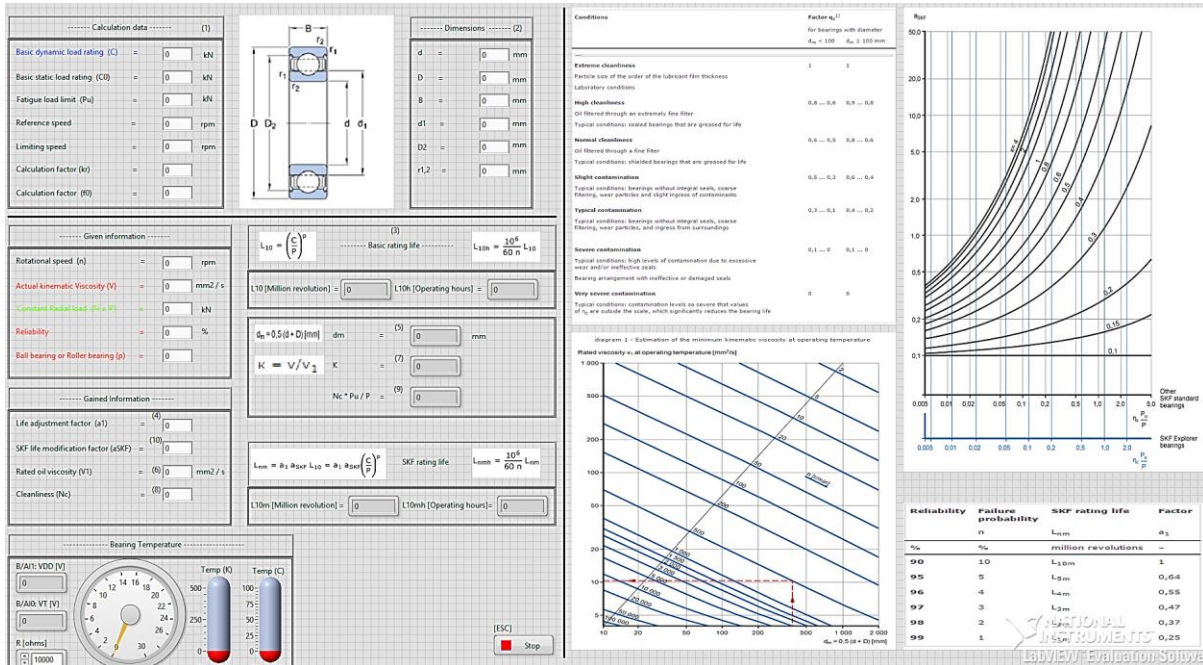


Figure 3. 53: Initial bearing life calculator (front panel) – offline code

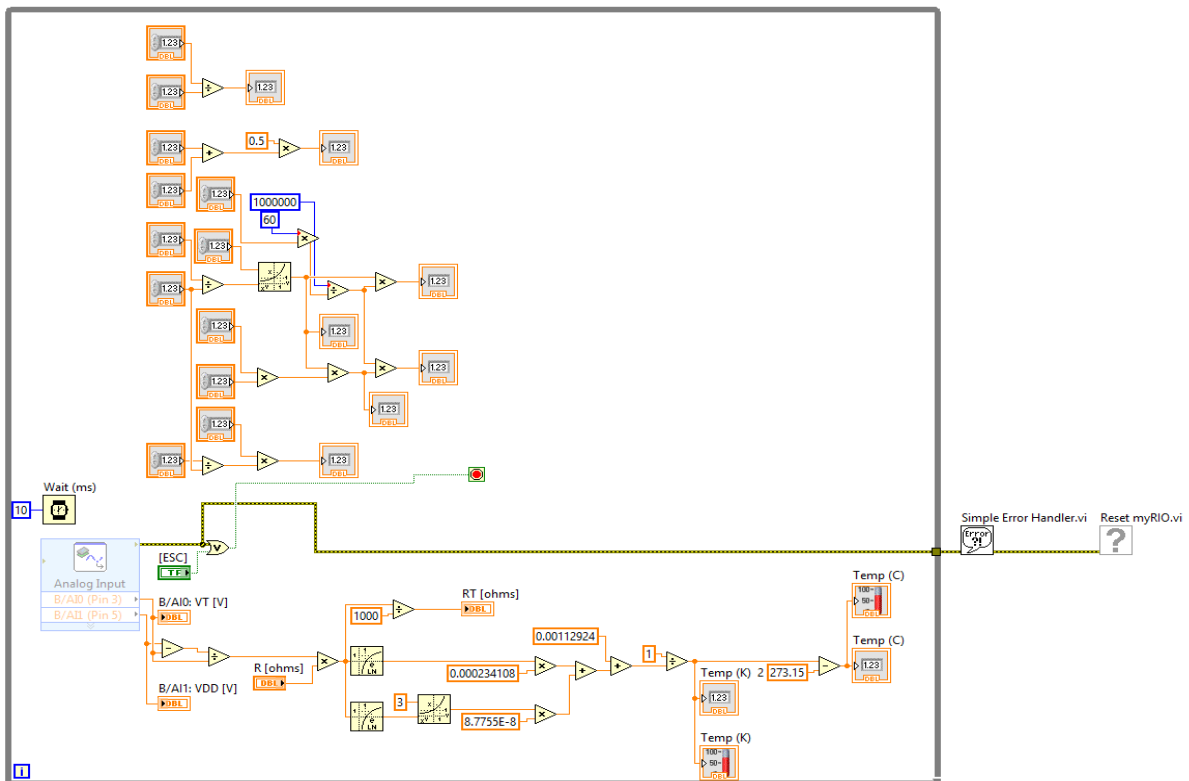


Figure 3. 54: Initial bearing life calculator (block diagram) – offline code

Hence, the code was developed to be an online code with interfacing with all the sensors, thus, following figures shows the modifications of the front panel and block diagram.

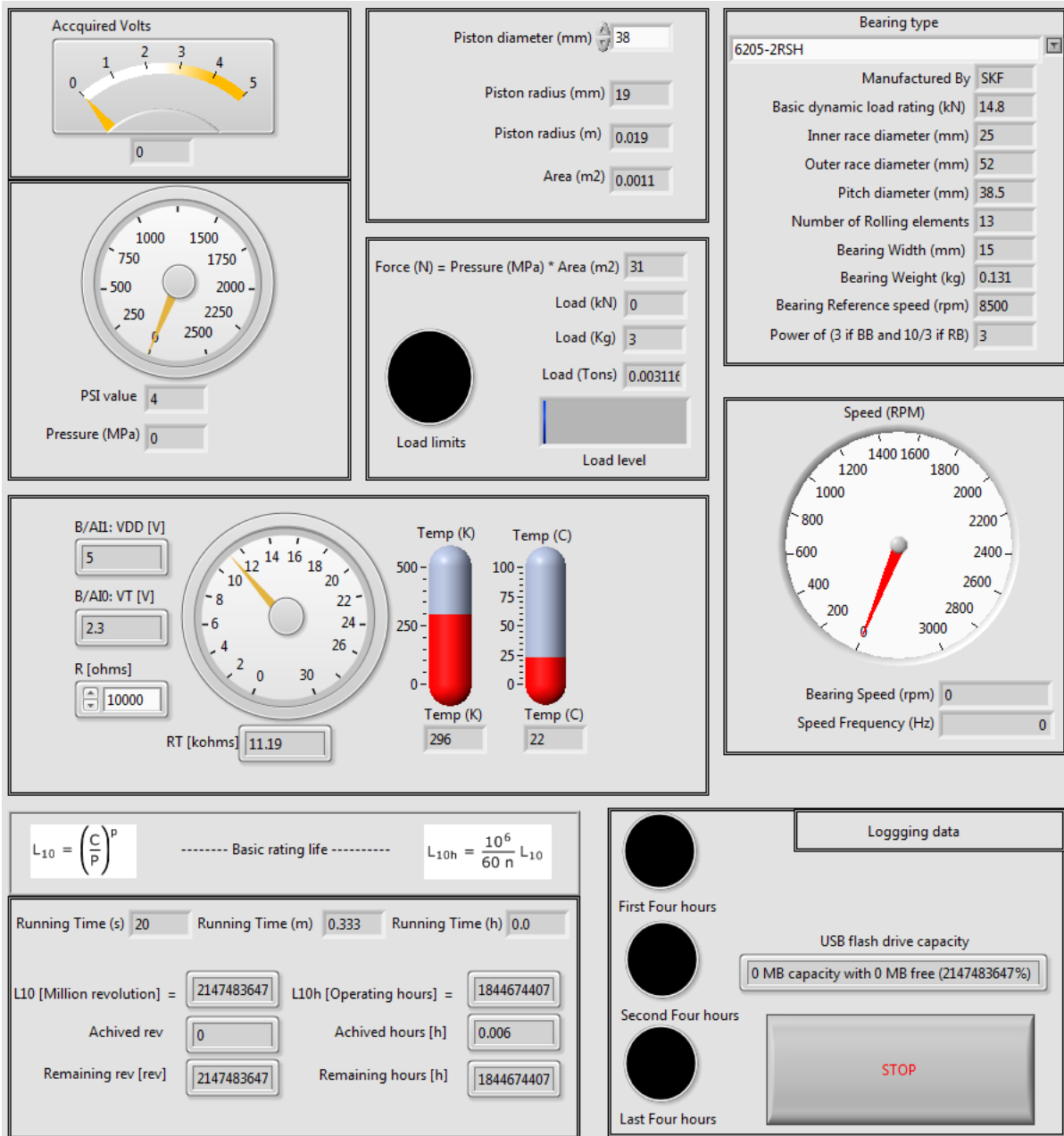


Figure 3. 55: Final bearing life code development - front panel

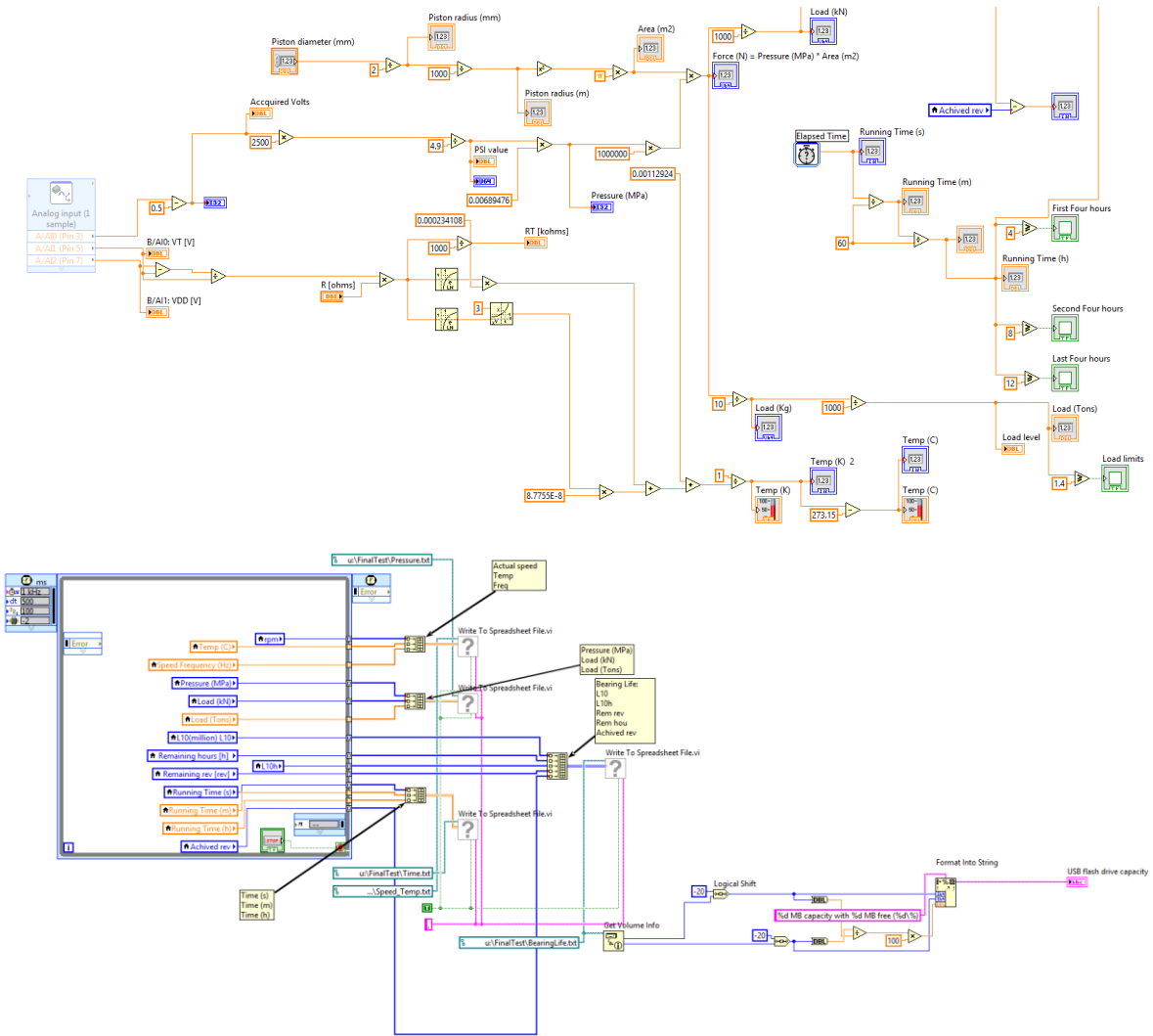


Figure 3. 56: Final bearing life development code - block diagram

Appendix F – Bearing diagnostic system code (Vibration analysis)

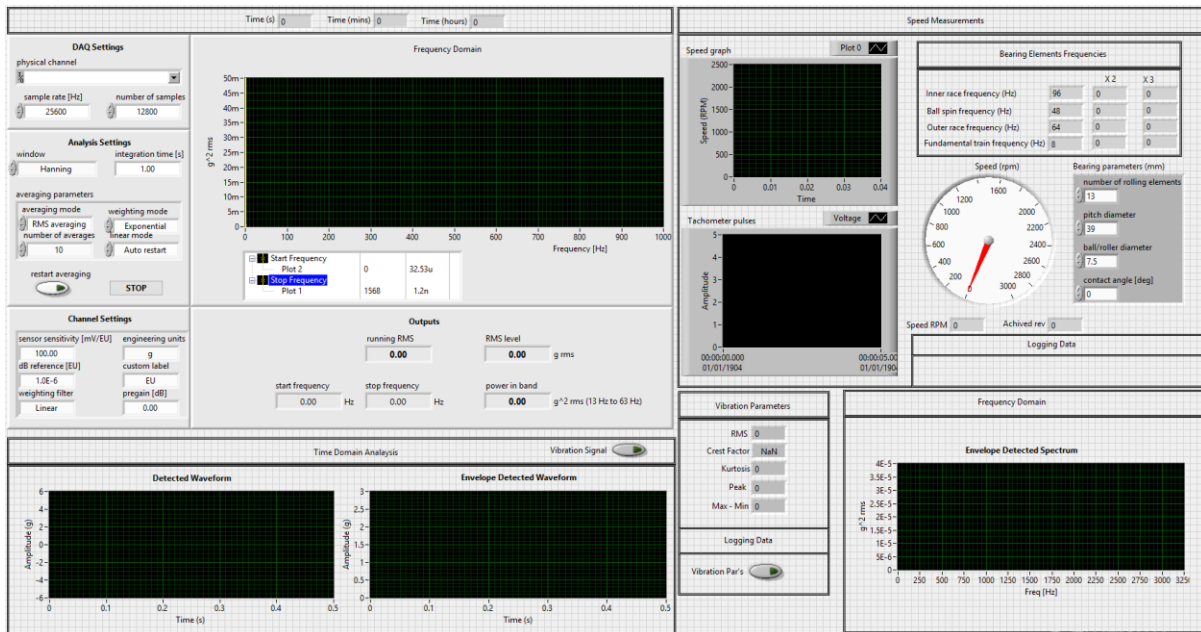


Figure 3. 57: Vibration analysis code – front panel of LabVIEW

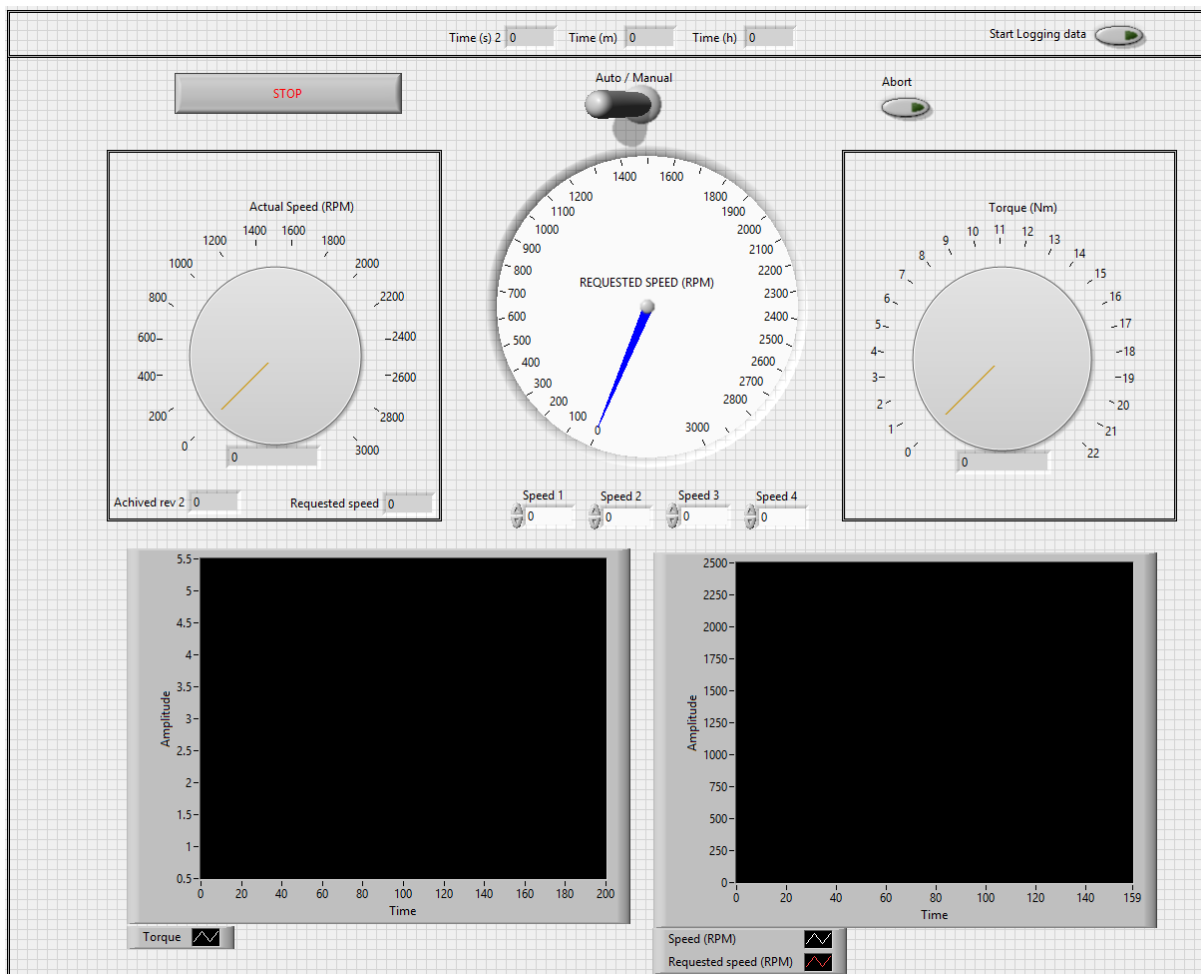


Figure 3. 58: Torque measurement code - Front panel of LabVIEW

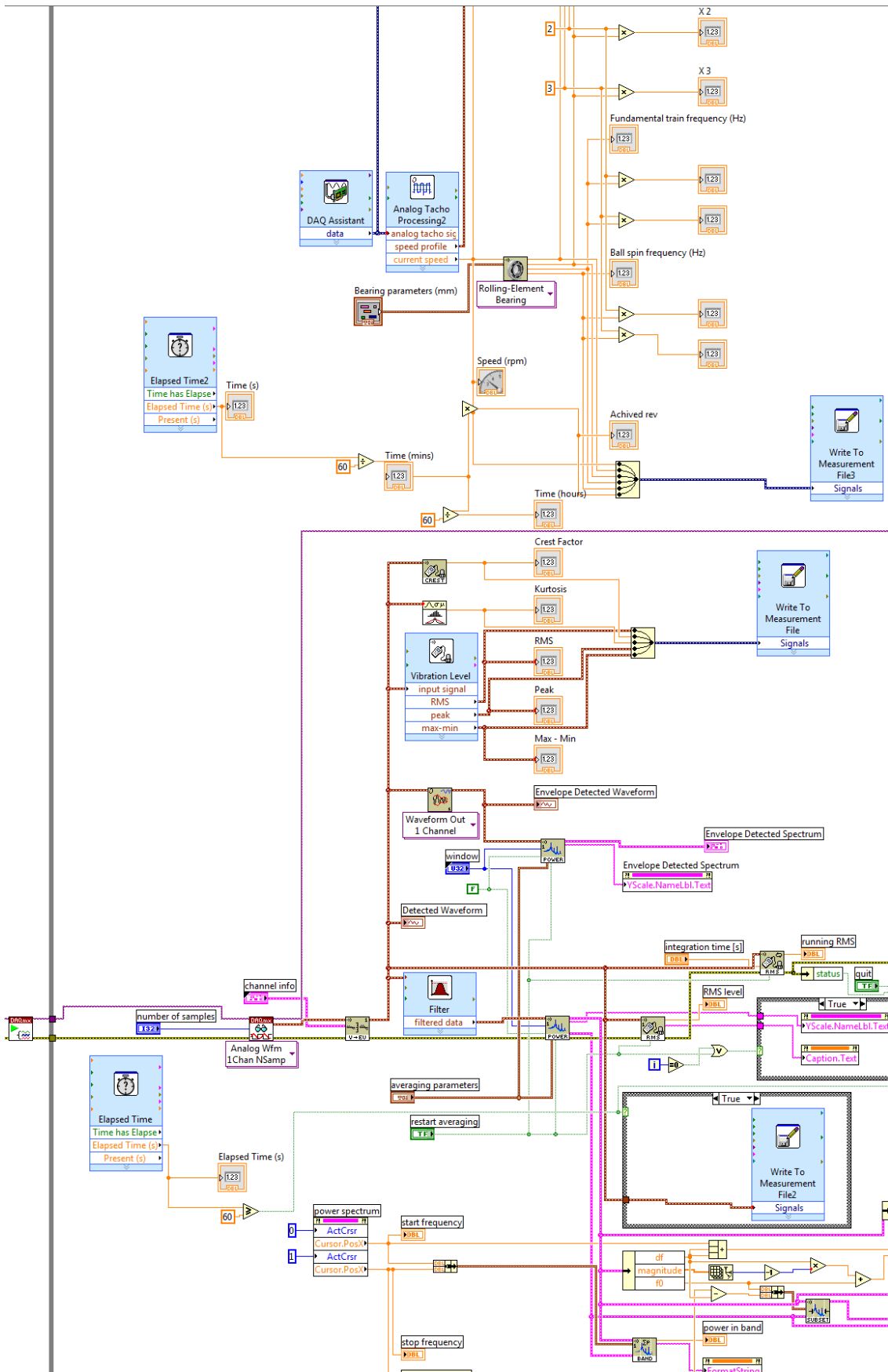


Figure 3. 59: Vibration analysis code – Block Diagram illustration

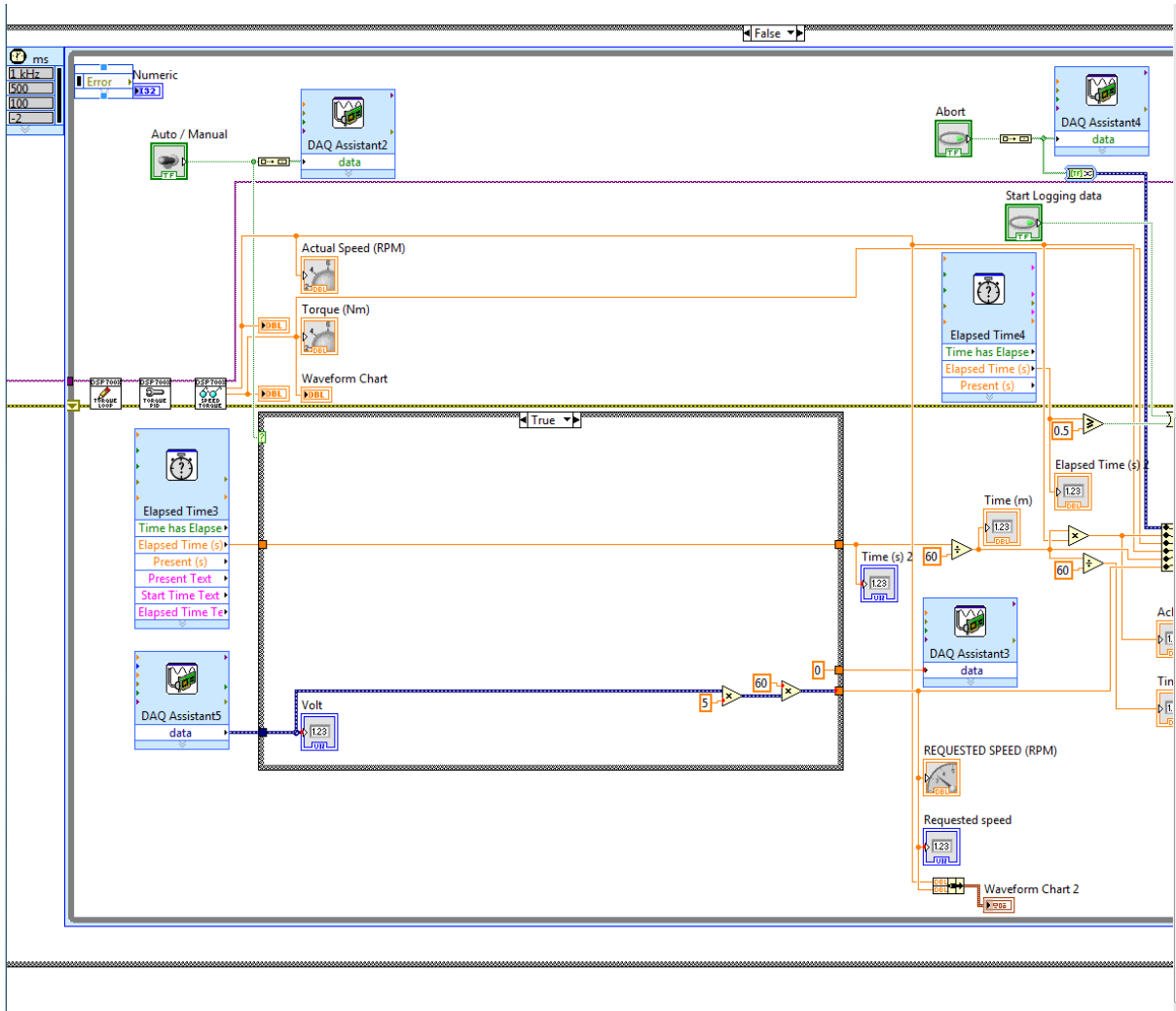


Figure 3. 60: Torque measurement code - block diagram

Appendix G – Relay PCB Board

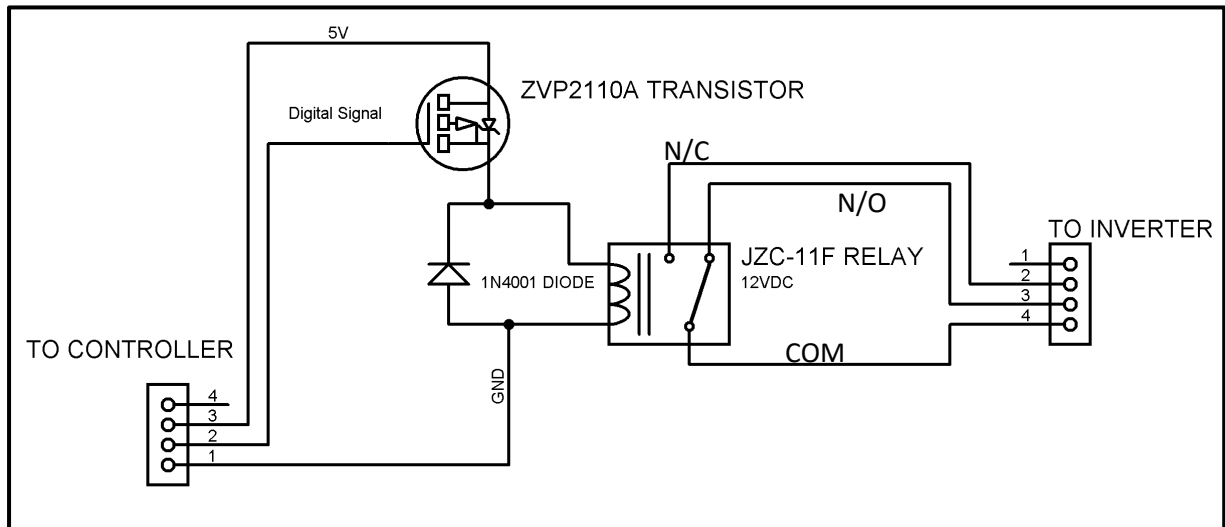


Figure 3. 61: Relay PCB Schematic – ISIS model

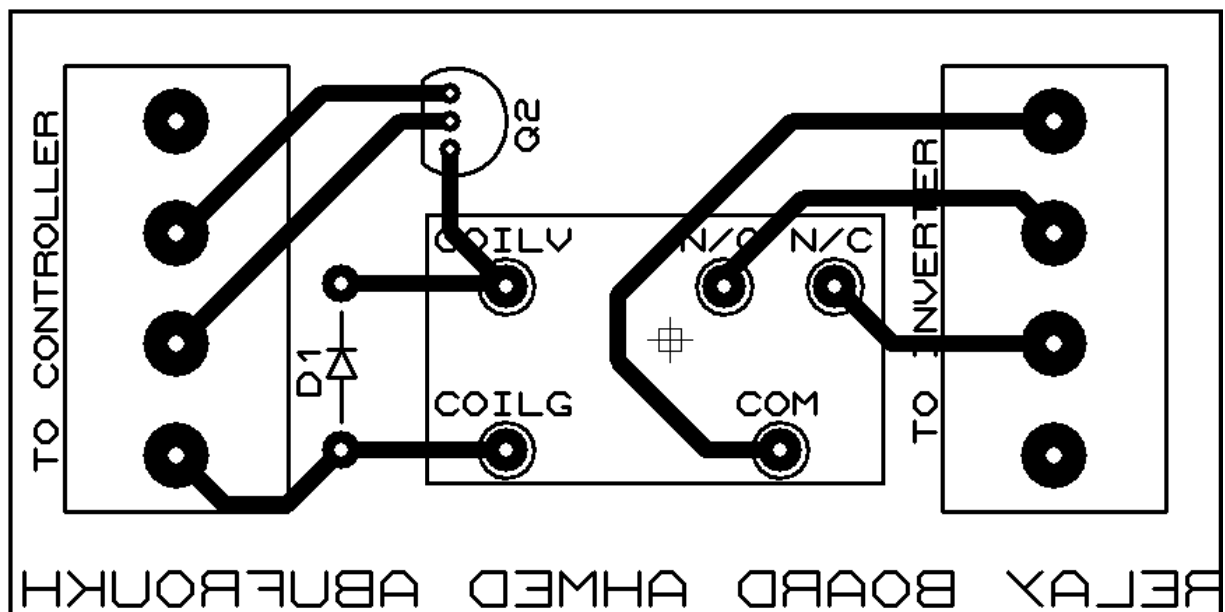


Figure 3. 62: Relay PCB Schematic - ARES model

Figure key:

- Q2 = ZVP2110A transistor
- D1 = 1N4001 Diode
- N/C = Normally closed, N/O = Normally opened, COM = Common
- COILG & COILV = Grounded coil and Powered coil

Appendix H – First Test: Bearing System Failure; Shaft Failure

The first test used a 10kN radial load on the bearing at a speed of 2000 rpm. The following graphs plot the acquired Load and Frictional torque:

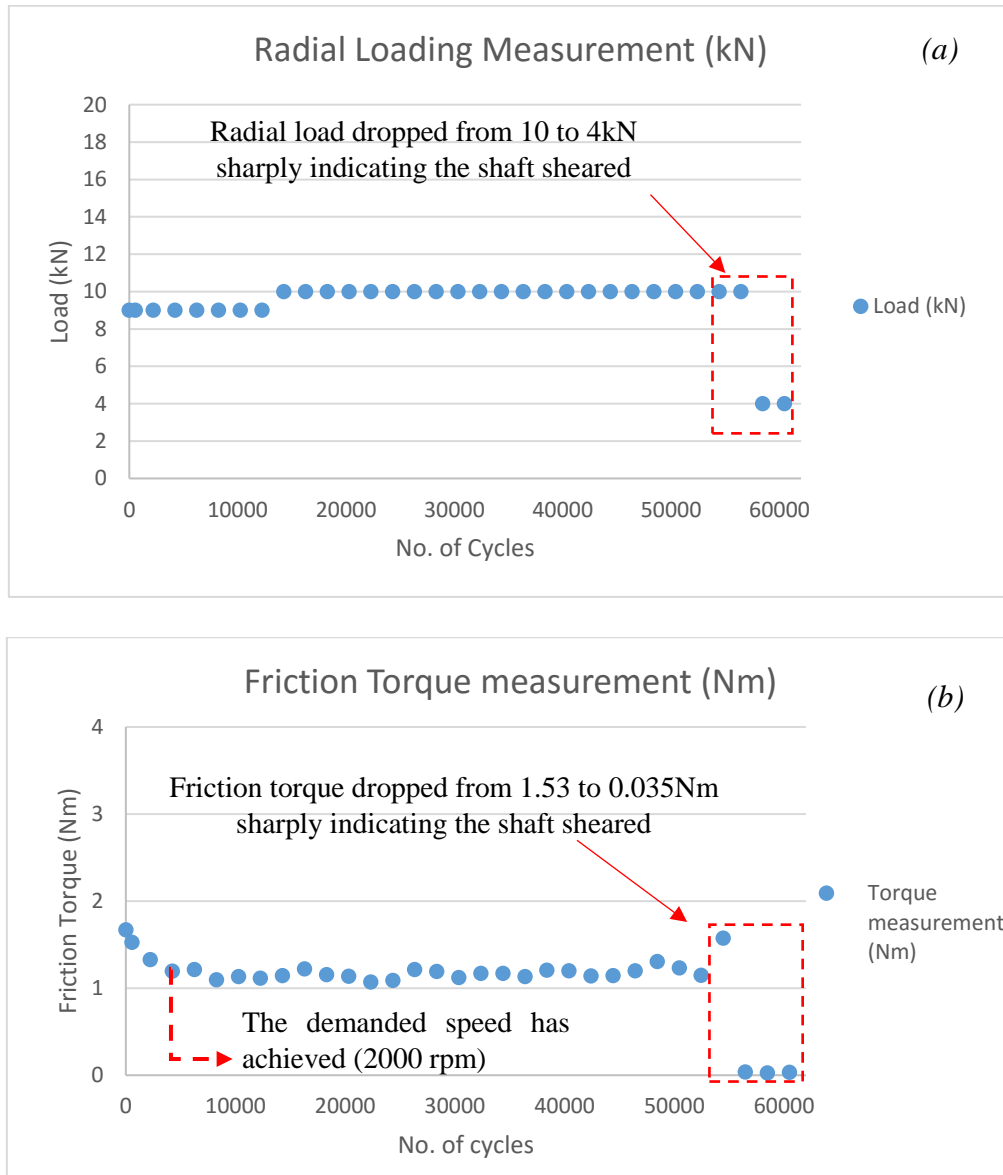


Figure 4. 56: First bearing system failure test results – (a) The applied radial load in kN, (b) the Frictional Torque in Nm

Figure (4.56) indicates the applied radial load and frictional torque of the bearing. In Figure (4.56 – b), it was shown that the plotted data increased to around 1.7 Nm, indicating the required frictional torque to start rotating the motor at the requested speed (2000 rpm) under the applied radial load. Then, it followed a pattern of fluctuating around 1.2 Nm until the fracture has occurred. The torque dropped to 0.035 Nm, indicating that the shaft is sheared and the bearing is not loaded anymore, i.e., the shaft is not linked to the other elements in the test bench.

Appendix I – Second Test: Bearing System Failure; Shaft Failure

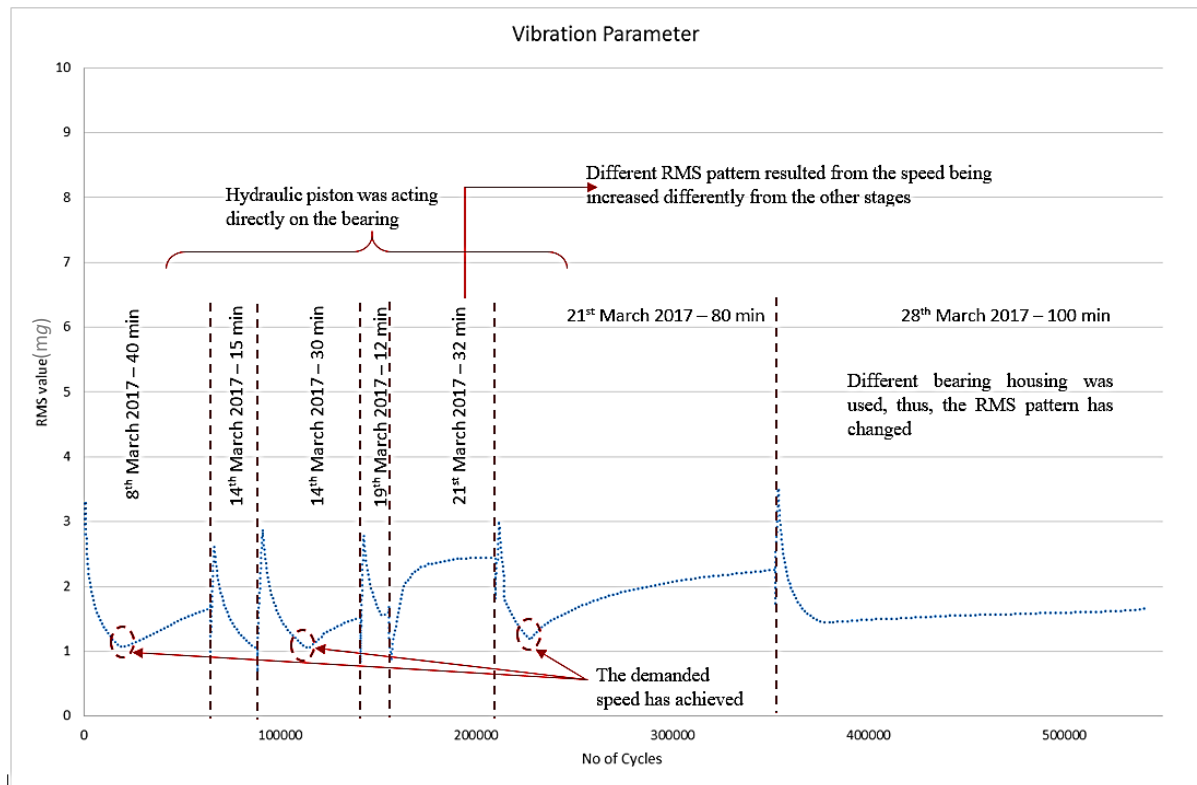


Figure 4. 57: RMS value throughout the second bearing system failure test

Figure (4.57) displays the RMS value using the time-domain technique. A closer look at the logged results shows that the RMS value increased at the beginning of the run, then decreased significantly until it reached the desired value, thus following a pattern. This was due to high energy in the bearing at the beginning. The bearing started running under a radial load after being constant, thus, high peaks are recorded / noticed at the outset of each stage. The first stage experienced an increment in the RMS level to 3.3mg at first, then dropped to 1.09mg, ending the stage with an increment to 1.7mg, as illustrated in Figure (4.57) above. The RMS recorded an increase to 2.7mg in the first segment of the second stage and dropped to 1.04mg, then from 1.01 to 1.6mg in the second segment with an initial RMS value of 2.9mg. In the third stage, the RMS value started from 2.8mg and followed a trend-line to 1.5mg. The outset segment of the fourth stage illustrated different patterns owing to the speed being increased from 0 to 131 rpm, whilst in the rest of the stages, the rotational speed of the bearing increased from 0 to around 445 rpm under a certain radial load. Therefore, the RMS value increased from 0 to 0.9mg, then followed a pattern to reach 2.5mg. The second segment verified incrementing the RMS value to 3mg at the start then a pattern from 1.1 to 2.3mg was followed. After that, in the last stage, the housing was changed so that the load is not applied directly to the bearing.

Therefore, the RMS value was depicted first as 3.5mg, then diminished to 1.45mg and followed a pattern towards 1.6mg, as shown in Figure (4.57) above.

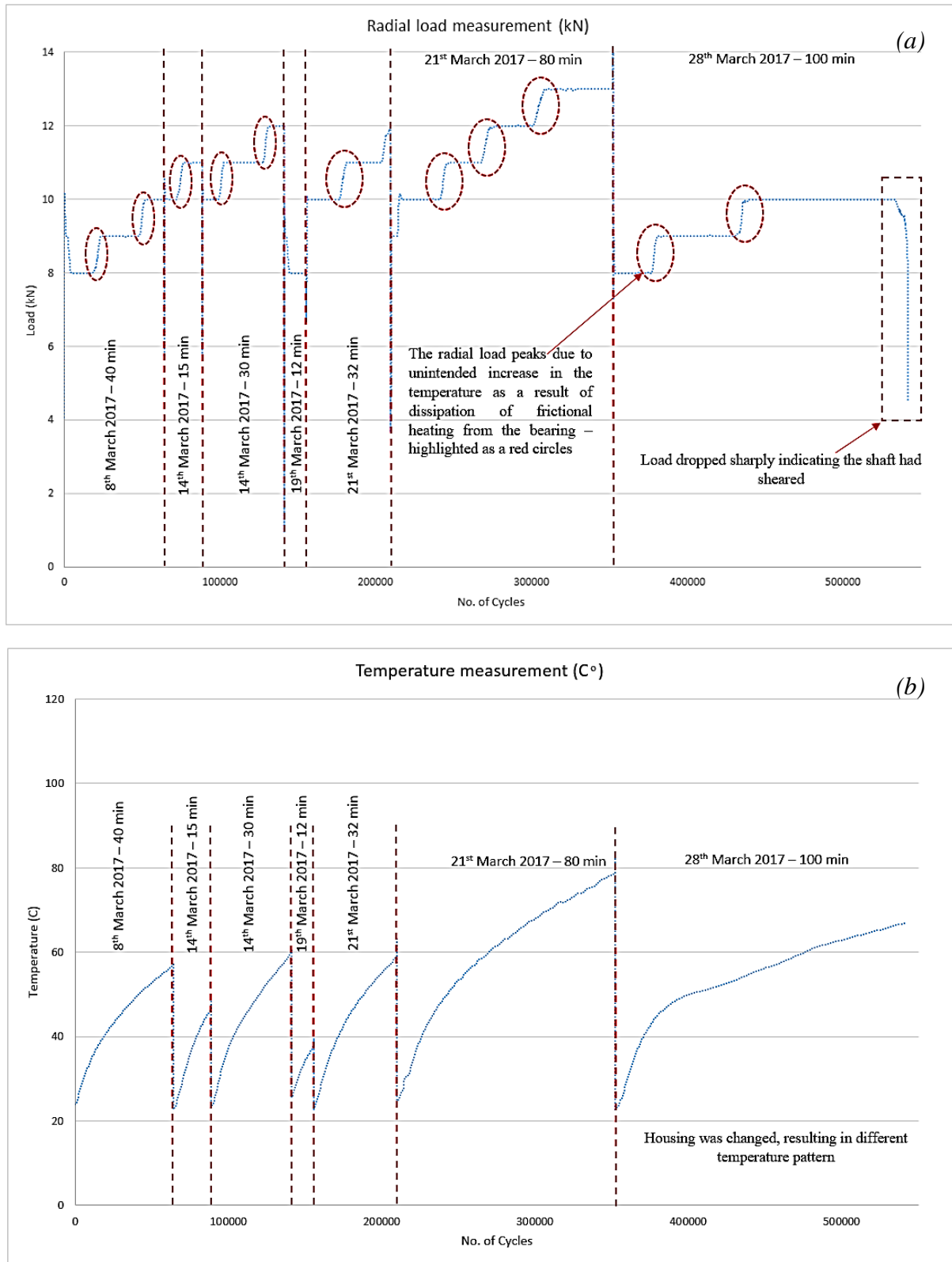


Figure 4. 58: Results during the Second bearing failure test – (a) the applied radial load in kN and (b) Operational Temperature in C°

Figure (4.58) represents the acquired data from the pressure sensor and NTC. These data illustrates the applied radial load in kN scale and the bearing temperature in C° scale. The shown data was taken for five different main test stages when the equipment was stopped then restarted as illustrated in the figure above.

- Figure (4.58 – a & b):

- In the first stage (8th March), the load varied between 8kN and 10kN and the temperature from 25 to 58 C°.
- The second stage (14th March) comprised two sections. The radial load fluctuated between 10kN and 12kN in both sections. In the first section, the temperature increased from 25 to 46 C°, whilst the second part saw an increment in the temperature from 25 to 60 C°.
- In the third stage (19th March), a 10kN load was applied, which unintently decreased to 8kN. Temperature increased from 26 to 38 C°.
- The fourth stage (21st March) comprised two segments. In the first segment, the load was varied 10kN to 12kN and between 10kN to 13kN in the second segment. This stage experiences an increment in the temperature from 23 to 79C°, with the first segment being increased from 23 to 58 C° and from 25 to 79 C° in the second segment.
- Finally, in the fifth stage (28th March), the load changed from 8kN and 10kN and the temperature increased from 25 to 65 C°.

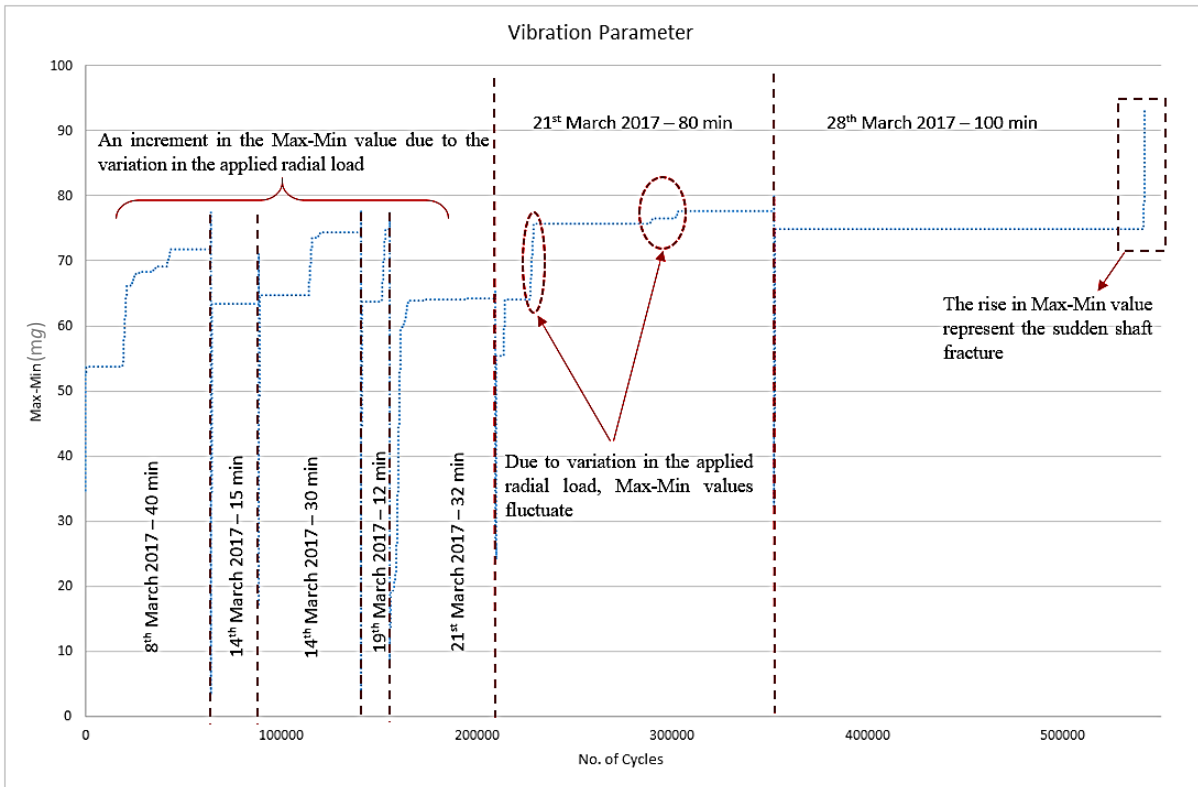


Figure 4. 59: The Max-Min value during the second test

This graph illustrated the Max-Min value of the vibration signal. It was recorded that the first stage experienced a variation of values starting from 0.0097 to 73.34 mg. The displayed fluctuation in the graph is due to the shaft running while bent, as well as variation of speed and radial load. The second stages logged data from 0.013 to 75 mg. Then, the third stage plotted data from 0.0096 to 75 mg. The fourth stage recorded values from 0.0059 to 77 mg. Finally, the last stage plotted values from 0.0053 to 93 mg.

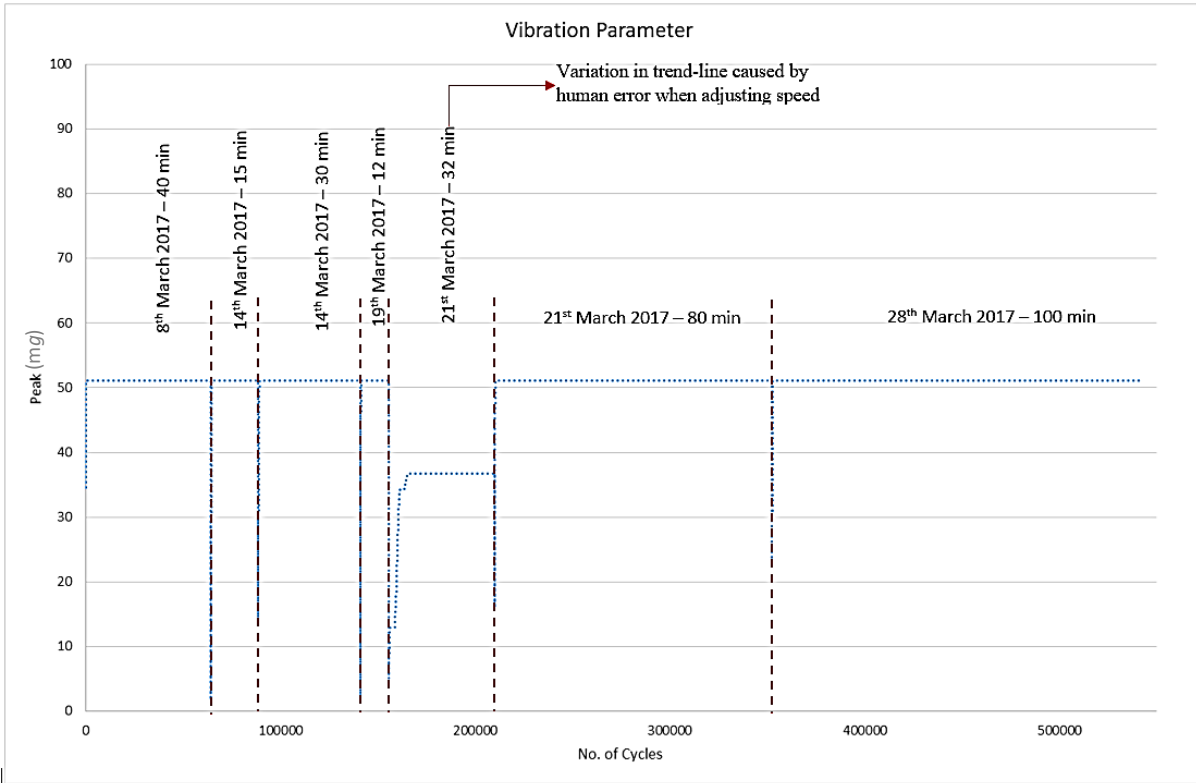


Figure 4. 60: Peak value during the second test

This graph clarified the peak value of the vibration signal. The first segment of the fourth stage recorded different peaks than the rest of the stages, from 0.005 to 36.7mg. This was due to the speed adjustment, as has already been explained. Therefore, the rest of the stages were logged as a straight line at 51.18015mg starting from 0.005mg until the shaft sheared and the peak increased to 51.18218mg.

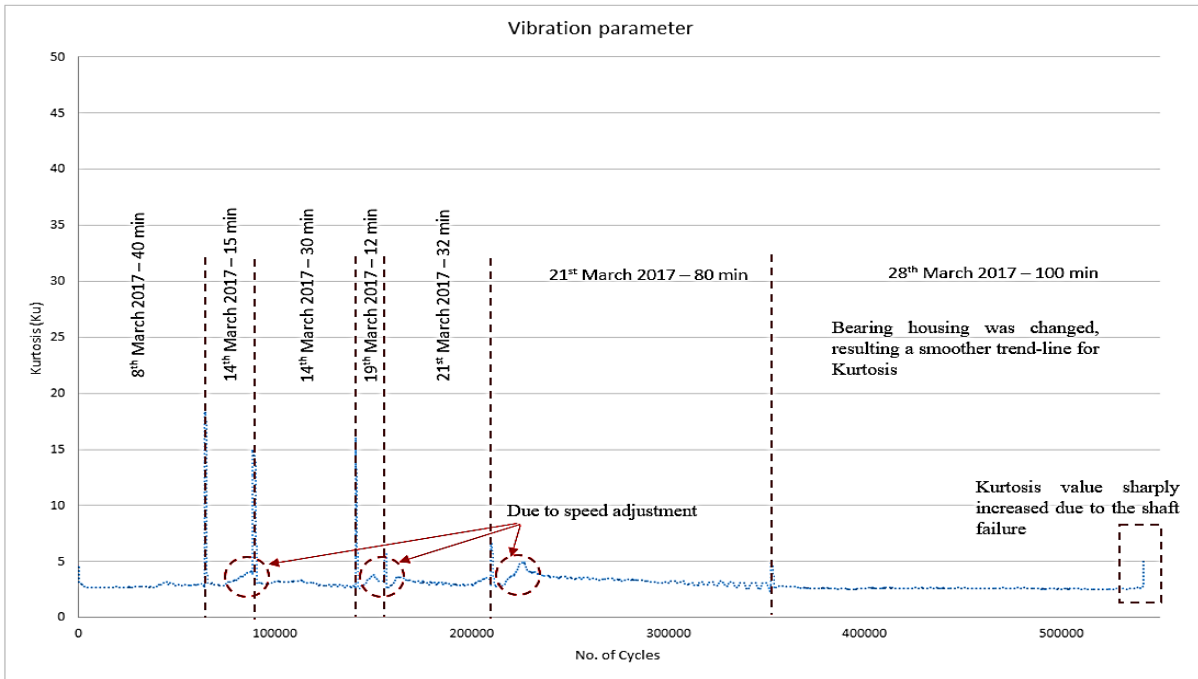


Figure 4. 61: Kurtosis value during the second bearing system failure test

This graph illustrated the Kurtosis value of the vibration signal. It was found that at the outset of each stage, there is an increase in the value as this indicates the high energy level in the vibration and signal owing to rotational speed. Then, a trend-line around 3 was noticed. At the last stage, it was noticed that the Kurtosis value increased sharply from 3 towards 5, indicating a catastrophic failure.

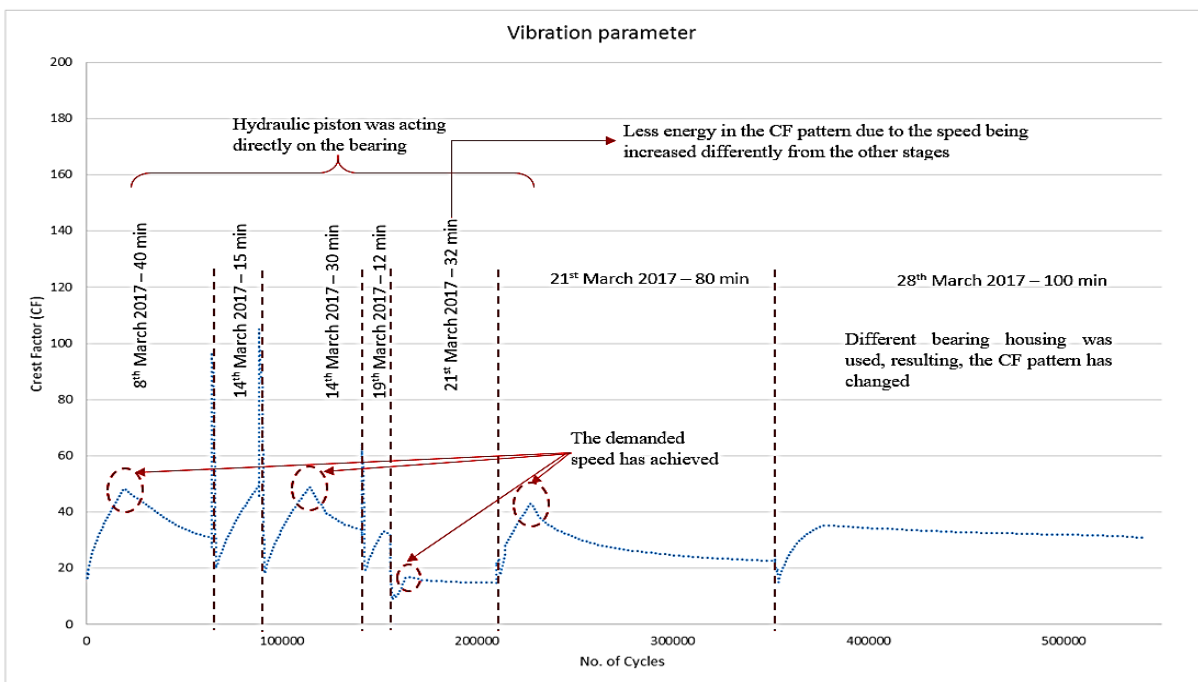


Figure 4. 62: CF value during the second test

This graph plotted the Crest Factor (CF) value, which is defined as the positive peak over the RMS value. At the beginning of each stage, high peaks can be observed owing to the high level of RMS, followed by a pattern of decreasing value as the RMS value increases. Therefore, the first stage experienced values from 0 to 19 at the start, then started increasing till 49 and decreasing to around 35. The second stage was similar to the first stage, with extra energy at the beginning of the first segment (from 0 to 21); this occurred due to the variation in the radial load. This then increased to reach around 49. The second part confirms the trend-line through increasing from 0 to 20 then later increased to 48 with and ending at 38. In the third stage, the CF value increased from being constant around 0 to 20 and increased to 32. In the fourth round, it increased from 0 to 15. The second part of the fourth stage was logged as increasing from 0 to 20 then increased to 42, after which the value decreased slightly to 21. The last stage verified a similar response to the others, increasing from 0 to 17, then increased to 37 and decreased to 32 until the shaft sheared. The CF value dropped to 30.4 significantly, indicating to a catastrophic failure occurred.

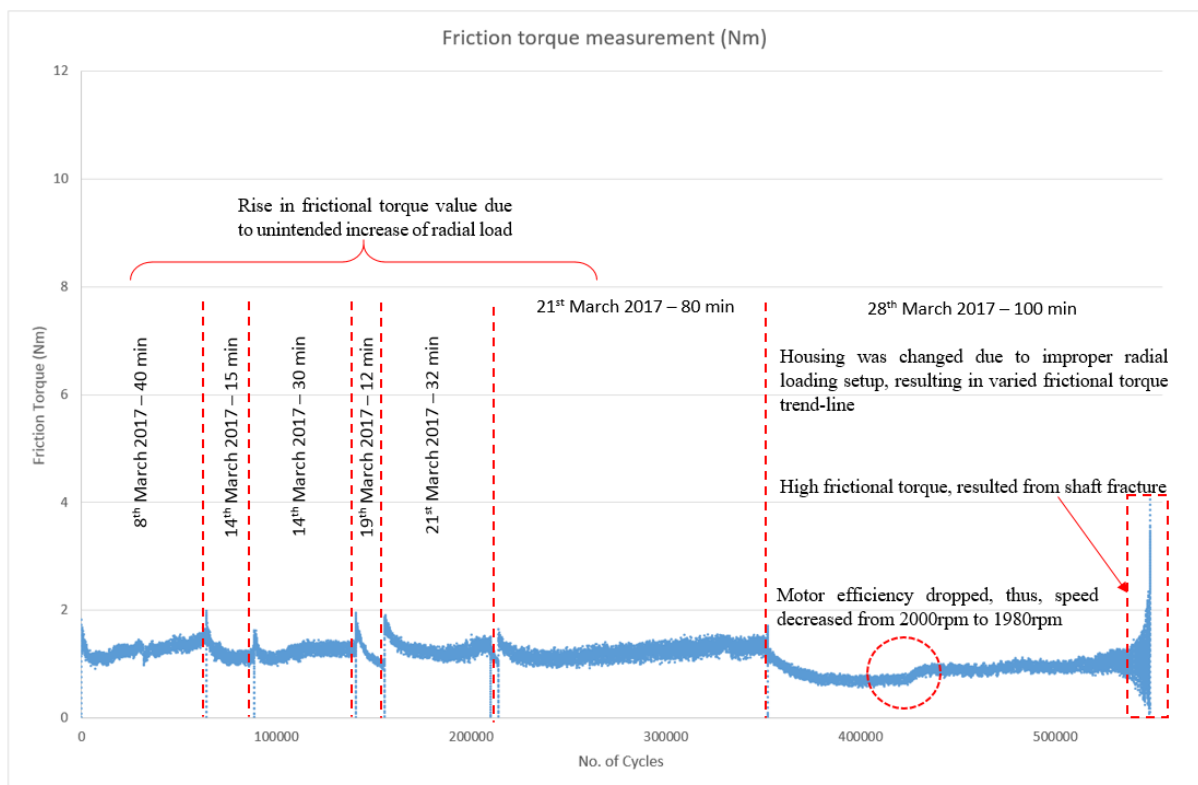


Figure 4. 63: Frictional torque during the second test

Figure (4.63) shows the friction torque measurement of the test bearing (6205-2RSH) during the second test. It can be observed that the torque showed a trend of increasing significantly at the beginning until the motor starts spinning, then dropping smoothly to follow another trend-

line owing to the load being applied. For instance, in the first round, the torque increased from 0.003 to 1.7Nm under 10kN of radial load, then fluctuating around 1.1Nm. A similar trend-line was followed in the second round. The third and fourth rounds recorded fairly similar results, reaching around 1.9Nm to start spinning the motor then changing to around 1.3Nm. The final round experienced the same trend-line at the beginning, but halfway through testing, the motor efficiency dropped down from 2000 rpm to 1980 rpm as this reflects the friction torque since the relation between the torque and rotational speed is proportional; this is shown in Figure (4.63) as a circle segment. Finally, at the end of the last round, the friction torque recorded a high changing in peaks, indicating growing fatigue in the main shaft as the torque rose to 4Nm, until finally, the system was aborted indicating the catastrophic failure.

Appendix J – Fourth Test: Bearing Life Test

This test considered 6kN instead of 10kN to avoid a heavy duty operation on the test element, as this causes initiation / propagation of failure by fatigue. Figure plots the logged data.

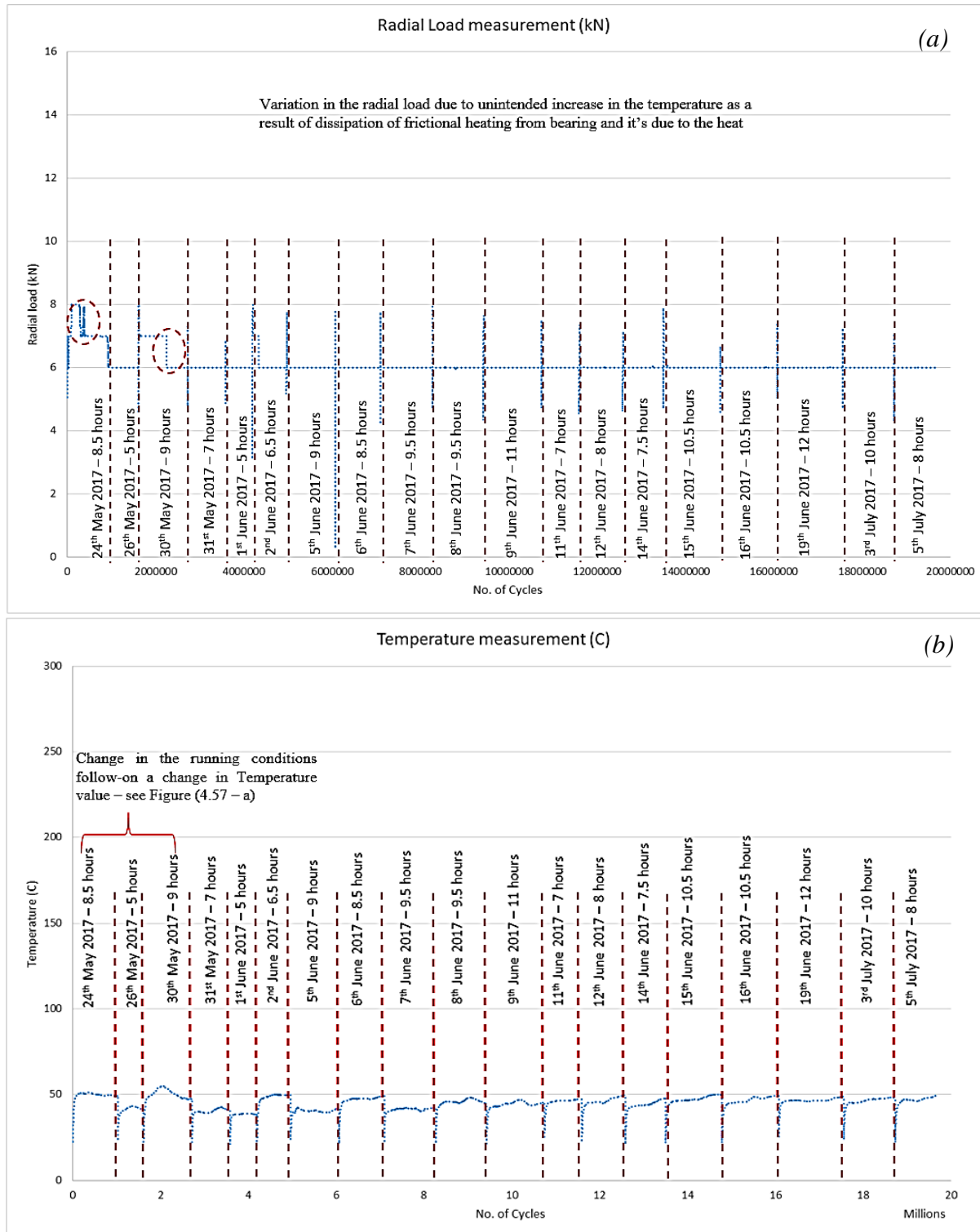


Figure 4.64: Logged data from the fourth sample – (a): applied radial load measurement and (b) operational temperature (C)

The temperature pattern increased smoothly from 22C° to 50C° in almost every stage; see Figure (4.64 – b). When the load varied the operational temperature fluctuated due to the high frictional action between the bearing elements, as observed Figure (4.64 – a & b).

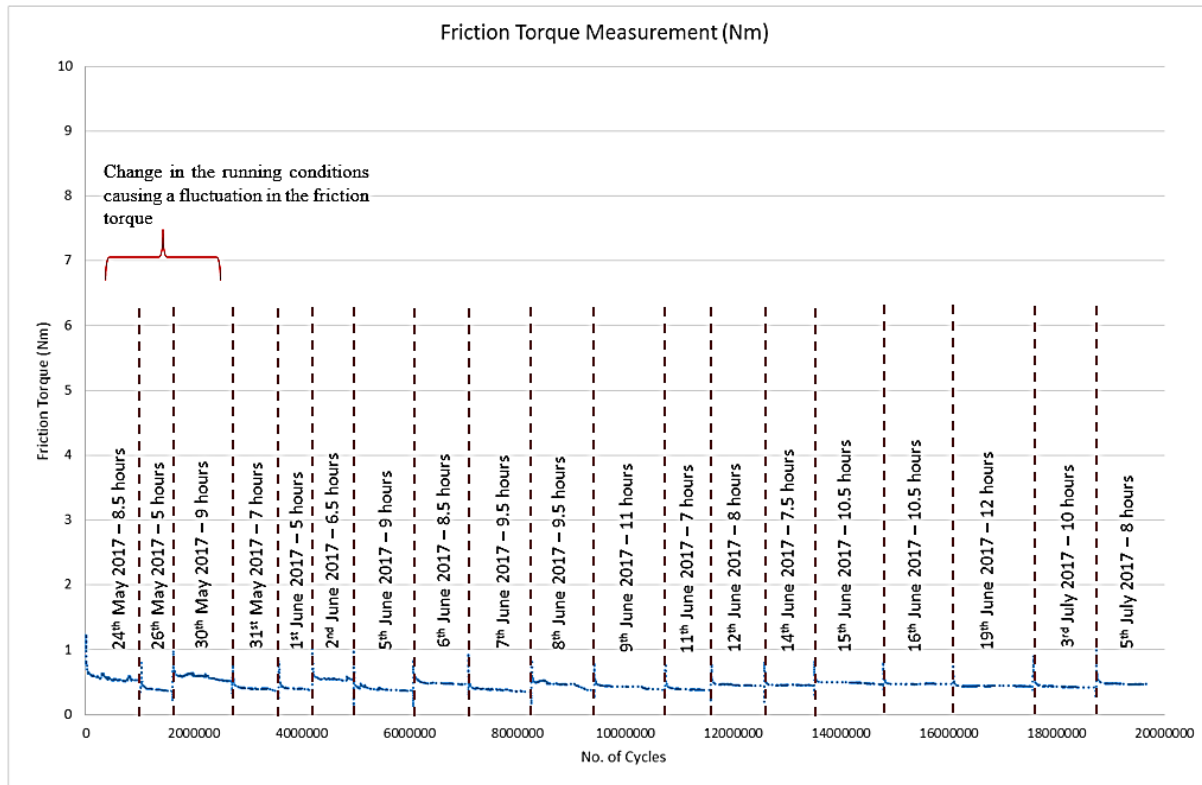


Figure 4. 65: Friction bearing torque (Nm)

Figure (4.65) shows the sensed friction bearing torque during the fourth test. The trend-line increased slightly, indicating that the bearing elements were experiencing fatigue. It started at around 0.541Nm on 31st May and reached approximately 0.6 Nm on 5th July, after 162 operational hours. This clearly indicates that the bearing was fatiguing which resulted in slight increase in the frictional torque.

When the theoretical life had been achieved (19th June), the trend-line experienced a slight change to 0.57, then carried on until it reached 0.6Nm after 162 operational hours. This can be interpreted as high frictional torque being obtained from the “test” bearing, illustrating that it was fatiguing and was undergoing the development of several failures in the bearing elements.

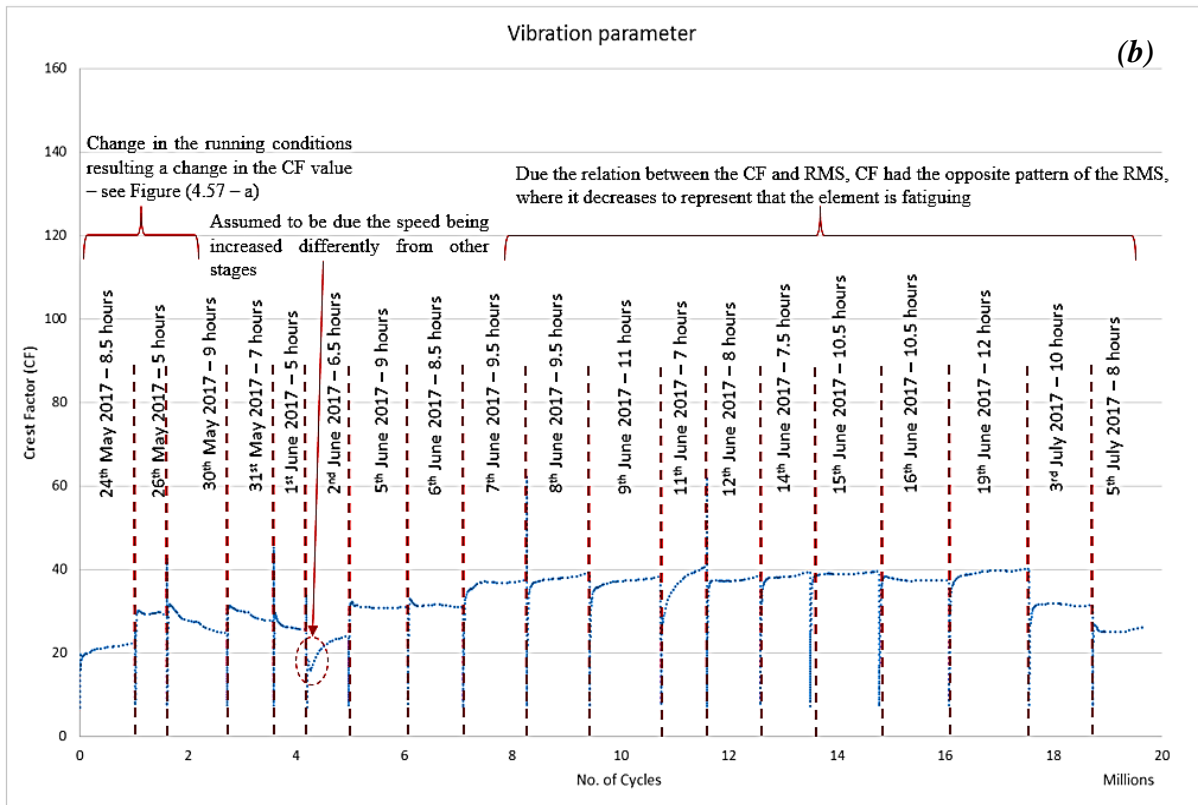
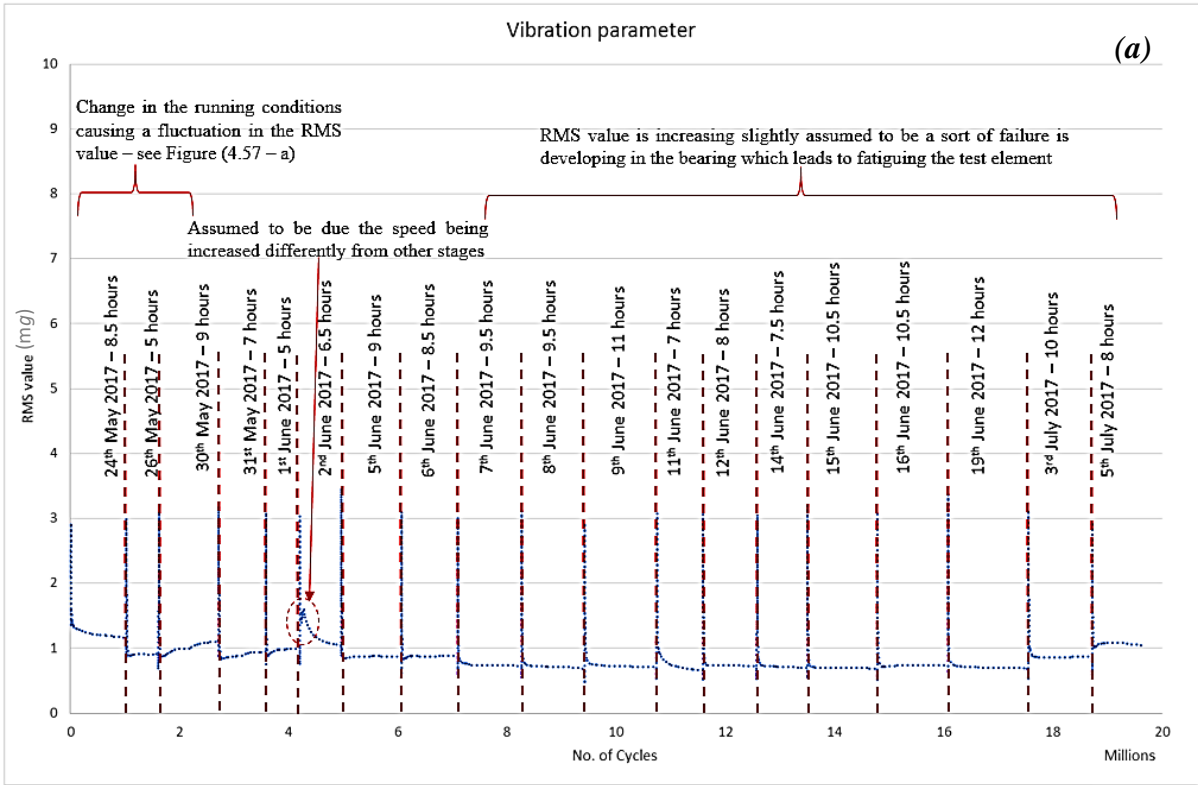


Figure 4. 66: Vibration parameters – (a): RMS level, (b): Crest Factor values

Figure (4.66 – a) shows that the RMS level started at around 1.3mg during the test on 24th May. It decreased slightly, towards 1mg, on 26th, 30th, 31st May and 1st June. After that, it returned to 0.7mg during the rounds from 5th to 19th June (after 144 operational hours), – confirming the development of some failures in the bearing elements. It increased from 0.7 to 0.75mg on 3rd July, then 1.13mg on 5th July. This proves that the bearing was fatiguing due to the high level of energy in the vibration parameter.

Figure (4.66 – b) plots the CF values for the fourth test. The test shows a pattern of the CF values elucidating the proportional relation with the RMS. It started at 20 on 24th May and increased slightly until it reached 40 on 19th June, after 144 hours. This pattern clarifies that the bearing elements were experiencing developing defects. The pattern of the CF value ended at 29 on 5th July, – assuming that the element was fatiguing.

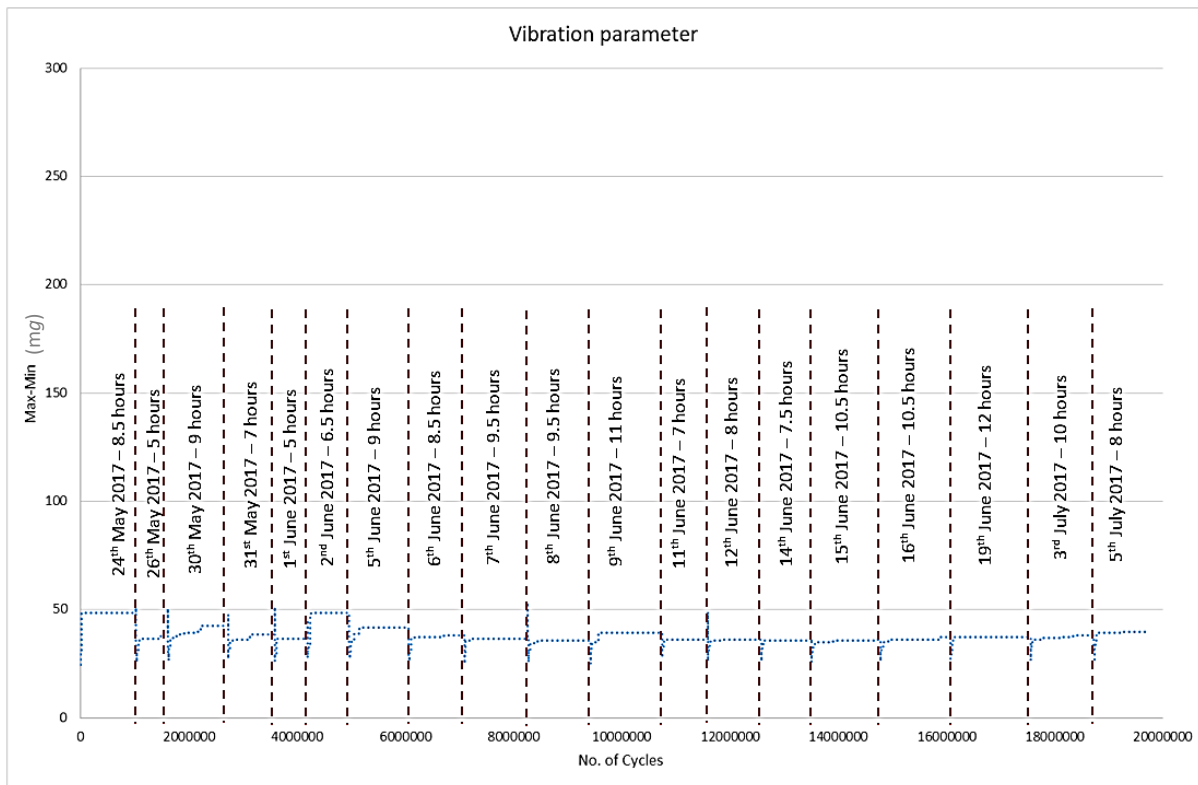


Figure 4. 67: Max-min value during the bearing life test

Figure (4.67) is a pictorial view of the max-min value obtained during the fourth test. Then, it followed a pattern of slight uniformed increase indicating that the bearing is fatiguing as the bearing had achieved 96 out of 125 hours. Therefore, it started increasing gradually from 36mg in 11th of June to reach 40mg in 5th July – after achieving 162 hours.

Appendix K – Image Subtraction Code

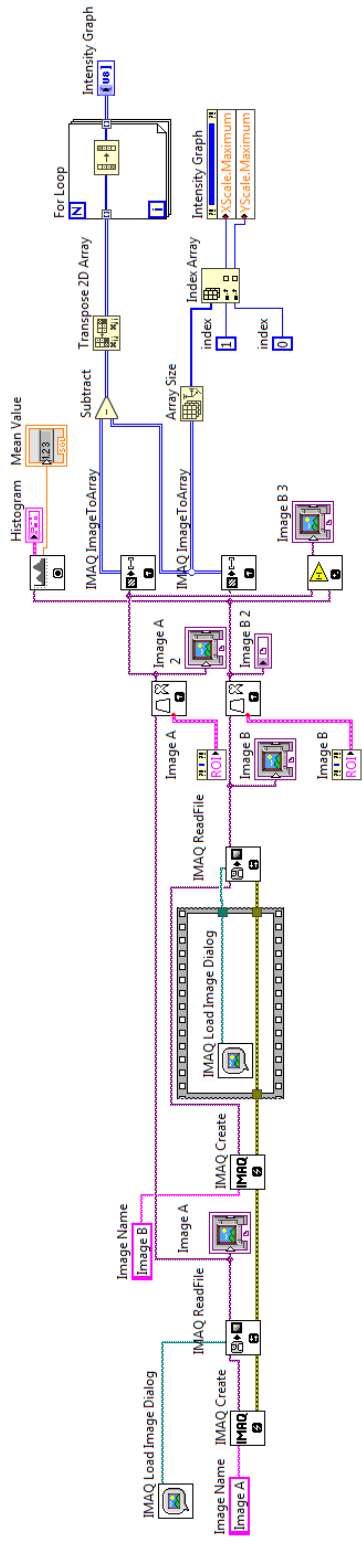


Figure 4. 68: Image Subtraction code in LabVIEW - block diagram pictorial

Appendix L – ARMA code in LabVIEW

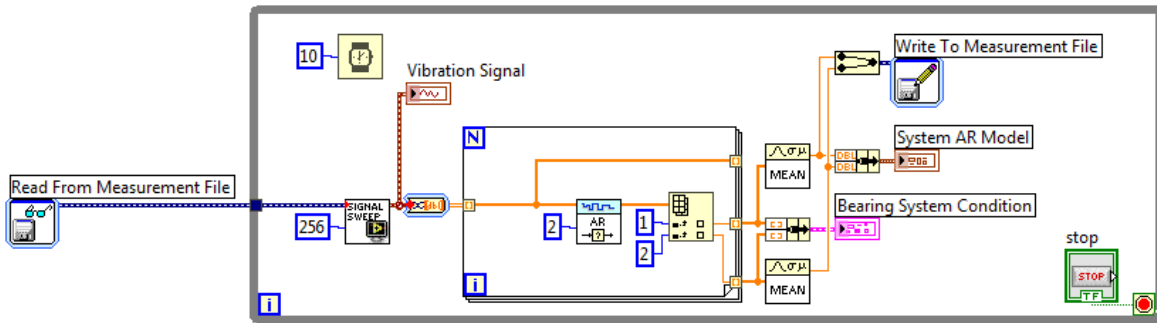


Figure 4. 69: Block diagram of the ARMA development

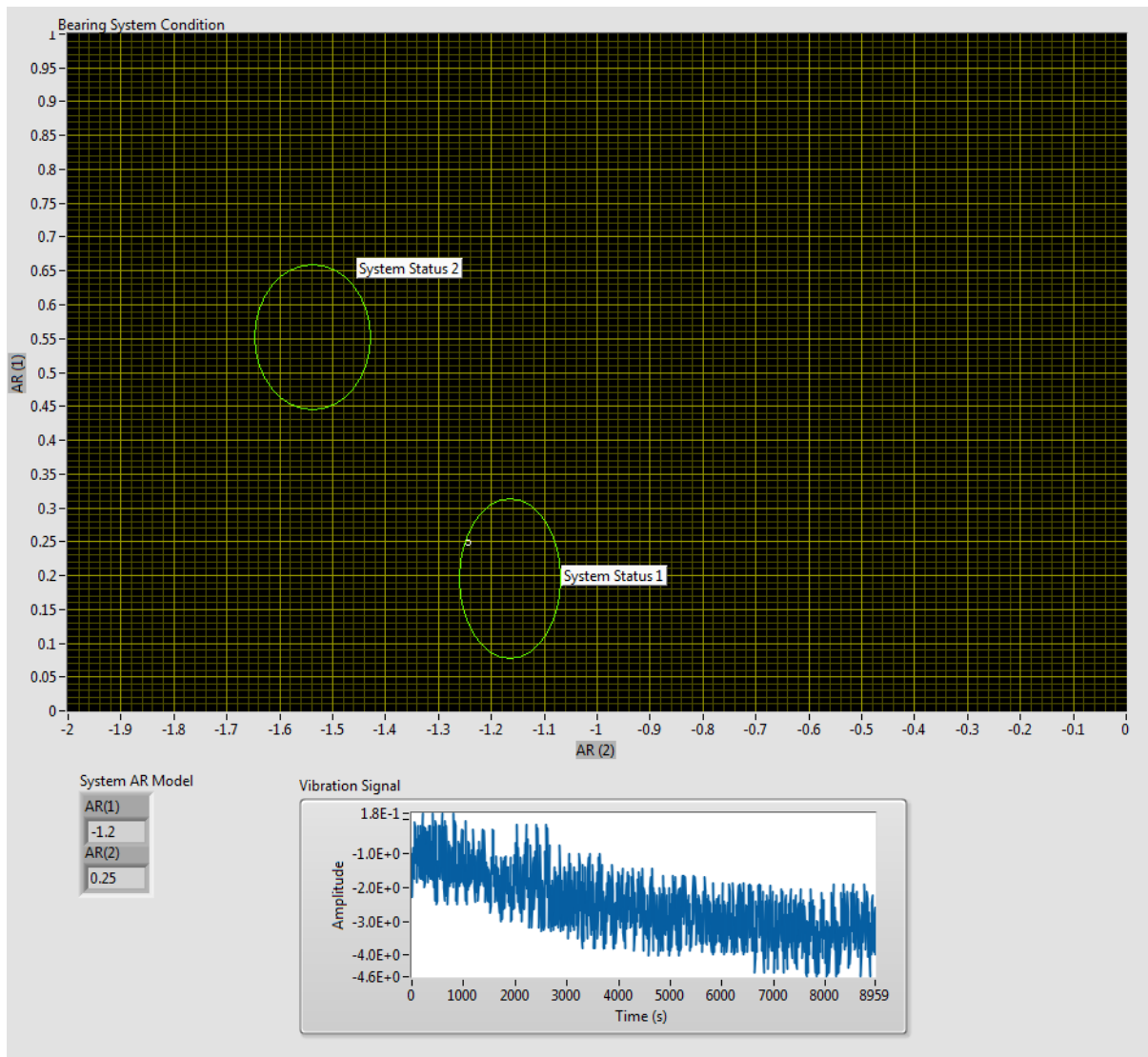


Figure 4. 70: Front Panel of the ARMA development in LabVIEW

Appendix M – Publications

Paper Title / Event	Location	Date	Description
i. <i>“Intelligent Management of Micro-scale Wind Turbine Bearings”</i>	JOST Institute – Annual Research Seminar Programme, Media Factory (ME109), University of Central Lancashire, Preston Lancashire, UK	15 th March 2016	Presentation – Main author
ii. <i>“Online Structural Health Monitoring for Oil and Gas Pipelines”</i>	Joint Conference: MFPT 2016 and ISA’s 62nd International Instrumentation Symposium, Dayton Convention Centre, Dayton, OH, USA	24 th – 26 th May 2016	Presentation – On behalf of the main author (Mazen Elwaseif)
iii. <i>“Intelligent Management of Wind Turbine Bearings”</i>	Joint Conference: MFPT 2016 and ISA’s 62nd International Instrumentation Symposium, Dayton Convention Centre, Dayton, OH, USA	24 th – 26 th May 2016	Presentation – Main author
iv. <i>“Monitoring Shaft Fatigue Using an Online System”</i>	30th International Congress & Exhibition on Condition Monitoring and Diagnostic Engineering Management, The Grange Hotel, Grange over Sands, Cumbria, UK	10 th – 13 th July 2017	Publication and Presentation – Main author
v. <i>“Life Guard Drone: An Autonomous Process of Search and Rescue”</i>	In Progress	-	Joint research paper

References

- Abhishiktha T., Ratna K. V., Dipankur K. S., V. Indrajaya, V. Hari K. (2016) '*A Review On Small Scale Wind Turbines*', Renewable and Sustainable Energy Reviews, 56, pp.1351-1371, doi: 10.1016/j.rser.2015.12.027
- Aeolos, (2017) '*1kW Wind Turbine*', Aeolos Wind Turbine 1kW Specifications, User manual, London, UK.
- Akash P. (2014a) '*A Presentation on Bearing*'. Module code (1429). Western Iowa tech community college. Available at: <http://www.slideshare.net/AKASH1001/bearing-42838274> [Accessed: 25 March 2015]
- Aleko, (2017), '*R4 Roof Wind Generator Top-Roof Mount Tower for Wind Turbine 4 Feet*', Aleko Production, User manual, Washington, USA.
- Ali B. (1999) '*4 Ton Hydraulic Bench Press data sheet*', User Manual, Model Number: SD0401, Retrieved from: https://www.alibaba.com/product-detail/4-ton-Bench-type-workshop-hydraulic_60535509259.html?spm=a2700.7724838.2017115.1.3c93b095OXjoVR&s=p, [Accessed: 25 March 2015]
- Arroyo I. (2016) '*Temperature Controller*', User manual, California, USA, pp. 1-60.
- Barden. P. B (2011) '*Bearing failure: causes and cures*', Schaeffler, Technical review, Plymouth, UK, pp. 1-15.
- Baydar, N. and B., A. (2003) '*Detection Of Gear Failures Via Vibration And Acoustic Signals Using Wavelet Transform*', Mechanical Systems and Signal Processing, 17(4), pp.787-804, doi:10.1006/mssp.2001.1435
- Belessiotis, V. And Delyannis, E. (2000) '*The History of Renewable Energies For Water Desalination*', Desalination, 128(2), pp.147-159, doi: 10.1016/S0011-9164(00)00030-8
- Benko, U., Petrovčić, J., Juričić, Đ., Tavčar, J., Rejec, J. and Stefanovska, A. (2004) '*Fault diagnosis of a vacuum cleaner motor by means of sound analysis*', Journal of Sound and Vibration, 276(3-5), pp. 781-806, doi: 10.1016/j.jsv.2003.08.041
- Berthold, H. (2005) '*Frequency of Causes for Failure*', Wind Energy Report Germany 2005, ISET Institut für Solare Energieversorgungstechnik, pp.Chapter 3.6.
- Bruel and Kjaer (1982) '*Introduction to vibration measurement*', Lecture Note no. BR0094, Nærum, Denmark, pp. 6-42.
- Bruel and Kjaer (1998) '*Vibration Measurement and analysis*', Lecture Note no. BA7676-12, Nærum, Denmark
- Canon (2017) '*Canon EOS 750D manual*', Product Specifications, New York, USA
- Chong P. K. (2013) '*Wind turbine Generator*', DoArm Engineering Co. Ltd., User manual, Korean, pp. 1-5.
- CPC (2000) '*Pressure Transducer Specifications and Installation Instructions*', User manual / guide – Technical Bulletin, Document Part#026-2105, [Online], Retrieved from: <http://www.emersonclimate.com/Documents/0262105Rev0%20Pressure%20Transducer.pdf> [Accessed 25 March 2017]

Cyndi N. M. (2007) '*Understanding Factors That Cause Shaft Failures*'. Getting the Most from Motors, Missouri, USA, pp. 1-4.

Damien H. (2003) '*Torque equation & calculation*', video & lesson transcript, [Online], Retrieved from: <http://study.com/academy/lesson/what-is-torque-definition-equation-calculation.html> [Accessed 16 August 2017].

El-Hajjar, M., Maunder, R. and Ng, S., (2012) '*Introduction to LabVIEW*', Lecture note, ELEC6021 Research Methods

Entezami, M. E. (2013) '*Condition Monitoring of Wind Turbine Brake system*', Renewable Energy, 42, pp. 175-182, doi:10.1016/j.renene.2012.04.031

Evans P. (2009) '*Optidrive E2 single phase output Installation and Operating Instructions*', User manual /guide, [Online], Retrieved from: <http://www.invertekdrives.com/client-uploads/download-manager/user-guides> [Accessed 16 Aug. 17]

Fenaflex (2014) '*Drive couplings*', User manual, UK, Section: 5, pp. 111-124.

Figliola, R.S. and E. Beasley, D. (2011) '*Theory and Design for Mechanical measurements*', Maintenance Science and Technology, 12(10), doi: 10.1088/0957-0233/12/10/701

Fischer, K., Besnard, F. and Bertling, L., (2012) '*Reliability-centered maintenance for wind turbines based on statistical analysis and practical experience*'. IEEE Transactions on Energy Conversion, 27(1), pp.184-195.

Fuentes, A. A., Vaipan, A. G., Navarro, L. A., Kypuros, J. A., Tarawneh, C. M. and Wilson, B. M. (2012) '*Thermal modelling of a railroad tapered-roller bearing using finite element analysis*', Journal of Thermal Science and Engineering Applications, 4(3), doi: 10.1151/1.4006273

Gan, T.H., Soua, S., Dimlaye, V. and Burnham, K., (2012) '*Real-time monitoring system for defects detection in wind turbine structures and rotating components*', In 18th World Conference on Non-destructive Testing, pp. 16-20.

Garcia, M. C., Sanz-Bobi, M. A. and Del Pico, J. (2006) '*SIMAP: Intelligent system for predictive maintenance*', Computers in Industry, 57(6), pp. 552–568. doi: 10.1016/j.compind.2006.02.011.

Gersch, W., Brotherton, T. and Braun, S., (1983) '*Nearest neighbor-time series analysis classification of faults in rotating machinery*', Journal of Vibration, Acoustics, Stress, and Reliability in Design, 105(2), pp.178-184.

Girdhar, P. and Scheffer, C. (2004) '*7 – oil and particle analysis*', Practical Machinery Vibration Analysis and Predictive Maintenance, pp. 168–220. doi: 10.1016/B978-075066275-8/50007-2.

Gonzalez, C. (2015) '*What is the difference between bearings?*', MachnieDesign, Technical Presentation, [Online], Ohio, USA, Retrieved from: <http://www.machinedesign.com/whats-difference-between/what-s-difference-between-bearings-1> [Accessed 17 Aug. 17]

Gritt, P.S. (2011) '*Brake Systems 101 energy conversion management*', Society of Automotive Engineers – SAE, [Online], Retrieved from: http://www.sae.org/students/presentations/brakes_by_paul_s_gritt.pdf [Accessed 16 Aug. 17]

- Hájek, P., (1998) *'Metamathematics of fuzzy logic'*, Springer Science & Business Media, (Vol. 4), pp. 1-7, ISBN 0-7923-5238-6.
- Harris TA, Kotzala MN (2006) *'Essential concepts of bearing technology'*, 5th edn, Taylor & Francis, New York, USA, ISBN-13:978-0-8493-7183-7
- Helmy, M., Onsy, A. Hussein, W. M., & El Sherif, I. (2014) *'Development of an Advanced Diagnostic System for Automotive Mechanical Transmissions'*, International Journal of COMADEM, 17(2), 39- 44. ISSN 1363-7681
- Hideyuki T. (1997) *'Introduction to Fuzzy Systems, Neural Networks, and Genetic Algorithms'*, pp. 3-33, P-ISBN: 978-1-46-13-7838-9, O-ISBN: 978-1-4615-6191.
- ISO 15243:2004 (2004) *'Rolling bearings – damage and failures – terms'*, characteristics and causes, International Organisation for Standardisation, Geneva, Switzerland
- ISO 20958:2013 (2013) *'Condition monitoring and diagnostics of machine systems – electrical signature analysis of three-phase induction motors'*, International Organisation for Standardisation, Geneva, Switzerland
- ISO 281:2007 (2007) *'Rolling bearings – dynamic load ratings and rating life'*, International Organisation for standardisation', Geneva, Switzerland
- J. P. Petersen. (2010a) *'Artificial Neural Network'*, Python Pattern Recognition – PyPR's documentation, [Online], Kongens Lyngby, Denmark.
- Jaber, A.A. and Bicker, R. (2014) *'The State of the Art in Research into the Condition Monitoring of Industrial Machinery'*, International Journal of Current Engineering and Technology, 4(3), E-ISSN 2277-4106, P-ISSN 2347-5161
- Jain, L. C. and de Silva, C. W. (1998) *'Intelligent Adaptive control: Industrial applications'*, CRC press, (Vo.6), ISBN 9780849398056
- Jason R. S., Thomas G. H. and Ronald G. H. (2004) *'Bearing fault detection via autoregressive stator current modelling'*, IEEE Transactions On Industrial Applications, 40(3), pp. 740-747, doi: 0093-9994/04\$20.00
- Katz S. and Mike S., (2017) *'Bearing failure and analysis'*, BearingTips, Technical Article, Chatsworth, California, USA.
- Kaydon (2014) *'Kaydon Bearing Solutions - Bearing load scenarios; angular contact, radial contact, four point contact'*, Technical review, Michigan, USA
- Klein, R., Masad, E., Rudyk, E. and Winkler, I., (2014) *'Bearing diagnostics using image processing methods'*, Mechanical Systems and Signal Processing, 45(1), pp.105-113.
- Kothamasu, R. and Huang, S. H. (2007) *'Adaptive Mamdani fuzzy model for condition-based maintenance'*, Fuzzy Sets and Systems, 158(24), pp. 2715–2733. doi: 10.1016/j.fss.2007.07.004.
- Kuhnell, B.T. (2004) *'Wear in rolling element bearings and gears - how age and contamination affect them'*, A Noria Publication Machinery Lubrication, Tulsa, USA

Kunal (2011) *What is Image Processing*, [Online], New Delhi, India, Available at: <https://www.engineersgarage.com/articles/image-processing-tutorial-applications> [Accessed 20 September 2017]

Leavers V.F., (2005) *Classifying wear debris particles with automatic image analysis*, A Noria Publication Machinery Lubrication, Tulsa, USA

Leturiondo, U., Salgado, O., Galar, D. and Mishra, M. (2016) *Methodology for the Estimation of the Fatigue Life of Rolling Element Bearings in non-stationery Conditions*, pp. 413–423, doi: 10.1007/978-3-319-20463-5_31

Lubsys (2003) *SKF bearing knowledge – Alignment*, User manual, [Online], Sweden, Retrieved from: http://www.lubsys.com/knowledge/knw_align01.htm [Accessed: 28 Nov. 15].

Maeda, R., Pitteloud J. D., Zhang P., Bechberger M., Whale J., Jacobson N., Renz K., Spinadel E., Gipe P., He D., Hossain J., Dimitrov M., Eklund E., Moreno C., Benhamou K., Dziamski P., Bryner C., Konechenkov A., Pirazzi L., Prokopenko A., Kasonen T., Rim M. S., Sanz B., Shen D., Son C. Y. Kharul R., Byrne R., Twu Y., Petersen M. V., Klimbie B., Mirza I., Aberu C. and Cruz I., (2013) *Small Wind World Report 2013*, Endurance wind power, World Wind Energy Association, Bonn, Germany, pp. 1-23.

Magtrol (2012) *Hysteresis Brakes and Clutches*, HB/HC User's manual, [Online] New York, USA, pp.1–5, Retrieved from: http://www.electrometers.com/Assets/PDF_files/Magtrol/Dynamometers/hysteresis.pdf [Accessed: 17 October 2016]

Magtrol (2013) *Series in-line torque transducers*, User manual / datasheet, [Online] New York, USA, pp. 1-5, Retrieved from: <http://www.magtrol.com/datasheets/tm-series.pdf> [Accessed: 17 October 2016]

Magtrol (2014) *Signal Breakout Box SBB14*, User manual / datasheet, [Online] New York, USA, pp. 1-3, Retrieved from: <http://www.magtrol.com/datasheets/sbb14.pdf> [Accessed: 17 October 2016]

Magtrol (2014a) *M-TEST 7.0 software*, User manual, [Online] New York, USA, pp. 1-10, Retrieved from: <http://www.magtrol.com/manuals/mtest7manual.pdf>[Accessed: 17 October 2016]

Magtrol (2014b) *VM series proportional amplifier/controller*, User manual / datasheet [Online] New York, USA, pp.1-3, Retrieved from: <http://www.magtrol.com/datasheets/vm8.pdf> [Accessed: 17 October 2016]

Magtrol (2015a) *Series Miniature Inline Couplings*, User manual, [Online] New York, USA, pp. 1-18, Retrieved from: <http://www.magtrol.com/datasheets/mic-coupling.pdf>[Accessed: 17 October 2016]

Magtrol (2015b) *BHB series blower cooled Hysteresis brakes*, User manual, [Online] New York, USA, pp. 1-11, Retrieved from: <http://www.magtrol.com/datasheets/bhb.pdf> [Accessed: 17 October 2016]

Magtrol (2015c) *Digital Signal Processing (DSP7000) series high-speed programmable Dynamometer controllers*, [Online], User manual, New York, USA, pp. 2-10, Retrieved from: <http://www.magtrol.com/datasheets/dsp7000.pdf>

- Mahdi K. (2006) '*Rolling Element Bearing Fault Diagnostic Using the blind deconvolution technique*', Doctoral dissertation, Dissertation Code: 16432, [Online], Queensland University of Technology, Iran, Retrieved from: <http://eprints.qut.edu.au/16432/> [Accessed 16 Aug. 17].
- Mahon N. M. (2013) '*Design of Wind Turbines*', *Lecture notes*, [Online], Retrieved from: http://www.niallmcmahon.com/msc_res_notes_wind_1_4_1.html [Accessed: 10 Feb. 17].
- Manney, D. (2014) '*Avoiding bearing misalignment*', Technical article, L&S electronics, [Online], Michigan, USA, Retrieved from: <https://lselectric.com/avoiding-bearing-misalignment/> [Accessed 19 Aug. 17]
- Marlec., (2013), '*Rutland FM910-4 Furlmatic Windcharger*', Marlec Renewable power, User manual, Doc No: SB-124, Issue D14.01.13, Corby, UK.
- Michael B., Laura Wisland, Jeff Deyette, Jeremy Richardson and Sam Gomberg (2015) '*Renewable energy: Unlimited resources*', Clean Energy, Union of Concerned Scientists, Massachusetts, USA.
- Mitchell, M. (1998) '*An introduction to genetic Algorithms*', MIT press, ISBN 0-262-13316-4 (HB), 0-262-63185-7 (PB)
- Mohammed. Z. M. A., (2014) '*Examples of Rolling Bearing Damage*', SlideShare Engineering, Technical Presentation, [Online], Retrieved from: <https://www.slideshare.net/mhzin68/fag-roller-bearing-damages-excellent> [Accessed 19 Aug. 17]
- Nam, J.S., Park, Y.J. and Chang, H.S. (2016) '*Dynamic life prediction of pitch and yaw bearings for wind turbine*', *Journal of Mechanical Science and Technology*, 30(1), pp. 249–256. doi: 10.1007/s12206-015-1228-1.
- National Instrument (2007) '*Machine condition monitoring*', Technical library, [Online], Berkshire, UK, Retrieved from: <http://www.ni.com/white-paper/6511/en/> [Accessed: 1 December 2015].
- National Instrument (2007) '*Methods for performing order analysis (Sound and Vibration measurement suite)*', Technical Library, [Online], Berkshire, UK, Retrieved from: http://zone.ni.com/reference/en-XX/help/372416A-01/svtconcepts/oa_methods/ [Accessed: 22 January 2016].
- National Instrument (2007) '*Vibration signals and transducers (Sound and Vibration measurement suite)*', User manual, [Online], Berkshire, UK, Retrieved from: http://zone.ni.com/reference/en-XX/help/372416A-01/svtconcepts/vbr_sig/ [Accessed 17 Aug. 17]
- National Instrument (2011) '*NI myRIO-1900 user guide and specifications*', User manual and specifications, Berkshire, UK, pp. 1-20.
- National Instrument (2014b) '*6003 device specifications*', User manual, Retrieved from: <http://www.ni.com/pdf/manuals/374259a.pdf> [Accessed 25 Mar. 2017].
- National Instruments (2014a) '*Specifications of NI cDAQ-9191*', User manual, Berkshire, UK, pp. 1-14.

- Neale, M. J. and Woodley, B. (2007) '*Condition monitoring methods and economics*', Symposium of the Society of Environmental Engineers. pp. 1-15.
- Nic, S. (2013) '*New safety brake for small wind turbines*', Windpower Engineering and Development, Suco Technologies Inc., Florida, USA.
- Nivedh, B. S. (2014) '*Major failure in the wind turbine components and the importance of periodic inspection*', Wind Action Organisation, New York, USA.
- NMB (2014) '*Ball bearing load ratings and life calculations – Miniature Precision Ball Bearings*', Technical Article, [Online], Tokyo, Japan, Retrieved from: <http://www.nmbtc.com/bearings/engineering/catalog-downloads-2/> [Accessed 19 Aug. 17].
- Noria C. (2010) '*How contaminants influence bearing life*', A Noria Publication Machinery Lubrication, [Online], Tulsa, USA, Retrieved-from: <http://www.machinerylubrication.com/Read/28999/contaminants-bearing-life> [Accessed 16 August 2017]
- NSK (2010) '*The right fit prevents premature wear*', Technical Insight, Motion and Control, Ref: TI/E/0109, pp. 1-3.
- NTN., (2013) '*Shaft & housing fits*', Technical Data, Illinois, USA, pp. 1-10.
- Oberhammer, J., Tang, M., Liu, A.Q. and Stemme, G., (2006) '*Mechanically tri-stable, true single-pole-double-throw (SPDT) switches*', Journal of Micromechanics and Microengineering, 16(11), p.2251.
- Olivia (2011) '*Difference between roller bearing and ball bearing*', Technical Article, [Online], Retrieved from: <http://www.differencebetween.com/difference-between-roller-bearing-and-vs-ball-bearing/> [Accessed 19 Aug. 17]
- Onsy, A. (2013) '*A New Acoustic Emission Remote Sensing System: an Experimental Validation of Wheel Bearing Condition Monitoring*', SAE International Journal Aerospace, 6(2), pp: 534 – 539, doi: 10.4271/2013-01-2221
- Onsy, A., Bicker, R. & Shaw, B.A. (2010) '*Intelligent Diagnostic Health Management of Power Transmission Systems: An Experimental Validation*', International Journal of COMADEM, 13(2), 46-58. ISSN 1363-7681
- Onsy, A., Bicker, R. & Shaw, B.A. (2013) '*Predictive Health Monitoring of Gear Surface Fatigue Failure Using Model-Based Parametric Method Algorithms; An Experimental Validation*', SAE Int. J. Aerosp. 6(1), doi: 10.4271/2013-01-0624
- Onsy, A., Shaw, B.A. & Jishan, Z. (2011) '*Monitoring the Progression of Micro-Pitting In Spur Geared Transmission Systems Using Online Health Monitoring Techniques*', SAE International Journal Aerospace, 4(2), pp: 1301 – 1315, doi: 10.4271/2011-01-2700.
- Paresh G. (2004) '*Practical Machinery Vibration Analysis and Predictive Maintenance*', Elsevier, ISBN: 0750662751
- PCB (2015) '*IMI sensors - A PCB Piezotronics DIV.*', User manual, New York, USA, pp. 2-8.

- Peacock, A.D., Jenkins, D., Ahadzi, M., Berry, A. and Turan, S. (2008) '*Micro wind turbines in the UK domestic sector*', *Energy and Buildings*, 40(7), pp. 1324–1333. doi: 10.1016/j.enbuild.2007.12.004.
- Peng, C., Xianke, H. and Jianming, X. (2009a) '*Miniature Relay – JZC-11*', User manual, Retrieved from: <https://www.sparkfun.com> [Accessed 25 Mar. 2017]
- Peng, Z. and Kirk, T. B. (1999) '*Wear particle classification in a fuzzy grey system*', *Wear*, s 225–229, pp. 1238–1247. doi: 10.1016/S0043-1648(98)00400-1.
- Radu, C. (2010) '*The Most Common Causes of Bearing Failure and the Importance of Bearing Lubrication*', [Online], RKB Technical review, Retrieved from: http://www.rkbbearings.com/admin/gest_docs_res/attach1/1271884609.pdf [Accessed 25 March 2016]
- Rafael G. and Richard W. (2008) '*Digital Image Processing*', 3rd Edition, Prentice Hall, Wesley, ISBN 0-13-168728-x 978-0-13-168728-8
- RenewableUK (2015) '*Small & Medium Wind Technologies*', Technical review, London, UK.
- Rob B. (2017) '*The Truth about Small Wind Turbines*', Solacity Inc., [Online], Ontario, Canada, Retrieved from: <https://www.solacity.com/small-wind-turbine-truth/> [Accessed: 16 Aug. 17]
- Roberds, K. (2017) '*Bearing Functions – Stability support*', SlidePlayer, [Online], Retrieved from: <http://slideplayer.com/slide/2623804/> [Accessed: 28 November 2015].
- Rofe, S., (1997) '*Signal processing methods for gearbox fault detection*'. Technical Report, DSTO-TR-0476
- Samuel, P. D. and Pines, D. J. (2005) '*A review of vibration-based techniques for helicopter transmission diagnostics*', *Journal of Sound and Vibration*, 282(s 1–2), pp. 475–508. doi: 10.1016/j.jsv.2004.02.058.
- Sarah Bray (2011) '*Wind and solar – Why Renewable Energy?*' – Clean Line Energy Partners, Technical review, Houston, USA
- Simmal (2009) '*Automotive case study for a client of Simmal*', User manual, [Online], Preston Lancashire, UK, Retrieved from: <http://www.simmal.com/project/automotive/> [Accessed: 17 October 2016].
- Singh, S., Kumar, A. and Kumar, N. (2014) '*Motor current signature analysis for bearing fault detection in mechanical systems*', *Procedia Materials Science*, 6, pp. 171–177. doi: 10.1016/j.mspro.2014.07.021.
- SKF (1994) '*Corrosion – deep-seated rust and fretting corrosion*', [Online] Technical Review, Gothenburg, Sweden, Retrieved from: <http://www.skf.com/cn/en/products/bearings-units-housings/roller-bearings/principles/troubleshooting/bearing-failures-and-their-causes/bearing-damage/corrosion/index.html> [Accessed: 17 October 2016]
- SKF (2008) '*Recommendation fits*', [Online] Technical Review, Gothenburg, Sweden, Retrieved from: <http://www.skf.com/uk/products/bearings-units-housings/ball-bearings/principles/application-of-bearings/radial-location-of-bearings/selection-of-fit/recommended-fits/index.html> [Accessed: 17 October 2016].

SKF (2013) '*SKF Insight*[®] - Next generation condition monitoring', [Online] Technical Review, Gothenburg, Sweden, Retrieved from: <http://www.skf.com/uk/products/condition-monitoring/skfinsight.html> [Accessed: 17 October 2016].

SKF (2017a) '*Single row Deep-groove ball bearing – 6205-2RSH*', User manual, [Online] Gothenburg, Sweden, Retrieved from: <http://www.skf.com/uk/products> [Accessed 25Mar. 2017]

SKF (2017b) '*Single row Cylindrical roller bearings – NJ 205 ECP*', User manual, [Online], Gothenburg, Sweden, Retrieved from: <http://www.skf.com/uk/products> [Accessed 25Mar. 2017]

Stanford research systems (2012) '*Calibrate Steinhart-Hart coefficients for Thermistors*', [Online], UK, Retrieved-from: <http://www.thinksrs.com/downloads/PDFs/ApplicationNotes/LDC%20Note%204%20NTC%20Calculator.pdf> [Accessed 16 Aug. 17]

Stefan G. and Jean P. (2014) '*Small Wind World Report - 2014 Update*', New Energy, World Wind Energy Association, Bonn, Germany, pp. 1 -15

Suhas, S. J. (2010) '*Fundamentals of limits and fits*', Module code: ME216, Engineering Metrology, [Online], Mumbai, India, Retrieved from: <http://www.me.iitb.ac.in/~ramesh/courses/ME338/metrology6.pdf> [Accessed 16 Aug. 17]

Sukhjeet Singh, Amit Kumar and Navin Kumar (2014) '*Detection Of Bearing Faults In Mechanical Systems Using Motor Current Signature And Acoustic Signatures*', Procedia Materials Science, Vol.6, pp. 171-177, doi: 10.1016/j.mspro.2014.07.021.

Takoutsing, P., René W., Mohand O., Fouad S., Tommy A. T. and Gabriel E. (2014), '*Wind Turbine Condition Monitoring: State-of-the-Art Review*', New Trends, and Future Challenges, Energies, 7(4), pp.2595–2630

Tallian TE. (1992) '*Failure atlas for Hertz contact machine elements*', 1st edn, ASME Press, New York, ISBN 0791800849, 9780791800843

Tan, C. K., Irving, P. and Mba, D. (2007) '*A comparative experimental study on the diagnostic and prognostic capabilities of acoustics emission, vibration and spectrometric oil analysis for spur gears*', Mechanical Systems and Signal Processing, 21(1), pp. 208–233. doi: 10.1016/j.ymsp.2005.09.015.

TEC Electric Motors Ltd. (2010) '*TEC Electric Motors Catalogue V3*', User manual [Online], Retrieved from: <https://inverterdrive.com/file/TEC-AC-Motor-Technical-Catalogue-IE1-IE2-v3> [Accessed 25 Mar. 2017]

Teja G. V., V. (2014) '*Chapter IV – learning from failures*', Lecture note, Module code: Mi 291, [Online] Slideshare.net, Retrieved from: <https://www.slideshare.net/varunteja7330/mi-291-chapter-4-learning-from-failure> [Accessed 25 Mar. 2017].

Thakar D. (2014) '*Bearing failure and its Causes and Countermeasures*', SlideShare Engineering, [Online], Retrieved from: <https://www.slideshare.net/dutt4190/bearing-failure-and-its-causes-and-countermeasures> [Accessed 16 Aug. 17]

Timken (2014) '*Bearing Damage Analysis with Lubrication Reference Guide*', User manual, Castleford, UK, pp. 1-40.

V. Mulani (2015) *'Metrology and instrumentation'*, Technical review, Unit 3: Fit and Tolerances, pp. 1-15.

Vallen (2006) *'AE Measurement Testing'*, Vol.6, [Online], Munich, Germany, Retrieved from: <http://www.vallen.de/zdownload/pdf/sea204E.pdf> [Accessed 16 August 2017]

Von Gesseneck, J.J., Caers, B., Overmeire, M.V., Lefeber, D., Vanderborght, B. and Schemuurmans, P. (2016) *'A torque-based method for the study of roller bearing degradation under poor lubrication conditions in a lead-bismuth environment'*, Nuclear Engineering and Design, 305, pp. 121–131.

Walker, J. O.S. (2005b) *'The physics of braking systems'*, StopTech LLC, [Online], Retrieved from: <http://www.stoptech.com/docs/media-center-documents/the-physics-of-braking-systems> [Accessed 16 Aug. 17]

Wes C. and Rick James (2013) *'Using a Grind Cage for In-Service Grease Analysis'*, A Noria Publication Machinery Lubrication, Tulsa, USA

William G. F., T.M McGinnity, and L.P. Maguire (2001) *'Fault diagnosis of electronic systems using intelligent techniques: a review'*, IEEE transactions on systems, Man, and Cybernetics, Part C, 31(3), pp: 269-281, doi: 10.1109/5326.971655

Windside., (2017), *'WS-0,30C Dimensions and technical info'*, OY Windside Production, User manual, Viitasaari, Finland, pp. 1.

Yates, T. (2015) *'UK wind energy database (UKWED)'*, RenewableUK, London, UK.

Zaretsky, E.V., (1997) *'A. Palmgren Revisited: A Basis for Bearing Life Prediction'* 97N24842.